Isotopic Enrichments of lanthanide based single molecule magnets

Jessica Flores Gonzalez

Jessica Flores Gonzalez. Isotopic Enrichments of lanthanide based single molecule magnets. Inorganic chemistry. Université de Rennes, 2019. English. NNT : 2019REN1S064 . tel-02511872

HAL Id: tel-02511872
https://theses.hal.science/tel-02511872v1

THESE DE DOCTORAT DE

L'UNIVERSITE DE RENNES 1
COMUE UNIVERSITE BRETAGNE LOIRE

ECOLE DOCTORALE N° 596
Matière Molécules et Matériaux
Spécialité : Chimie Moléculaire et Macromoléculaire

Par
Jessica FLORES GONZALEZ

Isotopic enrichment of lanthanide based single molecule magnets

Thèse présentée et soutenue à Rennes, le 03 Décembre 2019
Unité de recherche : Institut des Sciences Chimiques de Rennes ISCR (UMR CNRS-6226)
Thèse N° :

Rapporteurs avant soutenance :

Floriana TUNA, Directrice de Recherche
Université de Manchester

Myrtil KAHN, Directrice de Recherche
Laboratoire de Chimie de Coordination de Toulouse

Composition du Jury :

Floriana TUNA, Directrice de Recherche
Université de Manchester

Myrtil KAHN, Directrice de Recherche
Laboratoire de Chimie de Coordination de Toulouse

Valérie MARVAUD, Directrice de Recherche
Sorbonne Université

Marc FOURMIGUÉ, Directeur de Recherche
Université de Rennes 1

Olivier CADOR, Professeur
Université de Rennes 1
Directeur de thèse

Fabrice POINTILLART, Chargé de Recherche
Université de Rennes 1
Co-directeur de thèse

ACKNOWLEDGEMENTS

« There is a driving force more powerful than steam,
electricity and nuclear power: the will.»
Albert Einstein

FIRST of all, I am grateful to the whole jury: to Marc Fourmigué, president of the jury, to Floriana Tuna and Myrtil Kahn, for having accepted to referee this manuscript, and to Valerie Marvaud. I really appreciated your presence in that day and the constructive comments you gave me in order to improve my work.

« Le travail individuel permet de gagner un match mais c'est l'esprit
d'équipe et l'intelligence collective qui permet de gagner la coupe du monde. »
Aimé Jacquet

À première vue, l'écriture d'une thèse se perçoit comme un exercice individuel. Pourtant, c'est le résultat de plusieurs années d'un travail qui n'aurait pu aboutir sans l'aide de nombreuses personnes, que je souhaite remercier sincèrement ici.

Tout d'abord, mes remerciements vont tout naturellement à Olivier Cador et Fabrice Pointillart. Merci de m'avoir accordé votre confiance il y a un peu plus de trois ans en m'offrant la possibilité de réaliser cette thèse avec vous. Merci pour tout le temps que vous m'avez accordé, pour votre support et votre aide, et surtout toute votre patience. Déménager dans un pays étranger loin de tous ses proches n'est jamais une affaire facile, mais vous (avec tout le groupe MIM) m'avez accueillie comme l'une d'entre vous depuis la toute première minute. Je vous remercie pour tous ces midis, conférences, journées scientifiques, « afterworks » où petit à petit vous vous êtes convertie en ma petite famille dans le laboratoire. Car depuis, nous avons échangé beaucoup de moments qui resteront dans mes souvenirs. Quelques exemples, comme la « remontada » du Barça face au PSG, la coupe du monde, les repas de noël de l'équipe avec ces particularités, les interminables phrases avec signature Jessica *« si je suis là, je ne suis pas là-bas »* et tous vos efforts pour enrichir ma connaissance culturelle et française.

Le temps au laboratoire ce n'est pas toujours évident, surtout lorsque nous ne sommes pas chimiste de formation, je voudrais remercier Bertrand Lefeuvre pour tout son aide dans le laboratoire, sa grande disponibilité et la bonne humeur qu'il apporte toujours. J'aimerais également remercier Vincent Dorcet pour tout le temps passé au CDIFX en cherchant la bonne « pomme » qui voulait toujours se cacher. Merci pour sa patience et sa disponibilité pour nous former. J'aimerais remercier Thierry Guizouarn pour son aide lors des mesures physiques, surtout pendant la première année mais aussi lors des années qui ont suivi. Merci aux différents services (CDFIX, CMEBA…) sans lesquels une partie importante de mes caractérisations n'aurait pu avoir lieu. Je tiens à remercier Boris Le Guennic et Vincent Montigaud pour leurs calculs sur les différents systèmes, ainsi que pour tous nos échanges qui font que j'ai une meilleure compréhension de la théorie. En même temps, j'aimerais remercier

Kevin Bernot, pour toute son aide et collaboration dans les mesures en température mais aussi les différentes discussions lors des conférences.

Mais il n'y a pas que la vie au laboratoire, que m'a aidé à m'installer et me faire à cette nouvelle vie. J'aimerais remercier toutes les personnes qui ont contribué d'une façon ou une autre à faire de Rennes chez moi, et sans qui cela n'aurait pas été possible.

Les gens de l'Université : Nico, Julien, Rajaa, Mehdi, Carlo… pour la plupart nous avons commencé ensemble, nous avons passé plein de bons moments et aussi nous avons souffert sur la fin. Merci beaucoup pour toutes ces bières, sorties, dîners et conversations. Carlo et Haiet, j'adorais être seule dans le bureau mais au final c'était bien mieux lors qu'il a commencé à avoir un peu plus d'ambiance avec vous. Merci pour toutes nos conversations échangées le long de ces années. Merci Vincent, Claudia et Fabrice, vous avez été là depuis la première année, on a commencé avec beaucoup de *V&B*, *fox&friends*, les marchés les samedis, et puis plein de sorties et même des vacances! Sans oublier nos footings le dimanche matin avec Claudia, ou les différentes soirées avec Mattéo et maintenant Liam.

Les différents co-locataires, spécialement Laura, con quien he compartido mucho más que un piso: han sido muchos momentos y mini-viajes. Y Junto con María, David, Fátima, Carlos, Clara, Saskia… algunos habéis coincidido y otros no, pero todos os habéis convertido en personas muy importantes para mí. Han sido muchas las confidencias, las charlas y los momentos en general pasados juntos, como para darse cuenta de la bonita amistad que hemos creado.

Quisiera agradecer de todo corazón a Celia, inseparables casi desde el primer día de Universidad, por todos esos años juntas, por venir a verme y sobre todo por seguir dándome ánimos y haber estado tan presente todos estos años aun y la distancia. Así como quisiera agradecer a Ivan, un gran escritor y apoyo, cuya ayuda y ánimo es irrefutable.

"No olvides que la causa de tu presente es tu pasado.
Como la causa de tu futuro es tu presente. »

Pablo Neruda

He querido acabar con esta frase de Neruda, ya que tu presente es consecuencia de tu pasado, y en ello tienen que ver mucho tres personas a quienes cualquier palabra de agradecimiento se me quedaría corta. Papá, mamá, yaya… desde siempre habéis hecho todo lo que ha estado en vuestras manos por mí, y es vuestro apoyo incondicional que hace de mi la persona que soy ahora.

Et tant qu'on parle du présent, j'aimerais remercier infiniment une dernière personne très importante qui a beaucoup allégé les moments de crises pendant la rédaction et à posteriori. Jérôme, merci beaucoup pour toutes tes attentions, ton extrême patience et support pendant tous ces mois.

TABLE OF CONTENTS

CHAPER IV:

FROM OBLATE TO PROLATE IONS: Isotopic effect in $[Ln(tta)_3(L^2)]\cdot C_6H_{14}$, with Ln=Yb and Er

CHAPTER V:

SMMs PROPERTIES IN Er- POLYOXOMETALATE MOLECULES

CHAPTER VI:

POLARIZATION EFFECT IN THE SMMS PROPERTIES AND ISOTOPIC BEHAVIOR

CHAPTER VII:

ANNEXES:

Abbreviations

M	Magnetization
M_{sat}	Magnetization at saturation
H	Magnetic field
χ	Susceptibility
χ_{M}	Molar susceptibility
χ_{para}	Paramagnetic susceptibility
χ'	In-phase susceptibility
χ''	Out-of-phase susceptibility
χ_{dia}	Diamagnetic susceptibility
χ_{T}	Isothermal susceptibility
χ_{s}	Adiabatic susceptibility
T	Temperature
T_{B}	Blocking temperature
E	Energy
S	Total electronic spin momentum
S_{eff}	Effective Spin
L	Total orbital angular momentum
J	Total angular momentum
MW	Molecular Weight
GS	Ground state
ES	Excited state
RE	Rare earth
Z	Atomic number
EM	Electromagnetic
Ln	Lanthanides
CF	Crystal/ Ligand Field
SO	Spin-orbit
g_{J} / g	Landé factor
DC	Direct current
AC	Alternating current
SQUID	Superconducting Quantum Interference Device
PPMS	Physical Property Measurement System
ν	Frequency
XRD	X-Ray diffraction
EPR	Electron Paramagnetic Resonance
I	Nuclear spin
HF	Hyperfine interactions
TTF	Tetrathiafulvalene
SEM	Scanning Electron Microscopy
EDS	Energy Dispersive Spectrometry
TI	Temperature independent
A	Mass number
POM	Polyoxometallate
//	Parallel
$\perp$	Perpendicular
TGA	Thermogravimetric analysis
SMMs	Single-Molecule Magnets

List of Compounds

List of the compounds that appear during this manuscript, the six underligned complexes correspond to the studied systems.

(1): $[Mn_{12}O_{12}(CH_3COO)_{16}(H_2O)_4]$.

(2): $[Fe_8O_2(OH)_{12}(tacn)_6]Br_8(H_2O)_9$, tacn= 1,4,7-triazcyclononane.

(3): $[Fe_4(OCH_3)_6(dpm)_6]$, Hdpm= dipivaloylmethane.

(4): (TBA)$[TbPc_2]$, TBA$^+$= tetrabutylammonium, Pc^{2-}= phthalocyanine.

(5): $[Ln(Cp^{ttt})_2][B(C_6F_5)_4]$, Cp^{ttt} = 1,2,4-tris-terbutilcyclopentadienyl.

(6): $[(\eta^5\text{-}Cp^{iPr5})Dy(\eta^5\text{-}Cp^*)][B(C_6F_5)_4]$, Cp^{iPr5}= penta-iso-propylcyclopentadienyl,

Cp***=**pentamethylcyclopentadienyl.

(7): $[Dy(hfac)_3(\mathbf{L^1})]$, hfac= hexafluoroacetylacetone,

L^1= 4,5-bis(propyl-thio)tetrathiafulvalene-2-(2-pyridyl)benzimidazole.

(8): $[Dy(hfac)_3(\mathbf{L^2})]$,

L^2=4,5-bis(propylthio)tetrathiafulvalene-2-(2-pyridyl)-3-(2-pyridylmethyl)benzimidazole.

(9)$\cdot C_6H_{14}$: $[Dy(tta)_3(\mathbf{L^2})]\cdot C_6H_{14}$, tta= 2-thenoyltrifluoroacetone, *in main text found as **Dy**.*

(10) $\cdot xCH_2Cl_2$: $[Dy(tta)_3(\mathbf{L^3})]\cdot xCH_2Cl_2$, x=0-1,

L^3=4-[6-(1,3-benzothiazol-2-yl)pyridin-3-yl]-4’,5’-bis(methylthio)tetrathiafulvene.

(11) : $K_{13}[Yb(SiW_{11}O_{39})_2]$.

(12) $\cdot 5CH_3OH\cdot 2H_2O$: $[Yb(H_3\mathbf{L^4})_2]Cl_3\cdot 5CH_3OH\cdot 2H_2O$,

$\mathbf{H_3L^4}$= tris(((2-hydroxy-3-methoxybenzyl)amino)ethyl)amine.

(13) $\cdot 2CH_2Cl_2$: $[Yb(tta)_3(\mathbf{L^5})]\cdot 2CH_2Cl_2$,

L^5= 4,5-ethylendioxy-4’,5’-bis(2-pyridyl-N-oxidemethylthio)tetrathiafulvalene.

(14) : $[N(C_2H_5)_4]_3[Yb(\mathbf{L^6})_3]\cdot 2H_2O$, **L**^{6} = pyridine-2,6-dicarboxylate

(15) : $Na[Yb\mathbf{L^7}(H_2O)]\cdot 4H_2O$, **L**^{7}=1,4,7,10-tetraazacyclododecane-1,4,7,10-tetraacetic

(16) $\cdot 11H_2O$: $[Yb(\mathbf{L^8})_3]\cdot 11H_2O$,

L^8=2,6-dioxo-5-[2,4,6-trioxo-5-hexahydropyridinylidene)amino]-3H-pyrimidin-4-olate.

(17) $\cdot CH_3OH\cdot 0.5H_2O$: $[Yb(\mathbf{L^9})_2](NO_3)\cdot CH_3OH\cdot 0.5H_2O$,

L^9 = hodamine-6G-2-(hydrozinomethyl) quinolin-8-ol

(18) $\cdot CH_3OH$: $Yb(\mathbf{L^9})(tta)_2]\cdot CH_3OH$

(19) : $[Yb(\mathbf{L}^{10})]$,

$\mathbf{L}^{10}$ = 2,2′,2″-tris(salicylideneimino)trimethylamine

(20)$\cdot 35H_2O$: $Na_9[Er(W_{10}O_{36})]\cdot 35H_2O$, *in main text found as* $\boldsymbol{ErW_{10}\cdot xH_2O}$.

(21) : $[Er(\mathbf{L}^{11})(\mathbf{L}^{12})]$, $\mathbf{L}^{11}$= pentamethylcyclopentadienide, $\mathbf{L}^{12}$= cyclooctatetraenide.

(22)$\cdot$2THF: $[K(18\text{-}c\text{-}6)][Er(\mathbf{L}^{12})_2]\cdot 2THF$

(23) : $[K(18\text{-}c\text{-}6)(THF)_2][Er(\mathbf{L}^{12})_2]$, THF= tetrahydrofuran.

(24) : $[Li(DME)_3][Er(\mathbf{L}^{13}{}_2]$, DME= 1,2-Dimethoxyethane,

$\mathbf{L}^{13}$=1,4-bis(trimethylsilyl)cyclooctatetraenyl

(25) :$Er[\mathbf{L}^{14}]_3$, $\mathbf{L}^{14}$= Bis(trimethylsilyl)amide

(26)$\cdot$2THF: $[Li(THF)_4][Er(\mathbf{L}^{14})_3Cl]\cdot 2THF$

(27) :$[Er(\mathbf{L}^{14})_3Cl][Li(THF)_3]$

(28) : $Er(\mathbf{L}^{14'})_3$,

$\mathbf{L}^{14'}$= 2,6-di-*tert*-butyl-*p*-cresolate

(29) : $Er(\mathbf{L}^{14''})_3$,

$\mathbf{L}^{14''}$= bis(trimethylsilyl)methyl

Yb$\cdot C_6H_{14}$*: Yb(tta)*$_3$$(\mathbf{L}^2)]\cdot C_6H_{14}$

Er$\cdot C_6H_{14}$*: Er(tta)*$_3$$(\mathbf{L}^2)]\cdot C_6H_{14}$

(30) : $[(\mathbf{L}^{15}Zn(NO_3)Dy(NO_3)_2(H_2O)]$,

$H_2\mathbf{L}^{15}$ = N, N′-bis (3-methoxysalicylidene)-1,2-diaminoethane

(31) : $[(\mathbf{L}^{15}ZnCl)_2Dy(H_2O)][ZnCl_4]_2$

$\boldsymbol{Dy(ZnL^{15})_2}$: $[(Zn\mathbf{L}^{15}Cl)_2Dy(H_2O)]_2[ZnCl_4]\cdot xH_2O$

(32) : $[(\mathbf{L}^{16}Zn(H_2O))_2Dy(H_2O)](CF_3SO_3)_3$

$H_2\mathbf{L}^{16}$= N,N′-2,2-dimethylpropylenedi(3-methoxysalicylideneiminato.

(33) : $[(\mathbf{L}^{16}ZnBr)_2Dy(H_2O)](ClO_4)$

(34)$\cdot$MeOH: $[(\mathbf{L}^{16}ZnCl)_2Dy(H_2O)](ClO_4)\cdot MeOH$

(35)$\cdot H_2O$: $[(\mathbf{L}^{17}ZnCl)_2DyCl]\cdot 2H_2O$, *in main text found as* $\boldsymbol{Dy(ZnL^{17})_2}$

$\mathbf{H_2L^{17}}$= N, N′-bis(3-methoxysalicylidene)phenylene-1,2-diamine.

(36)$\cdot 3H_2O$: $[(\mathbf{L}^{17}ZnBr)_2Dy(MeOH)](Br)\cdot 3H_2O$

(37) : $[(\mathbf{L}^{17}ZnBr)_2Dy(H_2O)](Br2)[ZnBr_4]_{0.5}$

(38)$\cdot 2H_2O$: $[(\mathbf{L}^{18}ZnCl)_2DyCl]\cdot 2H_2O$,

$H_2\mathbf{L}^{18}$=N,N′-bis(3-methoxysalicylidene)-1,2-diaminocyclohexan

GENERAL INTRODUCTION

Magnetism has been known to humans for millennia, and for millennia different interpretations of this phenomenon of attraction between bodies have been given. The same way as magnetism, the meaning of molecules has evolved from the ancient ages until now, from this “extremely minute particles” to the complete understanding of this entities today. The evolution of both has been guided by different discoveries within the ages, until arriving to a common point, with the understanding that discrete molecules can display magnetism.

This phenomenon has fascinated people ever since the first indications of “magnets”, which had nothing to do to the ones we found commonly in our fridges as memories of the different places we have visited. We need to move to the ancient Greece, around 600 B.C., where the firsts manifestations of a mineral magnetite called lodestone (containing iron oxide, Fe_3O_4*) attracting iron, were given. Actually, the word “magnet” comes from the greek “magnetis lithos”, due to its ability to attract (or repulse) other pieces of the same material and iron. It was in 1600 when the firsts scientific studies took placed, thus stablishing the relation between magnetism and electricity, and further during the nineteenth and twentieth centuries that the nature of magnetism was finally understood. Research during these two centuries were focused in the reaction of molecules under an applied magnetic field, the correlation between electric and magnetic properties, as well as the origin of the atomic magnetism.*

The evolution of this field is closely linked to the evolution of our civilization. Progress in magnetism have changed in the last century our way of living. Actually, one of the most important applications of magnets, from both a social and economic point of view, is the production and use of electricity. The use of permanent magnets, which exhibit a magnetization loop that is both wide (maximum coercive field) and high (maximum magnetization), facilitate the reduction of the size and weight of a device made of them, as it could be for electric motors or audio speakers.

The modern understanding in both economics and scientific research, passes through the size minimization, thus increasing the performance. A step forward, with the apparent important emergence of the nanoscience, consisted in the development of quantum mechanics, which provided the tools for describing the magnetic properties in the nano-scale systems.

During the last twenty years the field of molecular magnetism, and with it the quantum events, have been extensively studied. Since, the magnetic properties of this permanent magnets are investigated in coordination clusters, which due to its small size and easy modulation of the structure, are proposed as exceptional candidates for the future information processing technologies, such as quantum computing or data storage. This new view of magnetism is based on the theory of the motion and interactions of electrons in atoms, coming from the work and theoretical models of Ernest Ising and Werner Heisenberg (also considered one of the founding fathers of modern quantum mechanics), among others.

This new field is created by the direct collaboration between chemists and physics, that would work together in order to design and synthesize challenging molecular architectures and experimentally measure their properties, in order to work out theoretical models needed for the interpretation of the events appearing in that level, like the coexistence of quantum and classical phenomena. [1,2,3,4]

As part of this doctoral work, we do not pretend to find new amazing structures so that they are included in the vast library of molecules displaying novel properties between the classical and the quantum behavior, but to selectively choose some examples existent in the literature so that we got a greater understanding on these events happening at low dimensionality. Thus, special appeal is done to paramagnetic molecules (presenting at least one unpaired electron), so that they can show a slow relaxation of the magnetization at low temperature, and thus behaving as tiny magnets (also known as single-molecule magnets, SMM). This manuscript is divided in three different parts:

- *A first part including Chapter I and II, in which all the fundamental information needed for the understanding of the following chapters is given.*
- *A second, comprising Chapters III-VI, in which the main work is presented: five different systems have been chosen among the different possibilities existent in the*

literature and their synthesis and magnetic characterization are presented within the different chapters. Starting from a well-known Dy-based mononuclear complex from the group, and taking different considerations thereafter (coordination sphere, polarization effect, electronic distribution of the metal ion, etc) in order to arrive to a general trend in the understanding of the evolution in the relaxation mechanisms. In the first chapter, the trend in the relaxation mechanism through dilution and isotopic enrichment, has been confirmed for a well studied sytem from the laboratory, thus evidencing the different hyperfine mark between two isotopes bearing same nuclear spin; Then, the study ofmagnetic properties of a system with the same environment but different metal ion (Yb and Er) aims to compare the relaxation mechanisms in ions with opposite electron density distribution. However, only the study of the first (Yb-based) has beenpossible; In Chapter V, an Er-based complex behaving as SMM and presenting the QTM regime has been chosen from the literature, thus with O_8 *as coordinating spehere and opposite trend in the isotopic behavior; Finally, chapter VI, proposes the study of two different systems based o Dy, with again an oxygenated coordination sphere and polarization of the electron density, with the aim to verify the dependence of this in the isotopic effect tendency and the effect of the polarization on both strategies.*

- *Finally, Chapter VII consists in a summary of the different ideas got from the previous systems followed by the conclusions and perspectives achieved at the end of those three years set in the previous six chapters.*

---

[1] a) "*Magnetism-History of Magnetism*" Science Encyclopedia: https://science.jrank.org/. b) "*Magnetism*". DISCovering Science. Gale Research, **1996**. Reproduced in Discovering Collection. Farmington Hills, Mich.: Gale Group. December, **2000**. http://galenet.galegroup.com/servlet/DC/ c) K. Khara, "*The Intriguing History of Magnetism You'd Like to Read Through*", *Sciencetruck*, **2017**: https://sciencestruck.com/history-of-magnetism.

[2] C. Benelli, and D. Gatteschi, Introduction to Molecular Magnetism: From Transition Metals to Lanthanides, Wiley-VCH, Weinheim, Germany, **2015**.

[3] J. Stöhr, and H. C. Siegmann, *Magnetism*: *From Fundamentals to Nanoscale Dynamics*, Springer- Verlag, Berlin Heidelberg, **2006**.

[4] D. Gatteschi, R. Sessoli, and J. Villain, *Molecular Nanomagnets,* Oxford University Press Inc., New York, United States, **2006**.

CHAPTER I

ORIGIN AND BASIS OF MAGNETISM

I. MOLECULAR MAGNETISM: General aspects[4,5]

In nature, atoms in molecules are commonly organized in a way that electrons are associated in pairs. Consequently, due to the balance between the different charges, no effective magnetic moment can be generated and they are diamagnetic (exception for O_2 which is paramagnetic). However, with regard to the magnetic properties in matter, what really interests us is the possibility of acquiring some systems with at least one unpaired electron. This unpaired electron can have both spin and orbital motion, which together generate a magnetic moment associated to it. It is the case of organic radicals, transition metal ions or the rare earth ions, which possess open-shell moieties, and it is from these open-shells that the molecular magnetic properties arise.

Molecular magnetism englobes the joint work of chemists, physicists and material science in order to create coordination magnetic complexes, with potential applications in high-density data storage, spintronics, and quantum computing.

A. *Magnetic moment and susceptibility:*

When studying the magnetic properties of a sample, the induced magnetic moment can be expressed according two different magnitudes: the magnetization M, gives information about the orientation of the magnetic moments parallel to an applied magnetic field, H, and the magnetic susceptibility χ, which is the response of the system to H.

Then, if a magnetic complex is placed within a homogenous external magnetic field H, it acquires a certain magnetization, M. The magnetic susceptibility can be then expressed as:

$$\chi = \partial M / \partial H \qquad (1.1)$$

When H is sufficiently weak, χ is independent of H, such that there is a linear relationship between M and χ. This will be the case during all this work.

$$\chi = M / H \qquad (1.2)$$

Several magnetic effects can be described, depending on the magnetic response to the *H* and the temperature dependence. Thus, one can classify the magnetic phenomena into three main groups:

Diamagnetism: this phenomenon can be found in all materials, as it appears from the interaction between the motion of the electrons in their orbits and *H*. A weak magnetic field is induced in the material so that it repels the magnetic field. One talks about diamagnetism, when no-other phenomena is present as, if the contrary, this would be counterbalanced. It is defined by small and negative susceptibility values which are constant with the temperature and magnetic field.

Paramagnetism: this effect happens in molecules with an unpaired electron. The different magnetic moments given by the unpaired electrons are randomly oriented giving to rise to a nil global moment. However, once they are submitted to *H*, they orientate partly in the direction of the magnetic field. It is characterized by small but positive susceptibility values, which are temperature dependent $\chi(T)$.

Collective magnetism: results from the interaction and reorientation of the different magnetic moments in the material, giving rise to long-range magnetic ordering and maintaining a lowered-energy state. Depending on the different orientation between neighboring moments we can differentiate between: 1) ferromagnetism, if they align with the same orientation ($M\neq0$); 2) antiferromagnetism, if they align so that they are in opposite sign than their neighbors (M=0); 3) ferrimagnetism, if they are also arranged with antiparallel-ordering but with the magnetic moments different for each orientation (($M\neq0$).

If we look at the atomic level, we have to deal with quantum mechanics as the system is considered to be a quantum system, constituted by discrete energies E_n(n= 1, 2,…). The magnetic moment of a free atom or ion, also called microscopic magnetization, is originated from the total electronic spin momentum (*S*), the orbital momentum of the electrons around the nucleus (total orbital angular momentum, *L*) and, when submitted to an external magnetic field, the induced change in the orbital moment. The two first sources give rise to a paramagnetic response, whether the last results into diamagnetism. Thus, the global susceptibility can be split into two different terms, a diamagnetic (χ_{dia}) and a paramagnetic (χ_{para}) susceptibility:

$$\chi = \chi_{dia} + \chi_{para} \quad (1.3)$$

where the diamagnetic susceptibility is estimated using an additive method which takes into account the different atomic susceptibilities and some constitutive corrections. These tabulated corrections take into account the difference in the diamagnetic character depending on the type of bonds, and are summarized together with the atomic susceptibilities, in the so-called Pascal Tables. However, for a faster approximation, when no so accurate value is needed, one can use the following expression:

$$\chi_{dia} = kM_W \times 10^{-6}\,\mathrm{cm^3\,mol^{-1}} \quad (1.4)$$

with M_W, the molecular weight of the compound and *k*, a varying factor between 0.4 and 0.5.

Hereafter, all χ_M are assumed to be corrected from the diamagnetic contribution and will correspond to the paramagnetic part in Equation 1.3. This paramagnetic response, originated from *L* and *S* and tuned by the interaction with *H*, is associated with the thermally populated states E_n. Thus, by applying *H*, a splitting of the different energy states in the molecule is induced (phenomenon known as Zeeman effect), and the variation in the different energies can be described as the microscopic magnetization:

$$\mu_n = -\partial E_n / \partial H \quad (1.5)$$

Consequently, the macroscopic magnetization M becomes the sum of the different microscopic magnetizations (μ_n) of the molecules of the sample, thus weighting the relative population of the different n levels at a given temperature, *T*, and magnetic field, *H*, with the Boltzmann distribution.

$$M = N \frac{\sum_n (\partial E_n / \partial H) \exp(-E_n / KT)}{\sum_n \exp(-E_n / KT)} \quad (1.6)$$

where k_B is the Boltzmann constant and N is Avogadro's constant, which, within the **cgs emu** system units used during this work, the value used for k_B is 0.695039 $\mathrm{cm^{-1}\,K^{-1}}$ and the partition function Z is defined by:

$$Z = \sum_n \exp(-E_n / KT) \qquad (1.7)$$

This leads to the following expression for magnetization (Equation 1.8) and susceptibility (Equation 1.9), which, without any approximation, may be considered as the fundamental expressions. These correlate the magnetic measurements (macroscopic world) with the interactions and/ or anisotropy constants of the system (microscopic world).

$$M = NkT \frac{\partial \ln Z}{\partial H} \quad (1.8) \qquad \chi = NkT \frac{\partial^2 \ln Z}{\partial H^2} \quad (1.9)$$

Nevertheless, the use of these fundamental formulas is not evident as it requires the knowledge of all the energy variations ($E_n = f(E)$) for all the thermally occupied states. That is why, in 1932 van Vleck proposed a simplified model taking into account some assumptions ($H / kT << 1$, linear approach of Equation 1.1) and following a perturbation method for which E_n could be decomposed: $E_n = E_n^{(0)} + E_n^{(1)}H + E_n^{(2)}H^2 + (...)$, where $E_n^{(0)}$ is the zero-field energy at n level and $E^{(i)}$ the different i^{th} order Zeeman coefficients. Hence, applying the definition of the magnetic susceptibility (Equation 1.2 and 1.5) the van Vleck formula up to 2nd order is defined as:

$$\chi = \frac{N \sum_n (E_n^{(1)^2} / KT - 2E_n^{(2)}) \exp(-E_n^{(0)} / KT)}{\sum_n \exp(-E_n^{(0)} / KT)} \qquad (1.10)$$

where the calculation of the derivatives is no longer needed, but the $E_n^{(0)}$, $E_n^{(1)}$ and $E_n^{(2)}$ quantities. Thus, by knowing the eigenvalues $E_n^{(0)}$ and eigenfunctions $|n\rangle$ the other two values are calculated through perturbation theory.

A.1. *From Curie Law and beyond:*

If one consider the simplest case, in which the molecule present a unique paramagnetic center, two different possibilities can be presented. Depending on the energetic terms generated from the ligand field effects, the system can have the orbital contribution quenched, in which the system is only desenbed by *S*, or, on the contrary, it can exhibit both momenta contributions, leading to an interaction between *S* and *L* known as first order spin-orbit coupling.

For the former case, in the absence of an external magnetic field, the $2S+1$states of spin are degenerated and this energy level is usually taken as the origin ($E_n^{(0)}=0$) in order to facilitate the later calculations. The degeneracy of the different states is then broken when applying *H*, and the different Zeeman components are described as:

$$E_n = M_s g \beta H \quad (1.11)$$

where M_S is the spin quantum number associated with S, $M_S=(-S,-S+1,\ldots,+S)$; g is the gyromagnetic factor (also called Landé-factor) which in the ideal case of well separated energy levels (no coupling between the ground-state (GS) and the excited-states (ES)) correspond to the values of a free electron (g= 2.0023); and, β is the electron Bohr magneton. Considering intermediate values of T and H, one can merge Equations 1.11 and 1.10 to obtain:

$$\chi_M = \frac{Ng^2\beta^2}{3kT} S(S+1) \quad (1.12)$$

with the molar magnetic susceptibility varying as χ_M=C/T , with $C=\frac{Ng^2\beta^2 S(S+1)}{3k}$ the Curie constant. This expression is known as the Curie Law, which is only valid for the case when the molecule does not present any first order spin-orbit coupling For systems with some spontaneous interaction between adjacent spins, thus causing some ordering at low temperature, a modified version is needed (Curie-Weiss law, Equation 1.13)

$$\chi_M = \frac{C}{T-\theta} \quad (1.13)$$

with θ the Weiss constant, which is the characteristic ordering temperature and give information about the character of the interactions.

There are different ways of representing the susceptibility, whether it is as $\chi_M T$ vs. T or χ_M^{-1} vs. *T*; the first (Figure 1. 1a) giving a direct insight of the number of single electrons and thus the C value, and the second (Figure 1. 1b) the character para-/ferro-/antiferro- magnetic depending on the origin of the x-axis.

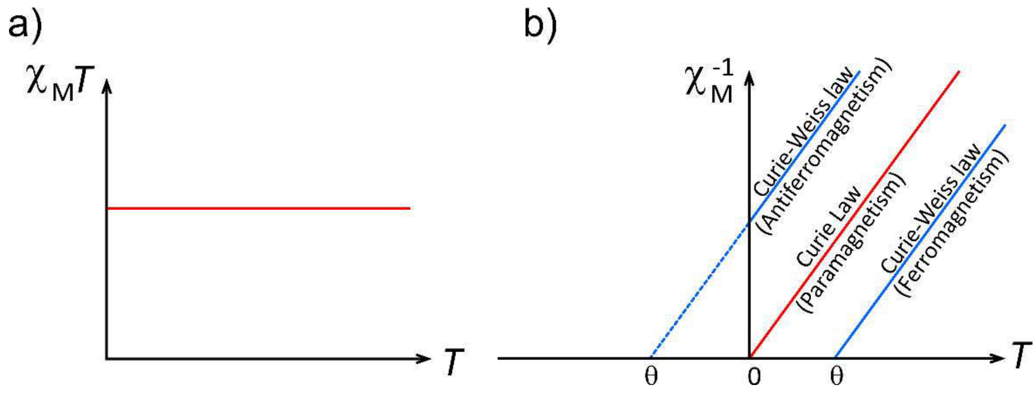

Figure 1. 1. Representation of the molar magnetic susceptibility a) as $\chi_M T$ vs. T and b) χ_M^{-1} vs. T. The slope in the second gives the value of C^{-1}.

Until now, only the spin *S* was considered, however, there is also an angular moment *L*, which is not always quenched. For those systems, S is not sufficient in order to calculate the magnetic properties of the ion, but instead the total angular momentum *J*, defined as $\mathbf{J} = \mathbf{S} + \mathbf{L}$. Thus, the susceptibility expression changes to Equation 1.14, and the Landé-factor does not coincide anymore with the free electron situation but need to be calculated by (Equation 1.15).

$$\chi_M = \frac{Ng^2\beta^2}{3kT} J(J+1) \quad (1.14)$$

$$g = \frac{3}{2} + \frac{S(S+1) - L(L+1)}{2J(J+1)} \quad (1.15)$$

B. *Magnets, from macro- to micro-: anisotropy and memory effect*

The fundamentals presented until now, did not present, at first, any sense of directionality but they were considered as isolated punctual charges with isotropic properties. In the last paragraph, we saw that these isolated points were not as much isolated as described before, but there were some interactions within the paramagnetic center (which gave us the notice of the total angular momentum, *J*). Moreover, with the Curie-Weiss approach, we started to get some insight of long ordering range, as the different magnetic moments could interact creating a ferro-/antiferro-/para- magnetic behavior within a certain temperature range.

Besides, only one single center has been considered per molecule, which is the case that will be studied all along this manuscript, but one can consider the possibility of polynuclear species, in which different centers interact magnetically. This, can be expressed as exchange-interaction, in the Heisenberg – Dirac – Van Vleck model, , which concerns the interaction of the spins from two different centers through an exchange constant.

An important concept in this field is, the non- isotropic character of the physical properties of the paramagnetic ions. The magnetic anisotropy is the phenomenon probing that a molecule can be more easily magnetized along one direction than along another, or in other words, the required energy for the rotation of the magnetic moment differs on the direction of the orientation. In a crystal, it can be given by two different sources: the magnetocrystalline anisotropy (the atomic structure of a crystal introduces preferential directions for the magnetization) and the shape anisotropy (when a particle is not perfectly spherical, the demagnetizing field will not be equal for all directions, creating one or more easy axes).

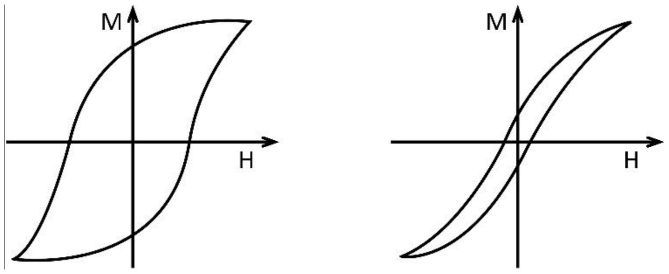

Figure 1. 2. Hysteresis loops of the M vs. H for a hard magnet (left) and soft magnet (right).

This phenomenon influences the spontaneous orientation of the magnetization (ferromagnetism or ferrimagnetism) in the macroscopic scale, which can be graphically represented as a hysteresis loop of the magnetization as a function of *H*. Thus, depending on the coercive field, magnets can be classified as hard or soft.

- Hard magnets: determined by a large coercive field. They are permanent magnets, which means that once magnetized to saturation, they remain in a magnetized state when the field is removed. They contain anisotropic metals like cobalt and the rare earths.
- Soft magnetic materials have very narrow loops. They are temporary magnets, as they lose their magnetization as soon as the field is removed.

This memory effect, characteristic of hard magnets, can also be observed at molecular level, by using paramagnetic units as lanthanides with high magnetic anisotropy, making them potential candidates for their application as information storage/ processing in quantum computers.

C. *Lanthanides and the magnetism behind them:*[6,7,8]

Much research has been done in the latter part of the last century, concerning the possible applications of rare earth elements (RE) which display numerous interesting and important properties with respect to their magnetic, optical, and electronic behavior: Their first applications date from 1891 and 1903, in which the luminescent properties of these elements were used is mantles for the gas lamps and flint stones; later, in 1942 it was discovered that by coordinating RE to β-diketonate, phenolate or salicylate ligands, the metal-centered luminescence could be triggered by ligand absorption and energy transfer; the use of some lanthanides (Pr, Eu and Yb) for the elucidation of NMR spectra; and other lanthanides (Gd) as contrast agents.

Lanthanide atoms, referred to as Ln, are elements presenting an atomic number, Z, ranging from 57 to 71; they are part of a large family called RE, with the inclusion of Sc (Z=21) and Y (Z=39). Following the series, the GS is characterized by the progressive filling of 4f shells, defined by two different electronic configurations: $[Xe]4f^n6s^2$ or $[Xe]4f^{n-1}5d^16s^2$, where [Xe] represents the electronic configuration of xenon and n a number from 1 to 14. This influences the stability of the tripositive cations that are obtained by the loss of the 5d and 6s electrons. Scandium and yttrium (which do not belong to the Ln series) do not have 4f electrons but they display similar chemical properties because of their outermost electrons configuration.

Interesting properties are present in these trivalent ions due to their valence-electrons occupying the well shielded 4f shell, and the obvious dependence of the angular momentum in the electron density distribution (see Figure 1. 3).

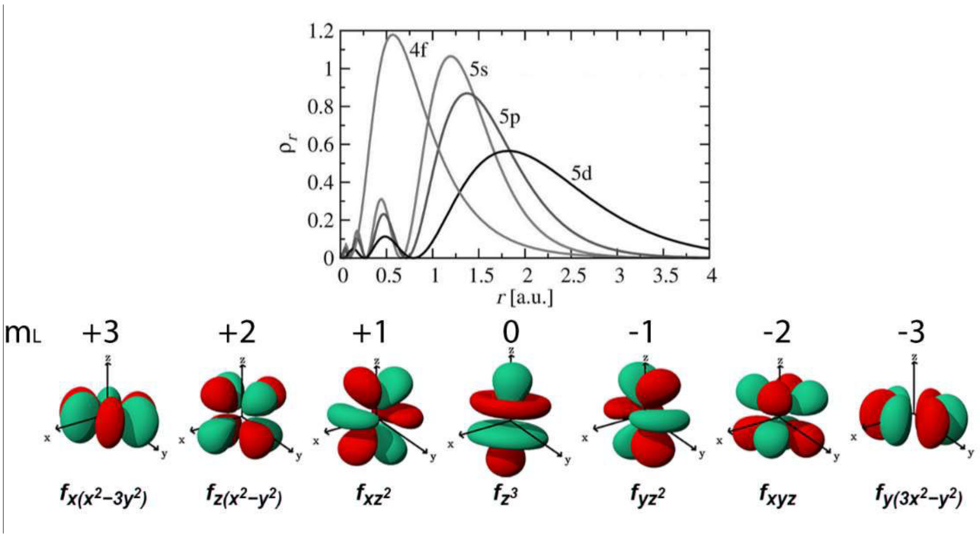

Figure 1. 3. Radial charge density (ρ_r) as a function of the distance from the nucleus, r, of the 5s, 5p, 4f and 5d orbitals of the Gd^{3+} ion, and the shape of the 4f orbitals.[7]

In the same Figure, it can be observed an example of the radial distribution of the charge density in a Ln^{3+} cation. The 4f orbitals (external shell in Ln^{3+}) appear to be shielded by the 5d/ 5s and, a priori, this relative internal position of the 4f orbitals (Ln^{3+}: [Xe]$4f^n$), favor a greater isolation from the coordination environment compared to the 3d transition metal series, thus diminishing the crystal field (CF) interactions. Additionally, a higher nuclear mass is presented for 4f compared with 3d cations, increasing the strength of the interaction between the electronic spin and the angular orbital momentum. Consequently, the energy splitting of 4f ions display a greater contribution of the spin-orbit (SO) coupling than the CF, opposite behavior to 3d metal centers. This results in sharp transitions when studying the optical spectra, and the extrapolation of the magnetic properties to those of a free ion, when using Ln^{3+}-based compounds.

Indeed, the energy level structure of the 4f states is determined by the combination of three different interactions, (Figure 1. 4) and will be described in spectroscopic terms: first, the electron repulsion split the $4f^n$ shell into different ^{2S+1}L states; then, the spin–orbit coupling, divide the different spectroscopic terms into $^{2S+1}L_J$ (with $|L\text{-}S| \leq J \leq |L+S|$) levels (*Russel-Saunders coupling*), with the addition of the unquenched total angular momentum; finally, the crystal field splits the level into the M_J multiplet states (with $-J \leq M_J \leq +J$).

Further degree of perturbations can be given by the application of the external magnetic field (*Zeeman* interactions) or by considering the small interactions between electrons and nuclei, named hyperfine interactions. Thus, the ground state in lanthanide cations is defined by the lowest energy ^{2S+1}L term, presenting the lowest lying J multiplet. Since, with the exception of Eu^{3+} and Sm^{3+}, the GS is sufficiently separated from the first ES of the same multiplet, only the ground one is populated at room temperature or below, therefore it can be considered as the only contribution for the description of the magnetic properties of the ion.[9]

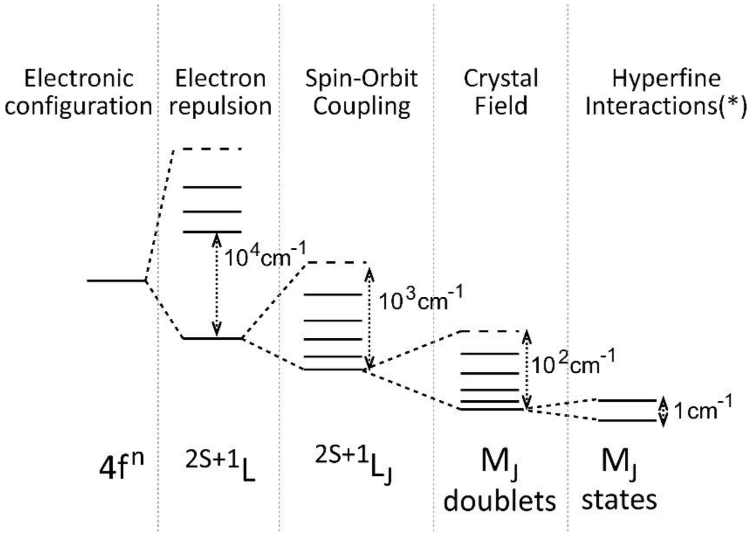

Figure 1. 4. Energetic structure of a lanthanide ion, taking into account the different interactions and the difference in the strength, evidencing the effect of progressively weaker perturbation. (*) Same effect of break of the degeneracy in ±M_J multiplets can be also induced by the presence of H.[8]

This ground state multiplet can be easily determined through Hund's rules, in which three different conditions need to be fulfilled: 1) S corresponds to the maximum allowed spin value, determined by Pauli's exclusion principle. 2) Among all the possible L values, it presents the maximum allowed angular momentum. 3) For ions in which the number of electrons do not half-fill the 4f subshell, the total momentum is $J=|L-S|$, whether in the opposite case $J=|L+S|$. As summarized in Table 1. 1, we can have different values for S, L, and J. Using the Russell–Saunder Coupling Scheme ^{2S+1}L, one can easily calculate the magnetic moment of the ion and thus the susceptibility. If we take Dy^{3+} as an example, its ground state is $^6H_{15/2}$ based on $S=5/2$, $L=5$ *and* $J=15/2$. By applying the Equations 1.14-1.15 and considering T as being the room temperature and $g_J= 4/3$ and $\chi T=14.17$ cm^3 K mol^{-1}.

Table 1. 1. Ground state information of the different Ln^{3+} at room temperature. Extracted from [8].

Ion	*$4f^n$*	*Ground state*	*S*	*L*	*J* *$J=\|L-S\|$*	*g_J*	*χT / cm^3 K mol^{-1}*
Ce^{3+}	f^1	$^2F_{5/2}$	1/2	3	5/2	6/7	0.80
Pr^{3+}	f^2	$^3H_4$	1	5	4	4/5	1.60
Nd^{3+}	f^3	$^4I_{9/2}$	3/2	6	9/2	8/11	1.64
Pm^{3+}	f^4	$^5I_9$	2	6	4	3/5	0.90
Sm^{3+}	f^5	$^6H_{5/2}$	5/2	5	5/2	2/7	0.09 (0.31)*
Eu^{3+}	f^6	$^7F_0$	3	3	0	0	0 (1.5)*
					$J=\|L+S\|$		
Gd^{3+}	f^7	$^8S_{7/2}$	7/2	0	7/2	2	7.87
Tb^{3+}	f^8	$^7F_6$	3	3	6	3/2	11.82
Dy^{3+}	f^9	$^6H_{15/2}$	5/2	5	15/2	4/3	14.17
Ho^{3+}	f^{10}	$^5I_8$	2	6	8	5/4	14.07
Er^{3+}	f^{11}	$^4I_{15/2}$	3/2	6	15/2	6/5	11.48
Tm^{3+}	f^{12}	$^3H_6$	1	5	6	7/6	7.15
Yb^{3+}	f^{13}	$^2F_{7/2}$	1/2	3	7/2	8/7	2.57
** Sm^{3+} and Eu^{3+} are special cases as they have low-lying excited states (ca. 350 cm^{-1} and 700 cm^{-1} respectively) which have interactions with the ground state. Consequently, a better approximation is needed to fit experimental values, thus taking into account the Van Vleck contribution.*							

In Figure 1. 5, the different χT are represented for the different trivalent cations, evidencing the different behavior between both types of lanthanide ions: those with unfilled half-shell, characterized by low magnetic moments (from La^{3+} to Eu^{3+}); and those with more than half-shell filled, characterized by higher magnetic moments (from Gd^{3+} to Yb^{3+}).

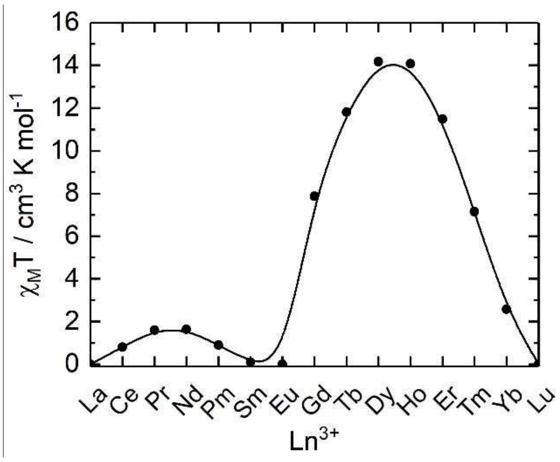

Figure 1. 5. χT values for the different Ln^{3+}.[10]

Lanthanides molecules (mainly from the second category) play an important role in the field of molecular magnetism, as those trivalent cations with relatively high magnetic moment, present an important magnetic anisotropy. This magnetic anisotropy, related with the symmetry of the orbital components, is determined by the quenching extent of the orbital moment after the competition of the SO coupling and the CF interactions. Following this idea, 3d metal ions that present largely quenched orbital moments due to the strong crystal-field interactions, will lead to small anisotropic systems; whereas the lanthanide (4f) ions, due to their larger spin orbit coupling energy relative to the crystal field, present systems with higher magnetic anisotropy. This microscopic anisotropy is one of the important pieces in the study of molecular systems, as it enhances large energy splitting in one direction, which can favor a slow relaxation of the magnetization and consequent magnetic hysteresis at low temperature, making them good candidates for Single-Molecule Magnets (SMMs), but also in quantum computing (QC) if the coherent manipulation of the isolated GS M_J multiplets is possible, as two-level systems, named qubits.[11] Depending on this microscopic anisotropy, the lanthanides will be roughly split in two different families, which will be introduced in more detail in the next section: those for which the electron distribution is expanded in a plane (oblate, this is the case of Ce^{3+}, Pr^{3+}, Nd^{3+}, Tb^{3+}, Dy^{3+} and Ho^{3+}) and those for which the electron distribution is centered along an axis (prolate, this is the case of Sm^{3+}, Er^{3+}, Tm^{3+} and Yb^{3+}).

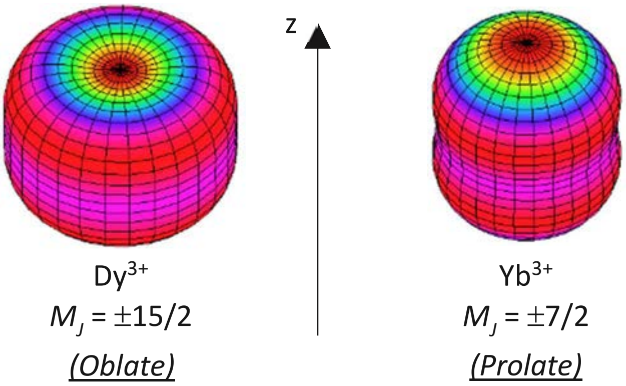

Figure 1. 6. Representation of two different examples of the categories of Lanthanides depending on their electronic density shape: oblate (Dy^{3+}) or prolate (Yb^{3+}).

II. SINGLE MOLECULE MAGNETS[6-8]

The magnetic behavior of single-molecule magnets (SMMs) is characterized by the presence of slow relaxation of the magnetization at low temperature, which gives rise to a magnetic memory effect similar to that found in hard magnets, together with quantum tunnel effects.[8] The particularity of this behavior is its molecular origin that, not depending on the long-range ordering between different centers, it is retained even in extremely diluted systems. This property, present in some coordination molecules, makes them promising candidates for high-density memory storage, or in quantum computing terms, the fundamental units of quantum information (qubits).[12]

A. *Energy barrier and magnetic hysteresis* [13,14]

In Single Molecule Magnets, the characteristic magnetic bistability is maintained during a certain range of temperatures until achieving the so-called blocking temperature (T_B), from which the magnetization is no longer retained after the removal of the external magnetic field in the magnetic hysteresis. This, at the same time can be triggered by choosing a proper ion with a suitable ligand structure, so that the difference between the GS and the first ES (called hereafter Energy barrier, Δ) is maximized. Different approaches have been investigated with maximization of the magnetic moment and the achievement of strong anisotropic systems, as key ingredients for the success in the creation of an energy barrier between the generated “spin up” and “spin down” sublevels.

In a first time, and marked by the publication of the first SMM compound (i.e. Mn_{12} acetate[15]), strategies involved the coupling of first-row transition metal ions, which give rise to large S systems. The absence of orbital angular momentum leads to energy splitting depending on the spin magnetic moment, and the orientation of the magnetization depends on the M_S quantum number. In that case, the anisotropy (D) is given by the zero-field splitting, which is the responsible of breaking the degeneracy between the different M_S sublevels. When D is negative, the maximum $M_S = \pm S$ become lower in energy than the intermediary sublevels (Figure 1. 7), thus enhancing Δ for the transition of one orientation ($+M_S$) to the other ($-M_S$).

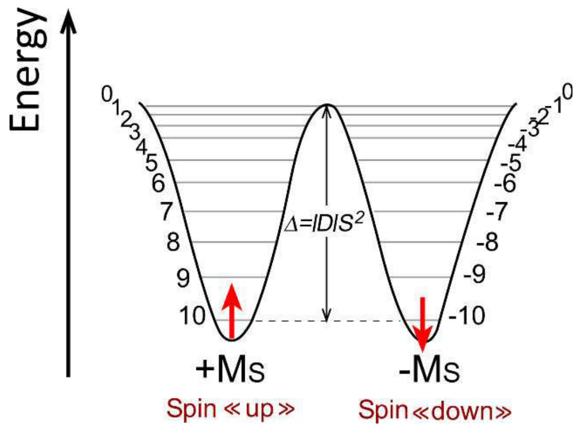

Figure 1. 7. Schematic representation of the splitting of the S = 10 ground state of Mn_{12} into 21 sublevels by ZFS and the relaxation of the magnetization from the "spin-up" (M_S= 10) to "spin down" (M_S= −10) state at H = 0 and low temperature.

Unfortunately, as this kind of systems with quenched *L* does not guarantee the anisotropy of the magnetization, this lead to further investigations containing 4f elements. When lanthanides or actinides are used, the obtained systems display high anisotropy, but this is counter-balanced by their poor coupling behavior. Similar description is given for these coordinated systems, with the major difference being the definition of the energy-states, which now are characterized by $\pm M_J$.

In both 3d and 4f systems the ligands play a fundamental role in determining the final magnetic properties, making important to reach a comprehensive understanding of the effects of a crystal field. During this thesis, strong emphasis will be given to lanthanide-based systems, and transition metal systems will appear only as examples for a better understanding on the evolution and the origins of these systems.

Mononuclear complexes of lanthanides contain formally all the ingredients to behave as SMM: large magnetic moments, magnetic anisotropy and a bistable ground state under the appropriate conditions. However, to trap the magnetic moment in two opposite directions the anisotropy needs to be axial (Ising type anisotropy). According to this idea, Rinehart and Long[16] proposed in 2011 a qualitative, but greatly extended, model in which they stated the way the electronic density of the ligand need to be placed depending on the electron density shape of the metal ion.

In a first approximation, if we take into account the two main different families of electronic density (Figure 1. 6), the ligand need to be optimized so that it is placed in a way that the overall oblate/ prolate shape distribution is favored, thus minimizing the repulsive interactions between the negative charges of the ligand and the electrons of the metal and maximizing an axial anisotropy. Following this idea, in Figure 1. 8 we can find two general optimum ligand architectures depending whether the free-ion is oblate (expansion in a plane, on the left) or prolate (expansion along an axis, on the right): for the first, the crystal field needs to be concentrated above and below the XY plane (sandwich-type geometry); whereas for the last, in order to minimize the electron repulsion, an equatorially-coordinating geometry is required.

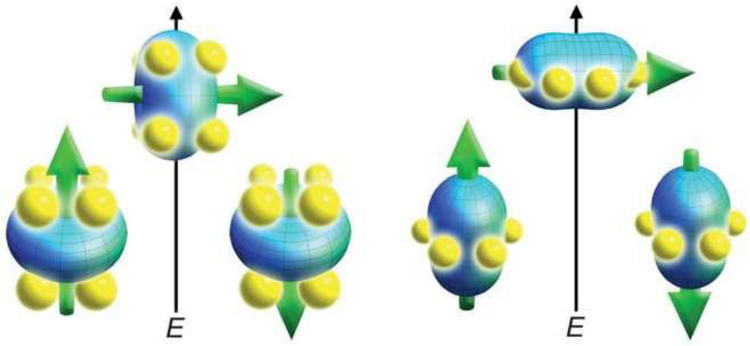

Figure 1. 8. Representation of the low- and high-energy configurations of the f-orbital electron density (blue) under the effect of emplacement of the ligand electron density (yellow) for a 4f ion of oblate (left) and prolate (right) electron density. The green arrow indicates the orientation of the spin angular momentum coupled to the orbital moment. Extracted from ref. [16].

The interaction of the ligand density and the metal ion, CF, leads to the separation of the different M_J states multiplets depending on the affinity or repulsion between both components. Hence, the M_J multiplet bearing less respulsion between the electronic charge of the metal and the ligand, will be placed lower in energy, thus letting the most unfavorable states occupy higher energies. For that, we make a rappel to the strong angular momentum dependence of the different electron configuration (Figure 1. 3); described in last term, by the different M_J. This angular dependence is now evidenced in Figure 1. 9, where it can be seen the difference in shape between the different M_J multiplets appertaining to a same spectroscopic term. The idea then, is to place the electronic distribution of the ligand so that the difference between the lowest energy M_J and the one after is big enough in order to have higher anisotropic systems, while the highest M_J value is preferable.

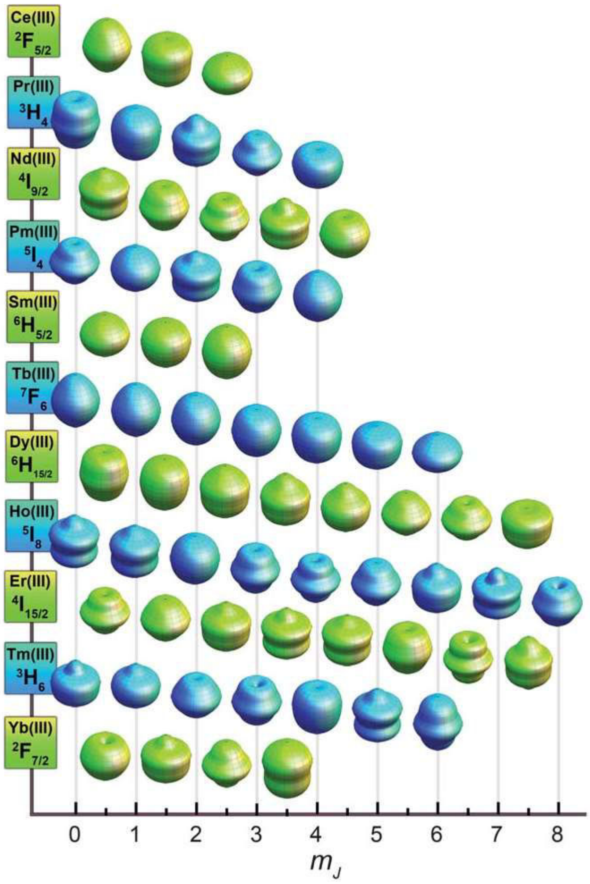

Figure 1. 9. Approximations of the angular dependence of the total 4f charge density for M_J states composing the lowest spin–orbit coupled (J) state for each lanthanide. In the absence of a crystal field, all M_J states for each lanthanide ion are degenerate. Extracted from ref. [16].

The careful selection of the M_J ground-state is especially important to guarantee the magnetic bistability, which is crucial for SMMs, where the GS is imperatively a doublet. Indeed, depending on the number of unpaired electrons the ions can be classified as Kramers (odd number of unpaired electrons, e.g. Dy^{3+}) or non-Kramers (even number of unpaired electrons, e.g. Tb^{3+}), depending on which the possibility of singlet M_J is possible. Accordingly, in the absence of H, Dy^{3+} will always maintain a degenerate ground state while Tb^{3+} ions must have a strictly axial CF symmetry to do so.

B. *Relaxation mechanism:*[7,13,14]

In general, if a system is induced out-of-equilibrium because of a determined perturbation, this will tend to a new equilibrium by a relaxation mechanism. In these systems, the perturbation is mainly a change in the magnetic field, H, and the characteristic time is called relaxation time of the magnetization.

In the absence of *H*, if we consider the schematic system in Figure 1. 7, the relaxation of the magnetization resulted from the transition of the state “up” to the state “down” follows an exponential dependence with the temperature, defined by the Arrhenius low:

$$\tau^{-1} = \tau_0^{-1} \exp(\Delta / T) \quad (1.16)$$

In order to overpass the energy barrier, the thermal energy (*T*) needs to be enough to compensate this gap. This gap can be also compensated by applying a magnetic field, which induces the alignment of the spin in its direction (being the most energetically favorable) thus stabilizing one state against another (Figure 1. 10). Again, when removing the magnetic field the degeneracy of both states is recovered and, if the T is sufficiently low, the spin will be trapped in this new orientation for some period of time.

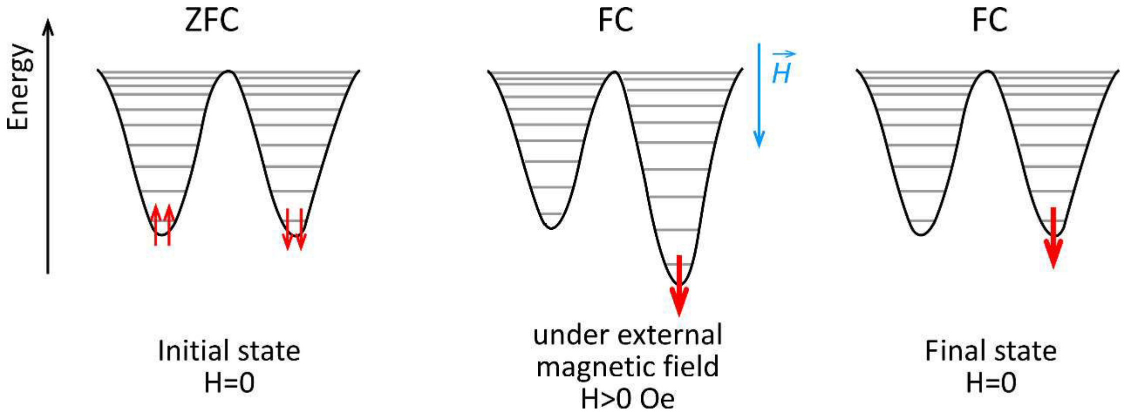

Figure 1. 10. Influence of the magnetic field in a double well diagram with a given orientation of the magnetic moment. At the initial state, if we lower T in absence of H (ZFC, zero-field cooling), the probability of spin is equal in both sides of the Energy barrier; whereas the orientation is forced by applying a magnetic field.

However, any transition or perturbation of the system does not only include the energy exchange within the spin system, but also the interaction with the lattice. Thus, it leads to a number of different possible relaxation mechanisms when referring to SMMs, which will contribute differently depending on the working temperature and the presence or not of an external magnetic field. The complete formula for the relaxation rate of the magnetization is a sum of the different possible contributing processes is given by equation 1.17[17,18]:

$$\tau^{-1} = \underbrace{\tau_0^{-1} \exp\left(\frac{\Delta}{T}\right)}_{Orbach} + \underbrace{CT^n}_{Raman} + \underbrace{\frac{B_1}{1 + B_2 H^2}}_{\tau_{TI}^{-1},QTM} + \underbrace{ATH^m}_{Direct} \quad (1.17)$$

with the different relaxation rates standing for the Orbach, the Raman, the QTM (Quantum tunneling of the magnetization), and the direct processes, respectively; and the different parameters (τ_0, Δ, τ_{TI}, C and A) are found by fitting the experimental data, whereas n and m exponent are supposed to be tabulated and known values.[7] During this manuscript, m will be maintained fixed (m=4, for a Kramers ion) while n will constitute another parameter (normally between 4 and 9 for a Kramers ions, but recently found that this is maybe not longer valid with n).[19,20]

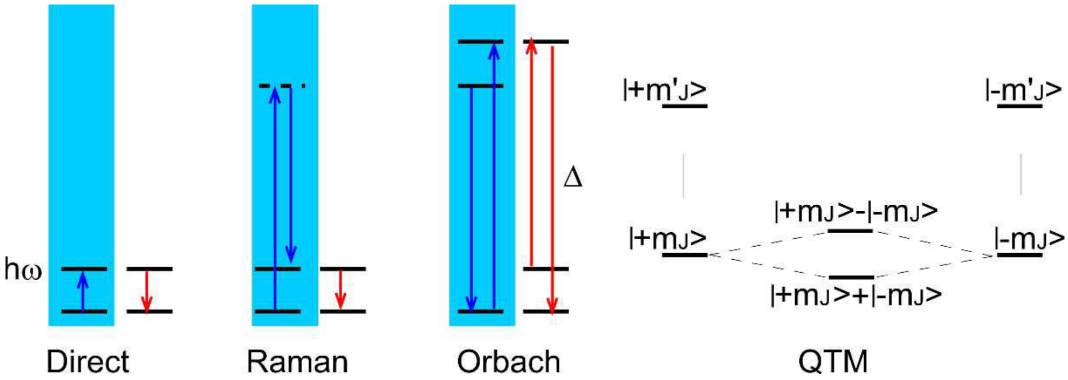

Figure 1. 11. Schematic overview over the different magnetization relaxation (spin-lattice relaxation) processes for a double M_J ground state. The horizontal lines correspond to the different states, with the blue region corresponding to those of the lattice and the others to the CF levels of the lanthanide ion. Adapted from [13].

<u>Direct process:</u> this is a single phonon process for which the relaxation of the spin (from up to down) passes by absorbing/ emiting a phonon with the same energy as the difference between both states, ω. The τ^{-1} from the direct contribution shows a linear dependence with *T* and m-exponent dependence of *H*.

<u>Raman process:</u> includes a two-phonon process in which the spin absorbs the energy released to a virtual excited state and the relaxation to the GS passes by emission of another phonon of same energy. This process is strongly dependent with the temperature and do not show any dependence with the magnetic field. Theoretically, the n factor corresponds to 7 for the non-Kramers ions and 9 for Kramers ions, but as it will be seen during this manuscript, the presence of both acoustic and optical phonons could lead to lower values between 1 and 7.[21]

<u>Orbach process:</u> as the previous, this is a two-phonon process for which the spin absorbs a sufficiently energetic phonon to overpass the energy barrier, and the later emission for relaxation. This, as already mentioned, is exponentially dependent with the temperature and is not sensible to the magnetic field, with greatest efficiency at relatively high temperatures.

QTM process: this process includes the mixing of the two different M_J GS states, which is forbidden in Kramers ions because of CF symmetry. However, because of the distortion from the axial symmetry given by transverse anisotropy, or because of environmental factors (as for example the presence of dipolar or hyperfine interactions) which add some perturbation to the system, this is usually efficient and temperature independent. In that case, and as depicted in equation 1.17, the QTM can be removed by applying a magnetic field which enhances an energy gap between both GS substates.

In general, if any of the process QTM, direct or Raman is efficient, they will compete with the Orbach process at a certain temperature region, mostly centered in the low T regime for which the Orbach is less efficient (the thermal-relaxation process slows down exponentially). This competition induces a loss in the performance of the SMM, enhancing a faster relaxation, and need to be suppressed which need to be suppress thereafter.

C. *Evolution from 3d to 4f systems and beyond.*

We just celebrated 25 years from the discovery that coordinated systems could retain the orientation of their magnetization at low temperature, and behave as little magnets called Single-Molecule Magnets (SMMs).[15,22] Thus, during a decade a large number of molecular clusters based on transition metal ions were characterized in order to investigate their SMM properties, but not all leading to slow relaxation of their magnetization because of the lack of axial anisotropy, especial citation to Mn_{19}[23] (with formula: $[Mn^{3+}_{12}Mn^{2+}_{7}(\mu_4-O)_8(\mu_3,\eta^1-N_3)_8(HL)_{12}(MeCN)_6]Cl_2\cdot 10MeOH\cdot MeCN$, being H_3L= 2,6 - bis(hydroxymethyl) - 4 - methylphenol) in 2006, with a record of S= 83/2 ground spin state but with no anisotropy.

The $[Mn_{12}O_{12}(CH_3COO)_{16}(H_2O)_4]$ complex (Mn12Ac) (Mn_{12}ac, **1**) constituted the first reported SMM (Sessoli *et al.,* 1993)[15] and was firstly synthesized by Lis in 1980.[24] It is formed by the four internal Mn^{4+} ions arranged in a cubane Mn_4O_4 motif and eight Mn^{3+} ions forming an external crown (Figure 1. 12). The antiferromagnetic coupling between the different Mn spins leaded to an overall non-compensation of the individual magnetic moment, with as a result *S*= 10. Furthermore, the anisotropy of the Mn^{3+} results in a small Zero Field Splitting (ZFS) generating two degenerated ground spin states separated by an energy barrier, and slow relaxation of the magnetization could be shown by ac measurements (with Δ= 62 K and τ_0 = $2.1\cdot 10^{-7}$ s) and hysteresis of the magnetization appeared below 2.5 K. Moreover, further studies demonstrated from the hysteresis loop of the magnetization, the dependence on the frequency of field swept, the temperature, and the molecular origin rather than a collective behavior (experiments on frozen dilutions of **1** maintained the opened hysteresis loops).[25]

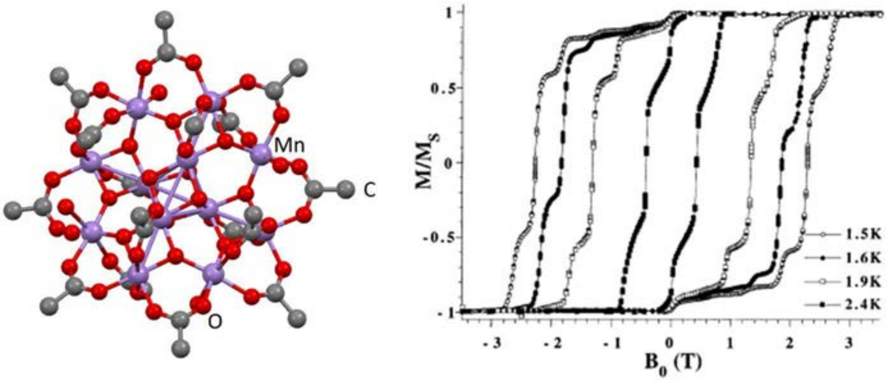

*Figure 1. 12. Representation of the structure of **1** (left), and temperature dependence of the hysteresis loop of the magnetization from -3 to 3 T and different temperatures from 1.5 to 2.4 K. Extracted from ref. [24].*

Another paramount example, is the commonly indicated as Fe_8 ($[Fe_8O_2(OH)_{12}(tacn)_6]Br_8(H_2O)_9$ with tacn= 1,4,7-triazcyclononane, **2**) whose first synthesis dates from 1983 by Wieghardt and coworkers[26]. This compound is formed by controlled hydrolysis of $Fe(tacn)Cl_3$ in a mixture of water and pyridine with the addition of sodium bromide. Different Fe^{3+} coordination sites are characterized in these clusters: thus, the internal Fe^{3+} are octahedrally coordinated to two oxides and four hydroxo bridges; Fe3 and Fe4 are coordinated to three nitrogen atoms of the tacn molecules, two hydroxides and one oxide ion; and finally, the external Fe^{3+} coordinate three nitrogen atoms and three hydroxides (Figure 1. 13, left). From the temperature dependence of the magnetic susceptibility, the total spin is determined to be S=10 which can occur because of the existent frustration between the Fe centers (in triangle distribution).[27]

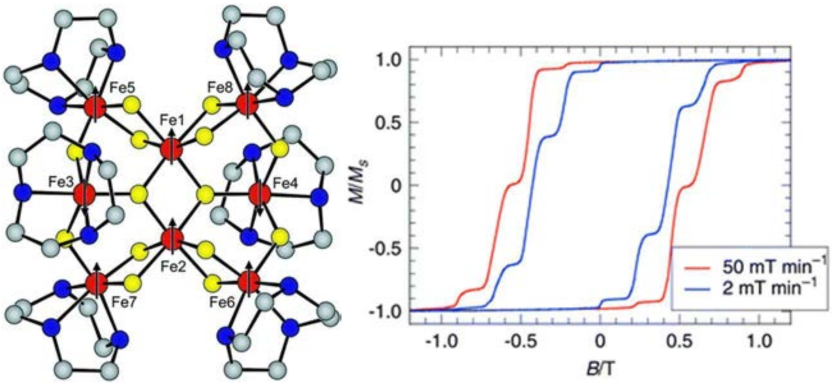

*Figure 1. 13. Representation of the molecular structure of **2** with the different arrows corresponding to the spin structure suggested by susceptibility measurements (left), and hysteresis loops of the magnetization at 0.30 K and different magnetic field sweep rates. Extracted from ref. [27].*

AC measurements lead to Δ= 24.5 K with τ_0= $3.4\cdot10^{-8}$s and the magnetization showed magnetic hysteresis at low temperature (0.3 K). For that system, the *H* sweep rate dependence of the hysteresis loops (Figure 1. 13, right) was verified, and the resulted shape coincided with the stepped appearance reported previously for **1**. These steps corresponded to fast relaxation processes (referred as thermally assisted QTM), whereas the flat regions correspond to fields at which the relaxation is slow. This QTM behavior was further evidenced by magnetic measurements at very low temperatures (0.35 K), for which the relaxation becomes temperature independent. This was suggested to be attributed by the role of the magnetic nuclei present in the cluster (^{1}H (I=1/2), ^{14}N (I=1), ^{79,81}Br (I=3/2), and ^{157}Fe (I=1/2)).

In this direction, using micro SQUID techniques Wernsdorfer *et al.* (2000)[28] were able to determine the difference in the intrinsic width of the tunnel splitting and the different relaxation times (Figure 1. 14), between **2** and its isotopic substituted **^{57}2**(I(^{157}Fe)=1/2) analogue, which slightly increased from 0.8 mT to 1.2 mT. This difference was also observed by partially substituting ^{1}H nucleus for a less magnetic ^{2}H deuterium (D, integer spin I=1). These studies constitute the first example of isotopic enrichment in metal centers for the study of the quantum effects in the relaxation mechanisms of SMM.

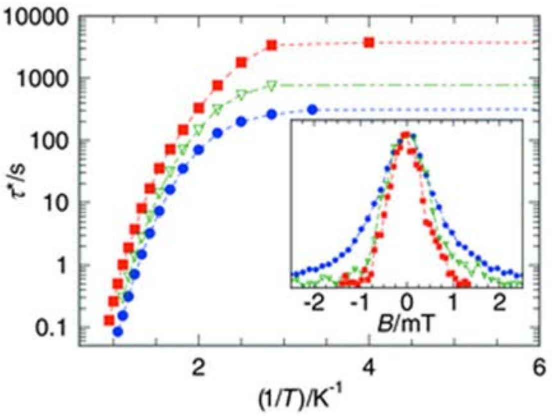

Figure 1. 14. Isotopic effect on the relaxation of the magnetization and, on inset, the intrinsic line-width of the resonant tunneling process. τ* is defined as the time that needs the magnetization to relax from 1% of the saturation value and its temperature dependence is studied for three isotopic samples of **2**: natural sample (green), isotopic ^{57}Fe enrichment (blue), partially deuterated sample (red).[28] Extracted from ref. [27].

A last example of 3d polynuclear systems that deserves to be mentioned is the Fe_4 ($Fe_4(OCH_3)_6(dpm)_6$ with Hdpm= dipivaloylmethane, **3**), whose first structure and magnetic characterization was reported by Barra *et al.* in 1999.[29] Thought the compound exhibits a smaller ground state S=5, it shows superparamagnetic-like behavior. The crystallographic structure is formed by four Fe atoms lying on a plane, the inner Fe atom being in the center of an isosceles triangle. AC measurements on the complex show really low performances of the relaxation of the magnetization, with a Δ value of only 3.5 K and τ_0 of $1.1\cdot10^{-6}$s. The breakthrough induced by this molecule does not concern its magnetic properties, even if it involves that simpler systems can display SMM properties, but from the fact that it has been possible to transfer the derivative **3** onto gold surfaces, thus maintaining the magnetic bistability, which constitutes a step forward for their applicability as molecular devices.[30,31]

Due to the inefficiency of obtaining both S and D large values in 3d-coordinated systems, research started to be focused on the possibility that lanthanides, highly anisotropic molecules, could display slow relaxation of the magnetization. Even though, research in this field has not been frozen. Instead, recent advances were achieved with low nuclearity and symmetry structures based on 3d-metal ions.[32]

Great progress in the field of molecular magnetism has been achieved in 2003, when Ishikawa *et al.* discovered for the first time, mononuclear complexes based on lanthanides ions that could display SMM properties.[33] This revolutionary system is a mononuclear molecule based on Tb^{3+} which has been reported in a family of complexes with general formula (TBA)[$LnPc_2$] (**4**), with Pc^{2-}= phthalocyanine and TBA^{+}= tetrabutylammonium, where the Ln^{3+} is embedded by two Pc^{-} moieties in a "double-decker" structure (or what we called previously "sandwich distribution"), and the charge counter-balanced by TBA^{+}. This new system (Figure 1. 15) showed an incredible enhancement of the effective energy barrier, compared to **1**, with Δ= 230 cm^{-1}.[34]

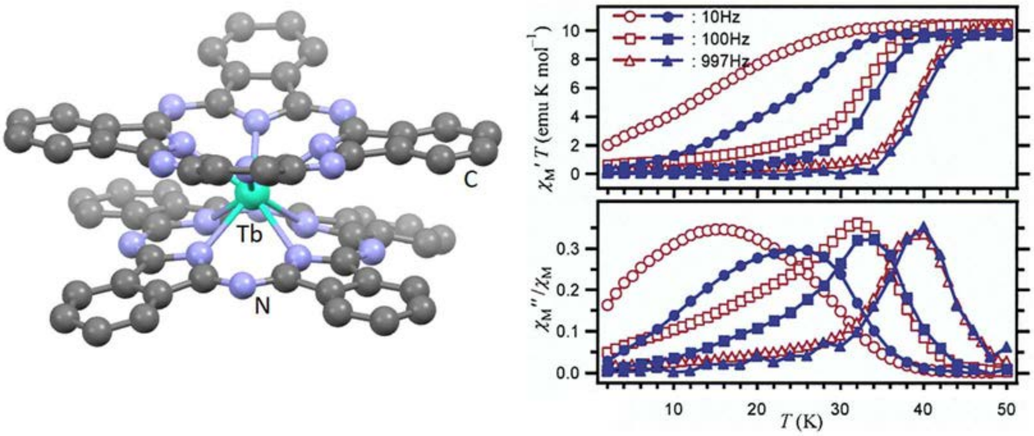

*Figure 1. 15. Representation of the molecular structure of **4**, H atoms and counter-ions have been omitted for clarity. Representation of χ'T/ χ''T against T for different frequency values. Adapted from ref. [33].*

Hundreds of articles concerning lanthanides for their use as SMM have been published[35,36] in order to analyze them as well as to propose different strategies for the optimization of the magnetic properties[13] (referred to the CF distribution[37], magnetic dilution[38] or/and isotopic enrichment[39,40,41,42,43]. Among them, Dy-based (also Tb^{3+}) complexes, are the most exploited systems for their study. Such importance of Dy^{3+} cations comes from the fact that, it usually leads to high energy barriers due to its high magnetic anisotropy and often large separation between the ground and first excited M_J levels. Furthermore, if we compare it to Tb^{3+}, which also shows large energy barriers, the Dy^{3+} is a Kramer ion (it has an odd number of f-electrons), meaning that the bistability of the ground state cannot be broken by any ligand field symmetry.

The Δ parameter has been largely increased since the firsts values, currently reaching values of more than 1260 cm^{-1}.[44]However, until recently it did not overpass 28 K.[45] Indeed, the increase of the energy barrier has been proven during the ages, to not be the solely parameter that need to be taken into account in order to increase the working temperature, but also the events shortcutting the barrier need to be suppressed. Indeed, if we look at the hysteresis loops of the different mononuclear Ln^{3+} based SMM systems, a typical butterfly-shape appears in the hysteresis loops of the magnetization, thus abruptly collapsing at zero magnetic field. A motivation for a better understanding of this low temperature quantum phenomena, bears to the use of two different strategies already mentioned above: whereas ones make use of the magnetic dilution and isotopic enrichment for the suppression of the “forbidden” relaxations;[39,40bd,41,43,42] others study the nuclear spin active isotopes in order to create multiple quantum bits for the quantum processing.[40a,41,43,46]

A recent step-change has been carried with the publication of a series of Dy^{3+} metallocenium complexes, for which the hysteresis of the magnetization has been preserved up to 60 K[47], and later increased up to 80 K[48], reaching temperatures accessible in the liquid nitrogen zone and favoring the insertion of this systems into electron or spin devices. First, in 2018 two different groups in Manchester, worked in parallel to publish the study of the extraordinary properties of a Dy based compound of family general formula $[Ln(Cp^{ttt})_2][B(C_6F_5)_4]$, with Cp^{ttt} = 1,2,4-tris-terbutilcyclopentadienyl (**5**). The idea of this work was to synthesis the simplest crystallographic structure in order to approximate the system to a perfect axiality, thus avoiding the transverse components and the undesirable relaxation phenomena for the information storage, which originately came from the theoretical work of N. F. Chilton in 2015.[49] Magnetic measurements on this compound lead to open hysteresis at and below 60 K using a sweep rate of 22 Oe s^{-1}, with 83% remnant magnetization and a coercive field of 20–25 kOe at 2 K, when the dynamic properties, the system showed Δ of 1760 K, and $\tau_0 = 1.986 \cdot 10^{-11}$ s.

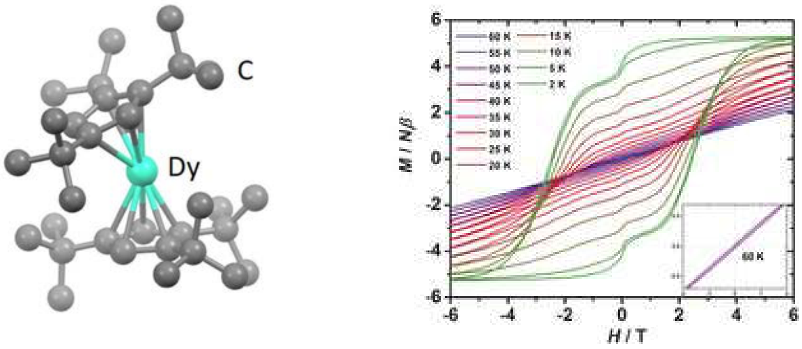

*Figure 1. 16. Representation of the molecular structure of **5**, H atoms and counter-ions have been omitted for clarity, and magnetic hysteresis of **5** from 2 to 60 K. Extracted from ref. [47]*

A little after, at the end of last year, Layfield and coworkers broke again the record with a slightly modified system $[(\eta^5\text{-}Cp^{iPr5})Dy(\eta^5\text{-}Cp^*)][B(C_6F_5)_4]$ (**6**), in which Cp^{iPr5}= penta-iso-propylcyclopentadienyl and Cp*=pentamethylcyclopentadienyl. This presented a larger angle Cp-Dy-Cp compared to **5**, leading to a temperature of 80 K with similar Orbach characteristics.

As it can be seen in the lasts few pages, much effort has been invested in this field and great advances have been achieve in only twenty years. However, we are still far from a complete understanding of such molecular systems. Until now, the understanding acquired makes us such consider a greater number of factors compared to its beginning (structure, nuclear moments, interactions…), so that we can go a step closer.

Finally, these mononuclear SMMs (also referred as SIMs, from Single Ion Magnets) have shown to be particularly sensible to changes in the CF (to small changes in the ligand structure), which means that in specific systems their slow magnetic relaxation effects can be controlled with structural modulation and an external stimulus (e.g., a magnetic field, light, solvation/desolvation, etc.) thus inducing switchable molecules,[50] which could also be of big appealing for new devices in molecular electronics and spintronics. However, whatever the possible application, once obtained the best SMM behavior, other considerations will need to be taken, as it is the robustness of the structure (note that in order to be applied in any device, the first step is to guarantee its properties in a surface where it can be manipulated).

REFERENCES:

[5] A. R. West, *Solid State Chemistry and its Applications*, Wiley-Blackwell, Hoboken, United States, **2014**.

[6] C. Huang, *Rare Earth Coordination Chemistry: Fundamentals and Applications*, Wiley, Singapore, Asia, **2010**.

[7] J. Tang, and P. Zhang, *Lanthanide Single Molecule Magnets*, Springer, Berlin, **2015**.

[8] R. A. Layfield, and M. Murugesu, *Lanhanides and Actinides in Molecular Magnetism*, Willey-VCH, Weinheim, Germany, **2015**.

[9] J. Luzon, and R. Sessoli, *Dalton Trans.*, **2012**, *41*, 13556.

[10] P. G. Huray, and S. E. Nave, *Handbook of the Physics and Chemistry of the Actinides*, Elsevier, **1987**.

[11] R. Sessoli, and A. K. Powell, *Coord. Chem. Rev.*, **2009**, *253*, 2328.

[12] M. N. Leuenberger, and D. Loss, *Nature*, **2011**, *410*, 789.

[13] S. T. Liddle, and J. van Slageren, *Chem. Soc. Rev.,* **2015**, *44*, 6655.

[14] H. L. C. Feltham, and S. Brooker, *Coord. Chem. Rev.*, **2014**, *276*, 1.

[15] R. Sessoli, D. Gatteschi, A. Caneschi, M. A. Novak, *Nature*, **1993**, *365*, 141.

[16] J. D. Rinehart, and J. R. Long, *Chem. Sci.*, **2011**, *2*, 2078.

[17] J. M. Zandrozny, M. Atanasov, A. M. Bryan, C.-Y. Lin, B. D. Rekken, P. P. Power, F. Neese, and J. R. Long, *Chem. Sci.*, **2013**, *4*, 125.

[18] R. L. Carlin, *Magnetochemistry*, Springer, Berlin, **1986**.

[19] a) J.-L. Liu, K. Yuan, J.-D. Leng, L. Ungur, W. Wernsdorfer, F.-S. Guo, L. F. Chibotaru and M.-L. Tong, *Inorg. Chem.*, **2012**, *51*, 8538; b) E. Colacio, J. Ruiz, E. Ruiz, E. Cremades, J. Krzystek, S. Carretta, J. Cano, T. Guidi, W. Wernsdorfer, E. K. Brechin, *Angew. Chem. Ed.*, **2013**, *52*, 9130; c) M. A. Palacios, J. Nehrkorn, E. A. Suturina, E. Ruiz, S. Gomez-Coca, K. Holldack, A. Schnegg, J. Krzystek, J. M. Moreno, and E. Colacio, *Chem. Eur. J.*, **2017**, *23*, 11649.

[20] J. Liu, D. Reta, J. A. Cleghorn, Y. X. Yeoh, F. Ortu, C. A. P. Goodwin, N. F. Chilton, and D. P. Mills, *Chem. Eur. J.*, **2019**, *25*, 7749.

[21] a) A. Singh, and K. N. Shrivastava, *Phys. Stat. Sol. B,* **1979**, *95*, 273; b) K. N. Shirivastava, *Phys. Status Solidi B,* **1983**, *177*, 437.

[22] R. Sessoli, H. L. Tsai, A. R. Schake, S. Wang, J. B. Vincent, K. Folting, D. Gatteschi, G. Christou and D. N. Hendrickson, *J. Am. Chem. Soc.*, **1993**, *115*, 1804.

[23] A. M. Ako, I. J. Hewitt, V. Mereacre, R Clérac, W. Wernsdorfer, C. E. Anson, A. K. Powell, *Angew. Chem. Int. Ed.,* **2006**, *46*, 4926.

[24] T. Lis, *Acta Crystallogr. Sect. B.,* **1980**, *36(9)*, 2042.

[25] a) C. Paulsen, J.-G. Park, B. Barbara, R. Sessoli, and A. Caneschi, *J. Magn. Magn. Mater.*, **1995**,*140-144*, 379; b) M. R. Cheesman, V. S. Oganesyan, R. Sessoli, D. Gatteschi, and A. J. Thomson, *Chem. Commun.*, **1997**, 1677; c) E. J. L. McInnes, E. Pidcock, V. S. Oganesyan, M. R. Cheesman, A. K. Powell, and A. J. Thomson, *J. Am. Chem. Soc.*, **2002**, *124(31)*, 9219.

[26] K. Weighardt, D.-C. K. Pohl, I. Jibil, G. Huttner, *Angew. Chem. Int. Ed. Engl.,* **1984**, *23(1),* 77.

[27] D. Gatteschi, R. Sessoli, and A. Cornia, *Chem. Commun.*, **2000**, 725.

[28] W. Wernsdorfer, A. Caneschi, R. Sessoli, D. Gatteschi, A. Cornia, V. Villar, and C. Paulsen, *Phys. Rev. Lett.,* **2000**, *84*, 2965.

[29] A. L. Barra, A. Caneschi, A. Cornia, F. Fabrizi de Biani, D. Gatteschi, C. Sangregorio, R. Sessoli, and L. Sorace, *J. Am. Chem. Soc.,* **1999**, *121*, 5302.

[30] M. Mannini, F. Pineider, Ph. Sainctavit, C. Danieli, E. Otero, C. Sciancalepore, A. M. Talarico, M.-A. Arrio, A. Cornia, D. Gatteschi, and R. Sessoli, *Nat. Mater.*, **2009**, *8*, 194.

[31] M. Mannini, F. Pineider, C. Danieli, F. Totti, L. Sorace, Ph. Sainctavit, M.-A. Arrio, E. Otero, J. C. Cezar,

A. Cornia, and R. Sessoli, *Nature,* **2010**, *468*, 417.

[32] a) W.H. Harman, T. D. Harris, D. E. Freedman, H. Fong, A. Chang, J. D. Rinehart, A. Ozarowsky, M. T. Sougrati, F. Grandjean, G. J. Long, J. R. Long, and C. J. Chang, *J. Am. Chem. Soc.*, **2010**, *132*, 18115; b) G. A. Craig, and M. Murrie, *Chem. Soc. Rev.*, **2015**, *40*, 3212; c) J. Vallejo, O. Castro, R. Ruiz-García, J. Cano, M. Julve, F. Lloret, G. De Munno, W. Wernsdorfer, and E. Pardo, *J. Am. Chem. Soc.*, **2012**, *134(38),* 15704; c) F.-S. Guo, A. K. Bar, and R. A. Layfield, *Chem. Rev.*, **2019**, *119(14)*, 8479.

[33] N. Ishikawa, M. Sugita, T. Ishikawa, S.-Y. Koshihara, and Y. Kaizu, *J. Am. Chem. Soc.,* **2003**, *125*, 8694.

[34] N. Ishikawa, M. Sugita, and W. Wernsdorfer, *Angew. Chem. Int. Ed.,* **2005**, *44*, 2931.

[35] R. Sessoli, and A. K. Powell, *Coord. Chem. Rev.*, **2009**, *253*, 2328.

[36] a) R. E. P. Winpenny, R.A. Layfield, *Chem. Rev.*, **2013**, *113*, 5110; b) H. L. C. Feltham, S. Brooker, *Coord. Chem. Rev.*, **2014**, *276*, 1; c) P. Zhang, Y.-N. Guo, and J. Tang, *Coord. Chem. Rev.*, **2013**, *257*, 1728; d) F. Pointillart, B. Le Guennic, O. Cador, O. Maury, and L. Ouahab, *Acc. Chem. Res.*, **2015**, *48*, 2834.

[37] J. D. Rinehart, and J. R. Log, *Chem. Sci.*, **2011**, *2*, 2078.

[38] G. Cosquer, F. Pointillart, S. Golhen, O. Cador, and L. Ouahab, *Chem. Eur. J.*, **2013**, *19*, 7895.

[39] a) F. Pointillart, K. Bernot, S. Golhen, B. Le Guennic, T. Guizouarn, L. Ouahab, and O. Cador, *Angew. Chem.*, **2015**, *127*, 1524; b) Y. Kishi, F. Pointillart, B. Lefeuvre, F. Riobé, B. Le Guennic, S. Golhen, O. Cador, O. Maury, H. Fujiwara, and L. Ouahab, *Chem. Commun.*, **2017**, *53*, 3575; c) G. Huang, X. Yi, J. Jung, O. Guillou, O. Cador, F. Pointillart, B. Le Guennic, and K. Bernot, *Eur. J. Inorg. Chem.* ***2018,*** 326.

[40] a) K. S. Pedersen, A.-M. Ariciu, S. McAdams, H. Weihe, J. Bendix, F. Tuna, and S. Piligkos, *J. Am. Chem. Soc.*, **2016**, *138*, 5801; b) L. Tesi, Z. Salman, I. Cimatti, F. Pointillart, K. Bernot, M. Mannini, and R. Sessoli, *Chem. Commun.,* **2018**, *54*, 7826; c) R. Hussain, G. Allodi, A. Chiesa, E. Garlatti, D. Mitcov, A. Konstantatos, K. S. Pedersen, R. De Renzi, S. Piligkos, and S. Carretta, *J. Am. Chem. Soc.*, **2018**, *140*, 9814; d) Fabrizio Ortu, Daniel Reta, You-Song Ding, Conrad A. P. Goodwin, M. P. Gregson, E. J. L. McInnes, R. E. P. Winpenny, Y.-Z. Zheng, S. T. Liddle, D. P. Mills and N. F. Chilton, *Dalton Trans.*, **2019**, *48*, 8541.

[41] E. Moreno-Pineda, M. Damjanović, O. Fuhr, W. Wernsdorfer, and M. Ruben, *Angew. Chem. Int. Ed.*, **2017**, *56*, 9915.

[42] Y.-C. Chen, J.-L. Liu, W. Wernsdorfer, D. Liu, L. F. Chibotaru, X. M. Chen, and M.-L. Tong*, Angew. Chem. Int. Ed.*, **2017**, *56*, 4996*.*

[43] E. Moreno-Pineda, G. Taran, W. Wernsdorfer and M. Ruben, *Chem. Sci.*, **2019**, *10*, 5138.

[44] a) Y.-C. Chen, J.-L. Liu, L. Ungur, J. Liu, Q.-W. Li, L. F. Wang, Z.-P. Ni, L. F. Chibotaru, X.-M. Chen and M.-L. Tong, J. Am. Chem. Soc., **2016**, *138*, 2829; b) S. K. Gupta, T. Rajeshkumar, G. Rajaraman and R. Murugavel, Chem. Sci., **2016**, 7, 5181; c) M. Gregson, N. F. Chilton, A.-M. Ariciu, F. Tuna, I. F. Crowe, W. Lewis, A. J. Blake, D. Collison, E. J. L. McInnes, R. E. P. Winpenny and S. T. Liddle, *Chem. Sci.,* **2016**, *7*, 155; d) J. Liu, Y.-C. Chen, J.-L. Liu, V. Vieru, L. Ungur, J.-H. Jia, L. F. Chibotaru, Y. Lan, W. Wernsdorfer, S. Gao, X.-M. Chen and M.-L. Tong, J. Am. Chem. Soc., **2016**, *138*, 5441; e) Y.-S. Ding, N. F. Chilton, R. E. P. Winpenny and Y.-Z. Zheng, *Angew. Chem., Int. Ed.*, **2016**, *55*, 1607.

[45] S. Demir, M. I. Gonzalez, L. E. Darago, W. J. Evans and J. R. Long, *Nat. Commun.*, **2017**, *8*, 2144.

[46] a) S. Thiele, F. Balestro, R. Ballou, S. Klyatskaya, M. Ruben, and W. Wernsdorfer, *Science,* **2014**, *344(6188)*, 1135; b) C. Godfrin, A. Ferhat, R. Ballou, S. Klyatskaya, M. Ruben, W. Wernsdorfer, and F. Balestro, *Phys. Rev. Lett.*, **2017,***119*, 187702.

[47] a) C. A. P. Goodwin, F. Ortu, D. Reta, N. F. Chilton and D. P. Mills, *Nature*, **2017**, *548*, 439; b) F.-S. Guo, B. M. Day, Y.-C. Chen, M.-L. Tong, A. Mansikkamäki, R. A. Layfield, *Angew. Chem. Int. Ed.,* **2017**, *56*, 11445.

[48] F.-S. Guo, B. M. Day, Y.-C. Chen, M.-L. Tong, A. Mansikkamäki and R. A. Layfield, *Science*, **2018**, *362*, 1400.

[49] N. F. Chilton, *Inorg. Chem.*, **2015**, *54(5)*, 2097.

[50] a) J. Vallejo, E. Pardo, M. Viciano-Chumillas, I. Castro, P. Amoros, M. Deniz, C. Ruiz-Perez, C. Yuste-Vivas, J. Krzystek, M. Julve, F. Lloreta and J. Cano, *Chem. Sci.*, **2017**, *8*, 3694; b) J.-L. Liu, Y.-C. Chen, Y.-Z.

Zheng, W.-Q. Lin, L. Ungur, W. Wernsdorfer, L. F. Chibotaru, and M.-L. Tong, *Chem. Sci.*, **2013**, *4*, 3310; c) L. Norel, M. Feng, K. Bernot, T. Roisnel, T. Guizouarn, K. Costuas, and S. Rigaut, *Inorg. Chem.*, **2014**, *53*, 2361; d) I.-R. Jeon, L. Sun, B. Negru, R. P. Van Duyne, M. Dincă, and T. D. Harris, *J. Am. Chem. Soc.*, **2016**, *138*, 6583; e) D.-Q. Wu, D. Shao, X.-Q. Wei, F.-X. Shen, L. Shi, D. Kempe, Y.-Z. Zhang, K. R. Dunbar, and X.-Y. Wang, *J. Am. Chem. Soc.*, **2017**, *139*, 11714; f) D. Pinkowicz, M. Ren, L.-M. Zheng, S. Sato, M. Hasegawa, M. Morimoto, M. Irie, B. K. Breedlove, G. Cosquer, K. Katoh, and M. Yamashita, *Chem. Eur. J.*, **2014**, *20*, 12502.

CHAPTER II

EXPERIMENTAL TECHNIQUES

This second chapter, which is split into two different sections, aims to explain all the specific details concerning the experimental techniques used in this work.

In the first section, the synthetic procedures used to obtain the different compounds are described, along with the the results of infrared (IR) spectroscopy. In the second section, all the different techniques for the physical and structural characterization of the different complexes is presented. Special emphasis will be given in the mechanisms and working principals of those related with the magnetism of the crystals.

I. SYNTHESES

A. *Synthesis of [Ln(tta)$_3$(L^2)]·C$_6$H$_{14}$*

A.1. *4,5-bis(propylthio)-tetrathiafulvalene-2-(2-pyridyl)benzimidazole-methyl-2-pyridine: L^2*

The synthesis of 4,5-bis(propylthio)-tetrathiafulvalene-2-(2-pyridyl)benzimidazole-methyl-2-pyridine ligand (**L^2**) was previously realized by Haiet Douib and Bertrand Lefeuvre, members of the group specialized in organic chemistry. The procedure, schematically represented in Figure 2.1, consisted in 6 different steps starting from *o*-phenylenediamine on one side, and zincate on the other. As a result, two different compounds **L^1** (305 mg of pale orange powder, 28% yield) and **L^2** (244 mg of bright orange powder, 19% yield) were collected.[51]

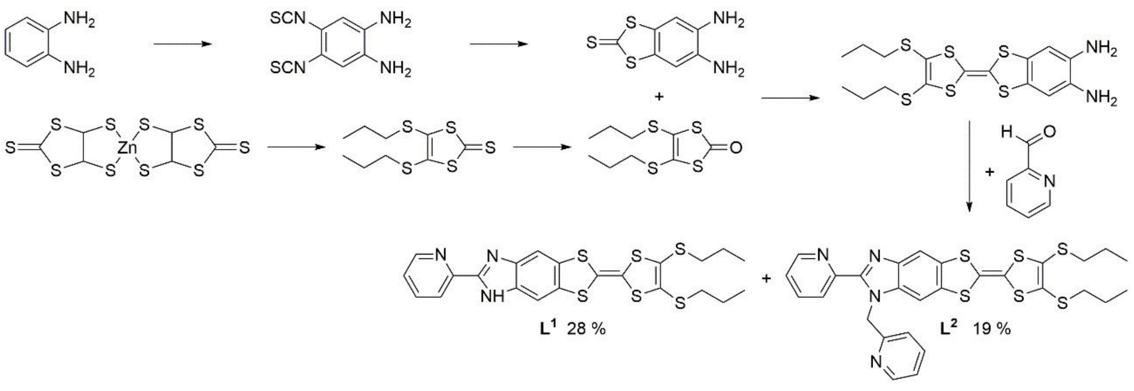

*Figure 2. 1. Scheme of the different steps for the synthesis of **L^2**.*

A.2. *Lanthanide-bis(aqueous)tris(2-thenoyltrifluoroacetonate), $Ln(tta)_3\cdot 2H_2O$*

In a flask, 2-thenoyltrifluoroacetone (224 mg, 1.010 mmol) was added to 180 mL of distilled water. The mixture was stirred at 60 °C and adjusted to pH 6-6.5 by dropwise of NH_4OH at 25%. Simultaneously, around 0.126 mmol of Ln_2O_3 (with Ln: $^{162/163}$Dy (47.1 mg); $^{173/174}$Yb and natural Yb (49.7/50/50 mg), and $^{166/167}$Er and natural Er (47.9/ 50.5/ 42 mg)) was dissolved in 130 μL of concentrated HCl (37%). After 30 min of stirring at 50 °C, the resulting solution containing $LnCl_3\cdot 6H_2O$ (0.205 mmol) was diluted with 1 mL of water before being added to the former. The pH of the solution was adjusted to 7-7.5 during the stirring leading to a white precipitate of $Ln(tta)_3\cdot 2H_2O$ which was filtered. Yields $^{162}Dy(tta)_3\cdot 2H_2O$: 115 mg (53 %); $^{163}Dy(tta)_3\cdot 2H_2O$: 110 mg (51 %); $^{166}Er(tta)_3\cdot 2H_2O$: 157.9 mg (73 %); $Er(tta)_3\cdot 2H_2O$: 121 mg (64 %); $^{167}Er(tta)_3\cdot 2H_2O$: 121.7 mg (53 %); $Yb(tta)_3\cdot 2H_2O$: 125 mg (57 %); $^{173}Yb(tta)_3\cdot 2H_2O$: 127.4 mg (58 %); $^{174}Yb(tta)_3\cdot 2H_2O$: 123.5 mg (56 %).[52]

IR: $^{162}Dy(tta)_3\cdot 2H_2O$: 1607(s), 1540(s), 1511(m), 1465(m), 1411(s), 1359(s), 1307(s), 1250(m), 1231(m), 1190(s), 1141(s), 1082(w), 1062(m), 1039(w), 936(m), 861(m), 791m), 769(w), 752(w), 720(m), 684(m), 643(m), 606(w), 583(m), 503(w), 463(w); $^{163}Dy(tta)_3\cdot 2H_2O$: 1609(s), 1541(s), 1507(m), 1457(m), 1412(s), 1367(s), 1308(s), 1250(s), 1232(m), 1190(s), 1143(s), 1083(w), 1063(m), 1039(w), 936(m), 861(m), 789(m), 770(w), 719(m), 683(m), 644(m), 606(w), 584(m), 503(w), 463(w), 419(w); $^{166}Er(tta)_3\cdot 2H_2O$: 1605(s), 1541(s), 1512(m), 1465(w), 1411(s), 1359(s),1306(s), 1251(m), 1232(m), 1191(s), 1140(s), 1082(w), 1063(m), 1039(w), 936(m), 861(m), 788(m), 752(w), 713(m), 684(w), 643(m), 606(w), 584(m), 503(w); $Er(tta)_3\cdot 2H_2O$: 1604(s), 1541(s), 1511(m), 1465(w), 1411(s), 1539(m), 1306(s), 1251(m), 1232(m), 1192(s), 1139(s), 1082(w), 1063(m), 1039(w), 936(m), 861(m), 788(m), 752(w), 722(m), 684(m), 644(m), 607(w), 583(m), 503(w); $^{167}Er(tta)_3\cdot 2H_2O$: 1604(s), 1541(s), 1508(m), 1465(w), 1411(s), 1359(s), 1306(s), 1251(m); 1232(w), 1191(s), 1139(s), 1080(w), 1063(m), 1039(w), 936(m), 861(w), 788(m), 752(w), 720(w), 713(m), 684(w), 644(m), 605(w), 584(m); $Yb(tta)_3\cdot 2H_2O$: 1060(s), 1543(s), 1513(m), 1459(m), 1412(s), 1358(s), 1308(s), 1256(m), 1234(m), 1188(s), 1142(s), 1085(w), 1063(m), 1036(w), 1014(w), 936(m), 862(m), 788(m), 772(w), 749(w), 732(m), 718(m), 686(m), 645(m), 607(w), 586(m), 505(w); $^{173}Yb(tta)_3\cdot 2H_2O$: 1603(s), 1543(s), 1512(m), 1467(w), 1411(s), 1359(s), 1306(s), 1251(m), 1232(m), 1192(s), 1137(s), 1071(w), 1063(m), 1039(w), 937(m), 862(m), 788(m), 769(w), 752(w), 736(m), 713(m), 695(w), 684(w), 643(m), 607w), 584(m); $^{174}Yb(tta)_3\cdot 2H_2O$: 1606(s), 1543(s), 1513(m), 1458(m), 1412(s), 1357(s), 1308(s), 1255(m), 1233(m), 1188(s), 1141(s), 1084(w), 1063(m), 1038(w), 936(m), 862(m), 788(m), 771(w), 750(w), 732(w), 718(m), 685(m), 644(m), 607(w), 585(m), 463(w).

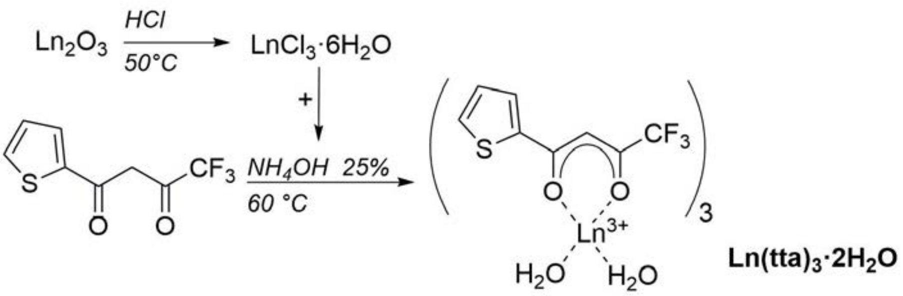

Figure 2. 2. Complexation reaction of $Ln(tta)_3\cdot 2H_2O$ being Ln= ^{A}Dy, ^{B}Yb, ^{C}Er and Y.

A.3. *Complexation of Lanthanide- tris(2-thenoyltrifluoroacetonate)(4,5-bis(propylthio)-tetrathiafulvalene-2-(2-pyridyl)benzimidazole-methyl-2-pyridine), $[Ln(tta)_3(L^2)]\cdot C_6H_{14}$[53]*

$[^ALn(tta)_3($**L²**$)]\cdot C_6H_{14}$ ($^{162/163}$**Dy**): **L²** (24.4 mg, 0.04 mmol) and $^ALn(tta)_3\cdot 2H_2O$ (34.5 mg, 0.04 mmol), being A the isotopic number, were first dissolved separately (8 mL of CH_2Cl_2 each) and then mixed and stirred during 15 minutes. *n*-hexane was layered gently to the solution for a slow diffusion. Red prismatic single crystals were obtained after two weeks of diffusion and then slow evaporation at room temperature. Yields ^{162}**Dy**: 47.7 mg (83 %) and ^{163}**Dy**: 50.0 mg (87 %). IR: ^{162}**Dy**: 3092(w), 2962(w), 2929(w), 2853(w), 1630(s), 1603(s), 1539(s), 1504(m), 1479(m), 1454(w), 1413(m), 1354(w), 1309(s), 1247(m), 1231(m), 1182(s), 1141(s), 1058(w), 935(w), 879(w), 858(w), 827(w), 785(m), 750(w), 713(m), 681(w), 641(m), 583(w), 499(w), 463(w); ^{163}**Dy**: 3905(w), 2963(w), 2925(w), 2868(w), 1627(m), 1601(s), 1540(m), 1505(m), 1478(m), 1452(w), 1413(m), 1355(m), 1312(s), 1248(m), 1231(m), 1183(s), 1138(s), 1058(w), 934(w), 876(w), 857(w), 829(w), 785(w), 777(m), 749(w), 713(w), 683(w), 643(w), 584(w), 495(w).

$[^ALn_{0.05}Y_{0.95}(tta)_3($**L²**$)]\cdot C_6H_{14}$ (^{A}**Dy@Y**, ^{A}**Er@Y**, ^{A}**Yb@Y**): A CH_2Cl_2 solution (15 mL) of **L²** (61.0 mg, 0.1 mmol) is added to a CH_2Cl_2 solution (10 mL) containing $^{162/163}Dy(tta)_3\cdot 2H_2O$ (3.4 mg, 0.004 mmol) and $Y(tta)_3\cdot 2H_2O$ (75.7 mg, 0.096 mmol) and stirred during 15 minutes. *n*-hexane is layered to the solution and red prismatic single crystals were obtained after two weeks of diffusion and then slow evaporation at room temperature. Same procedure was followed in order to synthetize the Er and Yb based systems (natural and $^{166/167}$**Er@Y,** and natural and

$^{173/174}$Yb@Y), thus with a slightly modified mass values: 42-42.5 mg of **L^2**, 3-3.2 mg of Ln(tta)$_3$·2H$_2$O and 51.4-51.8 mg of Y(tta)$_3$·2H$_2$O. Yields **^{162}Dy@Y**: 47.7 mg (80 %); **^{163}Dy@Y**: 50.0 mg (85 %); **Er@Y**: 69 mg (69%); **^{166}Er@Y**: 70.5 mg (71%); **^{167}Er@Y**: 66.9 mg (67%); **Yb@Y**: 54.2 mg (54%); **^{173}Yb@Y**: 72.2 mg (72%); **^{174}Yb@Y**: 70.9 mg (71%). IR: **^{162}Dy@Y**: 3084(w), 2962(w), 2930(w), 2859(w), 1630(s), 1602(s), 1539(s), 1506(m), 1478(m), 1412(s), 1355(m), 1311(s), 1244(m), 1129(m), 1184(s), 1140(s), 1059(m), 1008(w), 933(w), 879(w), 855(w)826(w), 784(s), 747(m), 715(m), 681(m), 639(m), 582(m), 495(w), 462(w), 418(w); **^{163}Dy@Y**: 3096(w), 2960(w), 2925(w), 2858(w), 1630(s), 1602(s), 1539(s), 1504(m), 1475(m), 1454(w), 1412(s), 1355(w), 1308(s), 1247(m), 1229(m), 1184(s)1138(s), 1058(w), 1010(w), 934(w), 881(w), 856(w), 826(w), 784(m), 748(w), 713(m), 681(w), 640(w), 581(w), 497(w), 463(w); **Yb@Y**: 3094(w), 2965(w), 2926(w), 2861(w), 1630(s), 1603(s), 1574(m), 1541(s), 1522(m), 1503(m), 1479(m), 1453(w), 1414(s), 1356(m), 1313(s), 1247(m), 1231(s), 1184(s), 1166(w), 1140(s), 1083(w), 1061(m), 1011(w), 935(w), 877(w), 858(w), 828(w), 785(s), 750(m), 714(m), 680(m), 642(m), 582(m), 497(w), 462(w); **^{173}Yb@Y**: 3096(w)2965(w), 2927(w), 2871(w), 1631(m), 1603(s), 1538(m), 1503(m), 1478(m), 1449(w), 1414(m), 1356(w), 1311(s), 1245(m), 1230(m), 1186(m), 1139(s), 1061(w), 934(w), 875(w), 856(w), 830(w), 785(m), 785(m), 750(w), 712(m), 682(w), 642(w), 582(m), 497(w), 465(w); **^{174}Yb@Y**: 3098(w), 2962(w), 2930(w), 2857(w), 1630(m), 1603(s), 1536(m), 1503(m), 1481(m), 1451(w), 1413(m), 1356(w), 1311(s), 1246(m), 1230(m), 1184(s), 1141(s), 1059(w), 935(w), 878(w), 858(w), 828(w), 784(m), 750(w), 712(w), 682(w), 641(w), 584(w), 496(w), 462(w); **^{166}Er@Y**: 3095(w), 2968(w), 2927(w), 2869(w), 1630(s), 1603(s), 1539(m), 1504(m), 1478(m), 1450(w), 1413(m), 1356(m), 1311(s), 1246(m), 1231(m), 1185(s), 1141(s), 1060(w), 935(w), 878(w), 856(w), 827(w), 785(m), 748(w), 717(m), 681(w), 641(w), 582(w), 498(w); **^{167}Er@Y**: 3097(w), 2961(w), 2927(w), 2868(w), 1631(m), 1631(s), 1604(s), 1573(m), 1505(m), 1478(m), 1455(m), 1414(s), 1356(m), 1311(s), 1245(m), 1230(m), 1186(s), 1141(s), 1061(w), 1014(w), 934(w), 880(w), 857(w), 831(w), 786(m), 749(m), 715(m), 681(m), 640(m), 583(m), 500(w), 457(w).

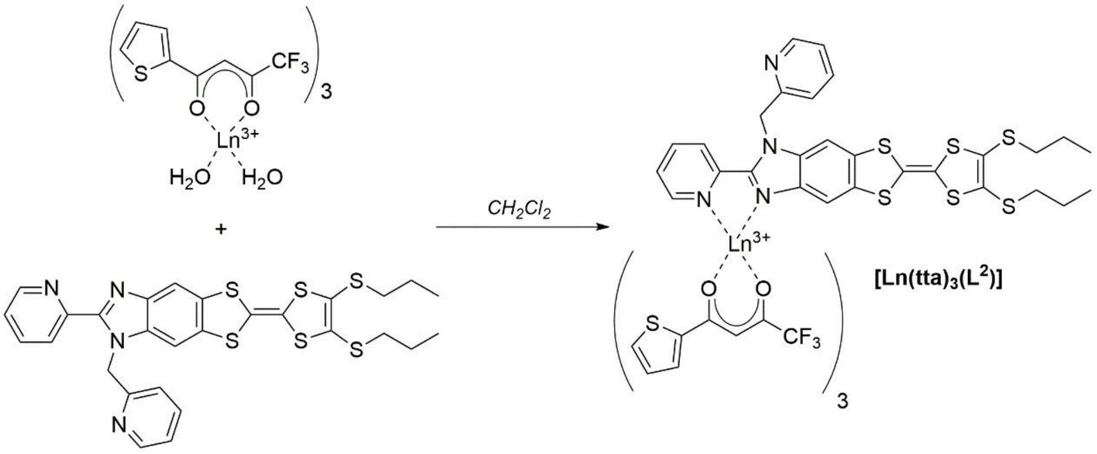

*Figure 2. 3. Complexation reaction of [Ln(tta)$_3$(**L^2**)]·C$_6$H$_{14}$.*

B. *Synthesis of Na$_9$[Er(W$_5$O$_{18}$)$_2$]·xH$_2$O, ErW$_{10}$·xH$_2$O*

B.1. *Na$_9$[Er(W$_5$O$_{18}$)$_2$]·xH$_2$O (with x= 35), ErW$_{10}$·35H$_2$O*

Na$_9$[^{A}Er(W$_5$O$_{18}$)$_2$]·xH$_2$O (with x= 35) (**ErW$_{10}$**) samples were prepared following a modified version of an already published method, as the isotopic enriched precursors are in the oxide form.[54,55] At first, isotopically enriched ErCl$_3$·6H$_2$O was formed by dissolving 30 mg of ^{A}Er$_2$O$_3$·6H$_2$O (being A= 166 or 167) in 400 µL of 37% HCl during 30 minutes at 80°C with continuous stirring. This first stage of the synthesis is of paramount importance, as the polyoxometallates are very sensitives to changes on the pH. Thus, 1 mL of distilled water was added and the pH was adjusted to 3 with a 3 M NaOH solution. Simultaneously, Na$_2$WO$_4$·2H$_2$O (15.2 mmol, 5 g) was dissolved in distilled water (10 mL) with continuous stirring, the pH was adjusted to 7.2 with acetic anhydride, and the resulting solution was heated up to 90 °C. Then, the former solution was poured dropwise and hold under vigorous stirring for 1 h. The mixture was filtered rapidly and left to evaporate at room temperature during 2 to 4 days. After this period, a mixture of different crystal types appeared and a second recrystallization in hot water (60°C) was needed in order to obtain the desired structure. As a result, needled-shaped pale-pink crystals were obtained. Yield: **ErW$_{10}$·35H$_2$O**: 263 mg (63%); **^{166}ErW$_{10}$·35H$_2$O**: 217.4 mg (52%); **^{167}ErW$_{10}$·35H$_2$O**: 179 mg (43%).

B.2. *Dehydration and hydration procedures of Na$_9$[Er(W$_5$O$_{18}$)$_2$]·xH$_2$O*

ErW$_{10}$·xH$_2$O (with x= 5) was prepared following two different methods. On one side, in order to warrant the dehydrated state during the magnetic study, the sample was dehydrated inside the SQUID and PPMS magnetometers. The dehydration process consists in a sequence of repeated purges at 300 K during 1 hour. On the other hand, a lab protocol was set consisting in heating the sample overnight up to 80 °C under vacuum.

Rehydration process of the samples consisted in keeping the dehydrated powder during 1 day in the proximity of some water drops.

B.3. $Na_9[^{A}Er(W_5O_{18})_2]\cdot xD_2O$ (with x= 35)

$ErW_{10}\cdot xD_2O$ (with x= 35) was obtained by collecting 100 mg of needled-shaped pale-pink crystals, dehydrating them following the protocol stablished in the laboratory. Once the dehydration finished, the container is filled by argon and deuterated water was added (15 mL). The solution was warm up to 50 °C under stirring during 30 minutes, and left to evaporate in order to obtain the deuterated crystals. The temperature was set at 30 °C during crystallization.

C. Synthesis of $Dy(ZnL^{15})_2$ complexes

$[Zn_2(\mathbf{L^{15}})_2{}^{A}DyCl_3]\cdot 2H_2O]$ (**$^{A}Dy(ZnL^{15})_2$**) complexes with **L^{15}**= N, N'-bis(3-methoxysalicylidene)phenylene-1,2-diamine and A= 162 and 163, were synthesized following a modified version of an already published procedure.[56]

C.1. N, N'-bis(3-methoxysalicylidene)phenylene-1,2-diamine, H_2L^{15}

3.35 g (22.0 mmol) of *o*-Vanillin was added to a previously prepared solution of 1.08 g (10.0 mmol) of 1,2-diaminobenzene in 50 mL of absolute ethanol, and let stirring and reflux overnight. The solution was cooled to room temperature and the orange crystalline precipitate was collected and washed with cold ethanol and petroleum ether. The product **H_2L^{15}** was finally evaporated to dryness. Yield: **H_2L^{15}**: 2.44g (58%). IR: 3335(w), 3058(w), 3015(w), 2954(w), 2923(w), 2828(w), 1892(w), 1824(w), 1751(w), 1612(s), 1577(s), 1569(s), 1497(m), 1469(s), 1440(s), 1399(m), 1375(m), 1345(w), 1248(s), 1204(s), 1097(m), 1076(m), 1043(w), 972(s), 876(m), 843(m), 824(m), 781(s),734(s), 649(w), 584(w), 538(w), 480(w). ^{1}H-NMR (400 MHz, $CDCl_3$): δ(ppm) 13.2 (s, 2H), 8.64 (s, 2H), 7.35 (d,1 H, J= 5.92), 7.34 (d, 1 H, J= 5.92), 7.22 (d, 1H, J= 5.82), 7.21(d, 1H, J= 5.82), 7.02 (dd, 2H, J=14.32, 1.34 Hz), 6.99 (dd, 2H, J= 14.4, 1.21 Hz), 6.88 (t, 2H, J= 7.90 Hz), 3.91 (s, 6H).

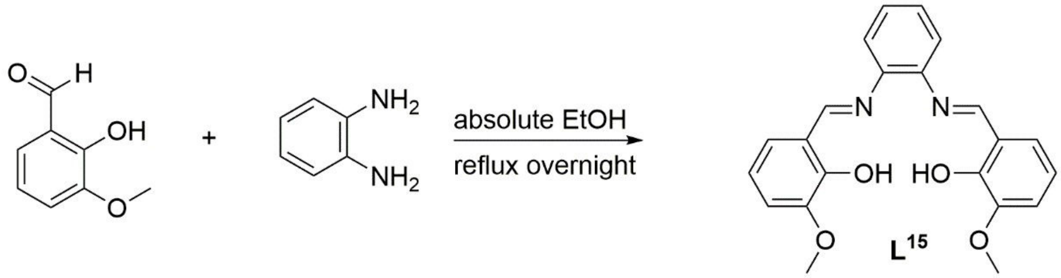

Figure 2. 4. Synthesis of N, N'-bis(3-methoxysalicylidene)phenylene-1,2-diamine.

C.2. *Zn (N, N'-bis(3-methoxysalicylidene)phenylene-1,2-diamine), ZnL^{15}*

0.845 g (3.85 mmol) of $Zn(OAc)_2 \cdot 2H_2O$ were added to a stirring suspension of H_2**L^{15}** (0.54 g, 2.23 mmol) in absolute ethanol (10 mL) and heated under reflux overnight. A yellow precipitate appeared which was filtered and washed with absolute ethanol, before dried under vacuum. Yield: **ZnL^{15}**: 713.7 mg (72%). IR: 3049(w), 2903(w), 2830(w), 1700(w), 1612(s), 1586(s), 1540(s), 1486(m), 1468(s), 1444(s), 1388(s), 1361(w), 1339(m), 1288(w), 1327(s), 1193(s), 1105(m), 1074(m), 1048(w), 976(m), 931(w), 863(m), 785(m), 736(s), 624(w), 584(w), 558(w), 535(w), 509(w), 420(w).

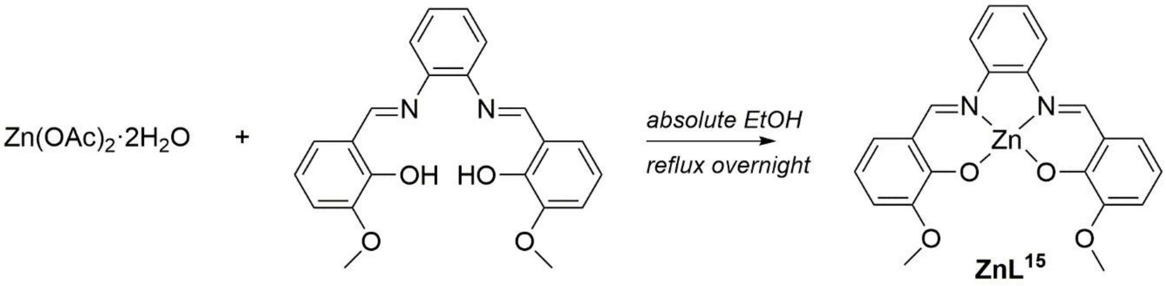

Figure 2. 5. Coordination reaction of Zn(N, N'-bis(3-methoxysalicylidene)phenylene-1,2-diamine).

C.3. *Complexation of (chloro)dysprosium-Bis(zincate(chloro)(N,N'-bis(3-methoxysalicylidene)phenylene-1,2-diamine), Dy(ZnL^{15})$_2$*

Isotopically enriched $DyCl_3 \cdot 6H_2O$ and the analogue $YCl_3 \cdot 6H_2O$ were obtained from the oxide following the method explained previously.

Dy(ZnL^{15})$_2$ and **$^{162/163}$Dy(ZnL^{15})$_2$**: a $^{A}DyCl_3 \cdot 6H_2O$ (12-13.1 mg, 0.03 mmol) solution in 10 mL of methanol was added to a suspension solution of **ZnL^{15}** (27-28 mg, 0.06 mmol) in the same volume of acetonitrile. The mixture was first stirred and heated under reflux for 6 h, and then filtered after cooling it to room temperature. The resulted solution was distributed into different tubes and crystallization took place by diffusion of diethyl ether in a sealed container. Yields **Dy(ZnL^{15})$_2$**: 4 mg (11%); **^{162}Dy(ZnL^{15})$_2$**: 4.8 mg (13%); **^{163}Dy(ZnL^{15})$_2$**: 4 mg (11%).

IR: **Dy(ZnL^{15})$_2$**: 3053(w), 3029(w), 2974(m), 2940(m), 2881(m), 2839(w), 1735(w), 1613(s), 1586(m), 1551(m), 1453(s), 1393(m), 1304(m), 1281(m), 1233(s), 1195(s), 1097(m), 1073(m), 1049(m), 969(m), 882(m), 846(m), 782(m), 741(s), 648(w), 631(w), 559(m), 511(m), 445(w); **^{162}Dy(ZnL^{15})$_2$**: 3060(w), 3029(w), 2936(w), 2841(w), 1733(w), 1613(s), 1587(m), 1552(m), 1457(s), 1392(m), 1234(s), 1194(s), 1098(m), 1073(w), 969(m), 848(m), 783(m), 742(s), 649(w), 633(w), 559(m), 512(m), 447(w); **^{163}Dy(ZnL^{15})$_2$**: 3058(w), 3029(w), 2974(w), 2935(w), 2839(w), 1612(s), 1587(m), 1551(m), 1453(s), 1392(m), 1301(w), 1281(m), 1235(s), 1196(s), 1097(m), 1071(m), 1044(w), 968(m), 848(m), 783(m), 742(s), 649(w), 633(w), 560(m), 510(m), 446(w).

^{A}Dy$_{0.1}$Y$_{0.9}$(Zn**L^{15}**), (**^{A}Dy@Y(ZnL^{15})$_2$**): a ^{A}DyCl$_3$·6H$_2$O (6 mg, 0.015 mmol) and YCl$_3$·6H$_2$O (43.3-43.5 mg, 0.14 mmol) solution in methanol (50 mL) was added to a suspension solution of **ZnL^{15}** (135 mg, 0.3 mmol) in the same volume of acetonitrile. The mixture was first stirred and heated under reflux for 6 h, and then filtered after cooling it to room temperature. The resulted solution was distributed into different tubes and crystallization took place by diffusion of diethyl ether in a sealed container. Yields **Dy@Y(ZnL^{15})$_2$**: 29.5 mg (17.2%);**^{162}Dy@Y(ZnL^{15})$_2$**: 10.6 mg (6%); **^{163}Dy@Y(ZnL^{15})$_2$**: 30.1 mg (16.9%). IR: **Dy@Y(ZnL^{15})$_2$**: 3061(w), 3028(w), 2974(m), 2937(w), 2885(w), 2840(w), 1612(s), 1586(s), 1552(s), 1453(s), 1390(s), 1303(m), 1282(s), 1235(s), 1195(s); 1098(m), 1047(s), 968(m), 880(w), 848(m), 783(m), 739(s), 649(w), 634(w), 589(w), 560(m), 511(m), 447(w); **^{162}Dy@Y(ZnL^{15})$_2$**: 3053(w), 3030(w), 2973(m), 2937(m), 2889(m), 2842(w), 1614(s), 1586(s), 1552(s), 1453(s), 1392(s), 1302(m), 1282(s), 1234(s), 1194(s), 1097(m), 1073(m), 1047(m), 881(m), 847(m), 783(m), 742(s), 649(m), 632(w), 586(w), 559(m), 510(m), 446(w); **^{163}Dy@Y(ZnL^{15})$_2$**: 3062(w), 3028(w), 2972(m), 2936(m), 2888(m), 2840(w), 1614(s), 1586(s), 1552(s), 1450(s), 1391(s), 1303(m), 1282(s), 1236(s), 1195(s), 1168(m), 1097(s), 1047(s), 968(m), 882(m), 848(m), 782(m), 739(s), 650(m), 632(m), 588(w), 560(m), 512(m), 446(w).

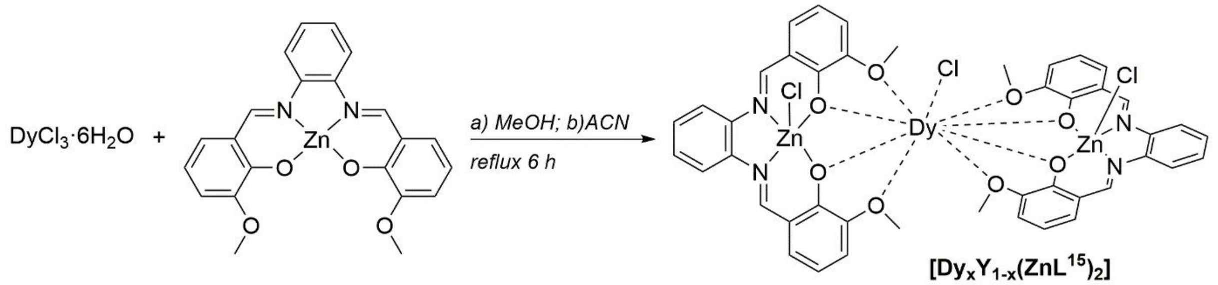

[Dy$_x$Y$_{1\text{-}x}$(ZnL^{15})$_2$]

*Figure 2. 6. Complexation reaction of [Dy$_x$Y$_{1\text{-}x}$(Zn**L^{15}**)$_2$].*

D. *Synthesis of Dy(ZnL^{17})$_2$ complexes*

[(Zn**L^{17}**Cl)$_2$^{A}Dy(H$_2$O)]$_2$[ZnCl$_4$]·xH$_2$O (**^{A}Dy(ZnL^{17})$_2$**) complexes were synthesized following a modified version of an already published procedure, being A the mass number being 163 and 164.[57,58]

D.1. *N, N'-bis(3-methoxysalicylidene)-1,2-diaminoethane, H$_2$L^{17}*

Similar procedure to H$_2$**L^{17}**, in which 3.35 g (22.0 mmol) of *o*-Vanillin was added to a previously prepared solution of 670 µL of diamino-ethane (10.0 mmol) in 50 mL of absolute ethanol, and let stirring and reflux overnight. The solution was cooled to room temperature and a yellow crystalline precipitate was collected and washed with cold ethanol and petroleum ether. The product **H$_2$L^{17}** was finally evaporated to dryness. IR: 3088(w), 2996(w), 2952(w), 2932(w), 2895(w), 2850(w), 1630(s), 1472(s), 1412(m), 1323(w), 1296(m), 1250(s), 1172(w), 1134(w), 1082(s), 1055(w), 1011(w), 986(w), 963(s), 882(w), 837(m), 791(m), 740(m), 622(w), 500(w). ^{1}H-NMR (400 MHz, MeOD 4D (HDO+D2O) < 0.03%): δ(ppm) 8.46 (s, 2H), 6.98 (dd, 2H, J= 23.3, 1.2 Hz), 6.96 (dd, 2H, J= 23.3, 1.2 Hz), 6.75 (t, 2H, J= 7.9 Hz), 4.00 (s, 4H), 3.85 (s, 6H).

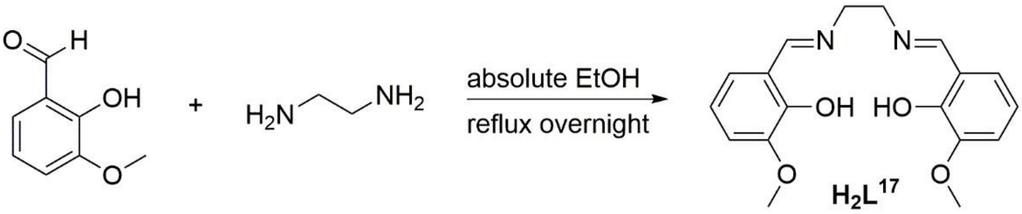

Figure 2. 7. Synthesis of N, N'-bis(3-methoxysalicylidene)-1,2-diaminoethane.

D.2. *Complexation of (chloro)dysprosium-Bis(zincate(chloro)(N, N'-bis(3-methoxysalicylidene)-1,2-diaminoethane), Dy(ZnL^{17})$_2$*

In 15 mL methanol was added 26.6 mg ZnCl$_2$·2H$_2$O (0.2 mmol), 65.6 mg of H$_2$**L^{17}** (0.2 mmol) and 14 µL (0.1 mmol) of triethylamine and let under stirring during 10 min. Then, 37.4 mg of DyCl$_3$·6H$_2$O (0.1 mmol, 37.4 mg) were included to the mixture and refluxed during 5 h. The resulted solution was filtered at room temperature, and let to slow evaporation in a beaker. Yields **Dy(ZnL^{17})$_2$**: 12 mg (5.4%); **^{164}Dy(ZnL^{17})$_2$**: 11.4 mg (5.1%); **^{163}Dy(ZnL^{17})$_2$**: 13.6 mg (6.1%). IR: **Dy(ZnL^{17})$_2$**: 3063(w), 2942(w), 1640(s), 1604(m),1556(w), 1461(s), 1394(m), 1334(w), 1276(s), 1239(m), 1220(s), 1168(w), 1075(m), 1035(w), 953(m), 849(m), 786(w), 736(m), 640(w); **^{163}Dy(ZnL^{17})$_2$**: 3067(w), 2941(w), 1640(s), 1606(m), 1559(m), 1457(s), 1396(m), 1334(w), 1279(s), 1220(s), 1170(m), 1075(m), 1038(w), 954(m), 849(m), 785(m), 736(s), 640(m); **^{164}Dy(ZnL^{17})$_2$**: 3067(w), 2981(w), 2942(w), 2842(w), 1640(s), 1605(m), 1557.5(m), 1461(s), 1397(m), 1335(w), 1275(s), 1221(s), 1170(m), 1073(m), 1036(w), 954(m), 849(m), 787(w), 738(m), 640(w).

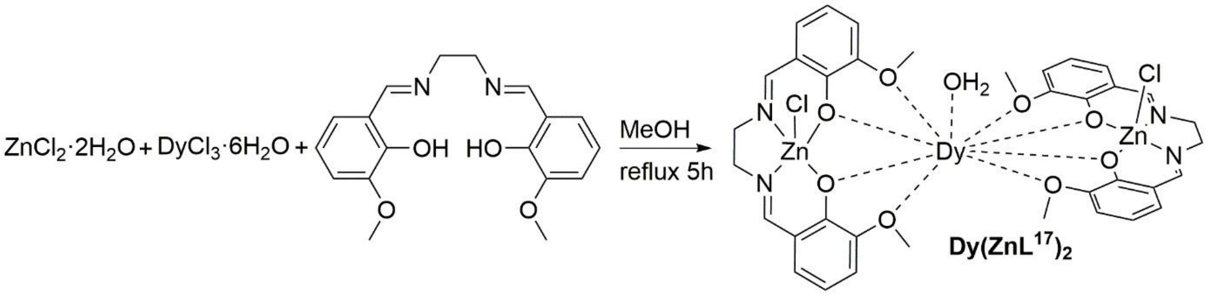

*Figure 2. 8. Complexation reaction of **Dy(ZnL^{17})$_2$**.*

II. PHYSICAL AND STRUCTURE CHARACTERIZATION

Infrared spectra were measured by the KBr-disk method on a PerkinElmer 1600 Series FTIR spectrometer (resolution 4 cm^{-1}).

Single crystals were mounted on a APEXIII D8 VENTURE Bruker-AXS diffractometer for data collection (MoK$_\alpha$ radiation source, λ = 0.71073 Å, T= 150 K) and crystal orientation, in the "Centre de Diffractométrie" (CDIFX), University of Rennes 1, France. The structures were solved with a direct method using the SHELXT program[59] and refined with a full matrix least-squares method on F^2 using the SHELXL-14/7 program[60].

The study of the evolution of the powder structure pattern by heating the sample was realized in the "Institut National des Sciences Appliquées de Rennes" (INSA Rennes). XRD patterns were recorded between 5 and 60° (2θ) by a PANalytical X'Pert PRO diffractometer with a precision of 0.026° by steps and a count time of 40 s per step using Cu Kα. The sample was placed in a HTK chamber with a refrigerating system based on a N$_2$ flow (100 mL/ min). This camber allows measurements until 1000°C. Voltage of 50 kV and current of 40 mA were set during analyses. Temperature rate was adjusted to 5°C/ min from 25 to 200°C. Measurements were done for each 5°C while heating. Polycrystalline sample was grounded for XRD analysis and back-loaded into steel sample holders. A silicon sample was used for calibration.

The Ln/Y ratio of the magnetically diluted compounds were determined using SEM (Scanning Electron Microscopy). All observations and measurements were carried out with a

JEOL JSM 6400 scanning electron microscope (JEOL Ltd., Tokyo, Japan) with an EDS (Energy Dispersive Spectrometry) analysis system (OXFORD Link INCA). The voltage was kept at 9 kV, and the samples were mounted on carbon stubs and coated for 5 min with a gold/palladium alloy using a sputter coater (Jeol JFC 1100). This analysis has been performed by the "Centre de Microscopie Electronique à Balayage et microAnalyse (CMEBA)" from the University of Rennes 1 (France).

The thermogravimetric analyses (TGA) were performed on **$ErW_{10}·xH_2O$** in the "Institut des Sciences Appliquées de Rennes (INSA)", France. Around 20 mg of polycrystalline sample is gently grounded and mounted in an opened support of Al in a N_2 environment (flow of 100 mL/min). The evolution of the mass and heat flow of the sample is analyzed by a Perkin Elmer analyzer, Diamond TG/ATD. Measurements comprising temperatures between 25 and 135 °C/ 200°C were performed by heating rate of 5°C/min. Once at the maximal temperature, the stability during 30 min was tested. Different scans were done after rehydration procedures similar to that of the synthetic part. The support was closed in a confined space saturated of water during 2 to 3 hours. Once rehydrated, the procedure was repeated.

Experimental results are in general complemented by computational calculations made by some collaborators in the "Institut de Sciences Chimiques de Rennes", University of Rennes 1, France. The different calculations appearing in this manuscript are made by Vincent Montigaud. The atomic positions were extracted from the X-ray crystal structure. Periodic-DFT calculations[61] using Vienna Ab Initio Simulation Package (VASP) were performed for the optimization of the structure[62]. This uses the Projector Augmented Wave (PAW) method, which consists in the use of pseudopotentials to define the atoms and a plane wave basis set for the environment. To modulate the magnetic properties, wavefunction-based calculations were carried out on the optimized molecular structures using the SA-CASSCF approach, as implemented in the MOLCAS quantum chemistry package (versions 8.0[63]). In this, the resolution of the wavefunction consists in splitting the orbitals into three subspaces: an occupied or inactive space; a virtual or empty space; and a fermi level, where we have access to the f-orbitals.[64] The resulting wavefunctions and energies are used to compute the magnetic properties and the g-tensors of the lowest states from the energy spectrum by using the pseudo-spin S = 1/2 formalism in the SINGLE-ANISO routine.[65]

A. *MAGNETIC MEASUREMENTS:*

Magnetic measurements were performed on two different measuring systems in the "Institut de Sciences Chimiques de Rennes": Direct-current (DC) measurements were realized in a SQUID detector (Superconducting Quantum Interference Device) Quantum Design MPMS-XL magnetometer. Alternating current (AC) measurements were performed on both Quantum Design MPMS-XL SQUID and Quantum Design PPMS magnetometers, the last coupled to an AC Measurement System (ACMSII).

For the preparation of the samples (Figure 2.9), a certain quantity of crystalline product (from 4 mg to 50 mg) is collected and pelletized inside Teflon tape. This pellet is disposed in the middle of a straw and immobilized between two plastic pieces.

Figure 2. 9. Picture of a pellet sample.

Quantum Design MPMS-XL SQUID magnetometer:

The SQUID magnetometer is a highly integrated instrument system, designed to be sensitive to subtle changes in the magnetic behavior of a sample when submitted to different temperatures or magnetic fields ($\leq 10^{-8}$ emu). The principal components of this measurement system comprises: a He flow cryostat to operate in a range of temperatures in between 1.8 K and 400 K; superconductor magnet coils that enables to apply magnetic fields up to 5 T (XL); a sample handling system; a SQUID (*Superconducting Quantum Interference Device)* detector and a computer operating system. The SQUID is mainly a Josephson junction consisting of two superconducting loops separated by a very thin electrical insulator. A complementary ^{3}He insert allows to cool down to 0.5 K.

Quantum Design PPMS ACMSII:

The PPMS of Quantum Design is a system for the study of physical properties. It is equipped by a superconductor coil of 14 T and operates between 1.9 and 375 K. ACMSII susceptometer, coupled to PPMS, allows measurements of magnetic susceptibility in AC mode from 10 to 10000 Hz.

A.1. *DC Magnetometry:*

DC magnetometry is used in order to study the evolution of the magnetic response of a compound with the temperature, under the presence of a static magnetic field.

Thus the sample is placed inside of the pickup coil system in the presence of a magnetic field. A vertical displacement through the superconducting coils induces a change in the magnetic flux, which is proportional to the magnetic moment of the sample (see Figure 2.10).

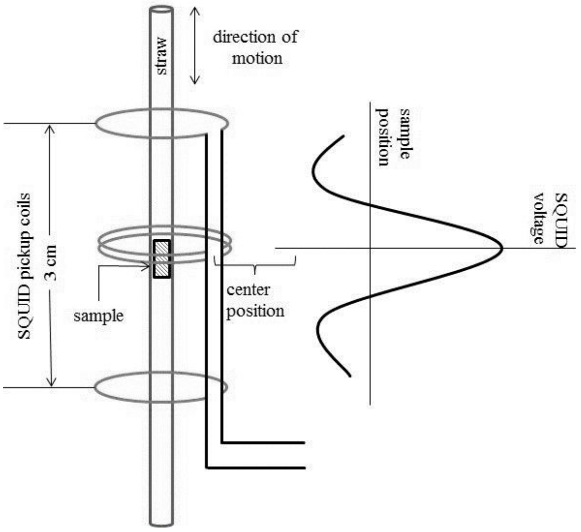

Figure 2. 10. Scheme of the SQUID detection system and the resulted signal.

DC magnetic susceptibility measurements were performed for temperatures between 2 and 300 K. Different magnetic fields were applied depending on the temperature range and the magnetic strength of the metal. Depending on the susceptibility of the metal center, the magnetic fields applied for DC measurements will be different. This means that for poorly magnetic systems, in order to obtain a good magnetic response, the strength of the applied H_{DC} needs to be higher. For Dy^{3+}/Er^{3+}-systems (highly magnetic): 200 Oe between 2 and 20 K, 2 kOe between 20 and 80 K and, 10 kOe for temperatures above; while for Yb^{3+}– systems (poorly magnetic: 2 kOe between 2 and 20 K and 10 kOe between 20 up to 300 K. These measurements were all corrected for the diamagnetic contribution as calculated with Pascal's constants.[66]

A.2. *AC Magnetometry:*

AC technique gives easy access to the susceptibility (*dM/dH*). The sample is placed inside the coil system, and a small oscillating magnetic field is induced by an alternating current flowing through the coils. As a result, the sample experiences a time dependent moment (*M(t)*) as an effect of this ac magnetic field (*H(t)*). In practice, the sample is submitted to a small AC magnetic field, *H(t)*, which can be superimposed to a DC magnetic field (H_{DC}):

$$H(t) = H_{DC} + H_{AC} = H_{DC} + h_0 \cos(\omega t) \ (2.1)$$

h_0 the amplitude of the oscillating magnetic field (h_0= 3 Oe (SQUID); h_0= 5 Oe (PPMS)) and $\omega = 2\pi\nu$, with ν the oscillation frequency. The detection system is configured so that only a narrow frequency band is detected, at the fundamental frequency, which differs on the measuring system (SQUID magnetometer (0.01- 1500 Hz) and PPMS system (10 and 10000 Hz)).

The induced magnetization *M(t)* can be written:

$$M(t) = M_{DC} + m_0 \cos(\omega t - \rho) \ (2.2)$$

With M_{DC} the static magnetization, m_0 the amplitude of the oscillating magnetization and ρ the phase shift of the oscillating magnetization. It can be rewritten with two different magnetization components: an in-phase (*m'*) and an out-of-phase (*m"*) signals:

$$M(t) = M_{DC} + m' \cos(\omega t) + m'' \sin(\omega t) \ (2.3)$$

By performing scans in frequency, we will obtain important information about the dynamics effects. So that, if the magnetic response is able to follow instantaneously the magnetic field oscillations no shifts is experienced (in that case, *m"*= 0). If the contrary, the response to the magnetic field suffers a certain delay, an out-of-phase susceptibility component will arise (*m"*>0), which is sign of relaxation effects. In the limit of the low frequencies, the magnetic response has time enough to orientate parallel to the magnetic field. In that situation, the ac magnetization will fit with the DC magnetization resulted from low applied fields and the imaginary phase is equal to zero. For intermediate frequencies, a delay in the response is observed, sign of the existence of relaxation mechanisms. In the limit of high frequencies, the magnetization is not able to follow the oscillation of the magnetic field and as a consequence *m'* and *m"* tends to zero. Hereafter, both limits will be addressed as isothermal and adiabatic susceptibilities respectively. Figure 2.11 shows the cases where first, the magnetization follows the magnetic field oscillation; and second, when this out-of-phase component appears.

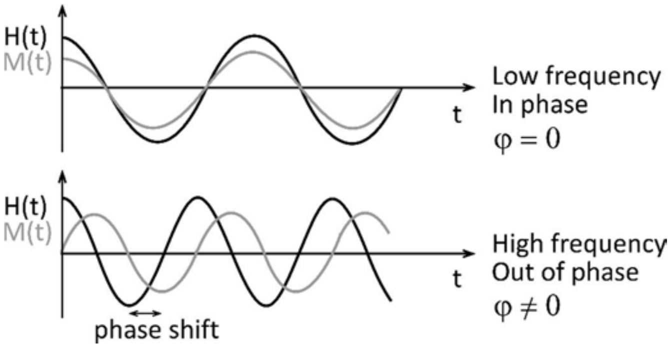

Figure 2. 11. Magnetic response to an applied ac magnetic field as a function of the frequency of the oscillations First, case where the magnetization follows instantaneously the magnetic field oscillation; and second, when some delay appears in this signal.

In terms of susceptibility (χ), if:

$$\chi = \frac{\partial M}{\partial H} \quad (2.4)$$

Then, the time dependent component of Equation 2.3 can be expressed as:

$$\chi(t) = \chi' \cos(\omega t) + \chi'' \sin(\omega t) \quad (2.5)$$

χ' being the real component of the susceptibility, and χ'' the imaginary component. In general, the decline of the in-phase susceptibility will be concomitant with the appearance of a peak in the out-of-phase component. This maximum in the χ'' component indicates a slow relaxation of the magnetization (Figure 2.12, left).

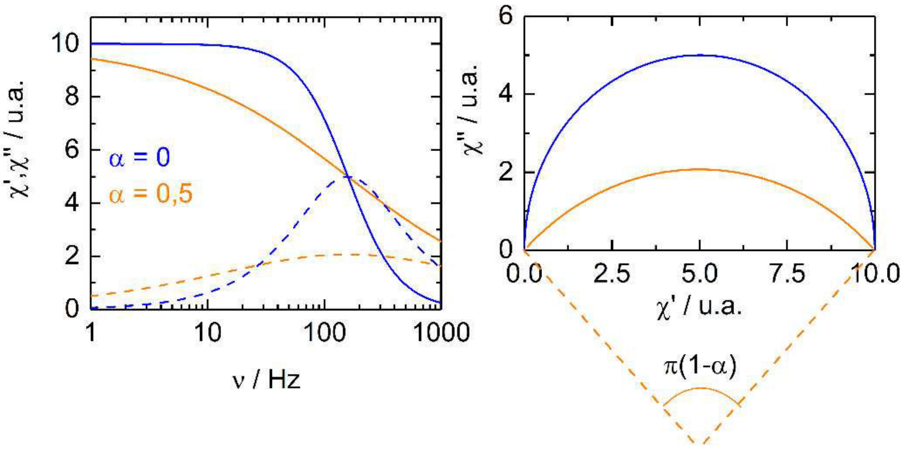

Figure 2. 12. Left: the in-phase (χ') and out-of-phase components of the susceptibility as a function of the frequency (χ''); Right: the so-called Argand diagram.

In order to have a better insight of the relaxation phenomena, a so-called Argand [67] diagram is systematically represented (Figure 2. 12, right). This consists in a χ'' vs. χ' plot, as analogy of the Cole-Cole plot used for dielectrics.[68] Casimir and Du Pré (1938) were the first to propose the thermodynamic model for spin lattice relaxation in which the susceptibility is related with the relaxation processes. The shape of the semicircle is related to the number of relaxation processes. If the system experienced a single relaxation process, the Argand diagram would show a perfect semicircle with its center on the x-axis.[69] A flattened semicircle would be the sign of a distribution of relaxation times. A mathematical relation analogous to dielectrics from Debye model (Cole and Cole 1941[68]) can be derived:

$$\chi'(\omega) = \chi_S + (\chi_T + \chi_S)\frac{1+(\omega\tau)^{1-\alpha}\sin(\alpha\frac{\pi}{2})}{1+2(\omega\tau)^{1-\alpha}\sin(\alpha\frac{\pi}{2})+(\omega\tau)^{2-2\alpha}}$$

$$\chi''(\omega) = (\chi_T - \chi_S)\frac{(\omega\tau)^{1-\alpha}\cos(\alpha\frac{\pi}{2})}{1+2(\omega\tau)^{1-\alpha}\sin(\alpha\frac{\pi}{2})+(\omega\tau)^{2-2\alpha}} \qquad (2.6)$$

With χ_T the isothermal susceptibility (low frequency limit), χ_S the adiabatic susceptibility (high frequency limit), τ the relaxation time and α an empiric parameter which describes the distribution of the relaxation time. For systems with only one relaxation time α is close to zero, corresponding to the blue curve, but if there is some distribution, this will tend to assimilate to the orange curve. The extended Debye model was applied to fit simultaneously the experimental variations of χ_M' and χ_M'' with the frequency ν of the oscillating field (Figure

2.11, left). Typically, only the temperatures for which a maximum on the χ_M'' vs. ν curves, have been considered. The best fitted parameters τ, α, χ_T, χ_S for each system are listed in Annex III with the coefficient of determination R^2.

A.3. *Angular-Resolved Magnetometry:*

The set-up is formed by the addition of a horizontal rotator system integrated to the SQUID magnetometer. Therefore, it consists in measuring the angular dependence of the magnetic moment of an oriented sample. Then, by measuring the magnetic moment of the sample rotating following three perpendicular planes, precise information about the anisotropy tensor of the molecule can be obtained (with the axial and transverse components). This, however, can be done only if there is one metal center in the molecule and low crystalline symmetry (triclinic). If for the contrary, the asymmetric unit is constituted by more than one center, the obtained tensor will correspond to the average of the different constituent contribution.

A single crystal of the sample is collected to be indexed by the XRD and placed on the sample holder of the rotator. To better handle the crystals, which are susceptible to solvent loss, they are embedded in grease on the surface of a transparent millimeter size plastic square, which at the same time is fixed on the sample holder. The set-up is represented in Figure 2.13, where it can be seen an example of XYZ frame (usually X in the direction of the H_{DC} for the first rotation) and the different rotations with as a reference the direction of the magnetic field and the indexed axes from the crystal.

Finally, the angular dependence of the molar magnetic susceptibility (χ_M) can be measured rotating the crystal in three perpendicular planes.

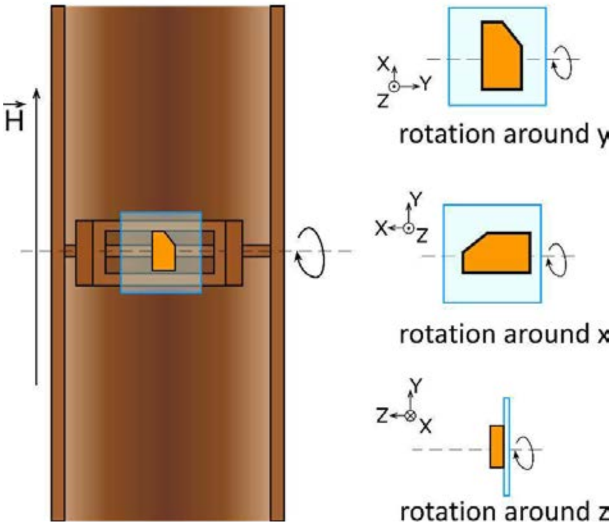

Figure 2. 13. Description of the angular resolved magnetometry operations. The first row illustrates the structure of a horizontal rotator. The rotation axis is perpendicular to the static magnetic field direction (H). The rotation is performed via the stretching of a Cu–Be wire bonded on the pulley, which shares the rotation axis with the sample holder. The second row is the different orientation adopted by the sample with respect to the three rotation axes. Magnetization is measured parallel to the field in three perpendicular planes XY, YZ and XZ.

χ_M vs. θ curves where fitted with Equation 2.7 in order to extract the susceptibility matrix 2.8.

$$\chi_M = \frac{M}{H} = \chi_{\alpha\alpha}\cos^2\theta + \chi_{\beta\beta} sin^2\theta + 2\chi_{\alpha\beta}\sin\theta cos\theta \quad (2.7)$$

Where α and β are the directions X, Y, and Z in a cyclic permutation and θ is the angle between H and α.

$$\chi_M = \begin{pmatrix} \chi_{xx} & \chi_{xy} & \chi_{xz} \\ \chi_{yx} & \chi_{yy} & \chi_{yz} \\ \chi_{zx} & \chi_{zy} & \chi_{zz} \end{pmatrix} \quad (2.8)$$

The above susceptibility tensor (χ_M) was diagonalized, thus providing the eigenvalues and eigenvectors of the susceptibility. Furthermore, the highest value can give information about the ground state and the axial g-factor by applying the effective spin ½ formalism. In that way, we consider that the magnetization at saturation can be expressed as: $M_{sat} = g_J J = g_{eff} S_{eff}$, with g_J (calculated by Eq. 1.15) and S_{eff}= ½. For example, for Er^{3+} ($^4I_{15/2,}$ J=15/2 and g_J= 6/2) the effective g value is 18.

B. *MAGNETIC RESONANCE: Electron Paramagnetic Resonance*

EPR measurements have been carried during a stay of three months in the group of Molecular Magnetism in the University of Manchester, under the supervision of Floriana Tuna. These measurements contribute to the research of understanding the spin signature in the different lanthanide complexes.[70,71]

The Electron Paramagnetic Resonance (EPR) is a powerful spectroscopic technique concerned by the interaction of an electromagnetic radiation with the unpaired electrons of the material. It gives information about the spin system related to the structure, symmetry and, electronic and dynamic properties.

EPR (Figure 2.14a) consists in irradiating the sample with electromagnetic (EM) energy ($E = h\nu$) in presence of an *H*. If the splitting of the electronic states produced by *H* is of the same order of energy as the applied radiation, the absorption of it gives raise to quantum resonance. According to the selection rules, the angular momentum of the molecule has to remain constant due to $\Delta m_S = \pm 1$ condition, with m_s being the spin quantum number. This means that resonance takes place when:[72]

$$\Delta E = h\nu = E_2 - E_1 = g_e \beta H \qquad (2.9)$$

For these measurements, the frequency (ν) at which the experiments are performed is fixed to a certain value depending on the measuring system (Table 2.1), and the resonance condition is fulfilled by varying the magnetic field. The most common is the EPR at X-Band; during this stay K- and Q-Band EPR have also been performed.

Table 2. 1. Energy details of the different possible bands in an EPR spectrometer.

Band	*Frequency (GHz)*	*Energy (cm^{-1})*	*Wave length (cm)*	*Magnetic field (T) at g= 2*
L	1.1	0.04	27.25	0.039
S	3.2	0.11	9.37	0.114
X	9.4	0.31	3.19	0.336
K	24	0.8	1.25	0.86
Q	34	1.13	0.88	1.215
W	95 115	3.17 3.84	0.32 0.26	3.394 4.108

EPR spectra (Figure 2.14b-c) show the microwave absorption as a function of the applied magnetic field, and it is usually represented from its first derivative. The information of interest is given by the position, width and intensity of the lines, as well as the distance, in field, between them: i) The position is specific of a certain g-value; ii) the distance between the different absorption lines give information about the Hyperfine interactions (A constant); and iii) the number of transitions (lines) is defined by the nuclear spin (*I*), which determines 2I+1 possible transitions. Other factors contribute to the width and intensity of the different signals as for example, the dynamic effects and hyperfine/superhyperfine interactions for the former; and the multiplicity of the different hyperfine states with the nuclei (*I*≥1/2) and the anisotropy for the later.

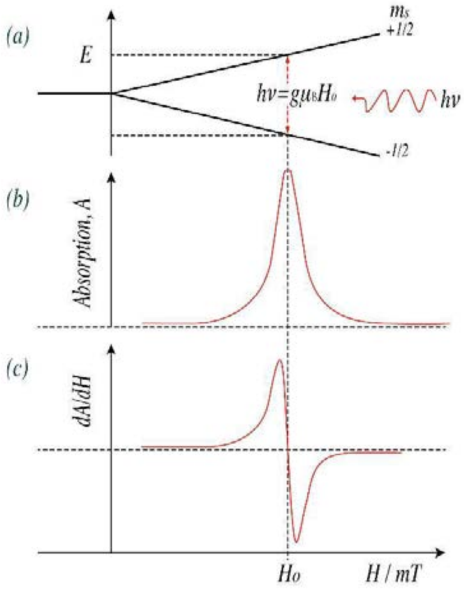

Figure 2. 14. Example for a single system of S=1/2. a) Splitting of the m_S levels in presence of a magnetic field, H ; b) Absorption spectrum at resonance; c) EPR spectrum, corresponding to the first derivative of the absorption.

The different samples have been prepared following two different methods: in the first, the samples were grounded and mixed with eicosane, at the same volume proportion. Eicosane is a linear alkane of formula $C_{20}H_{42}$ that helps to fix the sample inside the quartz tubes for the EPR experiments, as it follows a phase transition at a moderate temperature. A second strategy has also been used, consisting in taking the pellets of samples used for the magnetic experiments. Before each measurement, the samples were purged with a He (g) flow in order to evacuate the oxygen, which can create interferences in the system response. Moreover, a reference system called “strong pitch” with a known g-value (g= 2) is used for calibration of the position of the magnetic field.

REFERENCES:

[51] G. Cosquer, F. Pointillart, S. Gohlen, O. Cador and L. Ouahab, *Chem. Eur. J.*, **2013**, *19*, 7895.

[52] A.I. Voloshin, N.M. Shavaleev and V.P. Kazakov, *J. Lumin.*, **2000**, *91*, 49.

[53] T. T. da Cunha, J. Jung, M.-E. Boulon, G. Campo, F. Pointillart, C. L. M. Pereira, B. Le Guennic, O. Cador, K. Bernot, F. Pineider, S. Golhen and L. Ouahab, *J. Am. Chem. Soc.*, **2013**, *135*, 16332.

[54] R. Shiozaki, A. Inagaki, A. Nishino, E. Nishio, M. Maekawa, H. Kominami and Y. Kera, J. Alloys Compd., **1996**, *234*, 193.

[55] M. A. AlDamen, S. Cardona-Serra, J. M. Clemente-Juan, E. Coronado, A. Gaita-Ariño, F. Luis and O. Montero, *Inorg. Chem.,* **2009**, *48(8)*, 3467.

[56] a) W.-K. Lo, W.-K. Wong, W.-Y. Wong, J. Guo, K.-T. Yeung, Y.-K. Cheng, X. Yang and R. A. Jones, *Inorg. Chem*, **2006**, *45(23)*, 9315; b) W.-B. Sun, P.-F. Yan, S.-D. Jiang, B.-W. Wang, Y.-Q. Zhang, H.-F. Li, P. Chen, Z.-M. Wang and S. Gao, *Chem. Sci.*, **2016***, 7(1)*, 684.

[57] X. Lü, W. Bi, W. Chai, J. Song, J. Meng, W.-Y. Wong, W.-K. Wong and R. A. Jones, *New. J. Chem,* **2008**, *32*, 1.

[58] A.-L. Boulkedid, J. Long, C. Beghidja, Y. Guari, A. Beghidja and J. Larionova, *Dalton Trans*, **2018**, *47*, 1402.

[59] G. L. Sheldrick, SHELXT – Integrated space-group and crystal-structure determination. *Acta Crystallogr. Sect. A Found Adv,* **2015**, *71*, 3.

[60] G. M. Sheldrick, Crystal structure refinement with SHELXL. *Acta Crystallogr. Sect. C,* **2015**, *71*, 3.

[61] P. E. Blöchl, *Phys. Rev. B*, **1994**, *50(17)*, 953.

[62] a) G. Kresse, J. Hafner, Phys. Rev. B, **1993**, *47*, 558; b) G. Kresse, J. Hafner, *Phys. Rev. B*, **1994**, 49, *14*, 251; c) G. Kresse, J. Furthmüller, *Phys. Rev. B*, **1996**, 54, *11*, 169.

[63] F. Aquilante, L. De Vico,N. Ferré, G. Ghigo, P. A. Malmqvist, P. Neogrady, T. Bondo Pedersen, M. Pitonak, M. Reiher, B. O. Roos, L. Serrano-Andrés, M.Urban, V. Veryazov, R.Lindh, R. MOLCAS 7: The Next Generation*, J. Comput. Chem.*, **2010**, *31*, 224.

[64] B. O. Roos, P. R. Taylor, P. E. M. Siegbahn, *Chem. Phys.*, **1980**, *48*, 157.

[65] L. Chibotaru, L. Ungur, A. Soncini, *Angew. Chem. Int. Ed.,* **2008**, *47*, 4126; b) L. Chibotaru, L. Ungur, *J. Chem. Phys.*, **2012**, *137*, 064112.

[66] O. Kahn, *Molecular Magnetism*, VCH, Weinheim, Germany, **1993**.

[67] W. Haase, S. Wróbel, *Relaxation Phenomena*, Springer, **2003**, Germany.

[68] K. S. Cole, R. H. Cole, *J. Chem. Phys.*, **1941**, *9*, 341.

[69] H.B.G. Casimir, and F.Q. Du Pré, *Fisica V*, **1938**, *6*, 507.

[70] a) K. S. Pedersen, A.-M. Ariciu, S. McAdams, H. Weihe, J. Bendix, F. Tuna, and S. Piligkos, *J. Am. Chem. Soc.*, **2016**, *138(18)*, 5801; b) E. Moreno-Pineda, M. Damjanovic, O. Fuhr, W. Wernsdorfer, and M. Ruben, *Angew. Chem. Int. Ed.*, **2017**, *56*, 9915.

[71] a) D. Aguilà, L. A. Barrios, V. Velasco, O. Roubeau, A. Repollés, P. J. Alonso, J. Sesé, S. J. Teat, F. Luis, and G. Aromí, *J. Am. Chem. Soc.*, **2014**, *136*, 14215; b) R. Hussain, G. Allodi, A. Chiesa, E. Garlatti, D. Mitcov, A. Konstantatos, K. S. Pedersen, R. De Renzi, S. Piligkos, and S. Carretta, *J. Am. Chem. Soc.*, **2018**, *140*, 9814.

[72] V. Chechik, E. Carter, D. Murphy, *Electron Paramagnetic Resonance*, Oxford Chemistry Primers, **2016**.

CHAPTER III

ISOTOPIC EFFECT IN [Dy(tta)$_3$(L^2)]·C$_6$H$_{14}$ COMPLEX

In the group, special attention has been dedicated to Dy^{3+}-mononuclear complexes due to their high anisotropy (SOC), result in ideal candidates to retain magnetic moment in zero field. However, the SMM performance shows dependence with the metal ion environment and the electronic configuration. In other words, the relaxation mechanism for the different compounds follow a modified Arrhenius law, with a temperature-dependence that is not uniform. Consequently, the low temperature region is characterized by other processes allowing the shortcut of the Energy barrier. In order to overcome it, research has been focused in understanding the relation between the relaxation effects and the contributing intermolecular[73,74] and hyperfine interactions[75,76] to the low temperature regime.

The different studies concerning the magnetic properties, can be summarized in three different approaches: For the first,(1) the influence of small changes in the coordination sphere or ligand and (2) influence of the magnetic dilution (liquid or solid) to the overall magnetic properties; and for the second, (3) the isotopic enrichment of the metal center. This tendency will be seen in the introduction part of this chapter, within the different examples given from studies of the group.

However, it must be noted that in order to study this relaxation mechanisms not all the existent systems displaying SMM properties are good candidates, and as we will see from now they must fulfill certain particularities: (1) First, we will only work with mononuclear systems, as the ordering interaction between the different centers would hinder the hyperfine/ dipolar interactions marks. (2) Moreover, in order to have a comparison of the isotopic effect, both metallic centers I= 0 and I≠ 0 need to be available (stable in the nature); (3) Concerning the SMM properties, if it is pretended to see a difference in the relaxation between the different systems, the maxima of the out-of-phase component of the susceptibility need to be centered around 50-100 Hz at 2 K. Slower systems would not guarantee a maxima within the measurement windows (0.01 Hz – 10 kOe) after dilution/ isotopic enrichement at the lowest temperatures, where those fast events are efficiently working; (4) And finally, the synthesis *need to be easy and reproductible, as the lanthanide precursors, because of their prize, are not widely available. $^{A}Dy(tta)_3(\mathbf{L^2})]\cdot C_6H_{14}$ (A= isotopic number, tta$^-$= 2-thenoyltrifluoroacetylacetonate and* $\mathbf{L^2}$ *= 2-{[2-methylpyridiyl]-4,5-[4,5-bis(propylthio)-tetrathiafulvalenyl]-1H-benzimidazol-2-yl}pyridine) system has been retrieved from previous works. In those, isotopic enrichment of the compound (^{161}Dy and ^{164}Dy isotopes), as well as magnetic dilution in an isomorphous diamagnetic matrix, were approached in order to get evidence about the influence of the nuclear spin and the dipolar interactions on the magnetic properties.*[74,75] *Dy^{3+} ion is constituted by seven stable isotopes with nuclear spin of values 0 and 5/2. Among them, the main contribution comes from the four $^{161\text{-}164}$Dy, representing 97.5% of the isotopic mixture: ^{161}Dy (18.9%) and ^{163}Dy (24.9%) have the same nuclear spin I= 5/2 but different nuclear magnetic moment*[77]*, and ^{162}Dy (25.5%) and ^{164}Dy (28.2%) are nuclear spin free.*

The aim of this chapter is to go one step further in the study of the nuclear effect in the SMMs properties. For that, compounds ^{162}**Dy**, ^{163}**Dy**, *and the diluted analogues* ^{162,163}**Dy@Y** *have been synthesized following the same procedure than for the previous studied complexes, detailed in Chapter II.*[74]

I. INTRODUCTION

In this section, several examples of the previous work performed in the laboratory will be reported, as well as the different strategies used for the characterization of the slow relaxation of the magnetization, in order to understand the general interest of the present work. It should be specified that the selected synthetic strategy followed by some of them, which it turns to be the benchmark of the group, is the coordination of Dy^{3+} ions to redox-active tetrathiafulvalene (TTF) based ligands in order to enhance different functionalities: redox-active coordination complexes,[78] SMMs,[73,74,76,79] luminescent compounds,[79e,80] and in some cases, multifunctional complexes.[81] From the wide number of publications, and in the context of this thesis, only the mononuclear systems behaving as SMM will be of interest.[73,74,79c]

In general, and as it can be seen next, the synthetic root followed in the group can be summarized by the coordination of a chelating nitrogenated ligand to a Dy(β-diketonate)$_3$ precursor, usually referring to tta= 2-thenoyltrifluoroacetone or hfac=

hexafluoroacetylacetone. As a result, the coordination sphere around the Dy^{3+} is usually N_2O_6 with the symmetry tuned by the different distances Dy-N and Dy-O.

In 2013, the coordination of two different ligands obtained simultaneously from the same synthetic work, **L**^{1}= 4,5-bis(propyl-thio)tetrathiafulvalene-2-(2-pyridyl)benzimidazole and **L**^{2}= 4,5-bis(propylthio)tetrathiafulvalene-2-(2-pyridyl)-3-(2-pyridylmethyl)benzimidazole to a $Dy(hfac)_3\cdot 2H_2O$, was reported with the magneto-structural characterization of the resulted systems.[73] $[Dy(hfac)_3(\mathbf{L^1})]$ (**7**) and $[Dy(hfac)_3(\mathbf{L^2})]$ (**8**) crystals were obtained with similar structural characteristics. Figure 3. 1 shows both molecular structures and, with it, the difference between both molecules, given by the substitution of a hydrogen atom on N3 by a methyl-2-pyridine arm in an alkylation reaction, can be observed.

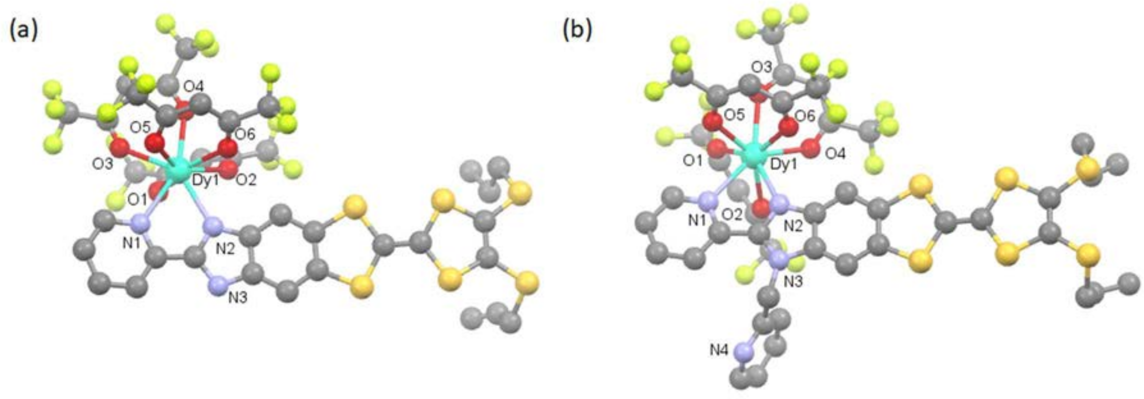

*Figure 3. 1. Molecular structure of **7** (a) and **8** (b). The solvent molecules and hydrogen atoms are omitted for clarity. From ref. [73].*

The presence of this arm leads to a different arrangement of the molecules and thus to a different behavior through the magnetic response. The dynamic study of the magnetic properties showed that **7** displayed SMM behavior at the molecular level when diluted in dichloromethane, however no out-of-phase signal was observed in solid-state. This is attributed to the presence of hydrogen bond in the condensed phase that is broken in solution. On the other hand, the substitution of the hydrogen atom by an alkyl group (compound **8**), restores the slow relaxation phenomena in solid state which is also present in solution up to 7 K. The different dilutions were reported to favor slower relaxation times, decreasing an existent temperature-independent regime (QTM) and remaining the Orbach constant. Compound **8** was magnetically diluted in an Y^{3+}-based isomorph matrix which consequently turned to 30 times slower QTM relaxation compared to the condensed.

In the same year, a different Dy^{3+} precursor ($Dy(tta)_3\cdot 2H_2O$) was used for the coordination to $\mathbf{L^2}$, thus creating $[Dy(tta)_3(\mathbf{L^2})]$ (**9**, inFigure 3. 2) which also showed SMM behavior in both solid-state and solution.[74] The substitution of the hfac$^-$ by the tta$^-$ moiety results in a greater negative charge centered on the oxygen atoms, because of the less electro-attractive character of the thiophene compared with $-CF_3$ groups. Moreover, it is expected to have lower degrees of freedom, thus enhancing the SMM behavior. This time, a more extended study was undertaken: the SMM behavior was studied by AC magnetometry and hysteresis loops of the magnetization, the Ising character of the molecular magnetic moment by angular resolved magnetometry measurements and theoretical calculations, and the different energy sublevels by both theoretical calculations and luminescent measurements. Moreover, the molecular origin was demonstrated by ac and hysteresis loop measurements in frozen solution.

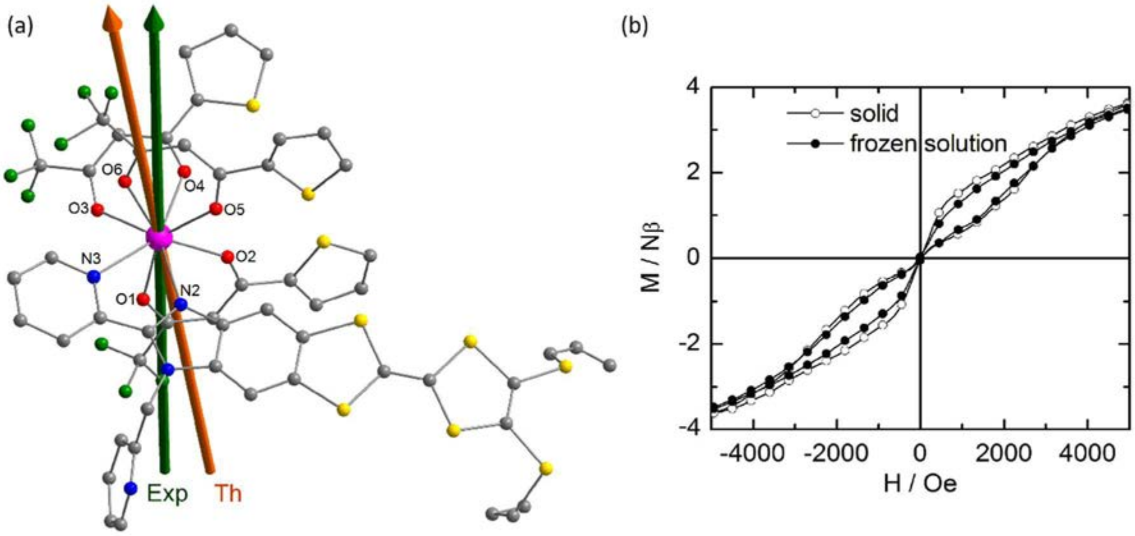

Figure 3. 2. a) Molecular structure of ***9*** *(H atoms and solvent molecules are omitted for clarity). Dark green and orange arrows represent the experimental and theoretical anisotropy axis, respectively. b) Out-of-phase component of the magnetic susceptibility from 2 to 15 K. From ref. [74].*

Actually, from **8** to **9** the dynamic characteristic of the SMM are enhanced with an effective energy barrier that doubles from around 18 K to 40 K, respectively, and slowing the relaxation phenomena to a point in which the hysteresis in the magnetization can be observed until 4 K. In both kind of measurements, the so-called QTM regime can be seen: in the first, characterized by a temperature independent region at the lowest temperatures, and the second, by a closed hysteresis in zero-field. This existent regime at low temperature results in an increased interest for further work on the events behind it.

In 2015 this system was examined again in order to optimize its SMM behavior. For that purpose, two different strategies were proposed and coupled in order to guarantee success. Intermolecular and hyperfine interactions are thought to be behind the quantum events visible at low temperature, thus magnetic dilution in an Y^{3+}-based isomorph matrix and isotopic enrichment have been proposed.[75] As reported, they proved the dependence of the QTM with the nuclear spin (I) and the dipolar interactions, thus optimizing the SMM behavior by the suppression of both. In Figure 3. 3 this is evidenced by the opening of the hysteresis loop at zero-field for the diluted form of ^{164}**9** (in red).

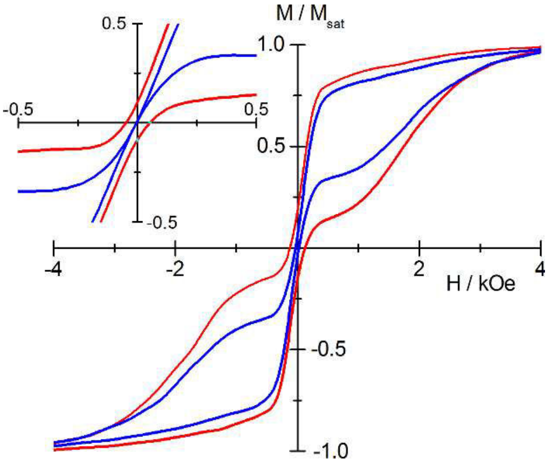

Figure 3. 3. Normalized magnetic hysteresis loops measured at 0.46 K on the diluted forms of ^{161}***9*** *(I=5/2, in blue) and* ^{164}***9*** *(I= 0, in red), with 20 s between each field. Inset: expended view. From ref. [75].*

Since, other systems have been reported with other interesting behavior, such as the coexistence of both magnetic and luminescent properties. Examples include the synthesis and characterization of the physical properties of the Yb- analogous of **9**, which behaves as a field-induced SMM (2014),[79e] and that of two optically-pure helicene-based Dy^{3+} system which compared to their racemic analogous favored a great enhancement of the SMM properties (2016),[81b] among others.

In 2017, a second publication concerning the isotopic enrichment (with $^{164}Dy^{3+}$, I=0) and magnetic dilution strategies for the formation of an SMM systems was published.[76] Within, two different polymorphs of $[Dy(tta)_3(\mathbf{L^3})]$ (**10**) (with $\mathbf{L^3}$= 4-[6-(1,3-benzothiazol-2-yl)pyridin-3-yl]-4',5'-bis(methylthio)tetrathiafulvene) are presented: one crystallizing in the triclinic (**10t**) and the other in the monoclinic (**10m**) space group (Figure 3. 4a). The main difference resides in the ligand conformation which turns up (**10t**) or down (**10m**) depending on the polymorph. SMM behavior is present in both in condensed and diluted samples, and the triclinic form presents a slower magnetic relaxation compared to the monoclinic analogue. Finally, the magnetic properties were enhanced using magnetic dilution and *I*=0 isotopic enrichment (Figure 3. 4c), thus suppressing the possible perturbations to the relaxation, in order to support the importance of isotopes for the control of the quantum events.

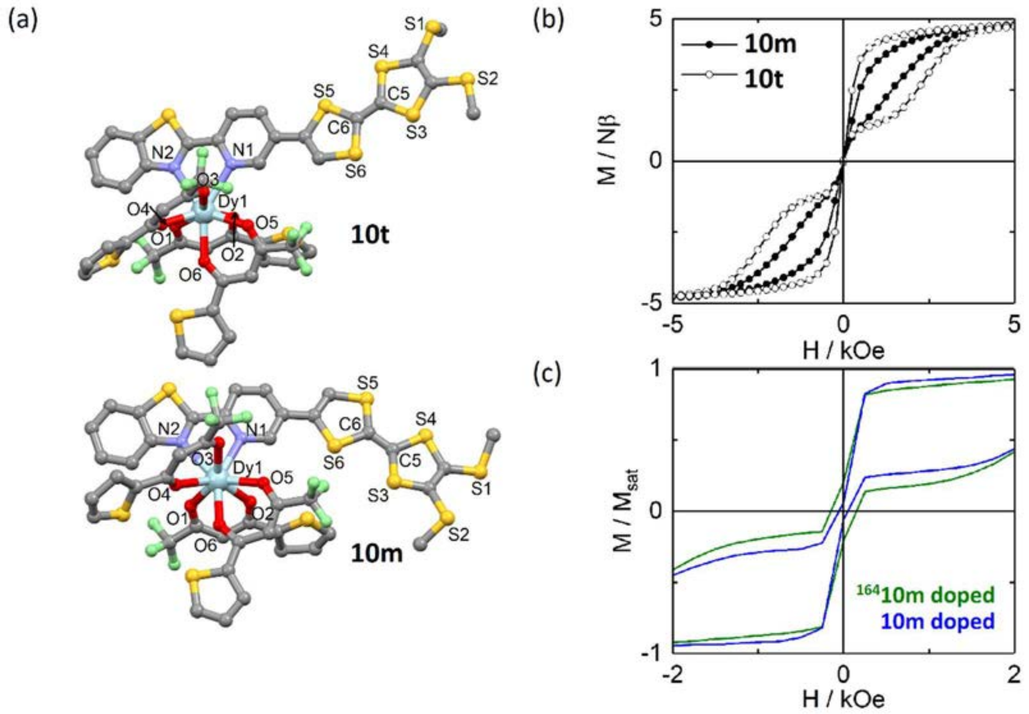

*Figure 3. 4. a) Molecular structure of **10t** (up) and **10m** (down) (H atoms and solvent molecules are omitted for clarity). b and c) Hysteresis loops for the condensed **10t** (circles) and **10m** (squares), and diluted ^{164}**10m** (olive) and **10m** (blue), respectively. Recorded at 0.5 K and 16 Oe s^{-1}. From ref. [76].*

Until now, it has been demonstrated the importance of suppressing the different interactions coming from the nucleus or the neighbor spins, but little is known about the real role of the nuclear moment in the QTM events. This first experimental chapter aims to retrieve compound **9**, hereafter defined as **Dy**, to go a step further in the understanding of the role of the isotopic effect in the fast relaxation process. As already mentioned before, ^{161}Dy and ^{164}Dy have been already studied and a more extended work is pretended to be done by including their ^{162}Dy (*I*=0) and ^{163}Dy (*I*=5/2) analogues.

II. RESULTS AND DISCUSSIONS

A. *Structural description*

^{A}**Dy**·C$_6$H$_{14}$ compounds are obtained by solubilizing ^{A}Dy(tta)$_3$·2H$_2$O with the ligand (**L^2**) in the same CH$_2$Cl$_2$ solution, followed by a layered diffusion of *n*-hexane. Same procedure with the simultaneous addition of Y(tta)$_3$·2H$_2$O in suitable proportions was needed for diluted samples. The four compounds **^{162,163}Dy** and **^{162,163}Dy@Y** are isostructural (Annex 1, table A1.1) and the X-ray structure (Figure 3. 2) was previously studied for the two other isotopologues (**^{161,} ^{164}Dy**). The ratio Dy/Y (0.05/0.95) for the two doped compounds [^{162}Dy$_{0.05}$Y$_{0.95}$(tta)$_3$(**L^2**)]·C$_6$H$_{14}$ **(^{162}Dy@Y**·C$_6$H$_{14}$**)** and [^{163}Dy$_{0.05}$Y$_{0.95}$(tta)$_3$(**L^2**)]·C$_6$H$_{14}$ **(^{163}Dy@Y**·C$_6$H$_{14}$**)** has been verified by EDS analysis (Annex 2, Figure A2.1) and then used to refine the X-ray structure on single crystals: ^{162}Dy/Y: 0.05/0.95 and ^{163}Dy/Y: 0.04/0.96.

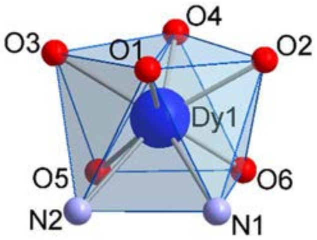

Figure 3. 5. Coordination environment of Dy1, polyhedron used for SHAPE analysis.

The molecular structure consists in a Dy cation surrounded by two nitrogen atoms coming from the ligand **L^2** and six oxygen from three tta$^-$ moieties (Figure 3. 5), forming a N$_2$O$_6$ antiprism coordination environment (D$_{4d}$ symmetry, found by SHAPE analysis,[82] table 3.1). As expected, the Dy-N (~2.52(4) Å) bond length are longer than the Dy-O (~2.33(1) Å) one due to the oxophilic character of the lanthanide. The central C=C bond length and the non-planar TTF core certifies the neutrality of **L^2**. The different molecules are disposed following a packing of head-to-tail dimers. The different dimers interact with the neighbor by π-π staking of tta$^-$ anions (Figure 3. 6). The closest distance between Dy^{3+} ions is of 9.33 Å.

*Table 3. 1. First three closest symmetries for the **Dy1** coordination environment.*

	CShMSAPR-8 (square antiprism D4d)	*CShMTDD-8 (triangular dodecahedron D2d)*	*CShMBTPR-8 (biaugmented trigonal prism C2v)*
Dy-N$_2$O$_6$	0.540	2.326	2.385

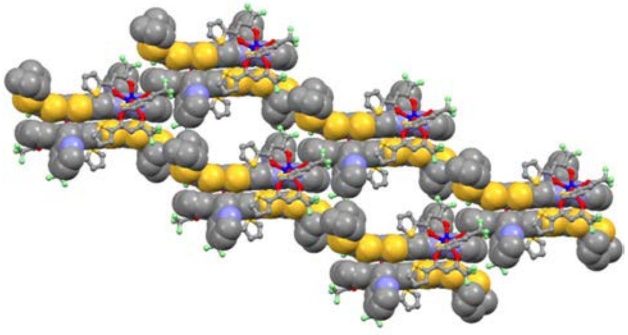

Figure 3. 6. Crystal packing view of **^{162}Dy** *highlighting the formation of "head-to-tail" dimers. The ligand* **L^2** *and* **Dy(tta)$_3$·2H$_2$O** *precursor are respectively shown in "space fill" and "ball and sticks" representations. From ref. [95].*

B. *DC magnetic properties*

Static magnetic measurements were performed for all the compounds, as it can be seen in Figure 3. 7 and Figure 3. 8. If we compare *M* vs *H* and $\chi_M T$ vs *T* curves for all the condensed samples, they appear to be perfectly superimpose one with another. This expected behavior can be explained by the fact that magnetic DC properties of a metal depends only on its electronic configuration (Dy^{3+}: [Xe] $4f^9$). The thermal dependence of the molar magnetic susceptibility was studied from 2 to 300 K. At room temperature, the $\chi_M T$ vs. *T* curve reaches 14.16 $cm^3\ mol^{-1}$ K which is in agreement with the molar magnetic susceptibility of a free Dy^{3+} ion ($^6H_{15/2}$, g= 4/3, $\chi_M T$= 14.17 $cm^3\ mol^{-1}$ K).[83] On cooling, the $\chi_M T$ product decreases monotonically down to 11.7 $cm^3\ mol^{-1}$ K at 2 K, which is mostly attributed to the progressive thermal depopulation of the excited-state Stark sublevels due to the crystal-field effects of Dy^{3+}. At 2 K, the field dependence of the magnetization shows a classic behavior with a saturation value M_{sat} at 5 Nβ. This value matches to the value obtained for the multiplet ground state $^6H_{15/2}$ when showing an Ising-anisotropy which corresponds to the stabilization of the Kramers doublet M_J = ±15/2.[83]

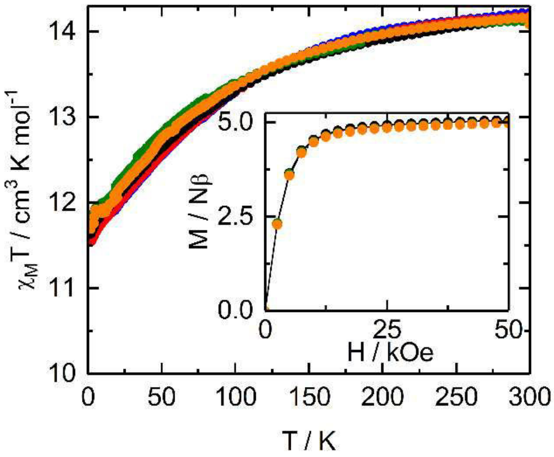

Figure 3. 7. Thermal dependence of the $\chi_M T$ for ^{A}Dy: being ^{161}Dy (blue), ^{162}Dy (orange), ^{163}Dy (green), ^{164}Dy (red) and Dy (black). The inset shows the field variation of the magnetization at 2 K.

For the **Dy@Y** series, magnetic field dependence of the magnetization has been performed in order to obtain the percentage of the paramagnetic unit in the sample. The ratio between the M_{sat} for this and the condensed phase gave contents of 2.4 % (^{161}Dy^{3+}), 3.7 % (^{164}Dy^{3+}), 5.2 % (^{162}Dy^{3+}) and 6.2% (^{163}Dy^{3+}) for the different diluted samples. These values are in agreement with the 3 % and 4 % Dy^{3+} found in the formers by F. Pointillart *et al.*[75], and the EDS analysis values for the two lasts (^{162}Dy^{3+}: 4.6 ± 0.7 % and ^{163}Dy^{3+}: 4.3 ± 0.2 %).

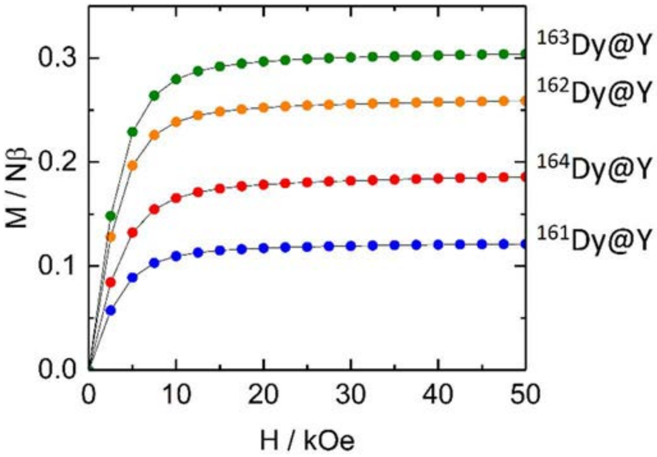

*Figure 3. 8. Magnetization curves of diluted samples at 2 K: ^{161}**Dy@Y** (blue) ^{162}**Dy@Y** (orange), ^{163}**Dy@Y** (red), ^{161}**Dy@Y** (blue) and ^{161}**Dy@Y** (blue).*

C. *AC magnetic properties*

The dynamic properties of the two isotopic complexes **^{162}Dy** (*I*=0) and **^{163}Dy** (*I*=5/2) have been determined by measuring the frequency dependences of the magnetic susceptibility at various applied field and various temperatures. At zero field, the ac susceptibility of **^{162}Dy** (*I*=0) and **^{163}Dy** (*I*=5/2) were performed for temperatures between 2 and 15 K. The resulted curves are presented on Figure 3. 9, showing a frequency dependence under these conditions.

Consequently, the out-of-phase susceptibility passes through a maximum evidencing a slowing down of the relaxation of the magnetization because of the need of overpassing a certain energy barrier.

By decreasing the temperature, the pass over this barrier is disfavored giving rise to the consequent slow-down in the relaxation, which can be seen by the shift of the maxima in the χ_M'' vs. ν curves to lower frequencies. At 2 K, and as previously observed for **^{161}Dy** (I = 5/2) and **^{164}Dy** (I = 0),[75] the maximum for the nuclear spin-free **^{162}Dy** (ν= 16 Hz) occurs at lower frequency than **^{163}Dy** (160 Hz).

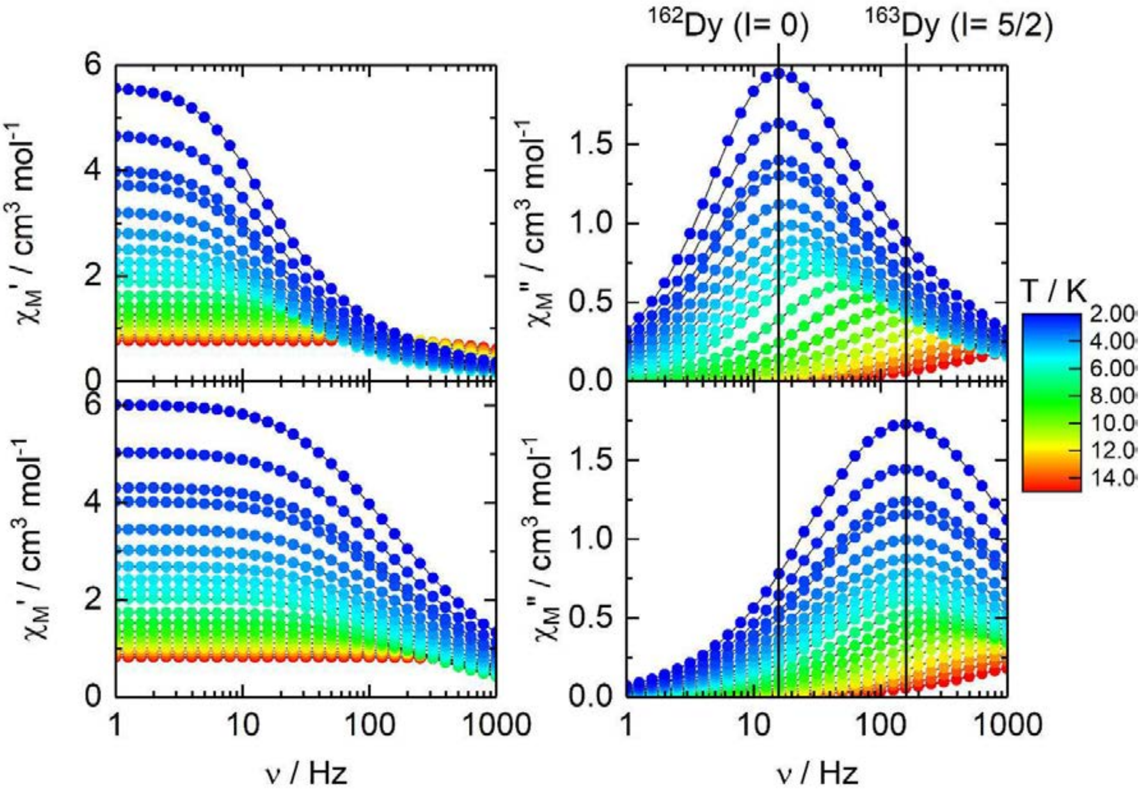

*Figure 3. 9. In-phase and out-of-phase molar magnetic susceptibility for **^{162}Dy** (I=0) (right) and **^{163}Dy** (I=5/2) (left) for temperature between 2 and 15 K and in zero external DC field. Vertical full lines correspond to the frequency position of the maxima at 2 K.*

By applying the extended Debye model (Equation 2.6) for the different temperatures, several information about the system can be extracted: the value in the limit of low and high frequencies (isothermal (χ_T) and adiabatic (χ_S) susceptibilities, respectively), the relaxation time of the magnetization (τ, corresponding to the position of the maximum susceptibility at a certain T), as well as the α parameter, which is an evaluation of the relaxation time distribution (Annex 3, tables A3.1-A3.2). An overview of the trends in α parameter, which is compressed between 0 and 1, is rapidly observed by the normalized Argand representation in

Figure 3. 10. Hence, greater is the distribution of the relaxation, closer is this value to 1, and the semicircle's shape flattens. Comparing the shape of both Argand plots, also confirmed by the values obtained during the fitting, α(**^{162}Dy**) is systematically smaller than α(**^{163}Dy**). This is in agreement with the fact that hyperfine interactions, caused by the nuclear spin *I*= 5/2 and the effective electronic spin *S*= 1/2, enhance a greater distribution of the relaxation.

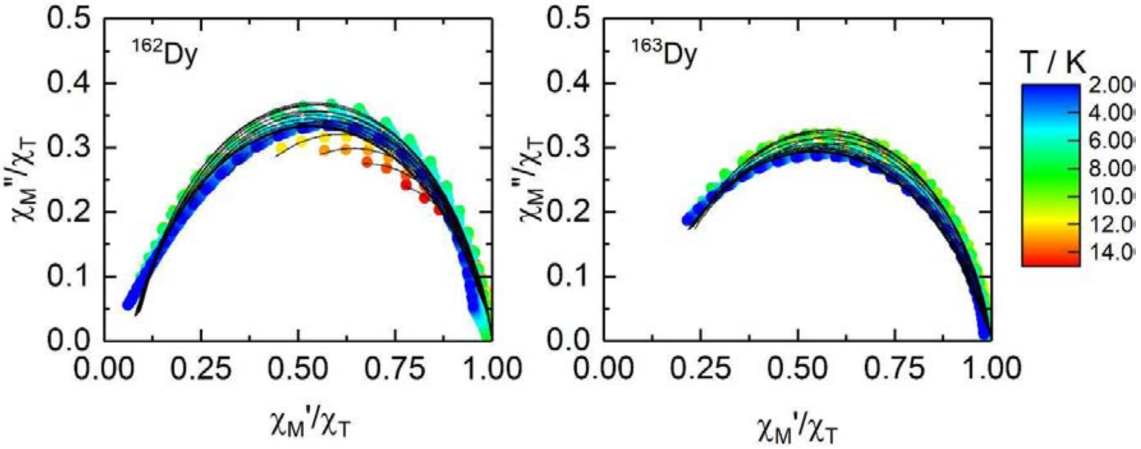

*Figure 3. 10. Argand Plot for **^{162}Dy** (right) and **^{163}Dy** (left). Full lines correspond to the best fitted curves using the extended Debye model.*

The thermal dependence of the relaxation time is represented on Figure 3. 11. So far, the description of the relaxation mechanism was described by an exponential contribution given by Orbach (slow relaxation) at higher temperatures, and a fast relaxation, temperature-independent, given by the QTM.[74,75,84]

$$\tau^{-1} = \tau_0^{-1}\exp(\Delta / T) + \tau_{TI}^{-1} \qquad (3.1)$$

Where τ_0 and τ_{TI} are the intrinsic and temperature independent relaxation times, respectively, and Δ the energy barrier.

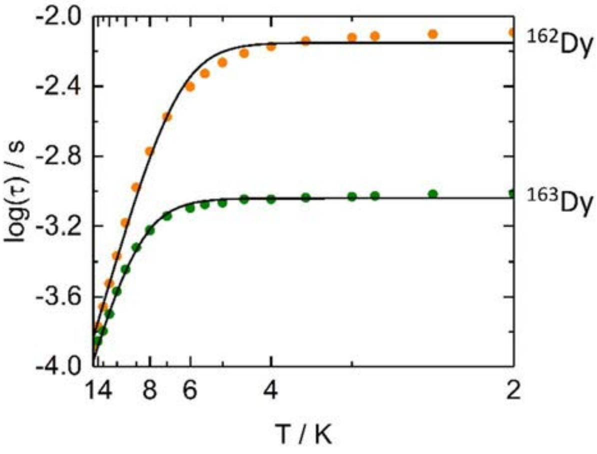

*Figure 3. 11. Temperature dependence of the relaxation time between 2 and 15K for H$_{DC}$= 0 Oe for **^{162}Dy** (orange) and **^{163}Dy** (green). Full lines correspond to the best fitted curves.*

The best fitted parameters are given in Table 3.2 and they evidence that the isotopic enrichment only influences the temperature-independent regime observed in zero field (QTM) and does not affect the thermally activated regime and the intrinsic relaxation time (τ_0).[85]

*Table 3. 2. Best fitted parameters for the relaxation mechanism of the ^{A}**Dy**- series, considering the Orbach and QTM as only contributions.*

Compound	Δ / K	τ_0 / s	τ_{TI} / s
Dy	42±3	$(8\pm1)\cdot10^{-6}$	$(1.62\pm0.04)\cdot10^{-3}$
^{161}Dy	45±2	$(6\pm1)\cdot10^{-6}$	$(1.17\pm0.02)\cdot10^{-3}$
^{162}Dy	44±2	$(7.8\pm0.1)\cdot10^{-6}$	$(8.1\pm0.1)\cdot10^{-3}$
^{163}Dy	46±2	$(5.6\pm0.7)\cdot10^{-6}$	$(1.0\pm0.1)\cdot10^{-3}$
^{164}Dy	43±2	$(8\pm2)\cdot10^{-6}$	$(7.27\pm0.3)\cdot10^{-3}$

Even if the QTM process is reduced when going from **^{163}Dy** to **^{162}Dy**, it is still operative at low temperature. To effectively cancel it, ac measurements were performed at a fixed temperature comprised in the QTM regime, 3 K, from 0 to 3 kOe (Figure 3. 12).

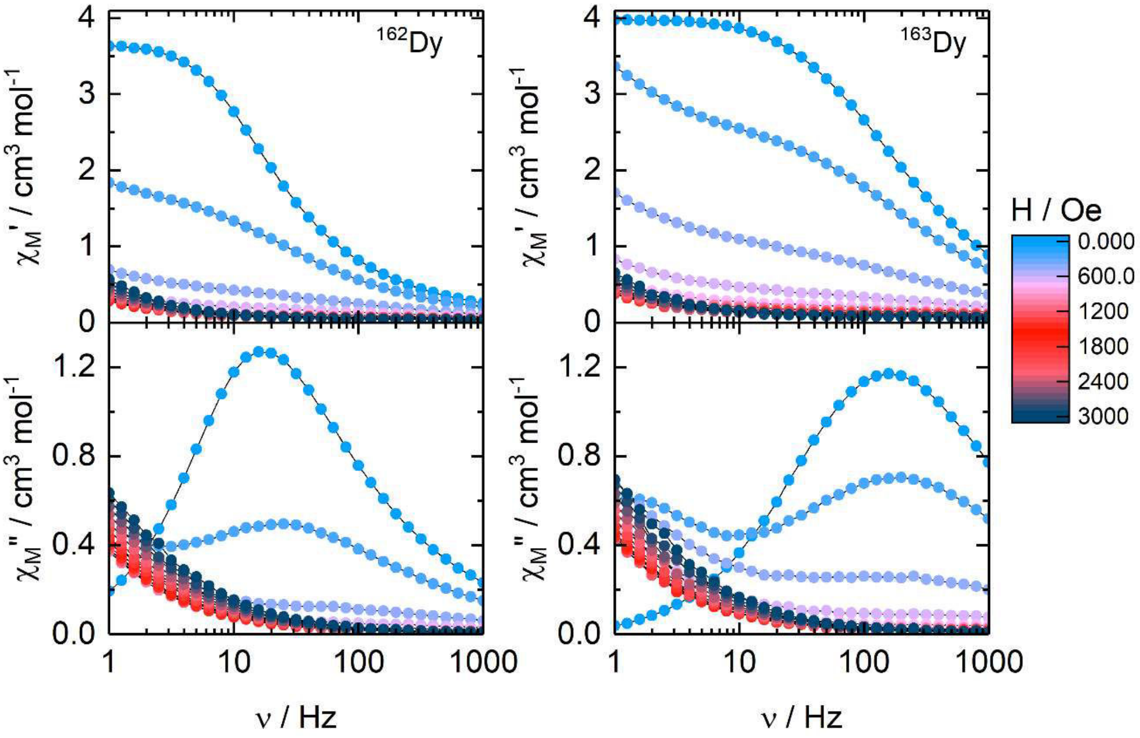

*Figure 3. 12. χ' and χ'' components of the molar magnetic susceptibility for **^{162}Dy** (I=0) and **^{163}Dy** (I=5/2) at 3 K with H_{DC} from 0 to 3 kOe.*

As it can be seen for the χ_M'' vs. ν curve, at low H_{DC} the curve is split in two different contributions, then the first at higher frequencies diminishes until it disappears and in parallel, the one at lower frequencies rises. This phenomenon has already been observed for other systems[73,86] and some studies attributed it to the presence of relatively important dipolar interactions.[87] The optimal magnetic field set at 1 kOe is characterized by the lowest relaxation time of the magnetization, which corresponds to the field for which the QTM is suppressed. By applying an H_{DC}, the system display a drastic slowdown of the relaxation in the out-of-phase component of the susceptibility. However, further information about the nature of the relaxation mechanism at low temperature and under various magnetic fields could not be extracted because of a lack of points in the lowest regime.

Nevertheless, by applying such an intense magnetic field compared to the field created by the hyperfine interactions, it causes the suppression of the isotopic effect. In fact, if we take a look at the temperature dependence of the ac susceptibility under 1 kOe, the two isotopologues behave identically and τ vs. ν curves are perfectly superimposed (Figure 3. 13, Anex 3, Table A3.3-A3.4).

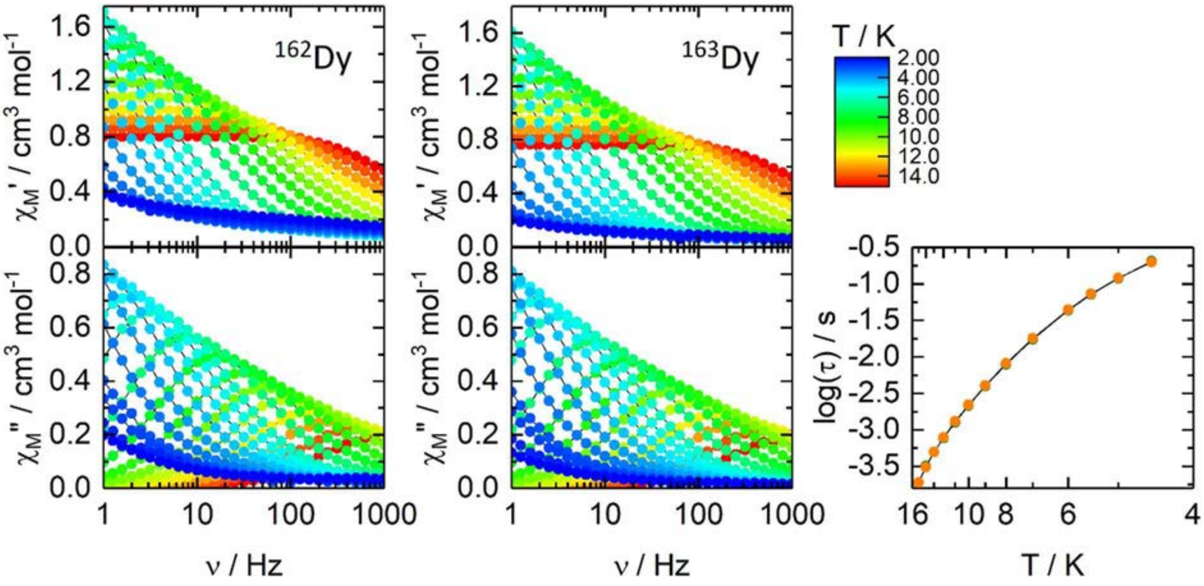

*Figure 3. 13. χ'/ χ" vs. ν plots for ^{162}**Dy** (I=0) and ^{163}**Dy** (I=5/2), respectively, under an optimal field of 1 kOe. In the right, comparison of the temperature dependence of the relaxation of both ^{162}**Dy** (orange) and ^{163}**Dy** (green). Full lines are guides to the eye only.*

Comparison between the different isotopologues is provided in Figure 3. 14. As expected, the two nuclear spin-free isotopes $^{162/164}$**Dy** behave the same whereas the two isotopes ^{161}**Dy** and ^{163}**Dy** (*I* = 5/2) display faster magnetic relaxation and the natural mixture in between. Furthermore, if we focus in the QTM regime, there is a significant difference in the relaxation times between the two I= 5/2 isotopologues.

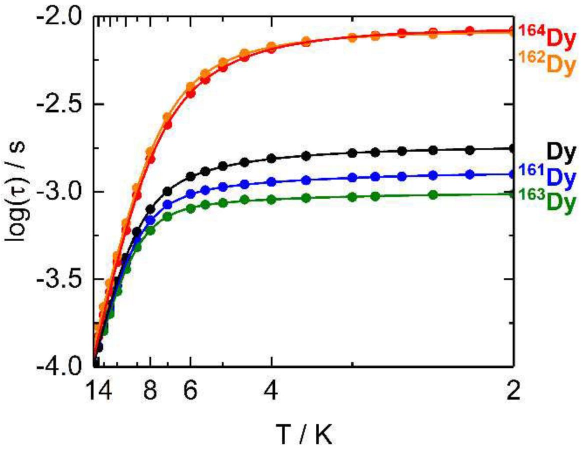

Figure 3. 14. Temperature dependences of the relaxation times τ of the four isotopologues $^{161-164}$**Dy** in a zero-magnetic field between 2 and 15 K. Full lines are guides to the eye only.

If we compare the study in temperature of the ac susceptibility for both compounds (Figure 3. 15), it can be seen as in the χ_M'' vs. ν curve, the maxima at 2 K is centered at 106 Hz for ^{161}**Dy** and at 160 Hz for ^{163}**Dy**.

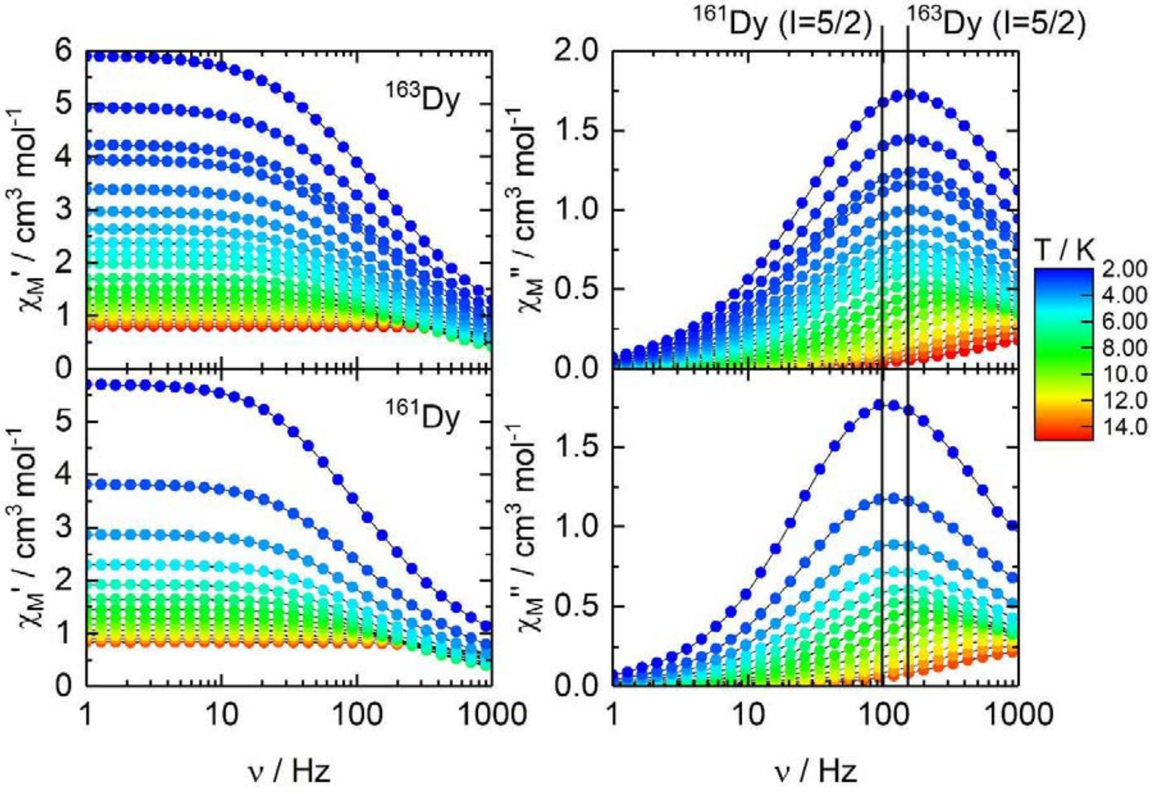

Figure 3. 15. χ′ and χ″ components of the molar magnetic susceptibility for ^{161}Dy and ^{163}Dy (I=5/2) for temperature between 2 and 15 K and in zero external DC field. Vertical full lines correspond to the frequency position of the maxima at 2 K.

The slightly faster relaxation of ^{163}**Dy** compared to ^{161}**Dy** can be explained through the hyperfine coupling definition[77]:

$$\begin{aligned} H_{HF} &= hA\vec{I}\cdot\vec{J} + hB\frac{\frac{3}{2}\vec{I}\cdot\vec{J}(2\vec{I}\cdot\vec{J}+1)-I(I+1)J(J+1)}{2I(2I-1)J(2J-1)} \\ &+hC\frac{\frac{5}{4}\{8(\vec{I}\cdot\vec{J})^3+16(\vec{I}\cdot\vec{J})^2+\frac{8}{4}(\vec{I}\cdot\vec{J})[-3I(I+1)J(J+1)+I(I+1)+J(J+1)+3]-4I(I+1)J(J+1)\}}{I(I-1)(2I-1)J(J-1)(2J-1)} \end{aligned} \tag{3.2}$$

where *I* and *J* are the nuclear spin and electronic angular moment, which are coupled through three different constants: *A*, *B* and *C*. These stand for the magnetic-dipole, electric-quadrupole, and magnetic-octupole hyperfine coupling constants, respectively. The different hyperfine-interaction constants for ^{163}Dy and ^{161}Dy (Dy: [Xe] 4f^{10}s^2) for the ground atomic state ^{5}I$_8$ was taken from the literature[77b] and are presented in Table 3.3. They give an approximate idea of the difference in magnitude between both isotopologues, so that we can have a better understanding about the hyperfine interactions.

Table 3. 3. Values of the A, B and C hyperfine-interaction constants and the g$_J$ value of the ^{5}I$_{8,7}$ atomic ^{161,163}Dy, taking into account the slight effects of hyperfine and Zeeman interactions with other atomic states. Table extracted from [77b].

Isotope	*Atomic state*	*Quantity*	*Values gJ and A, B and C (cm^{-1})*
^{163}Dy	^{5}I$_8$	A	5.4289(1)·10^{-3}
		B	3.84556(7)·10^{-2}
		C	3(1)·10^{-8}
		g$_J$	1.24160(5)
^{161}Dy	^{5}I$_8$	A	-3.877(1)·10^{-3}
		B	3.6401(2)·10^{-2}
		C	-6(1)·10^{-8}
		g$_J$	1.24161(4)

As exposed in Table 3.3, the resulted values from the ground state multiplet ^{5}I$_8$ show slightly different constant values from one to the other, but the most remarkably is the opposite sign of A , being negative for ^{161}Dy. The major contribution comes from the two firsts: *A* and *B* constants, *C* being negligible. For instance, the ratio between the A's and B's constants between both ^{161,163}Dy can be observed (Table 3.4) for a faster comparison:

*Table 3. 4. Comparison of ratio of A and B values for the two isotopes, where the ratios between both isotopes are the same for both atomic states. Table extracted from Phys. Rev. A, W. J. Childs (**1970**).*[77b]

Ratio	$^5I_8$
A(^{163}Dy)/ A(^{161}Dy)	-1.40026(3)
B(^{163}Dy)/ B(^{161}Dy)	1.05615(6)

If taking into account the resulted ratios (in absolute values), the contribution of *A* and *B* for the ^{163}Dy isotope are greater than for ^{161}Dy. This is in accordance with the fact that the effect of the hyperfine interactions in the QTM are more present in the first, allowing a faster relaxation of the magnetization. Actually, the H$_{HF}$ Hamiltonian contributes to the mix of $M_J=\left|\pm 13/2\right\rangle$ and $M_J=\left|\pm 15/2\right\rangle$ sublevels, which favors the increase of the transversal components of the g-tensor, cause of the appearance of the quantum tunneling of the magnetization (QTM).

The effect of the nuclear spin value and, a fortiori, the effect of the hyperfine constant value are very sensitive to any magnetic field (external or internal) because of the hyperfine interaction with values of the order of 10^{-1} cm^{-1}, is easily destroyed by the dipolar magnetic field generated by intermolecular interactions. Therefore, in order to obtain a real insight about the hyperfine interactions, the magnetically diluted samples have been studied. As for the condensed samples, the temperature evolution has been studied at zero magnetic field. By diluting the Dy^{3+} in a diamagnetic Y^{3+}-matrix, the interaction between metal centers is suppress and thus the internal magnetic field too.

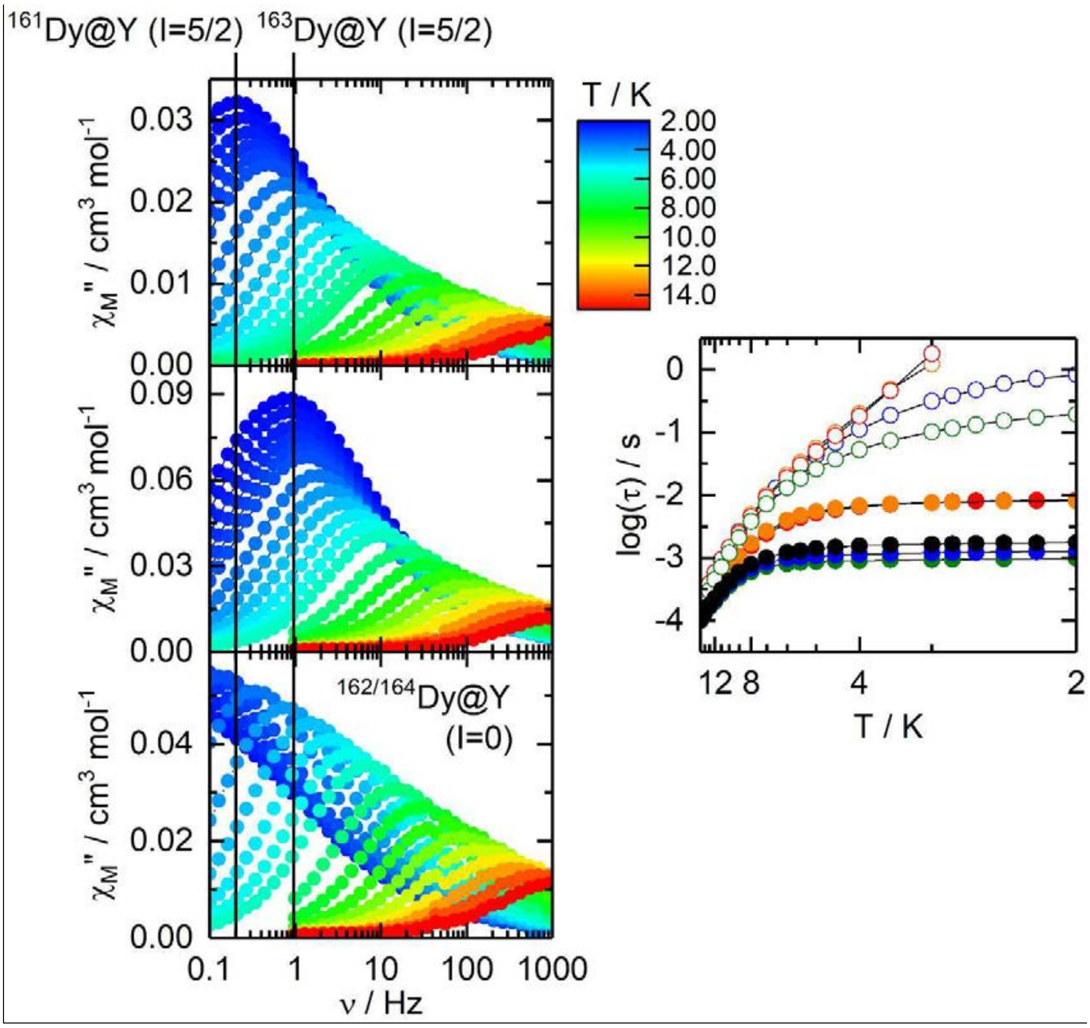

Figure 3. 16. Left: χ_M" vs. ν representation of ^{A}Dy@Y, A=161,162,163 and 164, from 2 to 15 K under zero magnetic field. Right: Temperature dependences of the relaxation times τ of the four isotopologues ***$^{161-164}$Dy*** *(full circles) and diluted samples* ***$^{161-164}$Dy@Y*** *(empty circles) in zero magnetic field from 2 to 15 K. Full lines are guides to the eye only. Vertical full lines correspond to the frequency position of the maxima at 2 K.*

The cancelling of the internal magnetic field induces two main changes on the magnetic properties of the doped samples: First, the maxima of the χ_M" component are significantly shifted to lower frequencies with respect to the condensed phase (Figure 3. 16). The two nuclear spin free isotopes **^{162}Dy@Y** and **^{164}Dy@Y**[75] are shifted to frequencies below 0.1 Hz at 2 K, while **^{161}Dy@Y** and **^{163}Dy@Y** are centered at 0.2 Hz and 0.8 Hz, respectively, reaching at the lowest temperatures relaxation times 1000 times slower than that in the condensed phase (Annex 3, Tables A3.5-A3.6). Secondly, the difference between the two diluted **^{161,163}Dy@Y** compounds is much more pronounced, with, at 2 K, the relaxation time of **^{161}Dy@Y** being four times slower than that of **^{163}Dy@Y**. So far, by magnetic dilution the dipolar interaction between dopant Dy-molecules is released, and it can be concluded that the existent difference is entirely because of the hyperfine coupling.

*Table 3. 5. Best fitted parameters for the relaxation mechanism of the ^{A}**Dy@Y**- series, considering the Orbach and QTM as only contributions.*

Compound	Δ / K	τ_0 / s	τ_{TI} / s
^{161}**Dy@Y**	58 ± 3	$(4 \pm 1)\cdot10^{-6}$	0.83 ± 0.06
^{162}**Dy@Y**	59 ± 3	$(3.5 \pm 0.9)\cdot10^{-6}$	≈100*
^{163}**Dy@Y**	57 ± 2	$(3.9 \pm 0.6)\cdot10^{-6}$	0.190 ± 0.004
^{164}**Dy@Y**	60 ± 3	$(3.8 \pm 0.8)\cdot10^{-6}$	≈100*

On Figure 3. 16 (right), the Arrhenius plots for the condensed (natural mixture and ^{161,162,163,164}**Dy**) and diluted (^{161,162,163,164}**Dy@Y**) samples are represented. The best fitted parameters of the diluted samples are summarized in Table 3.5. As already mentioned, going from a condensed to a diluted phase, the QTM region is significantly decrease and the hyperfine footprint can be directly observed. Nevertheless, the hyperfine interaction is also contributing to the fast relaxation process (^{161,163}**Dy@Y** tends to a constant value at lower temperatures). In order to completely suppress this QTM, the metal center needs to be substituted by a nuclear spin free isotope. Although if we take a look to ^{162,164}**Dy@Y**, a curvature in the linear regime appears, sign of another process such as Raman, which until now has not been considered.

The hysteresis loops of the different isotopologues have been performed down to 0.5 K. Classical butterfly shaped hysteresis loops for the Dy^{3+}-based mononuclear SMM are recorded with a constriction at zero field which is more important depending on the isotope, as already seen in previous work.[75]

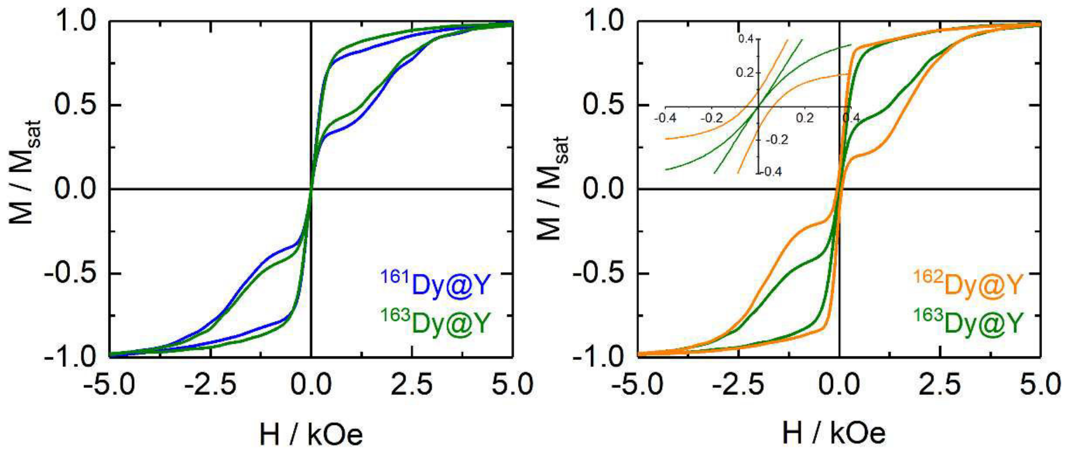

*Figure 3. 17. Normalized magnetic hysteresis loops at 0.48 K and at a sweep rate of 16 Oe s^{-1} for ^{161}**Dy@Y** (blue lines), ^{162}**Dy@Y** (orange lines) and ^{163}**Dy@Y** (green lines). The inset is a zoomed view of the origin to visualize the remnant magnetization.*

The hysteresis loops for **^{161}Dy@Y** and **^{163}Dy@Y** are compared on Figure 3. 17, but no significant differences are observed between the two isotopes, for both there is an important constriction at zero field because of a remnant QTM. On the other hand, if we compare the hysteresis loops of the doped compounds with the fastest (**^{163}Dy@Y**) and the slowest (**^{162}Dy@Y** or **^{164}Dy@Y**) relaxation of magnetization (Figure 3.13, right) there is a significant difference with a clear magnetic bistability at a zero-magnetic field for the nuclear spin-free **^{162}Dy@Y** (see inset). In contrast, **^{163}Dy@Y** is closed at zero field in agreement with the relaxation measurements. Recently, a difference in the Raman mechanism for different isotopic enriched centers has been suggested by Ruben *et al.*, hence justifying the different aperture of the hysteresis loops in field.[88] In this way, nuclear spin *I* would enhance the interaction between the molecular spins and the vibrational acoustics modes, leading to an increase of the Raman relaxation. This, in terms of magnetic hysteresis should be manifested as a narrowing of the hysteresis loop. Indeed, if we observe Figure 3. 17(right), the difference in the aperture can be clearly seen between I=0 (**^{162}Dy@Y**) and I=5/2 (**^{163}Dy@Y**) with, at 1 kOe, ΔM values of 0.63 against 0.40 for **^{162}Dy@Y** and **^{163}Dy@Y**, respectively.

III. A STEP FURTHER

Previous results englobe the studies presented in *Angewandte* **2015**[75] and more recently in *Inorg. Chem. Front.* **2019**[95]. However, when taking into account published CASSCF calculations[75], the energy difference between the GS and the first ES (or here expressed as the energy barrier, *Δ*) is of the order of 181 K. The values obtained from the previous description are far from the expected ones, thus evidencing the importance of other under barrier contributions in the relaxation mechanism that could partially suppress the energy barrier of the molecule. Furthermore, the curvature in the temperature-dependent regime also points to this remark. The spin−lattice relaxation time is formulated as:[84,89,90]

$$\tau^{-1} = \tau_0^{-1} \exp(\Delta / T) + CT^n + \tau_{TI}^{-1} \quad (3.3)$$

with the different relaxation rates standing for the Orbach, the Raman and QTM, respectively. Actually, for a better characterization of the magnetic properties, further measurements have been performed for the natural mixture **Dy** complex as a function of temperature and DC magnetic field: on one side, the evolution of the ac susceptibility with the magnetic field was measured down to lower frequencies (and a temperature set at 4.5 K)

(Figure 3. 18); on the other, the evolution of the same with the temperature up greater frequencies was recorded under both zero and 1000 Oe H_{DC} (Figure 3. 19). Consequently, we want to give an answer to the events happening at the high temperature regime, as well as the mechanism occurring at low temperature under the so-called optimal H_{DC}.

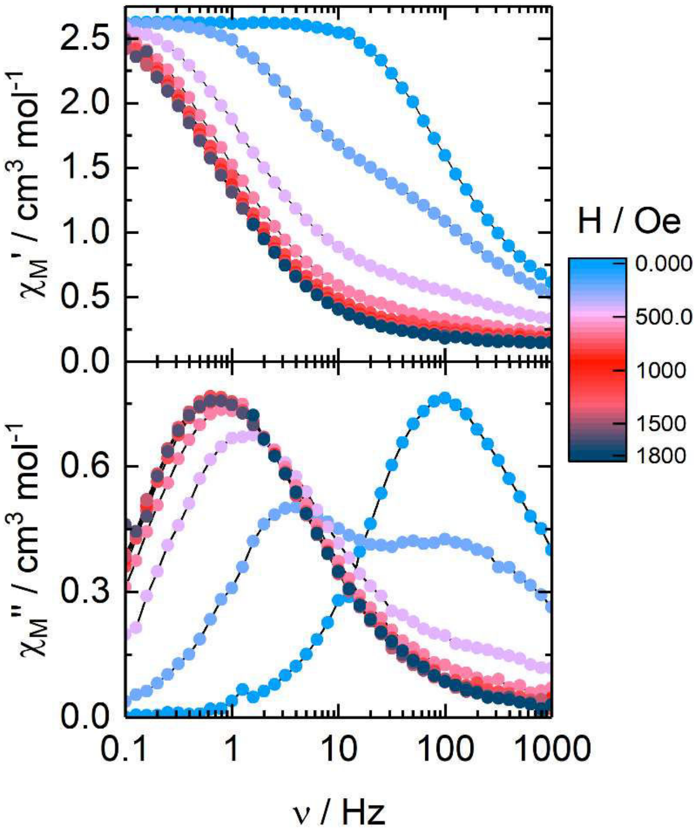

*Figure 3. 18. χ_M' and χ_M'' components of the molar magnetic susceptibility for **Dy** at 4.5 K with H_{DC} from 0 to 1800 Oe.*

The ac components of the magnetic susceptibility at 4.5 K are represented in Figure 3. 18. At this temperature (still in the QTM regime) and widened frequency windows (from 0.1 to 1000 Hz), the evolution of the maxima can be observed. Thus, from 200 to 1000 Oe, the LF (low frequency) peak is gradually left-shifted, while after this optimal field it gently starts to come back to greater *ν*. This confirms that 1 kOe corresponds to the optimal magnetic field, in which the spin-lattice relaxation is no more governed by the QTM and the direct process is still not effective.

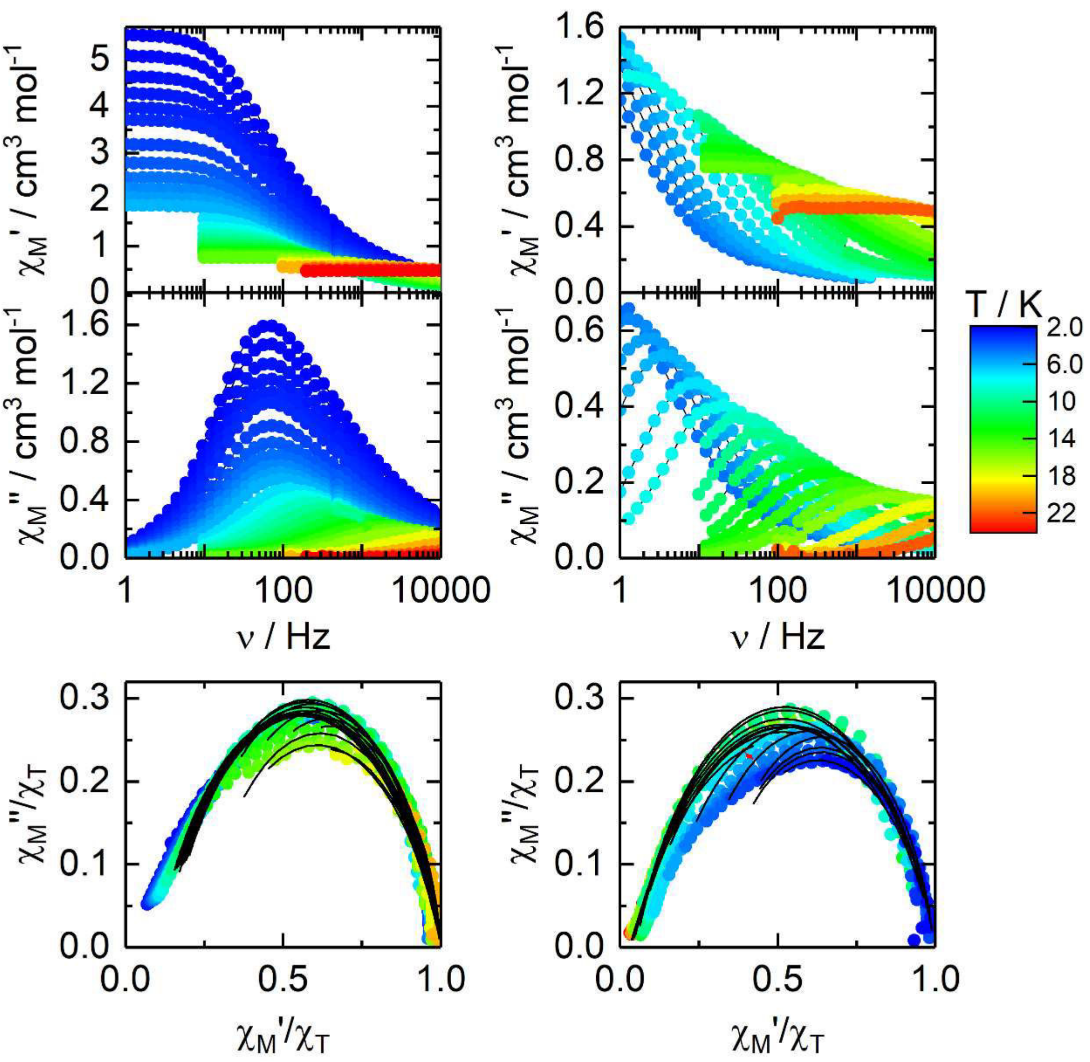

*Figure 3. 19. Ac magnetic measurements of **Dy** compound in a temperature range of 2 to 24 K, under zero magnetic field (left) and 1 kOe (right). At the bottom, the Argand representation of each with full lines the best fitted parameters from the Extended Debye model.*

The different components of the ac susceptibility are represented in Figure 3. 19, in a larger frequency windows from 1 to 10^4 Hz permitting to achieve information about the dynamics from 2 up to 20 K. The extended Debye model has been applied and the best parameters are summarized in Annex 3, Table A4.7. As a result, the temperature dependence of the relaxation times have been plotted simultaneously for 0 and 1 kOe (Figure 3. 20) giving the possibility of fitting both curves at the same time:

$$\begin{cases} \tau_{H=0}^{-1} = \tau_0^{-1}\exp(\Delta/T) + C_1T^{n_1} + \tau_{TI}^{-1} \\ \tau_{H=1kOe}^{-1} = \tau_0^{-1}\exp(\Delta/T) + C_2T^{n_2} \end{cases} \quad (3.4)$$

Thus, the thermal activated Orbach is common in both as it is well-known to be field-independent;[85] the Raman process is differentiate whether the measurements are done under applied field or not, as it may exhibit some magnetic field dependence as suggested by C. Boskovic et al.;[91] and the QTM is just maintained under zero H_{DC} as this is suppressed by the optimal field. In order to facilitate the fitting, the energy barrier has been set from the ab initio calculations,[74] and the results are summarized in Table 3.6.

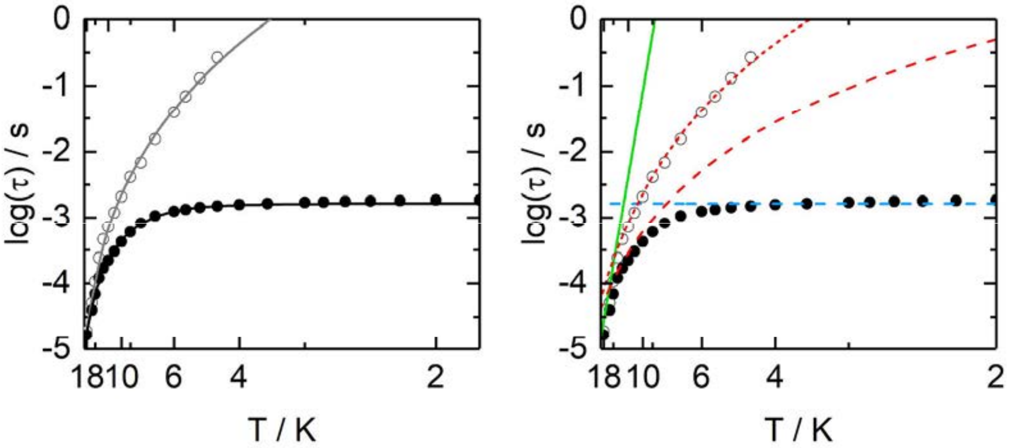

Figure 3. 20. Correlation between the relaxation time (τ) and the temperature (T) under zero H_{DC} (full circles) and 1kOe (open circles). The general resulted curves are visualized in the left, whether the different contributions of Orbach (green), Raman (Red) and QTM (blue), are presented in the right.

As a result, the relaxation mechanism is well characterized by the addition the rate coming from a Raman relaxation. The Raman, which is related with the flexibility of the architecture of the complexes, contributes to the high temperature regime deviating the resulted curve from the linearity cause by a non-exponential but a power-low temperature dependence with an *n* factor. The expected n value for Kramers ion should be 9 but, as it will be seen during this manuscript, the presence of both acoustic and optical phonons could lead to lower values between 1 and 7.[92]

Table 3. 6. Best fitted parameters for the relaxation mechanism of ***Dy****, considering the Orbach, Raman and QTM.*

Dy	*Δ / K*	*τ_0 / s*	*$C / K^{-n}s^{-1}$*	*n*	*τ_{TI} / s*
H= 0	181	$(1.1 \pm 0.1)\cdot 10^{-9}$	0.11 ± 0.09	4.2 ± 0.3	$(1.7 \pm 0.2)\cdot 10^{-3}$
H= 1 kOe	181		$(8 \pm 2)\cdot 10^{-4}$	5.7 ± 0.1	-

To summarize, at higher temperatures the relaxation is described by a competition of Orbach and Raman, while at lower temperature the QTM is prevailing.

Same description of the relaxation mechanism is then applied to the isotopic analogues. In that case, higher temperatures haven't been measured due to the time-consuming of the experiments and the no additional information that they would provide; as it is well known that neither the field nor the isotopic enrichment contribute to the Orbarch relaxation[85]. Raman contribution is also maintained fixed in a first approximation, in order to simplify the fit and avoid over-parametrization. In Figure 3. 21, the relaxation curves of the different isotopologues are illustrated, thus with the different fits, proving the good accordance with the experimental values.

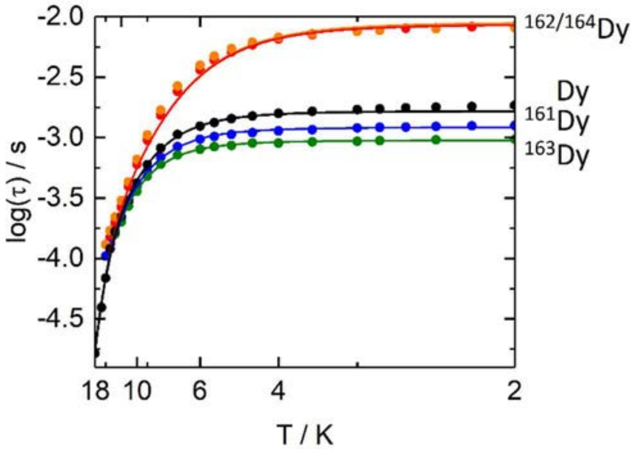

*Figure 3. 21. Arrhenius plot for $^{161\text{-}164}$**Dy** (blue, orange, green and red, respectively) and **Dy** (black) with best-fitted curves in black, taking into account all the contributions of the magnetic relaxation.*

The best fitted parameters applying Equation 3.3 are collected in Table 3.7, evidencing the different relaxation times (τ_{TI}) of the tunneling effect, depending on the isotopologue.

*Table 3. 7. Best fitted parameters for the relaxation mechanism of ^{A}**Dy** series, considering the Orbach (fixed), Raman (fixed) and QTM.*

Compound	*Δ / K*	*τ_0 / s*	*C / K^{-n}s^{-1}*	*n*	*τ_{TI} / s*
Dy	181	$(1.1\pm 0.1)\cdot 10^{-9}$	0.11±0.09	4.2±0.3	$(1.7 \pm 0.2)\cdot 10^{-3}$
^{161}**Dy**					$(1.26 \pm 0.05)\cdot 10^{-3}$
^{162}**Dy**					$(10.4 \pm 1)\cdot 10^{-3}$
^{163}**Dy**					$(0.98 \pm 0.05)\cdot 10^{-3}$
^{164}**Dy**					$(9.8 \pm 0.7)\cdot 10^{-3}$

Once more, $^{162/164}$**Dy** (I=0) isotopes show same parameters in the relaxation rates, coinciding with the slowest relaxation; **Dy** shows 6 times faster τ_{TI}; and the two isotopes with I= 5/2 (^{161}**Dy** and ^{163}**Dy**) display around 10 times faster magnetic relaxation, compared to the nuclear spin free analogues.

In order to complete the study, the different diluted samples need to be taken into account for the new definition of the relaxation, thus having in mind the non-dependence of the Orbach or Raman rates on the small fields coming from the hyperfine interactions. However, C and n parameters can differ from the condensed to the diluted samples, as seen for other systems.[91, 93] This can be explained by the fact that the Y^{3+}-matrix can affect somehow the structure or physical properties, even if those are always neglected at first sight. Considering the difference in the mass number A(Y)= 89 and A(Dy)= 163, perturbations given by Y^{3+} cations in the mechanisms could be justified. To avoid overparametrization and try to find a closest Raman definition, the four relaxation curves for the diluted isotopologues **$^{161-164}$Dy@Y** have been simultaneously fitted with a common Raman and Orbach parameters and different QTM, τ_{TI}, for each.

*Table 3. 8. Best fitted parameters for the relaxation mechanism of ^{A}**Dy** series, considering the Orbach, Raman (fixed) and QTM.*

Compound	Δ / K	τ_0 / s	C / K^{-n}s^{-1}	n	τ_{TI} / s
^{161}Dy@Y	181	(1.1±0.1)·10^{-9}	(3.3±0.3) ·10^{-3}	5.36±0.04	0.31±0.05
^{162}Dy@Y					-
^{163}Dy@Y					0.067±0.006
^{164}Dy@Y					-

As it can be seen in Figure 3. 22, the high temperature regime is well defined but at low temperature we do not have all the information about our system. As a result, the relaxation times given by the fit are not in accordance with the experimental curve, hence providing a faster relaxation QTM for **^{161,163}Dy@Y**.

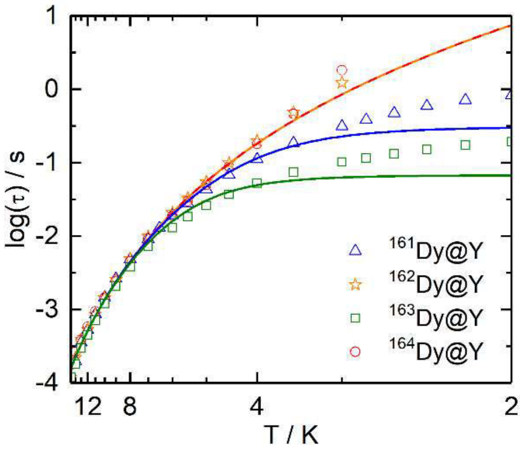

*Figure 3. 22. Arrhenius plot for ^{161}**Dy@Y** (blue), ^{162}**Dy@Y** (orange), ^{163}**Dy@Y** (green) and ^{164}**Dy@Y** (red) with full lines the best-fitted curves under zero magnetic field.*

Different possible explanations could be given in order to rationalize the obtained results, starting from the fact that the independent-regime is not totally achieved and thus, the mathematic fitting could not perfectly reproduce the given data; or that there are other mechanisms which we are not being considered that could, as the Raman, minimize the effective barrier and give rise to another different description, as the transition between off-resonance phonon modes. The last would mean to describe the relaxation as a double exponent Arrhenius curve with two effective barriers.[94]

IV. CONCLUSIONS

Because of its SMM characteristics, Dy(tta)$_3$(**L^2**)·C$_6$H$_{14}$ resulted to be a good starting point for the study of the importance of the inner magnetic field created by inter- (dipolar) and intra- (hyperfine) molecular interactions in the relaxation mechanisms. Diamagnetic dilution and isotopic enrichment was already performed by some people in the group, using two different isotopes (^{161}Dy and ^{164}Dy) out of the four stables isotopes in the nature.

In this chapter, the different results of ^{162}Dy^{3+} and ^{163}Dy^{3+}-based systems, which were published this year,[95]are presented and compared with all the previous work. Indeed, as previously seen from comparison of **^{161}Dy** (I= 5/2) and **^{164}Dy** (I= 0), the nuclear spin-free isotope (**^{162}Dy**) displayed a slower magnetic relaxation in the thermally independent regime compared to the isotope **^{163}Dy** (I= 5/2) due to the cancelling of the hyperfine interactions coming from the metal center. As expected, the two nuclear spin-free **^{162}Dy** and **^{164}Dy** display same behavior through relaxation while a significant difference in the relaxation time of magnetization was observed between **^{161}Dy** and **^{163}Dy** isotopic isomers (both with I = 5/2). At 2 K, the **^{163}Dy** isotope relaxed 1.5 times faster than **^{161}Dy** because of the greater hyperfine coupling caused by the greater coupling constants for the ^{163}Dy, compared with ^{161}Dy. Finally, doping in an isomorph Y^{3+}-matrix the Dy^{3+}-based system, and therefore removing the dipolar magnetic interactions, the effect of the hyperfine coupling constants on the magnetic relaxation is directly observed with **^{163}Dy@Y** which relaxed 300% faster than **^{161}Dy@Y**.

For what concerns the description of the relaxation mechanisms, there are many different ways at present, which try to explain the relaxation process occurring at the low temperature regime. A more exhaustive characterization has been proposed for the present system, by adding the contribution of Raman to our previous studies. Nevertheless, even if the new description of the magnetic relaxation contributes to a better characterization of the system, there is still some events contributing at low temperature which are still not known. Same proposals intending to obtain a more accurate description of the relaxation will be attended during the next chapters of the present manuscript, so that we find common tips for the definition of the relaxation mechanisms.

Future chapters will include the isotopic and dilution study of different lanthanide ion, with a different electronic distribution from Dy (oblate), in order to verify if in prolate systems the evolution of the magnetic properties points to the same direction. Also, systems with different coordination sphere will be presented as by changing the symmetry of the coordination sphere, the electronic distribution around the metal cation does it too and, thus, the stabilization of the M_J sublevels can be different, changing the SMM properties.

REFERENCES:

[73] G. Cosquer, F. Pointillart, S. Golhen, O. Cador, and L. Ouahab, *Chem. Eur. J.*, **2013**, *19*, 7895.

[74] T. T. da Cunha, J. Jung, M.-E. Boulon, G. Campo, F. Pointillart, C. L. M. Pereira, B. Le Guennic, O. Cador, K. Bernot, F. Pineider, S. Golhen, and L. Ouahab*, J. Am. Chem. Soc.* **2013**, *135*, 16332.

[75] F. Pointillart, K. Bernot, S. Golhen, B. Le Guennic, T. Guizouarn, L. Ouahab, and O. Cador, *Angew. Chem.*, **2015**, *127*, 1524.

[76] Y. Kishi, F. Pointillart, B. Lefeuvre, F. Riobé, B. Le Guennic, S. Golhen, O. Cador, O. Maury, H. Fujiwara, and L. Ouahab, *Chem. Commun.*, **2017**, *53*, 3575.

[77] a) N. F. Ramsey, Molecular Beams, Oxford U. P., New York, **1956**; b) W. J. Childs, *Phys. Rev. A*, **1970**, *2(5)*, 169.

[78] a) F. Pointillart, Y. Le Gal, S. Golhen, O. Cador, and L. Ouahab, *Chem. Commun.*, **2009**, 3777; b) F. Pointillart, Y. Le Gal, S. Golhen, O. Cador, and L. Ouahab, *Inorg. Chem.*, **2009**, *48*, 4631.

[79] a) F. Pointillart, Y. Le Gal, S. Golhen, O. Cador, and L. Ouahab, *Chem. Eur. J.,* **2011**, *17*, 10397. b) F. Pointillart, S. Klementieva, V. Kuropatov, Y. Le Gal, S. Golhen, O. Cador, V. Cherkasov, and L. Ouahab, *Chem. Commun.*, **2012**, *48*, 714; c) F. Pointillart, B. Le Guennic, T. Cauchy, S. Golhen, O. Cador, O. Maury, and L. Ouahab, *Inorg. Chem.*, **2013**, *52*, 5978; d) F. Pointillart, B. Le Guennic, S. Golhen, O. Cador, and L. Ouahab, *Chem. Commun.*, **2013**, *49*, 11632; e) J. Jung, T. T. da Cuhna, B. Le Guennic, F. Pointillart, C. L. M. Pereira, J. Luzon, S. Golhen, O. Cador, O. Maury, and L. Ouahab, *Eur. J. Inorg. Chem.*, **2014**, 3888.

[80] a) F. Pointillart, T. Cauchy, O. Maury, Y. Le Gal, S. Golhen, O. Cador, and L. Ouahab, *Chem. Eur. J.*, **2010**, *16*, 11926; b) F. Pointillart, A. Bourdolle, T. Cauchy, O. Maury, Y. Le Gal, S. Golhen, O. Cador, and L. Ouahab, *Inorg. Chem.*, **2012**, *51*, 978; c) A. D'Aléo, F. Pointillart, L. Ouahab, C. Andraud, and O. Maury, *Coord. Chem. Rev.*, **2012**, *256*, 1604; d) F. Pointillart, B. Le Guennic, S. Golhen, O. Cador, O. Maury, and L. Ouahab, *Inorg. Chem.*, **2013**, *52*, 1610; e) G. Cosquer, F. Pointillart, J. Jung, B. Le Guennic, S. Golhen, O. Cador, Y. Guyot, A. Brenier, O. Maury, and L. Ouahab, *Eur. J. Inorg. Chem.*, **2014**, 69.

[81] a) F. Pointillart, B. Le Guennic, S. Golhen, O. Cador, O. Maury, and L. Ouahab, *Chem. Commun.*, **2013**, *49*, 615; b) J.-K. Ou-Yang, N. Saleh, G. Fernandez Garcia, L. Norel, F. Pointillart, T. Guizouarn, O. Cador, F. Totti, L. Ouahab, J. Crassous, and B. Le Guennic, *Chem. Commun.* **2016**, *52*, 14474.

[82] M. Llunell, D. Casanova, J. Cirera, and J. M. Bofill, P. Alemany, S. Alvarez, SHAPE (version 2.1), Barcelona, **2013**.

[83] O. Kahn, *Molecular Magnetism*, VCH, Weinheim, Germany, **1993**.

[84] J. Tang, and P. Zhang, *Lanthanide Single Molecule Magnets*, Springer, Berlin, Heidelberg, **2015**.

[85] R. Orbach, *Proc. Phys. Soc.,* **1961**, *77,* 821s.

[86] P.-E. Car, M. Perfetti, M. Mannini, A. Favre, A. Caneschi, R. Sessoli, *Chem. Commun.*, **2011**, *47*, 3751.

[87] L.T.A. Ho, and L. F. Chibotaru, *Phys. Rev. B,* **2018**, *98*, 174418.

[88] E. Moreno-Pineda, G. Taran, W. Wernsdorfer, and M. Ruben, *Chem. Sci.*, **2019**, *10*, 5138.

[89] N. Ishikawa, M. Sugita, T. Ishikawa, S. Koshihara, and Y. Kaizu, *J. Phys. Chem., B*, **2004**, *108*, 11265.

[90] A. Abragam, and B. Bleaney, *Electron Paramagnetic Resonance of Transition Ions*, Clarendon Press: Oxford, **1970**.

[91] E. Rousset, M. Piccardo, M.E. Boulon, R. W. Gable, A. Soncini, L. Sorace, and C. Boskovic, *Chem. Eur. J.* **2018,** *24(55)*, 14768.

[92] a) A. Singh, and K. N. Shrivastava, *Phys. Status Solidi B,* **1979**, *95*, 273-277; b) K. N. Shirivastava, *Phys. Status Solidi B,* **1983**, *177*, 437.

[93] X. Zhang, S. Liu, V. Vieru, N. Xu, C. Gao, B.W. Wang, W. Shei, L. F. Chibotaru, S. Gao, P. Cheng, and A. K. Powell, *Chem. Eur. J.*, **2018**, *24(23),* 6079.

[94] A. Lunghi, F. Totti, R. Sessoli, and S. Sanvito, *Nat. Commun.¸* **2017**, *8*, 14520.

[95] J. Flores Gonzalez, F. Pointillart, and O. Cador, *Inorg. Chem. Front.*, **2019**, *6*, 1081.

Chapter IV

FROM OBLATE TO PROLATE IONS: Isotopic effect in [Ln(tta)$_3$(L^2)]·C_6H_{14}, with Ln=Yb and Er

---

In the previous chapter, the different contributions to the relaxation mechanism in a mononuclear Dy-based system has been discused. Indeed, special effort has been focused in order to probe the direct contribution of both hyperfine and dipolar interactions in the appearance of an effective relaxation through the so-called barrier, the QTM. By substituting the metal center with their isotopic analogous and by diluting the different samples in a diamagnetic isomorph Y-based matrix, it has been proven not only the importance of the dilution and the suppression of the nuclear spin to the opening of the magnetic hysteresis at zero field, but also the importance of the hyperfine coupling constants for elements with the same nuclear spin number. Until now, this has been demonstrated for a system in which the metal center has an oblate electronic distribution in a N_2O_6 *environment, but there are no sufficient studies in order to confirm a general direction on the evolution of the SMM properties.*

Actually, the electronic distribution of the free metal cation is described in terms of the quadrupole moment of the f-electron charge cloud, which will be split into: prolate (if axially elongated), oblate (equatorially expanded), or isotropic (spherical). Thus, in order to enhance the magnetic anisotropy required to observe the SMM behavior, the greatest crystal fieldas well as the biggest M_J *GS doublets, need to be guaranteed. An easy model for the design of this kind of structures is proposed by J. D. Rinehart and J. R. Long,*[96] *determining the position of the ligand electron density situated so that the less repulsion with the electron cloud is achieved, this meaning: in the axial position for oblate cations, while in the plane for the prolates.*

Ligand $\mathbf{L^2}$ *used in the previous chapter, was constructed so that the* N_2O_6 *pocketfavored an axial distribution because of the greatest electronegativity in the oxygen-side. This distribution is favorable for* Dy^{3+}*, which showed good SMM properties. In this chapter, the same ligand* $\mathbf{L^2}$ *is used in order to observe this environment dependence. Then, two different* *systems are presented, each with a different prolate lanthanide cation: Er^{3+} and Yb^{3+}, where the greatest M_J states show a moderate axial distribution (M_J= 15/2, Er^{3+}) for the first, and a more accentuated one (M_J= 7/2, Yb^{3+}) for the second.*

To summarize, the different strategies are applied in those systems in order to characterize their SMM properties, focusing in the isotopic effect of oblate/ prolate type distribution and the importance of the crystal field. Both systems were subject to EPR studies to explore their applicability as quantum systems (Qudits). Only some results for the Er system were possible, and they are presented in the last part of the chapter.

I. INTRODUCTION

As already mentioned in previous chapters, lanthanides trivalent cations of SMM compounds are extensively studied in order to gain understanding of their behaviors, so we can enhance their magnetic properties. However, very little focus has been plored in other cations other than Dy^{3+} and Tb^{3+}[97], and slightly the less popular Er^{3+}. This quasi-monopoly of the first two ions, can be explained by the fact that Dy and Tb present the larger magnetic moments, which makes it relatively easy to dispose the ligand electron density above and below the flattened surface of the electronic distribution in high coordination environment (the most popular being 8).

In this section, an extensive list of less common Ln-based SMM is presented, containing the different examples of the two most popular prolate cations: ytterbium, because of its extreme axiality in the electron density, and erbium, because of its already mentioned large magnetic moment.

A. *Ytterbium-based SMMs*

To the best of our knowledge, in the literature there are no examples of molecules based on Yb^{3+} displaying good SMM properties, as under zero H_{DC} they do not show slow relaxation of the magnetization. Actually, as depicted in Table 4. 1, the majority of systems are field induced SMM[100-106] or with a maximum of the relaxation at frequencies not experimentally observable[99].

Table 4. 1. Mononuclear Ytterbium SMMs. Table taken from ref. [98].

Yb-SMM	*Δ / cm^{-1}*	*τ_0 / s*	*H / Oe*	*M_J GS^e*	*Ref.*
$K_{13}[Yb(SiW_{11}O_{39})_2]$ (**11**)	-	-	0	±5/2	[99]
$[Yb(H_3$**L^4**$)_2]Cl_3$ (**12**)	4.9^a/ 156.9-187.9^d	$2.0\cdot10^{-5}$	400	±5/2 + ±1/2	[100]
$[Yb(tta)_3($**L^5**$)]$ (**13**)	4.2^a/ 234^b	$1.9\cdot10^{-5}$	1000	±5/2 + ±7/2	[101]
$[N(C_2H_5)_4]_3[Yb($**L^6**$)_3]$ (**14**)	130^b	-	1000	±5/2 + ±7/2	[102]
$Na[Yb$**L^7**$(H_2O)]$ (**15**)	24.3^a/ 197^d	$4.0\cdot10^{-5}$	1000	-	[103]
$[Yb($**L^8**$)_3]$ (**16**)	11^a/ 73^b/20^c	$2.7\cdot10^{-5}$	2000	±5/2 + ±1/2	[104]
$[Yb($**L^9**$)_2]\cdot(NO_3)$ (**17**)	3.7^a	$1.0\cdot10^{-5}$	1000	-	[105]
$[Yb($**L^9**$)(tta)_2]$ (**18**)	11.4^a	$1.8\cdot10^{-5}$	1000	-	[105]
$[Yb($**L^{10}**$)]$ (**19**)	38^a / 464^b/ 463.8^c	$1.5\cdot10^{-5}$	2000	-	[106]

[a] Effective energy barrier determined from ac measurements.
[b] Effective energy barrier determined from luminescence measurements.
[c] Effective energy barrier determined from dc measurements.
[d] Effective energy barrier predicted by ab initio calculations.
[e] When the G.S. M_J value is not given is because it was not determined in the corresponding article.

A possible explanation comes from the shape of the electron density distribution of the different M_J states of ytterbium ion. According to the general model published by J. D. Rinehart and J. R. Long, and as already mentioned, the ytterbium as prolate ion should stabilize its highest M_J states while coordinated to an equatorial ligand. However, while most of the ions show a general progression from the highest to the lowest M_J (from more to less prolate, or *vice versa*), the Yb^{3+} evolution is more complicated. In Figure 4. 1 the different M_J values of the $^2F_{7/2}$ state multiplet are represented, exposing a more varied angular dependence: M_J= ±7/2 state has almost no oblate density, making it clearly the highest energy state, whereas the M_J= ±5/2 is mostly composed of oblate density, with some extending along the z-axis. At the same time, the lower M_J states ±3/2 and ±1/2 have considerable prolate lobes which will enhance interactions with the ligand between those of ±5/2 states and ±7/2 state.[96] As a consequence, even if in theory the ±7/2 should be highly favorable when equatorial coordination environment, the true is that SMM behavior has no yet been well characterized under zero magnetic field. Depicted in Table 4. 1, the ground state description of the different examples shows a combination of different M_J, which for instance can contribute to the transverse components of the anisotropy tensor which afford to a fast relaxation.

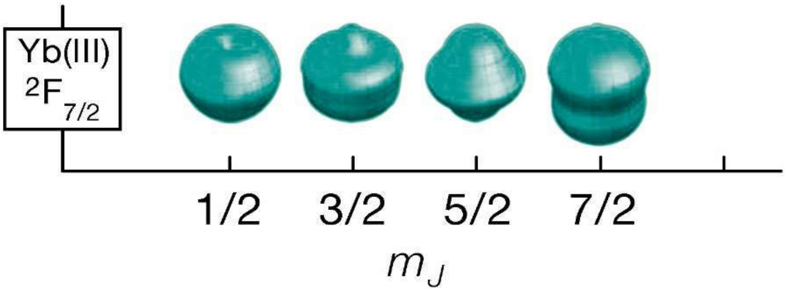

Figure 4. 1. Approximation of the angular dependence of the 4f charge density distribution for different m_J states composing the lowest spin-orbit coupled (J) state for Yb^{3+}. [96]

Following the order in Table 4. 1, the first examples to be described are those with a full oxygenated coordination environment (Compounds **11** to **13**), followed by those which coordination sphere is constituted by a mixture of both N and O atoms (Compounds **14** to **19**), which will be closer to the one presented in the following pages.

The first Yb-based (**11**, Figure 4.2) complex surrounded entirely by O, was published in 2009 by AlDamen *et al.*[99], and resulted from the encapsulation of the Yb^{3+} ion between two monolacunary polyoxometallate (POM) β-[SiW$_{11}$O$_{40}$]$^{-4}$ anions, and a surrounding network of water molecules and K$^+$ for the balance of charge. These POM moieties acted as tetradentate ligands, creating a CF symmetry of pseudo-D$_{4d}$ around the metal. A full study of the ligand field determined that the stabilized m_J doublet corresponded to ±5/2 with a separation of 100 cm^{-1} from the ± 7/2 first ES. This splitting description made possible a frequency dependence behavior for temperatures below 10 K. Published results mentioned the appearance of a shoulder at high frequencies and a divergence in the χ_M'' at lower temperatures. However, no maximum was observed and as a consequence no further ac characterization was done.

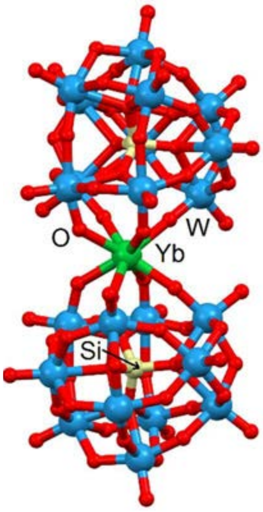

*Figure 4. 2. Molecular structure of **11**.Potassium cations, water molecules of crystallization and hydrogen atoms are omitted for clarity. From Ref. [98].*

Later, in 2012 a six-coordinated Yb- complex (**12,** Figure 4. 3) was reported by Liu *et al.* based on **H$_3$L^4**= tris(((2-hydroxy-3-methoxybenzyl)amino)ethyl)amine as ligand. This

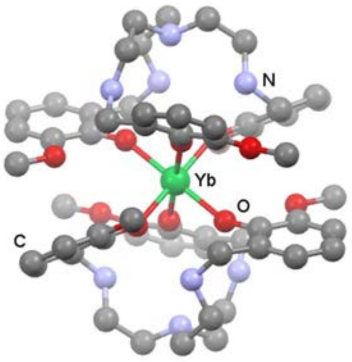

*Figure 4. 3. Molecular structure of **12**. Anions, solvent molecules of crystallization and hydrogen atoms have been omitted for clarity. Adapted from Ref. [100].*

was produced by *in-situ* condensation and reduction of *o*-vanillin, tris(2-aminoethyl)amine and NaBH$_4$.[100] The resulted symmetry adopted for the O$_6$ environment was trigonally distorted octahedron. In this system, magnetic measurements and ab initio calculations were used to characterize the SMM behavior. No out-of-phase component of the magnetic susceptibility was observed under zero magnetic field. This was explained because of the strong admixture of different M$_J$ found in the ground Kramers doublet, which results to large transversal g-factors that enhance an efficient QTM at zero field. As a result, this system was defined as a molecule showing field-induced blockage of the magnetization with an optimal field of 400 Oe. The relaxation mechanism at that field was formulated as: $\tau^{-1} = AT + BT^n + Cexp(-\Delta / k_B T)$,[107,108,109] the three terms refer to the direct, the Raman, and the Orbach process, respectively. However, due to a large divergence between experimental and calculated energy barrier, they suggested the admixture of only two types of spin-lattice interaction mechanisms, being the single-phonon direct process and the optical-acoustic Raman-like process with an n exponent of 2.37(4).

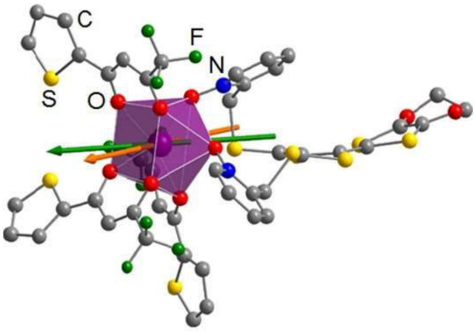

*Figure 4. 4. Molecular structure of **13** with experimental (orange) and theoretical (green) anisotropy axis. Adapted from Ref. [101].*

Compound **13** combines a redox-activity with metal-centered luminescence and SMM behavior.[101] Here, the two pyridine-N- oxide arms of a TTF-based ligand **L^5**= 4,5-ethylendioxy-4’,5’-bis(2-pyridyl-N-oxidemethylthio)tetrathiafulvalene are coordinate to the [Yb(tta)$_3$]·2H$_2$O precursor (Figure 4. 4). This turns into an octa-coordinated oxygen sphere around the Yb with a distorted square antiprism D$_{4d}$ symmetry. **3** crystallized in the triclinic P-1 space group allowing the experimental determination of the magnetic anisotropy axis which was compared to the calculated one. Indeed, this is not a common procedure but the magnetic anisotropy is mainly studied from a theoretical point of view, which may lead to important misinterpretation.[110] As a result, both orientations were in agreement with a difference of only 12°, signaling an Ising character of the anisotropy with slight transverse contributions. Ab initio calculations determined well separated GS and first ES multiplets (234 cm^{-1}) but being the GS a combination of ±5/2 and ±7/2. Hence, the molecule shows SMM behavior only when the QTM coming from the admixture of different states is suppressed (1 kOe). The thermal dependence of the relaxation was defined by an exponential dependence with the temperature, giving rise to an energy barrier of 4.2 cm^{-1}. This energy barrier is much lower than the value determined from ab initio calculations or from the luminescence spectrum, which can be viewed as a photography of the energy splitting of the $^2F_{7/2}$ multiplet ground-state. The significant difference of energy barrier determined from the ac measurements with respect to luminescence and calculations seems to suggest that the Orbach process can be discarded from the relaxation mechanism, as happened with the previous system **12**.

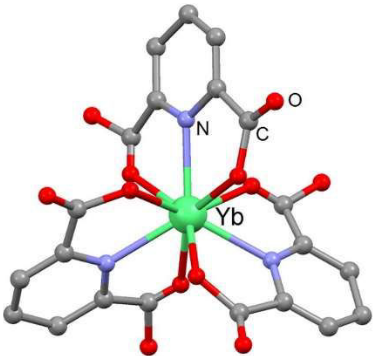

Figure 4. 5. Molecular structure of **14**. The tetraethylamonium cations and hydrogen atoms are omitted for clarity. Adapted from Ref. [102].

Until now, the different coordination sphere of the Yb^{3+} was formed by oxygen atoms. However, there are other examples reported in literature that include the combination of oxygen and nitrogen atoms. Actually, the first Yb-based molecule showing a slow relaxation of the magnetization was published in 2006 by Sugita *et al.,*[102] this with a N$_3$O$_6$ environment. Tris(dipicolinato)ytterbium with formula [N(C$_2$H$_5$)$_4$]$_3$[Yb(**L^3**)$_3$]·2H$_2$O (**14**·2H$_2$O**,** Figure 4. 5) (where **L^6** = pyridine-2,6-dicarboxylate) possesses a trigonal (D$_3$) symmetry around the metal center. The system displayed out-of-phase signal of the magnetic susceptibility by applying H_{DC}= 1000 Oe below 7 K. The characterization of the LF interactions leaded to the constitution of the ground-state multiplet which is mainly composed of M_J= ±5/2, and separated from the first ES of 130 cm^{-1}. This energy barrier was estimated to be one order of magnitude higher from their Er^{3+} or Dy^{3+} analogues, however no sign of delay in the relaxation of the magnetization was shown.

Complex **15** (Figure 4. 6) is included in the DOTA-based lanthanide complexes (DOTA expressed as **L**^{7}=1,4,7,10-tetraazacyclododecane-1,4,7,10-tetraacetic), which are of great importance because of their luminescent properties.[111] The magnetic study of the lanthanide series, among them $Na[Yb\mathbf{L^7}(H_2O)]\cdot 4H_2O$ (**15**), are reported by Boulon *et al.*. A proposal was set consisting in the correlation between the orientation of the easy axes of the magnetization with the prolate/oblate electronic density distribution of the 4f ion and the ligand geometry, even if the coordination of water molecules was enough to drastically change this orientation.[103] In the present example, Yb^{3+} is coordinated to 4O and 4N in a capped square antiprism environment, concentrating the negative charges of the ligand in the equatorial plane. The g-tensor was settled experimentally and theoretically, confirming the easy anisotropy along the axial direction, expected because of the ligand field charge distribution. By applying an optimal magnetic field of 1000 Oe, compound **5** behaves as a SMM with exponential dependence at high temperatures with Δ=35(2) cm^{-1} (Orbach) and an alternative mechanism depending on T^n, with n= 1.2(1) (Raman). Ab initio calculations performed on this system gave an energy barrier of 197 cm^{-1} which is much higher than the value determined from the ac measurements probably due to transverse components of the crystal field which allow efficient under-barrier mechanisms of relaxation.

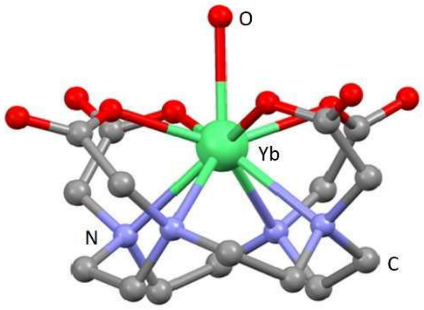

*Figure 4. 6. Molecular structure of **15**. Water molecules of crystallization, hydrogen atoms and sodium cations are omitted for clarity. Adapted from ref. [103].[98]*

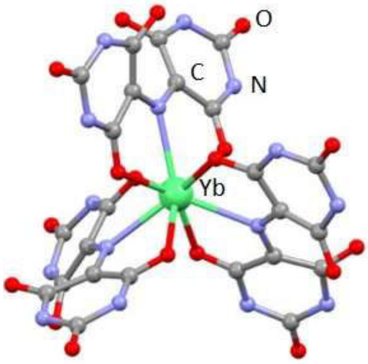

*Figure 4. 7. Molecular structure of **16**. Solvent molecules and H-atoms were omitted for clarity. Adapted from Ref. [104].*

On the same idea of correlating different physical properties, complex **16** was published by Yi *et al.*, thus showing magnetic and photophysical properties.[104] $[Yb(\mathbf{L^8})_3]\cdot 11H_2O$ (**16**$\cdot 11H_2O$**,** Figure 4. 7) with murexide as ligand **L**^{8}= 2,6-dioxo-5-[2,4,6-trioxo-5-hexahydropyridinylidene)amino]-3H-pyrimidin-4-olate is formed by the coordination of three tridentate anionic murexide. The resulted 9-coordianted Yb^{3+} can be seen as analogous of **14** because of the same N_3O_6 environment.

The symmetry surrounded the metal ion was described by point charges and reported as D_{3h}. Indeed, the oxygens being more negative are closer to the Yb^{3+} than the respective N-atoms. Considering this coordination symmetry, the GS is composed mainly of M_J = ±5/2 doublet and the first ES lies at 20 cm^{-1}. Concerning the dynamic properties, field induced SMM properties were displayed by applying the optimal magnetic field of 2 kOe with an energy barrier of 11 cm^{-1}, and a temperature dependence deviating from the exponent at lower temperatures.

Yb-compounds **17** and **18** (Figure 4. 8) were synthesized with a green light rhodamine donor as a ligand, in order to ensure the efficient near-infrared (NIR) emission.[112] A step further on the characterization of these components was performed in 2015, by studying the magnetic properties.[105] Unlike previous examples, the coordination number of **17** and **18** is 8 instead of 9, which is actually, the more common number of coordination for the Yb^{3+} ion. Both complexes contain the same ligand **L^9** = hodamine-6G-2-(hydrozinomethyl) quinolin-8-ol, but in different stoichiometric proportion with the ytterbium cation. Indeed, two different anionic precursors of ytterbium, each with different chelating strength, were used in order to favor a 1:1 or 1:2 ratio. For the first, a weak chelating nitrate favored a 1:2 ratio forming complex **17**·CH_3OH·$0.5H_2O$ ([Yb(**L^9**)$_2$](NO_3)CH_3OH·$0.5H_2O$, whereas the stronger tta$^-$ anion led to the formation of **18**·CH_3OH complex, with a 1:1 ratio [Yb(**L^9**)(tta)$_2$]CH_3OH. As a result, coordination spheres of O_4N_4 and O_6N_2 environments for **17** and **18** were obtained, respectively. Despite the different environments, the Ising character of the magnetic anisotropy was confirmed for both by EPR and DC magnetic measurements. Finally, under an intermediate field of 1 kOe, **17** and **18** display SMM behavior with energy barriers of 3.7 and 11.4 cm^{-1}, respectively.

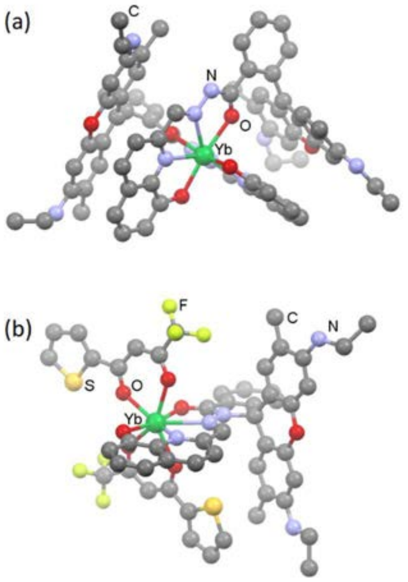

*Figure 4. 8. Molecular structure of (a) **17** and (b) **18**. Solvent molecules and H-atoms were omitted for clarity. Adapted from Ref. [105].*

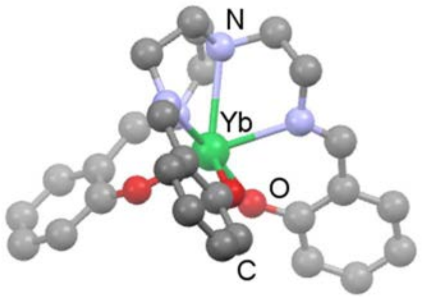

Figure 4. 9. Molecular structure of ***19.*** *Hydrogen atoms are omitted for clarity. Adapted from Ref. [106].*

Finally, Pedersen *et al.*,[106] exposed the existent problematic of determining the composition of the GS multiplet as well as the difference in energy with the first excited multiplet, by means of Stevens operator (dc data), ac data, ab initio calculations or luminescence spectra; and at the same time he proposed the absorption spectroscopy as an adequate spectroscopic technique for the characterization of the compound. While during emission the number of lines can vary because of possible participation of the excited multiplet states, from absorption data we can obtain a clear picture of the energy splitting of the multiplet excited-state. Compound **19**, [Yb(**L^{10}**)] (where **L^{10}** = 2,2',2"-tris(salicylideneimino)trimethylamine), is an Yb derivative of the trigonal lanthanide-trensal series for which the ligand field parameters was recently reported by Riley and co-workers,[113] and the magnetic properties by Sorace, Dreiser, Sessoli and they co-workers.[114,115,116] The X-ray structure of **19** revealed an Yb^{3+} ion in a N$_4$O$_3$ coordination environment as it can be seen in Figure 4. 9. Combination of emission (5 K) and absorption (10 K) studies turned into a complete description of the energy splitting of both the $^2F_{7/2}$ multiplet ground-state and $^2F_{5/2}$ multiplet excited-state. An energy barrier value of 464 cm^{-1} was extracted from the spectroscopic measurements and the axial behavior of the magnetic anisotropy was confirmed by EPR. A full study of the dynamic properties was performed as a function of both the temperature and the magnetic field, thus obtaining a field-induced SMM under an applied H$_{DC}$ of 2 kOe. In conclusion, the relaxation of the magnetization of **19** is governed by Raman, direct and QTM processes while the Orbach relaxation mechanism is not important for the description.

B. *Erbium-based SMMs*

Among the different prolate ions, Er^{3+} is especially attractive for its applicability in molecular magnetism, since it presents high magnetic moment and the possibility of high M$_J$ values. As seen in Figure 4. 10 depending on the location of the electron density coming from the ligand field, one or another GS multiplet will be stabilized first.

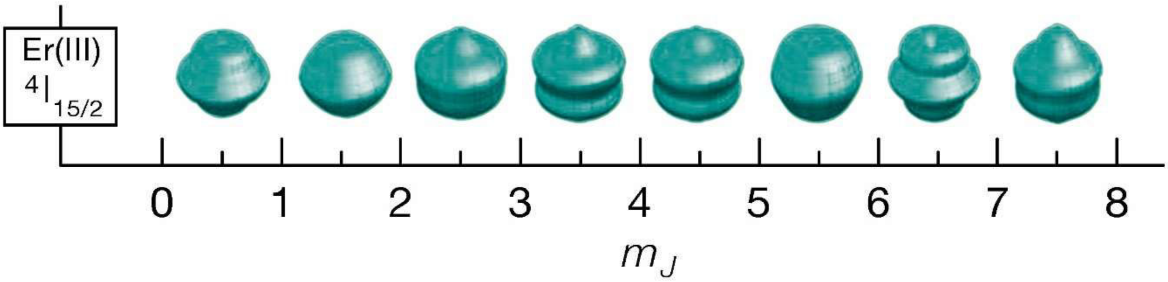

Figure 4. 10. Approximation of the angular dependence of the 4f charge density distribution different m_J states composing the lowest spin-orbit coupled (J) state for Yb^{3+}.[96]

Thus, by forming a LF distribution around the axe in the equatorial plane, as for the ytterbium, an easy-axis of the anisotropy will be enhanced. This strategy has been followed by different researchers to obtain a mononuclear Er^{3+}-SMM, and the most important examples are presented in Table 4. 2.

Table 4. 2. Mononuclear Erbium SMMs under zero magnetic field.

Er-SMM	Δ / K *	τ_0 / s	M_J GS	Ref.
$Na_9[Er(W_{10}O_{36})]$ (**20**)	55.2	$1.6\cdot10^{-8}$	±13/2	[118]
$[Er(\mathbf{L^{11}})(\mathbf{L^{12}})]$ (**21**)	197 / 323	$3.13\cdot10^{-9}$ /$8.17\cdot10^{-11}$	±15/2	[119]
$[K(18\text{-c-}6)][Er(\mathbf{L^{12}})_2]$ (**22**)	147	$8.3\cdot10^{-8}$	±15/2	[121]
$[K(18\text{-c-}6)(THF)_2][Er(\mathbf{L^{12}})_2]$ (**23**)	150	$6.9\cdot10^{-8}$	±15/2	[121]
$[Li(DME)_3][Er(\mathbf{L^{13}}_2]$ (**24**)	187	$4.0\cdot10^{-8}$	±15/2	[122]
$Er[\mathbf{L^{14}}]_3$ (**25**)	122	$9.33\cdot10^{-9}$	±15/2	[126]
$[Li(THF)_4][Er(\mathbf{L^{14}})_3Cl]$ (**26**)	63.3	$1.07\cdot10^{-7}$	±15/2	[127]
$[Er(\mathbf{L^{14}})_3Cl][Li(THF)_3]$ (**27**)	70.5	$4.48\cdot10^{-7}$	±15/2	
$[Er(\mathbf{L^{14'}})_3]$ (**28**)	55.7	$1.37\cdot10^{-6}$	±15/2	[129]
$[Er(\mathbf{L^{14''}})_3]$ (**29**)	114.5	$9.52\cdot10^{-8}$	±15/2	[129]
* Effective energy barrier determined from ac measurements.				

The substitution of the metal center in the famous series reported by Ishikawa[117], in which a “double decker” structure of the bis(phthalocyanine) lanthanide showed SMM properties for Dy^{3+} and Tb^{3+}, didn’t stabilized the greatest M_J for the trivalent erbium. However, if a compression in the axial directions was achieved, thus concentrating the electronic density in the plane, this geometrical strategy could work. Indeed, AlDamen *et al.* saw in POMs the possibility of creating similar structures with the characteristics needed, so that the problem of equatorial LF density was solved and could give rise to

SMM behavior.[118] Na$_9$[Er(W$_{10}$O$_{36}$)] (**20,** Figure 4. 11) consists of an Er^{3+} encapsulated by two monolacunary POM moieties of [W$_5$O$_{18}$]$^{6-}$. This ionic complex is surrounded by a framework of water molecules and Na$^+$ cations for the balance of charge. The eightly- coordination sphere entirely oxygenated creates a square antiprismatic (D$_{4d}$) geometry around the metal, which is expected to give a high m$_J$ description of the GS and thus an easy axis of the anisotropy. Using the susceptibility data, they determined a GS ±13/2 multiplet not far from the ±1/2 and ±15/2 ES which were separated by energies of 3 and 18 cm^{-1}, respectively, but by 100 cm^{-1} from the rest. The ac measurements, showed frequency-dependence under zero magnetic field for temperatures up to 7.5 K and the relaxation mechanism as characterized by the contribution of a thermally activated region with an energy barrier of 55.2 K, and QTM at the lowest temperatures.

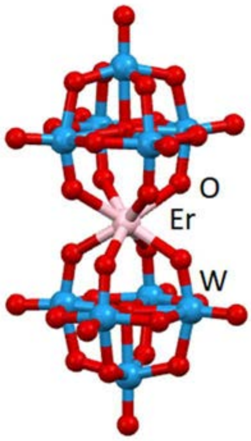

*Figure 4. 11. Molecular structure of **20.** The Na$^+$-water framework is omitted for clarity. Adapted from Ref. [99].*

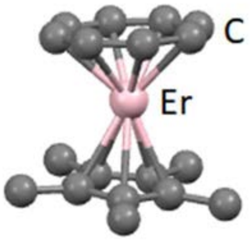

*Figure 4. 12. Molecular structure of **21**. Hydrogen atoms are omitted for clarity. Adapted from Ref. [119].*

With the same idea of "double decker" structure, Jiang *et al.* prepared the first Er^{3+}-organometallic based complex displaying SMM behavior. [Er(**L^{11}**)(**L^{12}**)] (**21**, Figure 4.12) consists in the coordination of the Er^{3+} by between two different ligands: **L^{11}**= pentamethylcyclopentadienide and **L^{12}**= cyclooctatetraenide.[119] Strictly speaking, the overall symmetry of the molecule is C$_S$, but after some symmetry assumptions, the local symmetry of the Er^{3+} ion can be approximated to $C_{\infty v}$, and thus by fitting the susceptibility data, one can obtain information about the GS composition and the Ising character of the magnetization. In this way, the GS was determined to be ±15/2, typical Ising-type GS, well separated from the 1st ES ±13/2. Two different conformers in the crystal structure lead to two different peaks in the out-of-phase component of the susceptibility bellow 25 K for **21**, consistent with the presence of two different relaxation processes with energy barriers of 197 and 323 K, respectively. Moreover, the system displayed butterfly hysteresis loop up to 5 K. Further characterization by Boulon *et al.* using angular magnetometry and ab initio calculations verified the nature of the energy splitting of $^4I_{15/2}$.[120]

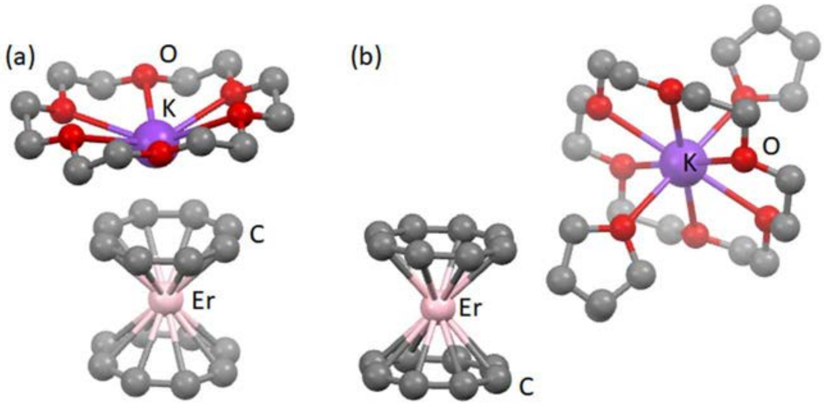

*Figure 4. 13. Molecular structure of a) **22** and b) **23**. Hydrogen atoms are omitted for clarity, as well as two THF molecules in **22**. Adapted from Ref. [121].*

More recently, homoleptic cyclooctatetraenide [Er(**L^{12}**)$_2$]$^-$ compounds (**22** and **23**, in Figure 4. 13) have been studied by Meihaus *et al.* under the assumption that its more equatorial CF symmetry, would enhance the slow magnetic relaxation properties.[121] Effectively, both compounds **22** with [K(18-crown-6)]$^+$ and **23** with [K(18-crown-6)(THF)$_2$]$^+$ exhibit slow magnetic relaxation under zero magnetic field and energy barriers of around 150 cm^{-1}, and a butterfly shaped hysteresis. While in the bulk the QTM process is evidenced, through dilution in a diamagnetic matrix using Y^{3+} causes this phenomenon to be quenched, thus resulting in an open hysteresis loop up to 10 K.

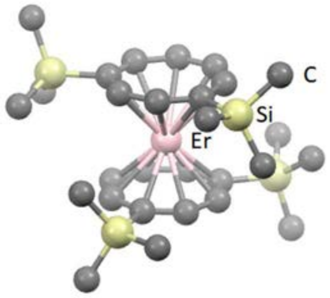

*Figure 4. 14. Molecular structure of **24**. Hydrogen atoms and Li(DME)$_3$ counter ions are omitted for clarity. Adapted from Ref. [122].*

Le Roy *et al.* took this “sandwich” type complex and added some substituents to **L^{12}** in order to study the evolution of the magnetic properties by lowering the symmetry around the metal.[122] In **24** (Figure 4. 14), the Er^{3+} cation was coordinated to two **L^{13}**= 1,4-bis(trimethylsilyl)cyclooctatetraenyl dianion, and the SMM properties were enhanced: the system presented an energy barrier of 187 K and hysteresis loop of the magnetization up to 8 K. Through solubilization of the compound, the energy barrier was drastically increased up to 335 K and the hysteresis was observable until 14 K.[123]

As observed, the most extensively used strategy to reach an equatorial CF density, has been the use of the so-called “sandwich” type encapsulation of the lanthanide, thus with compressed distances between both coordination planes in order to enhance the electronic density within the two ligand moieties. Instead, an equatorially coordinated geometry is predicted to be preferable for Er^{3+} which was not a very popular method owing to the high coordination number of the lanthanides ions. So far, there has been some examples reported in the literature with only equatorially coordinated ligands, some of them presenting good SMM properties and thus mentioned here.[124,125,126,127,128,129]

In 2014, Zhang *et al.* proposed the study of a low-coordinated lanthanide [Ln(**L^{14}**)$_3$] complex with **L^{14}**= Bis(trimethylsilyl)amide and Ln= Dy^{3+} and Er^{3+}, which to the best of our knowledge, resulted to be the first compound equatorially coordinated displaying SMM properties. [126] The metal in $Er[N(SiMe_3)_2]_3$ (**25**, Figure 4. 16) is coordinated by three N atoms forming a flat trigonal pyramid leading to an effective LF of C_{3v} symmetry. Such geometry of the full architecture around the Er^{3+}, minimizes the repulsion with the axially located f-element electron density, stabilizing the greatest M_J value of ±15/2. Dynamic measurements from 4 to 15 K gave rise to frequency dependence with relaxation times too slow under 4 K in order to be treated. The relaxation mechanism didn't show any QTM behavior, as expected for such a geometry, but it did present some deviation from the expected thermally activated behavior given by possible Raman or weak QTM. At high temperature, the effective barrier is 122 K (85 cm^{-1}), which is in agreement with the energy separation (82 cm^{-1}) between the first ES and the GS determined by the simulation of crystal field splitting.

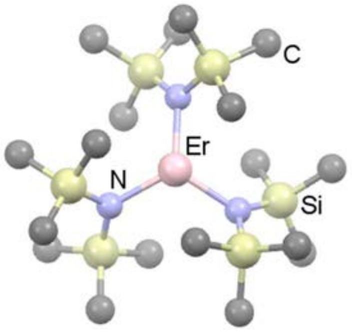

*Figure 4. 16. Molecular structure of **25**. Hydrogen atoms are omitted for clarity . Adapted from Ref.[126b].*

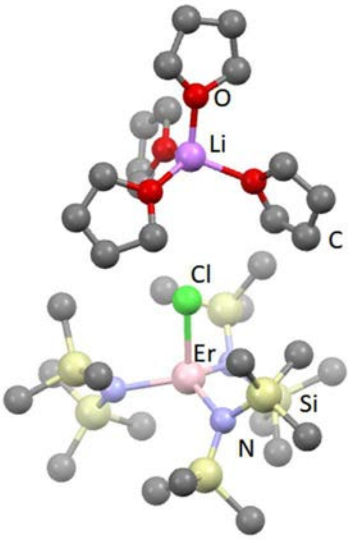

*Figure 4. 15. Molecular structure of **26**. Hydrogen atoms are omitted for clarity. Adapted from Ref. [127].*

One year later, a slightly different structure of the trigonal-pyramidal coordinated erbium (**25**) was reported by Brown *et al.*, containing a chloride anion in the axial position of [Li(THF)$_4$][Er(**L^{14}**)Cl] (**26**, Figure 4. 15).[127] Like the precedent example, the system displayed SMM behavior in the absence of zero H_{DC} with an effective barrier of 63 K, lower than that of **25** because of the moderate destruction of the equatorial geometry due to the chloride ion.

The same magnetic architecture changing the counter-ion part leads to compound **27**(Figure 4. 17), published by Zhang *et al.* in 2016.[128] In this compound, a Li(THF)$_3^+$ ion bounds to Cl$^-$ thus joining both moieties, forming an angle of 180° between Er-Cl-Li. The coordination between both, from the electrostatic point of view, was reported to be simply a balance of the negative charge of the Cl$^-$; and as a result, the equatorially coordinating ligand field found in **26** is still assured. Concerning the magnetic properties, the relaxation mechanism is really close to the previous one, with an energy barrier of 70 K.

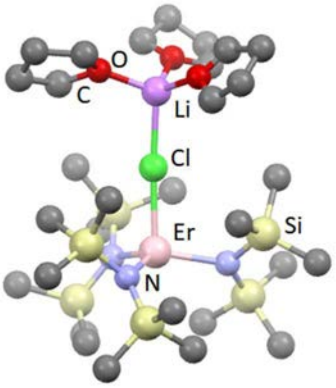

*Figure 4. 17. Molecular structure of **27**. Hydrogen atoms are omitted for clarity . Adapted from Ref. [128].*

By adding small changes in the ligand, compounds (**28**) [Er(**L$^{14'}$**)$_3$] (**L$^{14'}$**= 2,6-di-*tert*-butyl-*p*-cresolate) and (**29**) Er(**L$^{14''}$**)$_3$ (**L$^{14''}$**= bis(trimethylsilyl)methyl) have been studied by Zhang *et al.*(Figure 4. 18).[129] The modified ligands lead to an O- coordinated (**28**) and a C- coordinated (**29**) erbium, both in the C_{3v} geometry, and both displaying SMM properties. In **28** the "hard" oxygen donor contributes to a minimization of the energy barrier (55.7 K) because of the electronic density delocalized on the aromatic rings. On the other hand, in **28** a deviation of the Er^{3+} from the C-coordinated plane minimizes the axial- CF contribution so that the energy barrier remains of 114.5 K, as for **29**. Finally, the deviations from the plane caused by the changes in the ligands result in an efficient QTM below 4 K.

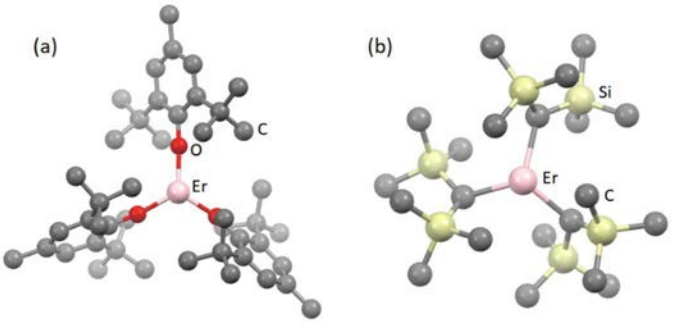

*Figure 4. 18. Molecular structure of **28** (a) and **29** (b). Hydrogen atoms are omitted for clarity . Adapted from Ref. [129].*

So far, after seen the main complexes based on Yb^{3+} and Er^{3+} cations which are reported in the literature, it has been evidenced the different evolution between the two. While there is a lack of Yb-based molecules behaving as SMM under zero DC magnetic field, the Er- SMM molecules are being reported since 2011 without further need of H_{DC}. If we remember from previous chapter, the sensibility of quantum events, or in other words the hyperfine and dipole interaction effects, through any type of magnetic field, it is apparent the need of finding a new SMM system not induced by the last.

In order to study the influence of the environment through the different 4f-electron density of the metal center, as well as the direction in the evolution of the SMM properties of the Er/Yb while dilution/ isotopic enrichment, the same coordination sphere need to be guaranteed. For that reason, even if for the Er-compound there are many examples in the literature that could be taken, it has been preferred to study at first the same molecular structure as **Dy** in Chapter III.

II. RESULTS AND DISCUSSIONS

A. *General structural description*

All ^{A}Yb(tta)$_3$(**L^2**)]·C$_6$H$_{14}$ and ^{A}Er(tta)$_3$(**L^2**)]·C$_6$H$_{14}$ compounds (A= isotopic number, tta$^-$=2-thenoyltrifluoroacetylacetonate and **L^2** = 2-{[2-methylpyridiyl]-4,5-[4,5-bis(propylthio)-tetrathiafulvalenyl]-1H-benzimidazol-2-yl}pyridine) (from here after ^{A}**Yb** and ^{A}**Er**, respectively) presented in this chapter crystallize in the triclinic P-1 (N°2) space group (Annex 1, tables A1.2 and A1.3) and they are isostructural to the Dy[130,131] analogue, discussed in the previous chapter.

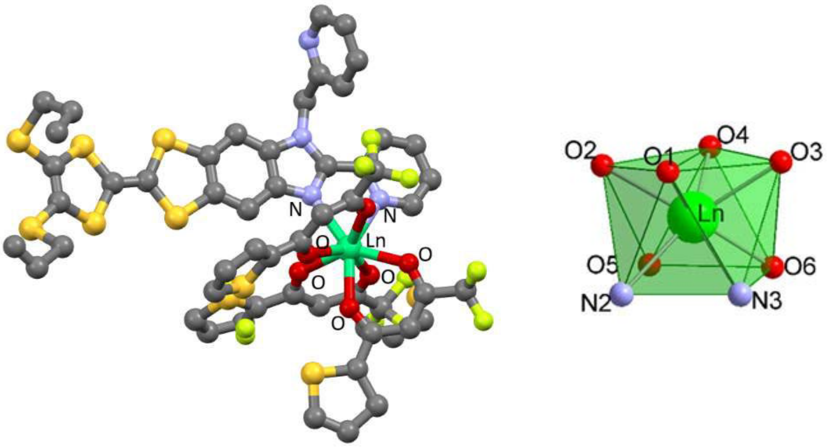

*Figure 4. 19. Right: Molecular structure of **Er**. Hydrogen atoms and solvent molecules are removed for clarity. Ln refers to both cations used in this chapter Er^{3+} and Yb^{3+}. Left: Coordination environment of Ln= Er1 and Yb1, polyhedral used for SHAPE analysis.*

The X-Ray structure is remembered in Figure 4. 19, with the Ln^{3+} cation eight coordinated to a N$_2$O$_6$ environment. The symmetry of this coordination sphere is found by Shape analysis[132], resulting in a distorted-square-antiprism (D$_{4d}$ symmetry, Table 4. 3). In the packing, the shortest Ln-Ln distance is of 9.46 Å and 9.76 Å for Yb-Yb and Er-Er respectively, distances considered enough in order to be considered as isolated molecules.

*Table 4. 3. First three closest symmetries for the **Yb** and **Er** coordination environment.*

Ln-N$_2$O$_6$	*CShM$_{SAPR-8}$ (square antiprism D$_{4d}$)*	*CShM$_{TDD-8}$ (triangular dodecahedron D$_{2d}$)*	*CShM$_{BTPR-8}$ (biaugmented trigonal prism C$_{2v}$)*
Yb	0.440	2.219	2.334
Er	0.478	2.310	2.358

The diluted compounds are obtained by solubilizing the Y(tta)$_3$·2H$_2$O together with the Ln(tta)$_3$·2H$_2$O and the ligand (**L^2**) in the same CH$_2$Cl$_2$ solution. The unit cell was collected by X-Ray Diffraction (XRD) (Annex 1, Tables A1.2-A1.3) in order to confirm that the structure was not changed and the ratio Yb$_X$Y$_{1-X}$ and Er$_X$Y$_{1-X}$ with (x= 5%) for the different diluted compounds have been verified by EDS analysis (Annex 2, Figure A2.2 and A2.3): ^{174}Yb$_X$Y$_{1-X}$: (x= 10 ± 1%), ^{173}Yb$_X$Y$_{1-X}$: (x = 6.6 ± 0.7 %) and Yb$_X$Y$_{1-X}$: (x$_1$= 9.1 ±0.6%), ^{166}Er$_X$Y$_{1-X}$: (x= 3.8 ± 0.5 %) and ^{167}Er$_X$Y$_{1-X}$: (x= 2.3 ± 0.4%).

B. *Yb- based complex:*

B.1. *Magnetic properties of the condensed phase*

SMM properties of [Yb(tta)$_3$(**L^2**)], here after referred as **Yb**, had been previously studied by the group and compared to those of the analogue **Dy**, discussed in the previous chapter. No out-of-phase component of the magnetic susceptibility was obtained for this system in zero external field and the results were rationalized by taking the results from angular-resolved magnetometry, luminescence, and ab initio calculations. [131]

DC magnetometry has been performed from 2 to 300 K (Figure 4.20). At high temperature, the $\chi_M T$ product for an isolated Yb^{3+}: [Xe]4f^{13} with an $^2F_{7/2}$ multiplet ground state and g_J= 8/7, is expected to be 2.57 cm^3 K mol^{-1} which is in agreement with the observed value of 2.33 cm^3 K mol^{-1} at room temperature.[133] Then, on cooling, the curve decreases monotonically to reach 1.28 cm^3 K mol^{-1} at 2 K, because of the depopulation of the ligand-field levels that are constituted of linear combinations of M$_J$ components of the total kinetic moment depending on the site symmetry. At 2 K, the magnetization curve reaches 1.65 Nβ at 50 kOe (Figure 4. 20).

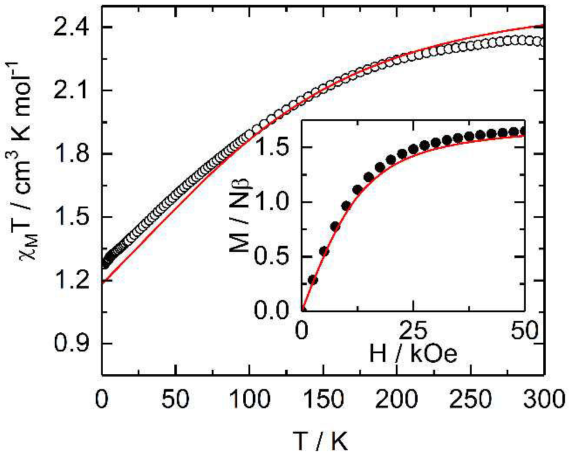

Figure 4. 20. Thermal variation of $\chi_M T$ of ***Yb*** *(empty circles) with the red curve simulated on the basis of SA-CASSCF/MS-CASPT2/RASSI-SO calculations. Inset: field variation of the magnetization at 2 K with the simulated curve in red obtained at the same level of calculation.*

No out-of-phase component of the susceptibility was observed for **Yb** even at the lowest temperatures. Consequently, a study of the ac susceptibility under different H_{DC} (from 0 to 3 kOe) has been performed and information about the relaxation mechanism governing this molecular entity was obtained by applying the extended Debye model. A small magnetic field of 200 Oe is enough to enhance a frequency dependence in the studied windows as it can be observed in the (χ_M',χ_M'') vs. ν plots, in Figure 4. 21. However, and as represented by the increasing radii of the dots in the τ vs. H curve, the system is not entirely relaxing at this field, but only a 43 % of the magnetization does. The relaxation portion increases with the applied magnetic field up to reaching the 100 % of the signal at 600 Oe. This information can be extracted from the difference between the susceptibilities at the limits of the low (χ_T, isothermic) and high (χ_S, adiabatic) frequency: $\frac{\chi_T - \chi_S}{\chi_T}$ (Annex 3, table A3.8).

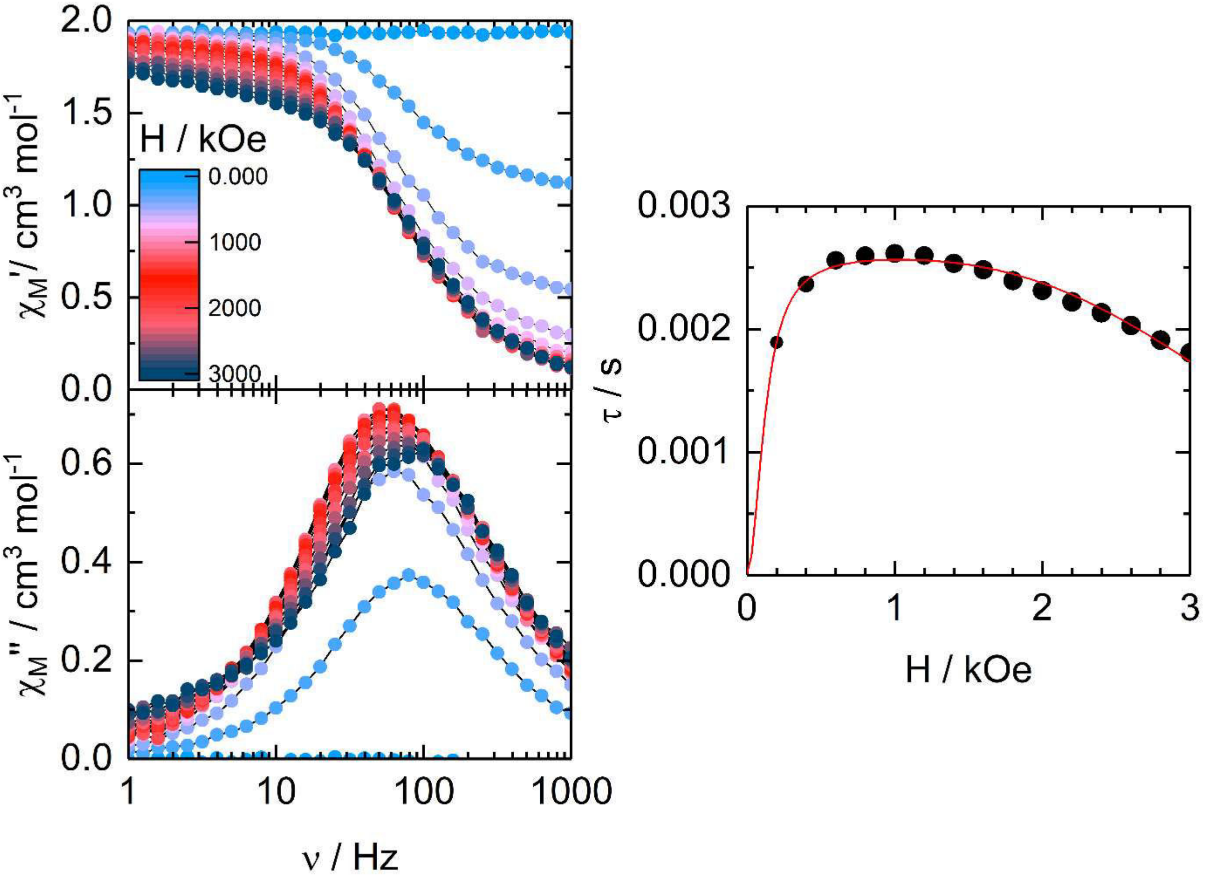

*Figure 4. 21. Left) ac susceptibility curves from 0 to 3 kOe at 2 K of **Yb**. Right) Magnetic field dependence of the Relaxation of the magnetization. Best fitted curve in red. Dot size mapped as a function of the portion relaxing of the sample ranging from the 43 % to the 100 %.*

If we come back to the τ *vs. H* representation, three different regions can be defined: first, from 0 to 800 Oe, the relaxation time increases with the field leading to a suppression of the QTM pathway; then, from 800 to 1200 Oe, where τ is field independent, demonstrating that the optimal H$_{DC}$ is reached and that a new phenomenon shortcutting the barrier is appeared resulting to a balance with the suppression of the tunneling; finally, for higher magnetic fields, the contribution of the last (direct process) is the more and more predominant, inducing the fasten of the magnetic relaxation. This behavior can be modeled by the expression:[134,135]

$$\tau^{-1} = \frac{B_1}{1+B_2H^2} + 2B_3H^m + B_4 \quad (4.1)$$

as the main contributions to the H dependent relaxation time are the QTM and the direct processes. At 2 K, the contribution given by the Orbach and Raman processes is small and constant (B_4), as they are only temperature dependent.[136] This makes possible a better interpretation of the temperature independent regime, taking into account the different parameters from the QTM (B_1 and B_2, being B_1>>B_2) and from the direct process (B_3), being m fixed to 4 for a Kramers ions.

The small number of points obtained within the QTM regime, give us values with an enormous error but everything points to the accuracy of the tendency, and the magnitude values are in agreement with other similar systems.[134] Further measurements need to be done in order to be more precise in the obtained results summarized in Table 4. 4.

Table 4. 4. Parameters obtained for the best fitted curve of the magnetic field variation of the relaxation time of the magnetization.

B_1 / s^{-1}	B_2 / Oe^{-2}	B_3 / s^{-1} K^{-1} Oe^{-4}	B_4 / s^{-1}
64590 ± 10^7	0.01 ± 14	$1.19{\cdot}10^{-12} \pm 8{\cdot}10^{-14}$	382 ± 5

A DC magnetic field of 1000 Oe has been chosen in order to study the temperature dependence of the magnetic response of this sample (Figure 4. 22). As it can be seen, the system shows frequency dependence from 2 to 5 K in the studied region. The relaxation time of the magnetizations have been extracted by applying the extended Debye model and the relaxation mechanism can be observed (Annex 3, Table A3.9).

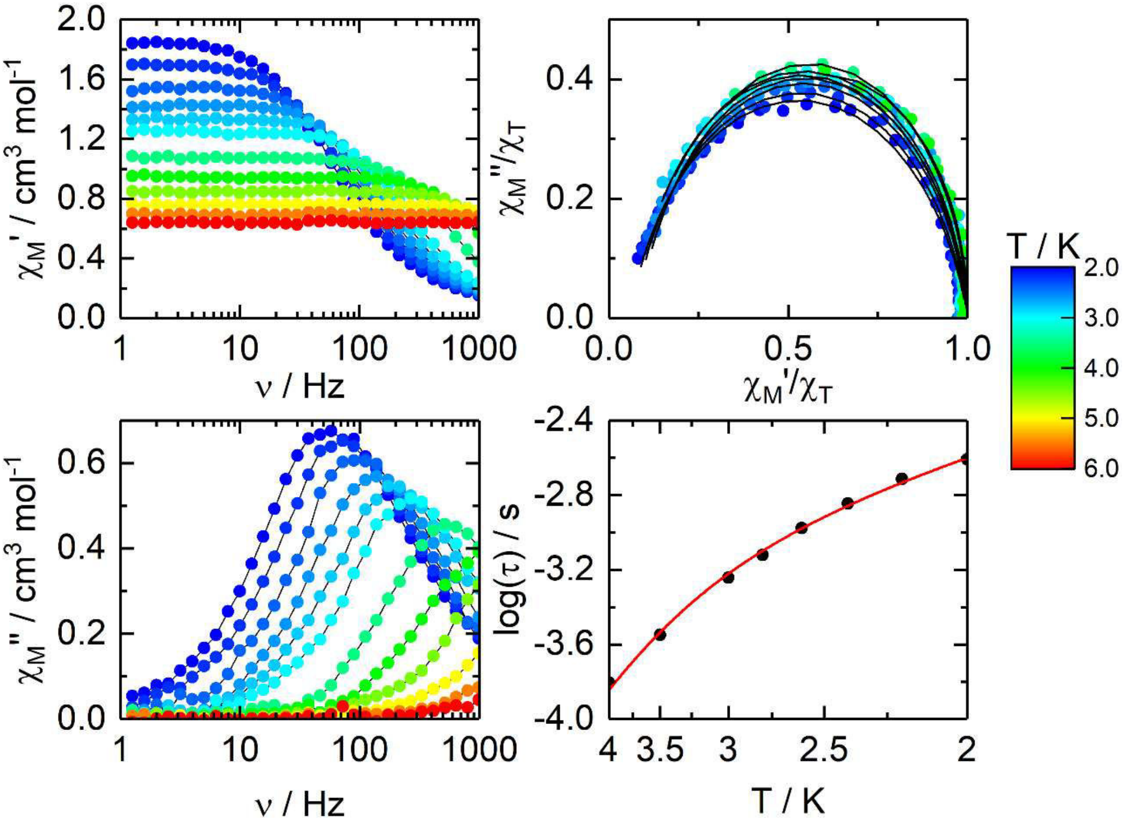

*Figure 4. 22. Left) in-phase (χ′) and out-of-phase (χ″) components of the ac susceptibility of **Yb** from 2 to 6 K under H$_{DC}$= 1000 Oe. Right) Argand representation and Magnetic field dependence of the Relaxation of the magnetization characterized by a Raman process. Lines best fitted curves.*

As a result, we obtained a temperature dependent curve which deviates from linearity. The observed curvature points to a non-negligible influence of direct and/or Raman processes in the relaxation rate,[109,137] the former confirmed using the field dependent measurements (Figure 4. 21). From the previous analysis (Figure 4. 21 and Table 4. 5), it was demonstrated that at 1000 Oe there is already some direct relaxation, which can affect this linearity. Furthermore, at the present field the contribution of the QTM process is of the order of the unit, which is far from the other contributing mechanisms. Thus, the general expression of the relaxation can be expressed by three different components:

$$\tau^{-1} = \tau_0^{-1} \exp\left(\frac{\Delta}{T}\right) + CT^n + B_3TH^4 \quad (4.2)$$

Corresponding to the Orbach, Raman and the direct relaxation rates, respectively. For the simplest case, a consideration of only Orbach and Direct is proposed. Then, an effective barrier much smaller than the expected theoretically (17.9 ± 0.2 K (Table 4. 5) experimentally and 340 K expected)[131] is found. This manifests the minor contribution of the Orbach tothe general mechanism, as a result of some Raman relaxation, minimizing it.

Table 4. 5. Parameters obtained for the best fitted curve of the thermal dependence of the relaxation time, taking into account the contribution of the Orbach and Direct processes.

Δ / K	τ_0 / s	B_3 / s^{-1} K^{-1} Oe^{-4}
17.9 ± 0.2	$(1.9 \pm 0.1)\cdot 10^{-6}$	$(1.71 \pm 0.03)\cdot 10^{-10}$

Consequently, the relaxation pathway of the magnetization is described by Raman (temperature dependent) as the major process with the possible contribution of direct and Orbach processes[100], respectively (Equation 4.2).The best fitted parameters are compressed in Table 4. 6.

*Table 4. 6. Parameters obtained for the best fitted curve of the thermal dependence of the relaxation time, taking into account the contribution of the Raman, Orbach and Direct processes. (*) values fixed during the fitting, obtained from **^{174}Yb@Y** analogue.*

C / K^n s^{-1}	n	Δ / K (*)	τ_0 / s (*)	B_3 / s^{-1} K^{-1} Oe^{-4}
46 ± 5	(3.1 ± 0.1)	31.38	$1.1\cdot 10^{-7}$	-

The expected n value for Kramers ion should be 9 but the presence of both acoustic and optical phonons could lead to lower values between 1 and 7.[108c-d]

So far, **Yb** show field-induced SMM behavior and the relaxation mechanism is governed by the competition of Raman and Orbach processes. Direct and QTM relaxations are considered negligible at that field.

B.2. *The effect of isotopic enrichment and magnetic dilution*

By diluting **Yb** in a diamagnetic Y-based matrix (**Yb@Y**), we aim to observe if the dilution effect is enough in order to have a SMM behavior inside of the experimental window without the need of applying a H_{DC}.

Additionally, an isotopic enriched substitution is performed for the diluted sample in order to enhance/ hinder the improvement due to magnetic dilution effect. Natural Yb is composed of 7 stable isotopes: ^{168}Yb (*I*= 0), ^{170}Yb (*I*= 0), ^{171}Yb (*I*= 1/2), ^{172}Yb (*I*= 0), ^{173}Yb (*I*= 5/2), ^{174}Yb (*I*= 0) and ^{176}Yb (*I*= 0). The nuclear spin free isotopes make 69.7% of the natural element. ^{174}Yb (31.8 %) is the focus of our studies aimed to observe the variation of the SMM properties when suppressing the hyperfine interaction coming from the nuclear spin. In order to study the opposite case, ^{173}Yb (16.1 %) was chosen, which has the highest nuclear spin, *I*= 5/2.

At 2 K the magnetic dependence of the magnetization has been studied for the diluted samples in order to obtain the percentage of magnetic material (Yb^{3+}) present in the sample (Figure 4. 23). The $M_{sat(\mathbf{Yb@Y})}/M_{sat(\mathbf{Yb})}$ ratio gave contents of 5.3 % (^{173}Yb^{3+}), 10.6 % (^{174}Yb^{3+}) and 5.2 % (Yb^{3+}) for the different diluted samples. These values diverge slightly from the EDS analysis (semi-quantitative technique) (^{173}Yb^{3+}: 6.6 ± 1 % and ^{174}Yb^{3+}: 9.6 ± 1 % and Yb^{3+}: 9.06 ± 0.7%), because of a possible high distribution in the content of different crystals and the addition of both instrumental errors. It must be taken into account also the fact that the studied population in EDS is much slower than in magnetic measurements, leading to another source of error. However, the significant difference between **Yb@Y** and **^{173}Yb@Y**, with **^{174}Yb@Y**, has at first sight no reason. Same quantities were used during each synthesis, but other external factors could play a role during the crystallization.

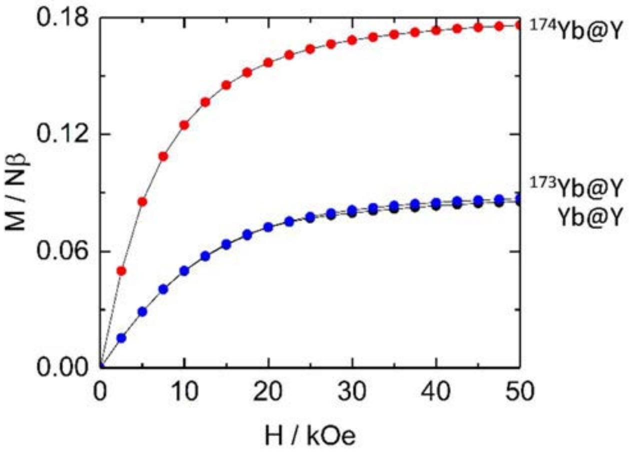

*Figure 4. 23.Magnetization as a function of the magnetic field at 2 K for ^{174}**Yb@Y** (red), **Yb@Y** (black) and ^{173}**Yb@Y** (blue).*

The dynamic properties of the three systems ^{174}**Yb** (I=0), **Yb@Y** and ^{173}**Yb@Y** (I= 5/2) have been determined by measuring the frequency dependences of the magnetic susceptibilities under different temperatures from 2 to 6 K under no applied magnetic field. In Figure 4. 24 the dependence with the frequency can be observed for the different isotopologues for all the temperature range.

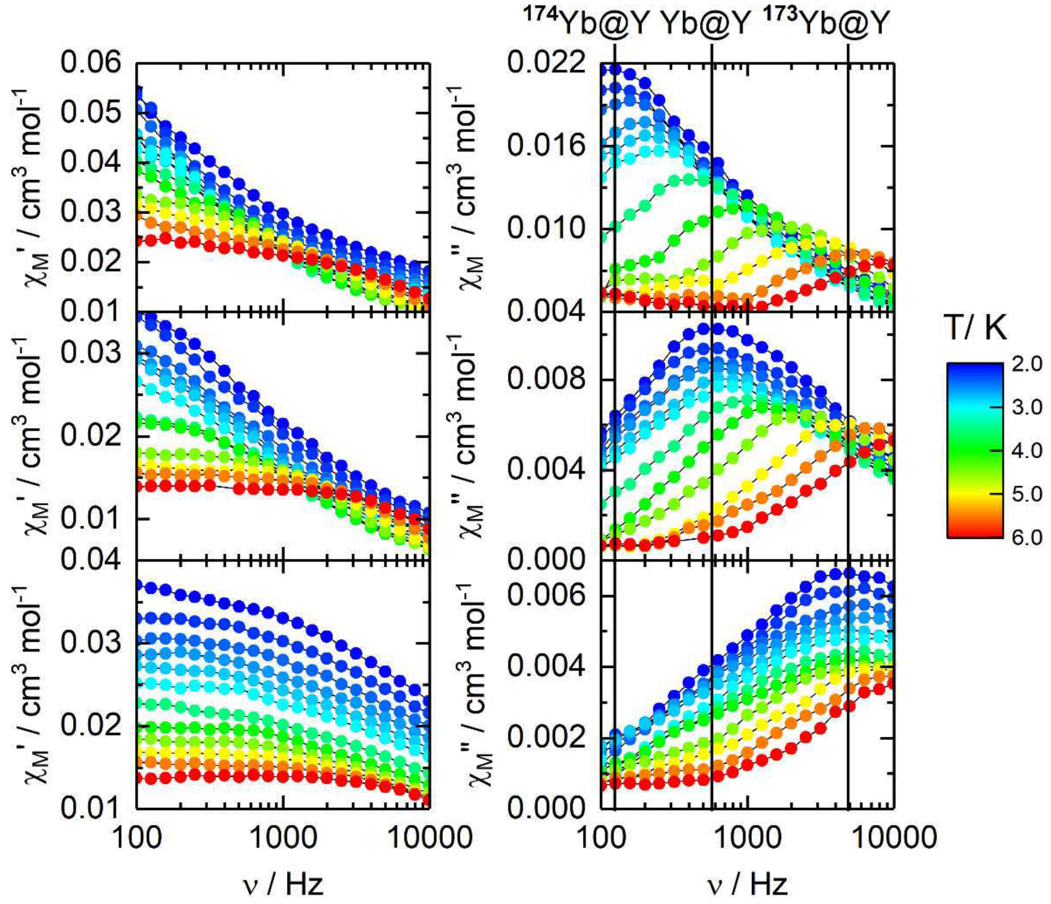

*Figure 4. 24. Left) in-phase (χ′) and right) out-of-phase (χ″) components of the ac susceptibility from 2 to 6 K under zero H$_{DC}$, for ^{174}**Yb@Y**, **Yb@Y** and ^{173}**Yb@Y**, respectively.*

The out-of-phase component of the three isotopologues passes through a maximum, sign of a slow in the relaxation of the magnetization, which is shifted to lower frequencies by decreasing the temperature. At 2 K, and as previously observed for **Dy** in *Chapter III*, the maximum of the nuclear spin-free **^{174}Yb@Y** (ν= 118 Hz) occurs at lower frequency than **Yb@Y** (536 Hz) and even lower than for the isotope with I= 5/2, **^{173}Dy** (4755 Hz). However, due to the fact that ytterbium samples are not highly magnetic and the paramagnetic fraction in the present ones is very small, the given response was hard to be treated as the signal was close to the limit of detection. As a result, a large signal given by a large distribution of the relaxation makes difficult the application of the extended Debye model, and the relaxation times needed to be taken by peaking the position of the maxima in χ_M'' vs. ν plots with $\tau = 1/2\pi\nu$. The representation of the temperature dependence of τ, Figure 4. 25, evidences the difference in the slope of the relaxation for the different isotopic situation.

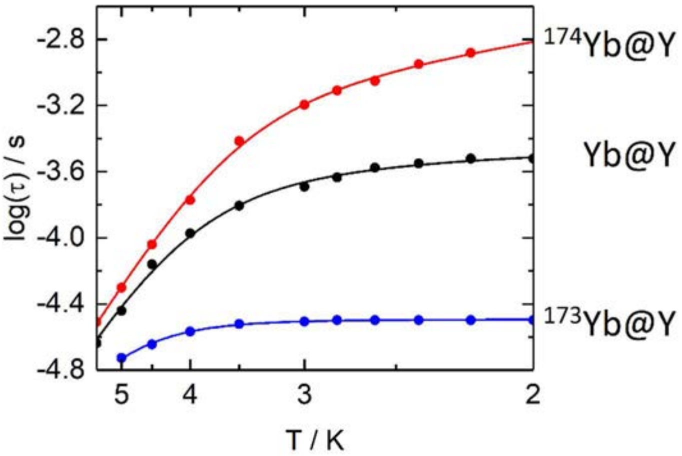

*Figure 4. 25. Comparison of the different temperature dependence of the relaxation time of the magnetization for **^{174}Yb@Y** (red), **Yb@Y** (black) and **^{173}Yb@Y**(blue), with full lines the best fitted curve.*

The thermal dependence of the relaxation time for each of the isotopologues has been modeled by a slightly different relaxation expression, with the contribution of QTM, as now we are dealing with zero field measurements (Equation 3.3). Orbach parameters have been found in **^{174}Yb@Y** and inject to the other systems. The best fitted parameters are presented in Table 4. 7, where it can be observed that the QTM regime is only efficient in the systems presenting hyperfine interactions.

Table 4. 7. Parameters obtained for the best fitted curve of the thermal dependence of the relaxation time, taking into account the contribution of the Raman and QTM processes.(*) values fixed during the fitting.

Compound	*Δ / K*	*τ_0 / s*	*C / K^n s^{-1}*	*n*	*τ_{TI} / s*
^{174}Yb@Y	31.38 ± 1.9	(1.1 ± 0.4)·10^{-7}	198 ± 57	1.7 ± 0.3	-
Yb@Y	31.38$^{(*)}$	1.1·10$^{-7(*)}$	91 ± 88	2.6 ± 0.6	(3.7 ± 0.6) ·10^{-4}
^{173}Yb@Y	31.38$^{(*)}$	1.1·10$^{-7(*)}$	8 ± 10	4.1 ± 0.8	(3.22 ± 0.02) ·10^{-5}

The relaxation mechanism does not involve a well-defined Orbach process, and the effective energy barrier is much smaller than the expected value. This means that Raman becomes the major contribution to relaxation.[100] Moreover, as recently seen by Wernsdorfer et al.[138], a divergence in Raman can be observed depending on the different nuclear spin value of the metal center, thus increasing the relaxation process by creating new virtual states with the hyperfine coupling. However, if the relaxation process is imagined as a competition of relaxation rates coming from the different contributors, the QTM effect present in the systems, hinders the increment of the Raman. As a consequence, the Raman constant C is underestimated because of the high QTM in **^{173}Yb@Y** and **Yb@Y**.

C. *Er-Based Complex*

DC magnetic measurements have been also performed for [Er(tta)$_3$(**L^2**)] (hereafter referred so as **Er**) (Figure 4. 26). The thermal dependence of the susceptibility has been studied from 2 to 300 K. At room temperature, the $\chi_M T$ curve saturates at 11.8 cm^3 K mol^{-1} which is close to the expected value for a free ion ($^4I_{15/2}$ ground state;g_J= 6/5, $\chi_M T$= 11.475 cm^3 K mol^{-1}).[133] Then, on cooling, $\chi_M T$ decreases to reach 5.5 cm^3 K mol^{-1} at 2 K, because of the depopulation of the different M_J sublevels. At 2 K, the magnetization curve reaches 4.5 Nβ (Figure 4. 26, Inset).

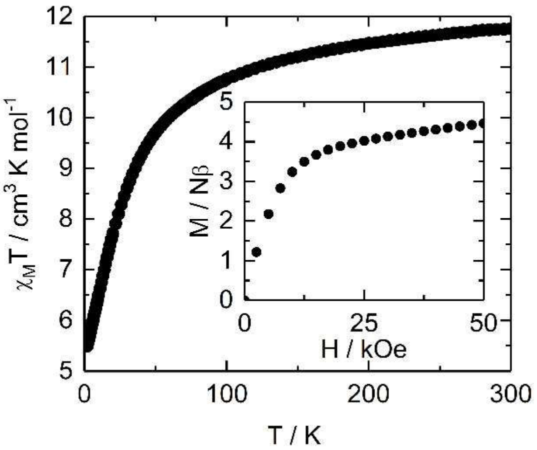

*Figure 4. 26. Thermal variation of $\chi_M T$ of **Er**. Inset: field variation of the magnetization at 2 K.*

If no H_{DC} is applied, **Er** do not present any sign of relaxation of the magnetization even at 2 K. At this temperature, and as for the previous case, different H_{DC} fields have been applied in order to observe the dependence of the relaxation mechanism with that (Figure 4. 27, Annex 3, Table A3.10).

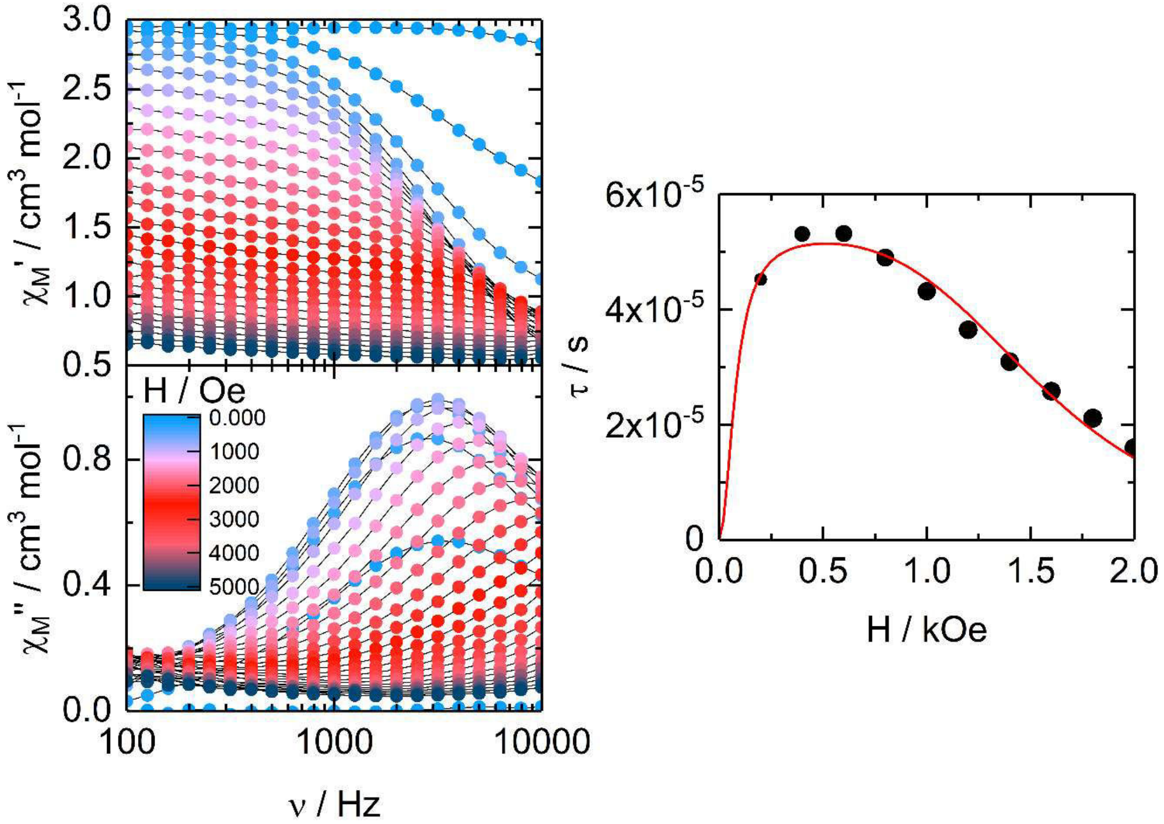

Figure 4. 27. Left) ac susceptibility curves of ***Er*** *from 0 to 3000 Oe at 2 K. Right) Magnetic field dependence of the Relaxation of the magnetization. Best fitted curve in red. Dot size mapped as a function of the portion relaxing of the sample ranging from the 46 % to the 100%.*

As previously occurred for **Yb**, a low field of 200 Oe is sufficient to enhance a frequency dependence in the ac susceptibility curve, but only for a relaxation of the 46 % of the total signal. The 100% is not achieved for fields below 1200 Oe. If we focus now on the evolution of the relaxation times with the magnetic field, the same three different regions can be distinguished: this time, from 0 to 500 Oe the relaxation time increases with the H_{DC} leading to a suppression of the QTM; then, from 500 to 800 Oe, the apparition of the direct process balances the suppression of the QTM; and finally, for higher magnetic fields, the direct is the major contributor, enhancing faster relaxation times. This H-dependence of the relaxation time can be modeled again following the Equation 4.1.[134,135] Thus, taking into account that the values found need to be taken as estimated values due to the lack of experimental points. The best fitted values are summarized in Table 4. 8.

Table 4. 8. Parameters obtained for the best fitted curve of the magnetic field variation of the relaxation time of the magnetization for ***Er****.*

B_1 / s^{-1}	B_2 / Oe^{-2}	B_3 / s^{-1} K^{-1} Oe^{-4}	B_4 / s^{-1}
$5.8 \cdot 10^6 \pm 1.7 \cdot 10^{10}$	0.05 ± 148	$(1.6 \pm 0.2) \cdot 10^{-9}$	$(1.8 \pm 0.1) \cdot 10^4$

These values have been taken into account in order to describe the system in the best way as possible, as this time we do not have the support of ab initio calculations in order to discriminate one relaxation process from another. The dynamic response of susceptibility has been studied from 2 to 6 K under a H_{DC} of 800 Oe, and the system showed frequency dependence from 2 to 3 K, sign of SMM behavior under applied magnetic field (Figure 4. 28).

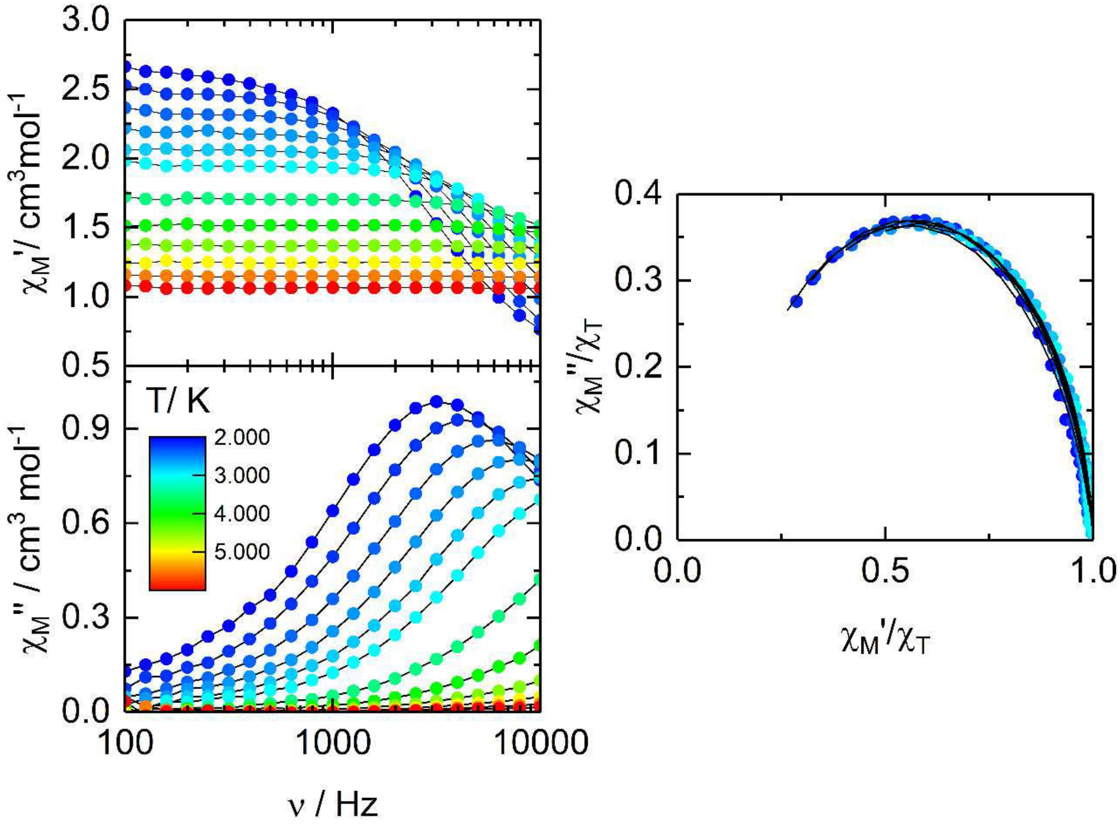

Figure 4. 28. Left: in-phase (χ') and out-of-phase (χ'') components of the ac susceptibility of ***Er*** *from 2 to 6 K under H_{DC}= 800 Oe, and right: the Argand representation.*

The extended Debye model has been applied within these temperatures and the information about the relaxation mechanism can be seen in Annex 3, table A4.11. The partial fraction relaxing can be again appreciated with the evolution of the temperature, going from 90 % down to 78 % over 2 - 3 K. The relaxation dependence with the temperature is represented in Figure 4.29 and 4.30. As already mentioned, for theoretical calculations for **Er** are not available in order to be compared to the experimental observations and help us in the understanding of the different mechanisms taking place in the magnetic response of the molecule. Consequently, two different options have been studied in order to opt for one description or discriminate another.

Before going into details, different considerations need to be regarded in order to simplify the general relaxation expression 1.17: First, the deviation from the linearity of the relaxation curve points to the contribution of at least another component apart from the Orbach relaxation. Moreover, at the chosen H_{DC}, the QTM regime can be considered suppressed (according to the values in Table 4.5, the contribution of the QTM (τ_{TI}^{-1}) should be $5\cdot10^{-3}$ s^{-1} compared to values of the order of 10^3-10^4 s^{-1} resulted from the other parameters). Finally, the direct process is not negligible at the working field and need to be maintained in the expression. Then, the relaxation mechanism can be summarized by the possibility of the different contributions given by the Orbach, Raman and direct processes, respectively (Equation 4.2).

Due to the small number of points, during the interpretation of the results it was found convenient to fix previously obtained direct parameter, B_3, (Table 4. 8) as this should remain constant. Then, if the simplest mechanism is considered, we should opt for a relaxation composed of a thermally activated Orbach and a field-dependent direct processes, which shortcuts the energy barrier, and fixing the Raman contribution at zero. As a result, the best fitted parameters (Table 4. 9) give rise to the red curve in Figure 4. 29.

*Table 4. 9. Parameters obtained for the best fitted curve of the thermal dependence of the relaxation time of **Er**, taking into account the contribution of the Orbach and Direct processes.*

Δ / K	τ_0 / s	B_3 (fixed value) / s^{-1} K^{-1} Oe^{-4}
8.2 ± 0.5	(9 ± 2)·10^{-7}	1.6·10^{-9}

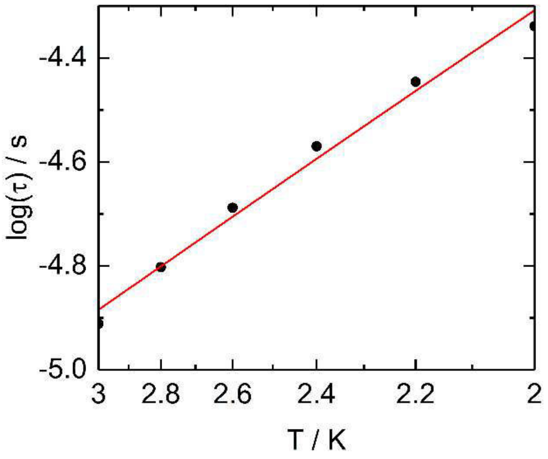

*Figure 4. 29. Temperature dependence of the relaxation time of the magnetization of **Er** from 2 to 3 K and 800 Oe. The red curve corresponds to the best fitted curve resulted from the contribution of Orbach and Direct processes.*

Otherwise, if an alternative description is considered, including this time the contribution of the Raman and direct relaxation pathways, as already done for other systems[100], the best fitted parameters (Table 4. 10) lead to the red curve in Figure 4. 30.

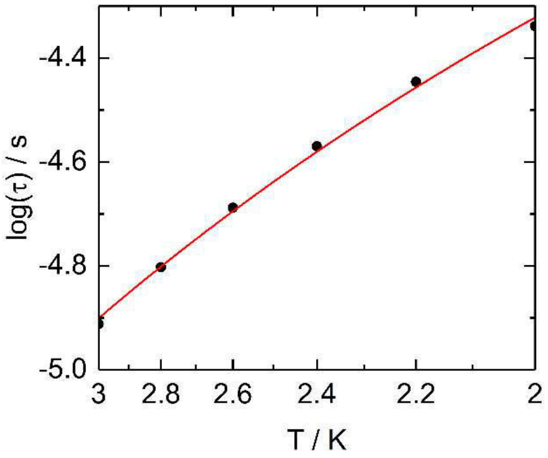

Figure 4. 30. Temperature dependence of the relaxation time of the magnetization from 2 to 3 K and 800 Oe. The red curve corresponds to the best fitted curve resulted from the contribution of Raman and direct processes.

*Table 4. 10. Parameters obtained for the best fitted curve of the thermal dependence of the relaxation time of **Er**, taking into account the contribution of the Raman and direct processes.*

C / K^n s^{-1}	n	B_3 (fixed value) / s^{-1} K^{-1} Oe^{-4}
1884 ± 160	3.39 ± 0.09	$1.6 \cdot 10^{-9}$

So far, the second mechanism seems to describe better the experimental behavior. Firstly, the resulted curve seems to be better adapted to the experimental one. Then, if the different extracted values are compared, the rate due to B$_4$ parameter (thermally dependent region, from τ *vs. H* curve, Figure 4. 27) should be on the order of $2{\cdot}10^4$ s^{-1} (values extracted from Table 4. 8), which is far from the value extracted from the Orbach process ($7{\cdot}10^7$ s^{-1}, from

Table 4. 9), hence noticing a smaller effective barrier that could be reduced because of the presence of a Raman relaxation process. The last is found to be around $1.2\cdot10^4$ s^{-1} (from Table 4. 10), which is in agreement with the first results.

Throughout, as previously seen for **Yb**, **Er** do not show SMM behavior without an applied magnetic field and the relaxation mechanism is governed by the competition of Raman and direct processes, thus neglecting the contributions coming from the Orbach and QTM relaxations.

C.1. *Effect of isotopic enrichment and magnetic dilution*

Same strategies of dilution and further isotopic enrichment are carried out of the with **Er** compound. Then, by diluting ^{A}**Er** in a diamagnetic Y-based matrix (**^{A}Er@Y**, with A the mass number), the SMM properties are expected to be embedded within the experimental frequency range, as for **^{A}Yb@Y**, without the need of an H_{DC}.

Natural Er is composed of 6 stable isotopes, all ^{162,164,166,168,170}Er with nuclear spin free (I=0) except for ^{167}Er with a nuclear spin active I= 7/2. The abundance of isotopic nuclear spin free is 77 %. As ^{166}Er is the most abundant, it will be taken together with ^{167}Er in order to study the isotopic effect.

Magnetic properties of Er@Y series:

At 2 K the magnetic dependence of the magnetization (Figure 4. 31) has been studied for the diluted samples (**Er@Y**) in order to obtain the percentage of ^{A}Er^{3+} (A= 166, 167) present in the system. The $M_{sat(\mathbf{Er@Y})}/M_{sat(\mathbf{Er})}$ ratio gave contents of 5.4% and 6.5% for the ^{166}Er^{3+} and ^{167}Er^{3+} diluted samples, respectively. The existent divergence with the EDS analysis values (^{166}Er^{3+}: 3.8 ± 0.7% and ^{167}Er^{3+}: 2.3 ± 0.5 %) can be given by the possible different distribution within the different crystals and the instrumental errors, as mentioned previously.

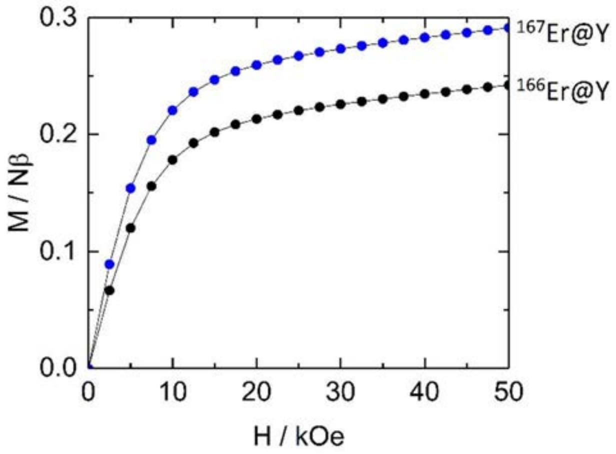

Figure 4. 31. Magnetization as a function of the magnetic field at 2 K for ^{166}Er@Y (black) and ^{167}Er@Y (blue).

Concerning the dynamic study of the systems, no out-of-phase component of the susceptibility was given even when adding dilution and isotopic enrichment strategies all together at 2K and going up to 10 kHz.

EPR characterization: Er-based complex

In order to go a step further, EPR measurements were performed on the isotopic samples. These measurements were performed at the University of Manchester under the supervision of Floriana Tuna, as a result of a three months mobility grant awarded by the Britany Region.

The EPR technique permits to get unique information about the structure, the symmetry and properties related to the electrons, from the spin **S** of the system. Then, one can obtain information about the electronic structure itself and the possible applicability of the compounds as qudits, whichare some of the purposes of this section. The best result was obtained with by an X band spectrometer (ν= 9.4 GHz) at the lowest accessible temperature i.e. 5 K.

A full scan up to magnetic fields of 1.4 T was performed for **^{166}Er@Y** and **^{167}Er@Y**. The spectra are represented in Figure 4. 32, which allows to see two different signals at each curve. First, at the lowest magnetic fields (greater g-values) there is the signal coming from the metal center, which is different depending on the isotope. Then, in the region corresponding to the g value of 2, there is a second signal coming from an organic radical species. Considering the structure of the studied molecule (Figure 4.1), we assign this signal to a small fraction of radical TTF$^\bullet$.

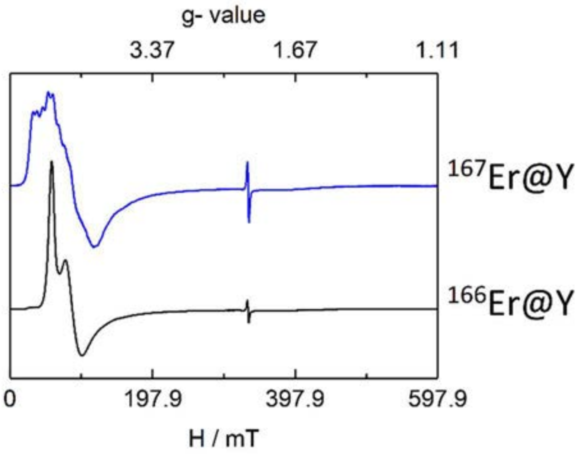

Figure 4. 32.EPR band spectra for the ^{166}***Er@Y*** *(black) and* ^{167}***Er@Y*** *(blue) at 5 K.*

If we zoom up in the zone where the Er^{3+} transitions are taking place (between 0 and 300 mT, approximately (Figure 4. 33)), the splitting due to the electronic structure can be modelled. We consider first the ^{166}**Er@Y** (Figure 4. 33, left) (S_{eff} = 1/2, I= 0), where the energy splitting is only governed by the spin-orbit coupling and the crystal field, but hyperfine interactions are suppressed. It can be observed that ^{A}**Er@Y** is an anisotropic molecular system determined by two different g values ($g_{//}$ and $g_{\perp}$). However, if we take a look now to the ^{167}**Er@Y** (Figure 4. 33, right) (S_{eff}= 1/2, I= 7/2), the two different g-peaks are split into 8 different contributions, or possible transitions. Hence, in the presence of nuclear spin (I= 7/2) the hyperfine mechanism takes also a role in the splitting of the energy levels by 2I+1= 8 contributions. As a result, if the different contributions are visible enough, the hyperfine constant (A) can be extracted, as it corresponds to the distance between each.

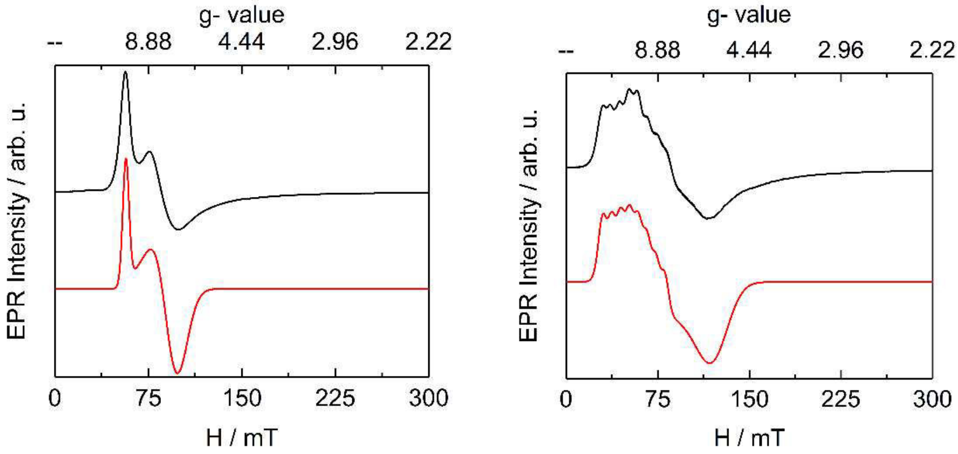

Figure 4. 33. Comparison between experimental (black line) and simulated (red line) curves for the ^{166}***Er@Y*** *(left) and* ^{167}***Er@Y*** *(right).*

EasySpin[139] program with the help of "pepper" model is used in order to simulate the different spectra. The best extracted values are presented in Table 4. 11;

Table 4. 11. Best values obtained by the simulation of the EPR spectra of ***$^{166/167}$Er@Y***.

Compound	*g-values*		*H$_{strain}$ / MHz*		*A / MHz*	
	// (or xy)	*⊥ (or z)*	*// (or xy)*	*⊥ (or z)*	*// (or xy)*	*⊥ (or z)*
^{166}Er@Y	7.1	11.54	2200	900	0	0
^{167}Er@Y	7.026	11.436	2793.23	1138.26	769.521	1194.68

Where, H_{strain} corresponds to a parameter for the width peak modulation.

Further measurements were tested for the present system, in order to get an insight of the quantum coherence. For that, the system is submitted to different electromagnetic radiation pulses, and the relaxation of the magnetic moment to the equilibrium is studied through the echoes coming from the molecule. Unfortunately, intramolecular interactions involving the spin center are really important for what concerns the relaxation phenomena, as they are the major cause of the loss of quantum properties.[140] The coordination sphere of the lanthanide is constituted of 2 N atoms (^{14}N(I= 1/2)), which through hyperfine interactions can be one of the sources of decoherence, leading to fast relaxation.

III. CONCLUSIONS

In the present chapter, the substitution of the metal center by two lanthanide prolate cations has been presented and with it the different magnetic characterization. [Ln(tta)$_3$(**L^2**)]·C$_6$H$_{14}$, with Ln= Yb and Er, are isostructural to the previous **Dy** system but their electronic density is placed along an axis instead of a plane. Thus, the SMM properties can change drastically from the Dy to the two others, as the electronic density of the ligand does not fit with the position in which the electronic repulsion is minimized, and thus, the highest M_J-sublevels may not be stabilized.

As a result, the SMM behavior is not evidenced for any of the prolate-systems mentioned here under zero magnetic field, corroborating an important contribution of the transverse components of the anisotropy which facilitates a fast relaxation of the magnetization via QTM. An insight of these transverse components, was already settled in previous published works in 2014 by angular rotation magnetometry and ab initio calculations.[131] Different attempts have been made (magnetic dilution and isotopic enrichment) in order to cancel this transverse component, created by the inner magnetic field. Despite the application of both strategies simultaneously, **Er** analogues have not shown any sign of slowing down of the relaxation, only after applying magnetic field, and also the quantum coherence study failed, when using pulsed EPR experiments, as the compounds did not show any echo signals.

On the other hand, results obtained with **Yb** systems are surprisingly satisfactory. For the first time, the SMM behavior under zero magnetic field has been demonstrated for an ytterbium ion. By diluting Yb in an isomorphous diamagnetic Y-matrix the slow relaxation of the magnetization it is enhanced, thus facilitating the isotopic study of the first system based on Yb^{3+}, in order to have a second example of isotopic enrichment in prolate ions.

To the best of our knowledge, **Yb@Y** results to the first molecules based on Yb^{3+} displaying SMM behavior under zero magnetic field. As a consequence, this study constitutes the first investigation of the role of the hyperfine interactions on Yb^{3+} compounds for magnetic applications. Furthermore, the relaxation of the magnetization has shown to be highly dependent on the dipolar interactions (effect on the dilution), as well as the hyperfine coupling which show a similar tendency than its previous analogous system **Dy**.

So far, we can conclude that by changing the electronic distribution of the metal center, in the same kind of coordination environment, the hyperfine interactions coming from the metal as well as the inner field created by the neighboring molecules, enhance the fast relaxation of the magnetization via QTM. Further studies will include the optimization of the doped system by using a diamagnetic cation of a more suitable size compared to Yb^{3+} (use of Lu^{3+}-based precursor), and the study of the role of the matrix in the Raman (relaxation phonon- matrix) mechanism.

REFERENCES:

[96] J. D. Rinehart, and J. R. Log, *Chem. Sci.*, **2011**, *2*, 2078.

[97] a) Y.-N. Guo, G.-F. Xu, P. Gamez, L. Zhao, S.-Y. Lin, R. Deng, J. Tang, and H.-J. Zhang, *J. Am. Chem. Soc.*, **2010**, *132*, 8538; b) Y.-N. Guo, G.-F. Xu, W. Wernsdorfer, L. Ungur, Y. Guo, J. Tang, H.-J. Zhang, L. F. Chibotaru, and A. K. Powell, *J. Am. Chem. Soc.*, **2011**, *133*, 11948; c) S.-Y. Lin, W. Wernsdorfer, L. Ungur, A. K. Powell, Y.-N. Guo, J. Tang, L. Zhao, L. F. Chibotaru, and H.-J. Zhang, *Angew. Chem. Int. Ed.*, **2012**, *51*, 12767; d) Y.-N. Guo, L. Ungur, G. E. Granroth, A. K. Powell, C. Wu, S. E. Nagler, J. Tang, L. F. Chibotaru, and D. Cui, *Sci. Rep.*, **2014**, *4*, 5471; e) R. A. Layfield, *Organometallics*, **2014**, *33*, 1084; f) Y.-N. Guo, G.-F. Xu, Y. Guo, and J. Tang, *Dalton Trans.*, **2011**, *40*, 9953; g) P. Zhang, L. Zhang, and J. Tang, *Dalton Trans.*, **2015**, *44*, 3923; h) L. Ungur, S.-Y. Lin, J. Tang, and L. F. Chibotaru, *Chem. Soc. Rev.*, **2014**, *43*, 6894; i) F.-S. Guo, B. M. Day, Y.-C. Chen, M.-L. Tong, A. Mansikkamäki and R. A. Layfield, Angew. *Chem., Int. Ed.*, **2017**, 56, 11445; j) C. A. P. Goodwin, F. Ortu, D. Reta, N. F. Chilton and D. P. Mills, *Nature*, **2017**, *548*, 439; k) F.-S. Guo, B. M. Day, Y.-C. Chen, M.-L. Tong, A. Mansikkamäki and R. A. Layfield, *Science*, **2018**, *362*, 1400; l) P. Zhang, Y.-N. Guo and J. Tang, *Coord. Chem. Rev.,* **2013**, *257*, 1728.

[98] F. Pointillart, O. Cador, B. Le Guennic, and L. Ouahab, *Coord. Chem. Rev.*, **2017**, *346*, 150.

[99] M. A. AlDamen, S. Cardona-Serra, J. M. Clemente-Juan, E. Coronado, A. GaitaArino, C. Marti-Gastaldo, and F. Luis, O. Montero, *Inorg. Chem.*, **2009**, *48,* 3467.

[100] J.-L. Liu, K. Yuan, J.-D. Leng, L. Ungur, W. Wernsdorfer, F.-S. Guo, L. F. Chibotaru and M.-L. Tong, *Inorg. Chem.*, **2012**, *51*, 8538.

[101] K. Soussi, J. Jung, F. Pointillart, B. Le Guennic, B. Lefeuvre, S. Golhen, O. Cador, Y. Guyot, O. Maury, and L. Ouahab, *Inorg. Chem. Front.*, **2015**, *2*, 1105.

[102] M. Sugita, N. Ishikawa, T. Ishikawa, S. Koshihara, and Y. Kaizu*, Inorg. Chem.*, **2006**, 45(3), 1299.

[103] M. E. Boulon, G. Cucinotta, J. Luzon, C. Degl'Innocenti, M. Perfetti, K. Bernot, G. Calvez, A. Caneschi, R. Sessoli, *Angew. Chem. Int. Ed.*, **2013**, *52*, 350.

[104] X. Yi, K. Bernot, V. Le Corre, G. Calvez, F. Pointillart, O. Cador, B. Le Guennic, J.Jung, O. Maury, V. Placide, Y. Guyot, T. Roisnel, C. Daiguebonne, and O. Guillou, *Chem. Eur. J.*, **2014**, *20*, 1569.

[105] W. Huang, J. Xu, D. Wu, X. Huang, and J. Jiang, *New J. Chem.*, **2015**, *39*, 8650.

[106] K. S. Pedersen, J. Dreiser, H. Weihe, R. Sibille, H. V. Johannesen, M. A. Sorensen, B. E. Nielsen, M. Sigrist, H. Mutka, S. Rols, J. Bendix, and S. Piligkos, *Inorg. Chem.*, **2015**, *54*, 7600.

[107] N. Ishikawa, M. Sugita, T. Ishikawa, S. Koshihara, and Y. Kaizu, *J. Phys. Chem. B*, **2004**, *108*, 11264.

[108] a) R. L. Carling, *Magnetochemistry*, Springer- Verlag, New York, **1986**; b) R. L. Carlin, and A. J. van Duyneveldt*, Magnetic properties of Transition Metal Compounds*, Springer- Verlag, New York, **1977**; c) A. Singh, and K. N. Shrivastava, *Phys. Status Solidi B,* **1979**, *95*, 273-277; d) K. N. Shirivastava, *Phys. Status Solidi B,* **1983**, *177*, 437.

[109] A. Abragam, and B. Bleaney, *Electron Paramagnetic Resonance of Transition Ions*, Clarendon Press. Oxford, **1970**.

[110] J. Jung, O. Cador, K. Bernot, F. Pointillart, J. Luzon, B. Le Guennic, *Beilstein J.Nanotechnol*, **2014**, 5, 2267.

[111] a) M. Bottrill, L. Kwok, and N. J. Long, *Chem. Soc. Rev.*, **2006**, *35*, 557; b) L. Armelao, S. Quici, F. Barigelletti, G. Accorsi, G. Bottaro, M. Cavazzini, and E. Tondello, *Coord. Chem. Rev.*, **2010**, *254*, 487.

[112] W. Huang, D. Wu, D. Guo, X. Zhu, C. He, Q. Meng, and C. Duan, *Dalton Trans.*, **2009**, 2081.

[113] B. M. Flanagan, P. V. Bernhardt, E. R. Krausz, S. R. Lüthi, and M. J. Riley, *Inorg. Chem.*, **2002**, *41*, 5024.

[114] K. S. Pedersen, L. Ungur, M. Sigrist, A. Sundt, M. Schau-Magnussen, V. Vieru, H. Mutka, S. Rols, H. Weihe, O. Waldmann, L. F. Chibotaru, J. Bendix, and J. Dreiser, *Chem. Sci.*, **2014**, *5*, 1650.

[115] E. Lucaccini, L. Sorace, M. Perfetti, J.-P. Costes, and R. Sessoli, *Chem. Commun.*, **2014**, *50*, 1648.

[116] M. Perfetti, E. Lucaccini, L. Sorace, J.-P. Costes, and R. Sessoli, *Inorg. Chem.*, **2015**, *54*, 3090.

[117] N. Ishikawa, M. Sugita, T. Ishikawa, S.-Y. Koshihara, and Y. Kaizu, *J. Am. Chem. Soc.,* **2003**, *125*, 8694.

[118] M. A. AlDamen, J. M. Clemente-Juan, E. Coronsado, C. Martí-Gastaldo, and A. Gaita-Ariño, *J. Am. Chem. Soc.*, **2008**, *130*, 8874.

[119] S.-D. Jiang, B.-W. Wang, H.-L. Sun, Z.-M. Wang, and S. Gao, *J. Am. Chem. Soc.*, **2011**, *133*, 4730.

[120] M.-E. Boulong, G. Cucinotta, S.-S. Liu, S.-D. Jiang, L. Ungur, L. F. Chibotaru, S. Gao, and R. Sessoli, *Chem. Eur. J.*, **2013**, *19*, 13726.

[121] K. R. Meihaus, and J. R. Long, *J. Am. Chem. Soc.*, **2013**, *135*, 17952.

[122] J. J. Le Roy, I. Korobkov, and M. Murugesu, *Chem. Comm.*, **2014**, *50*, 1602.

[123] J. J. Le Roy, L. Ungur, I. Korobkov, L. F. Chibotaru, and M. Murugesu, *J. Am. Chem. Soc.*, **2014**, *136*, 8003.

[124] A. Yamashita, A. Watanabe, S. Akine, T. Nabeshima, M. Nakano, T. Yamamura, and T. Kajiwara, *Angew. Chem. Int. Ed.*, **2011**, *50*, 4016.

[125] M. A. Palacios, S. Titos-Padilla, J. Ruiz, J. M. Herrera, S. J. A. Pope, E. K. Brechin, and E. Colacio, *Inorg. Chem.*, **2014**, *53*, 1465.

[126] a) P. Zhang, L. Zhang, C. Wang, S. Xue, S.-Y. Lin, and J. Tang, *J. Am. Chem. Soc.*, **2014**, 136, 4484; b) W. A. Herrmann, R. Anwander, F. C. Munck, W. Scherer, V. Dufaud, N. W. Huber, and G. R. J. Artus, *Z. Naturforsch.* **1994**, *B49*, 1789.

[127] A. J. Brown, D. Pinkowicz, M. R. Saber, and K. R. Dunbar, *Angew. Chem. Int. Ed.*, **2015**, *54*, 5864.

[128] P. Zhang, J. Jung, L. Zhang, J. Tang, and B. Le Guennic, *Inorg. Chem.*, **2016**, *55*, 1905.

[129] H. Zhang, R. Nakanishi, K. Katoh, B. K. Breedlove, Y. Kitagawa, and M. Yamashita, *Dalton Trans.*, **2018**, 47, 302.

[130] T. T. da Cunha, J. Jung, M-E. Boulon, G. Campo, F. Pointillart, C. L. M. Pereira, B. Le Guennic, O. Cador, K. Bernot, F. Pineider, S. Golhen, and L. Ouahab, *J. Am. Chem. Soc.*, **2013**, *135*, 16332.

[131] J. Jung, T. T. da Cunha, B. Le Guennic, F. Pointillart, C. L. M. Pereira, J. Luzon, S. Golhen, O. Cador, O. Maury, and L. Ouahab, *Eur. J. Inorg. Chem.*, **2014**, 3888.

[132] M. Llunell, D. Casanova, J. Cirera, J. M. Bofill, P. Alemany, S. Alvarez, SHAPE (version 2.1), Barcelona, **2013**.

[133] O. Kahn*, Molecular Magnetism*, VCH, Weinheim, Germany, **1993**.

[134] E. Lucaccini, L. Sorace, M. Perfetti, J.-P. Costes, and R. Sessoli, *Chem. Commun.*, **2014**, *50*, 1648.

[135] K. S. Pedersen, J. Dreiser, H. Weihe, R. Sibille, H. V. Johannesen, M. A. Sorensen, B. E. Nielsen, M. Sigrist, H. Mutka, S. Rols, J. Bendix and S. Piligkos, *Inorg. Chem.*, **2015**, *54*, 7600.

[136] R. Orbach, *Proc. R. Soc. Lond. A*, **1961**, *264*, 458.

[137] J. M. Zadrozny, M. Atanasov, A. M. Bryan, C.-Y. Lin, B. D. Rekken, P. P. Power, F. Neese and J. R. Long, *Chem. Sci.,* **2013**, *4*, 125.

[138] E. Moreno-Pineda, G. Taran, W. Wernsdorfer, and M. Ruben, *Chem. Sci.*, **2019**, *10*, 5138.

[139] Easyspin.org/documentation/pepper.htmls.

[140] a) F. Pointillart, Y. Le Gal, S. Golhen, O. Cador, and L.Ouahab, *Chem. Eur. J.,* **2011**, *17*, 10397; b) X. Yi, K. Bernot, O. Cador, J. Luzon, G. Calvez, C. Daiguebonne, and O. Guillou, *Dalton Trans.* **2013**, *42*, 6728; c) S.-F. Guo, and R. A. Layfield, *Chem. Commun.*, **2017**, *53*, 3130; d) H. Tian, B.-L. Wang, J. Lu, H.-T. Liu, J. Su, D. Li, and J. Dou, *Chem. Commun.,* **2018**, *54*, 12105; e) L. Zhang, Y.-Q. Zhang, P. Zhang, L. Zhao, M. Guo, and J. Tang, *Inorg. Chem.,* **2017**, *56*, 7882; f) M. J. Giansiracusa, E. Moreno-Pineda, R. Hussain, R. Marx, M. Martinez Prada, P. Neugebauer, S. Al-Badran, D. Collison, F. Tuna, J. van Slageren, S. Carretta, T. Guidi, E. J. L. McInnes, R. E. P. Winpenny, and N. F. Chilton, *J. Am. Chem. Soc.,* **2018**, *140*, 2504.

CHAPTER V

SMMs PROPERTIES IN Er- POLYOXOMETALATE MOLECULES

Previous Er-based systems, field induced-SMM, did not show suitable characteristics in order to get information about the isotopic effect on the SMM behavior for prolate-ion based molecules. Therefore, a suitable system showing the desired magnetic properties has been searched in the literature.

$Na_9[Er(W_5O_{18})_2]\cdot xH_2O$ (**20**$\cdot xH_2O$, *hereafter referred to as* ^{A}**ErW**$_{10}$$\cdot$**xH**$_2$**O**), *with A the mass number and x the hydration quantity) is a prolate ion based system showing slow relaxation of the magnetization under no magnetic field and relaxing at the same frequency magnitude as* **Dy** *in chapter III, which make it interesting for the isotopic study. Some research has already been published by F. Luis et al.*[141] *concerning the isotopic and dilution study of a* ^{167}*Er (I= 7/2) sample, which do not agree with the obtained conclusions for our* **Dy** *and* **Yb** *system. A complete study is proposed here, adding the results of the nuclear spin-free isotope* ^{166}*Er (I= 0), in order to understand the existent divergences and try to find a possible explanation for this change in the tendency. Moreover, the great hydration of the system makes us consider the correlation of the water molecules with the structure, and thus, the SMM properties. As the release of coordinated solvent could dramatically change the properties since the coordination sphere changes and therefore the crystal field splitting.*[142]

I. INTRODUCTION

The different interactions present in a system may contribute somehow to the physical properties. In particular, the modification of dipolar and hyperfine interactions in the studied systems may contribute to the relaxation mechanism, thus favoring or cancelling the processes that take place under the characteristic energy barrier. In other words, a suitable system would consist in a molecule displaying slow relaxation of the magnetization under zero applied H_{DC} which relaxation mechanism results from the contribution of a temperature activated process followed by a temperature independent regime (QTM) at lower temperatures, with a frequency maximum on the out-of-phase susceptibility between 10 and

100 Hz. Finally, the isotope chemistry is not easy achievable and thus forces us to work with relatively easy and reproducible chemistry.

In the previous Chapter, the main Er^{3+}-based compounds presenting SMM properties under zero DC field were discussed. Amongst them, those presenting the preferred SMM characteristics are **20**[143], **26**[144], **27**[145] and **28**[146] the others showing too slow relaxations of the magnetization for the study (Figure 5. 1).

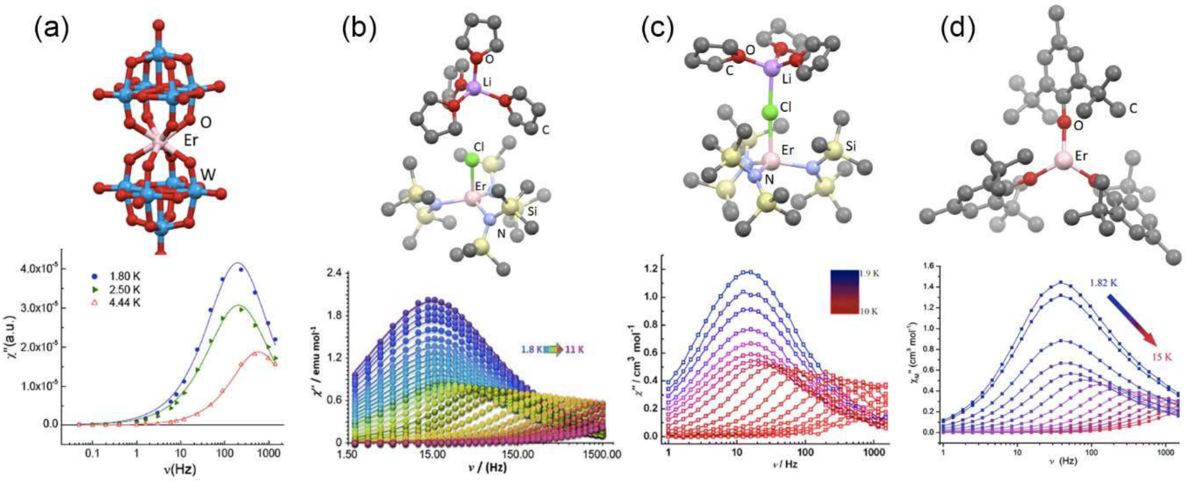

Figure 5. 1. Above, molecular structure and below, the χ_M'' vs. ν curves under zero H_{DC} for a) ***20****, b)* ***26****, c)* ***27*** *and d)* ***28****. All the solvent molecules, counter-ion framework and H atoms are omitted for clarity. Figure adapted from ref. [143]-[146] and [149].*

From a magnetic point of view, any of these systems could fulfil the mentioned requirements. However, the difficulty of the synthetic protocol is of the same importance. That is the reason why the chosen compound is **20**, as the maximum of the χ_M'' at 1.8 K is placed at 100 Hz and its chemistry is of easy approach and fits with the historical culture of the laboratory.

Actually, Ln^{3+}-polyoxometalate systems (Ln-POM) have been largely reported due to their potential applicability in various technological areas, such as catalysis, optical and magnetic sensors, and medical imaging.[143,147,148,149,150] Firstly described by Peacock and Weakley[151] (for Ln^{3+}= La^{3+}, Ce^{3+}, Pr^{3+}, Pr^{3+}, Nd^{3+}, Sm^{3+}, Eu^{3+}, Ho^{3+}, Er^{3+} and Yb^{3+}), and later characterized as SMM by Coronado *et al.*[149,152] (for Ln^{3+}= Ho^{3+} and Er^{3+}), the system studied in this chapter are decatungstates composed by two monolacunary Lindqvist units $[W_5O_{18}]^{6-}$ coordinated to an Er^{3+} cation.

The POMs are inorganic clusters characterized by metallic centers (M= V, Mo, W), usually in high oxidation state, bounded by terminal or bridging oxygen atoms. Other elements can be also incorporated (heteroatoms) to the cluster. For the case where no heteroatoms are added to this structure, this is called isopolyanion polyoxometalate ($[M_xO_y]^{m-}$). The lacunar form of this cluster is formed by the removal of one MO_x group, and can act as an inorganic ligand by coordinating the lanthanide cation via the free sites on the oxygen atoms. This inorganic cluster appears to be a good candidate for enhancing SMM properties as, due to the steric hindrance and intrinsic diamagnetism of its oxidized form, it can ensure a greater insulation from the neighboring molecules and minimize the intermolecular interactions, source of unwanted quantum tunneling and loss of magnetization. Furthermore, the wide variety of possible coordination to the metal center make possible the optimization of the crystal field depending on the lanthanide cation; an important feature for this kind of molecules.[153,154]

II. RESULTS AND DISCUSSIONS

A. Structural description

^{A}ErW$_{10}$ were synthesized following a modified version of a published method, for which a controlled reaction of acidification and condensation of the $NaWO_4$ monooxoanion in the presence of acetate buffer and the addition of Er^{3+} precursor, from the chloride salt, give rise to the Er^{3+}-POM cluster. The three compounds **ErW$_{10}$·xH$_2$O**, **^{166}ErW$_{10}$·xH$_2$O** and **^{167}ErW$_{10}$·xH$_2$O** (x= 35) are isostructural (Annex 1, table A1.4). The system crystalizes in the triclinic P-1 (N°2) space group, and the X-ray structure (Figure 5. 2) has been determined on single crystal and compared to published works of M. A. Aldamen *et al.*.[149]

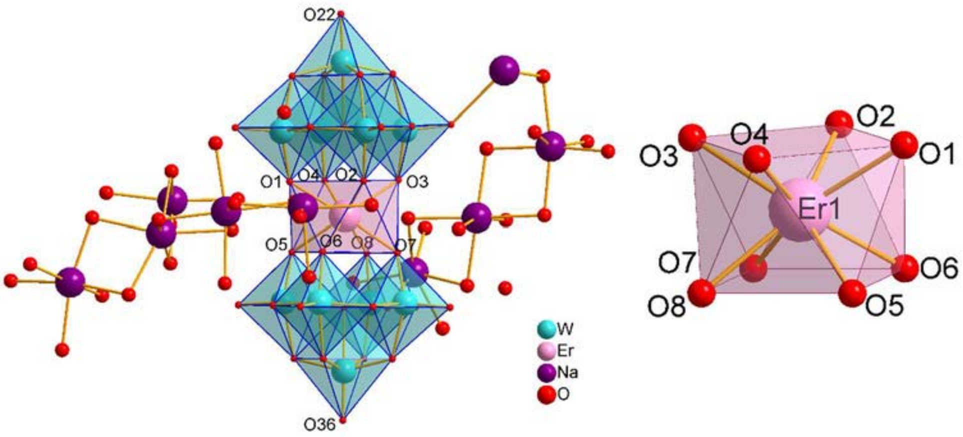

*Figure 5. 2. Left: Molecular structure of **ErW$_{10}$**. Hydrogen atoms are omitted are drawn for clarity. Right: Coordination environment of Er1, polyhedral used for SHAPE analysis.*

As already mentioned, the molecule consists of an Er^{3+} cation coordinated to two anionic moieties of lacunar polyoxometallate $[W_5O_{18}]^{6-}$. This anionic cluster is surrounded by a framework of Na^+ cations and water molecules, the formers balancing the negative charges and the later occupying the octahedral sites of the counter ions in order to form the given distribution. The tetradentate $[W_5O_{18}]^{6-}$ ligands generate a O_8 coordination sphere around the magnetic center in square antiprism symmetry (D_{4d}, found by SHAPE analysis)[155] (Table 5. 1). Thus, noticing a greater electronic density in the plane compared to the vertical. If we take a look at the intermolecular distances, the closest distance between two neighboring erbium is of 12.8 Å, assuring a minimal interaction between two consecutives molecules.

Table 5. 1. First three closest symmetries for the Er-coordination environment.

	$CShM_{SAPR-8}$ (square antiprism D_{4d})	$CShM_{BTPR-8}$ (biaugmented trigonal prism C_{2v})	$CShM_{TDD-8}$ (triangular dodecahedron D_{2d})
Er-O_8	0.079	2.264	2.452

B. DC magnetic properties

Static magnetic measurements were performed for all the isotopologues, as it can be seen in Figure 5. 3. As previously exposed, the different compounds possess the same DC behavior and all the curves are superimposed. At room temperature, the $\chi_M T$ product is 11.47 cm^3 K mol^{-1} which is in agreement with the expected value for the free trivalent ion ($^4I_{15/2}$ multiplet ground state and g_J= 6/5, $\chi_M T$= 11.475 cm^3 K mol^{-1}).[156] At this temperature, the appearance of a void points to the existence of an oxygen flow from the sample, which is a footprint of the dehydration of the system. The repetition of the temperature dependence of $\chi_M T$ confirms the disparisation of this void. When cooling, the $\chi_M T$ product remains constant down to 150 K. For temperatures below, the depopulation of the crystal field levels causes a progressive and continuous decrease down to 2 K (7.5 cm^3 K mol^{-1}). At this temperature, the magnetization curves as a function of the magnetic field show a classic behavior with a value of 4.59 Nβ at 50 kOe.

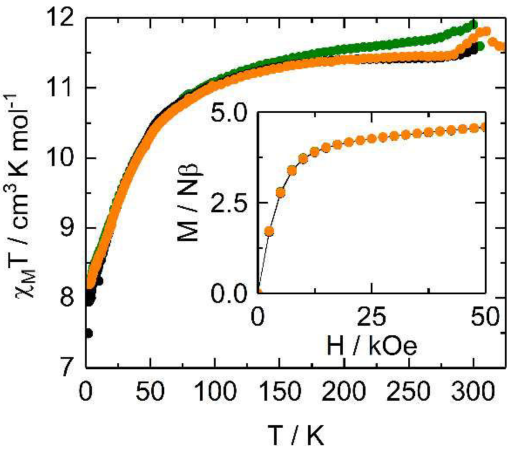

Figure 5. 3. Thermal dependence of the $\chi_M T$ product for ^{A}**ErW$_{10}$·35H$_2$O**: *being* ^{167}**ErW$_{10}$·35H$_2$O** *(green),* ^{166}**ErW$_{10}$·35H$_2$O** *(orange) and* **ErW$_{10}$·35H$_2$O** *(black). The inset shows the field variation of the magnetization at 2 K.*

C. Isotopic effect in the relaxation mechanism

F. Luis *et al.* already studied this system. [141] In their work, the relaxation mechanisms of the magnetization were studied while magnetic dilution and isotopic enrichment of a nuclear spin active erbium was used. They concluded that in this case, the relaxation rate was decreased by an external magnetic bias (H_{DC}) and the hyperfine interactions enhanced by increasing the concentration of Er^{3+} ion (increasing the dipole interactions).

In the present work, we go a step further in including to the study a nuclear spin free ^{166}Er-based compound. AC magnetic measurements are performed for the three isotopologues and their dynamic magnetic properties are presented and compared to those in the literature.

The frequency dependence of the magnetic susceptibility was studied, Figure 5. 4, for temperatures between 2 and 6.25 K under no applied magnetic field. The out-of-phase component of the three isotopologues passes through a maximum, indication of slow magnetic relaxation. The black vertical lines in Figure 5.3 are used to compare the position of the maxima at 3.5 K for the three isotopologues. This temperature corresponds to the limit for which the nuclear spin active system (**^{167}ErW$_{10}$·35H$_2$O**) passes from a Gaussian characteristic peak (one single relaxation process, α=0) to a shoulder shaped curve (infinite number of relaxation process, α=1). At 3.5 K, the frequency at which the system relaxes is very close for both $^{166}Er^{3+}$ (I= 0) and Er^{3+} analogues (83 Hz and 92 Hz, respectively) and considerably faster than $^{167}Er^{3+}$ (I= 7/2, 10 Hz). The relaxation time τ was extracted at each temperature using an extended Debye model (Annex 3, table A3.12-A3.14) by fitting simultaneously the frequency dependence of χ_M' and χ_M''. The normalized Argand diagram are represented on the third column in Figure 5. 4. The resulting plots adopt a semicircle shape giving a narrower distribution of the relaxation time for the nuclear spin free (0.06<α<0.14) and wider for the nuclear spin active metal center (0.04<α<0.24), while the natural erbium is placed in between both (0.03<α<0.24). However, α values from **^{167}ErW$_{10}$·35H$_2$O** are expected to be even higher as under 4 K, the relaxation mechanism that governs the system is much more complicated as the probability of relaxation is equally distributed along the frequency windows, and as a consequence, the relaxations curves could not be fitted following the extended Debye model.

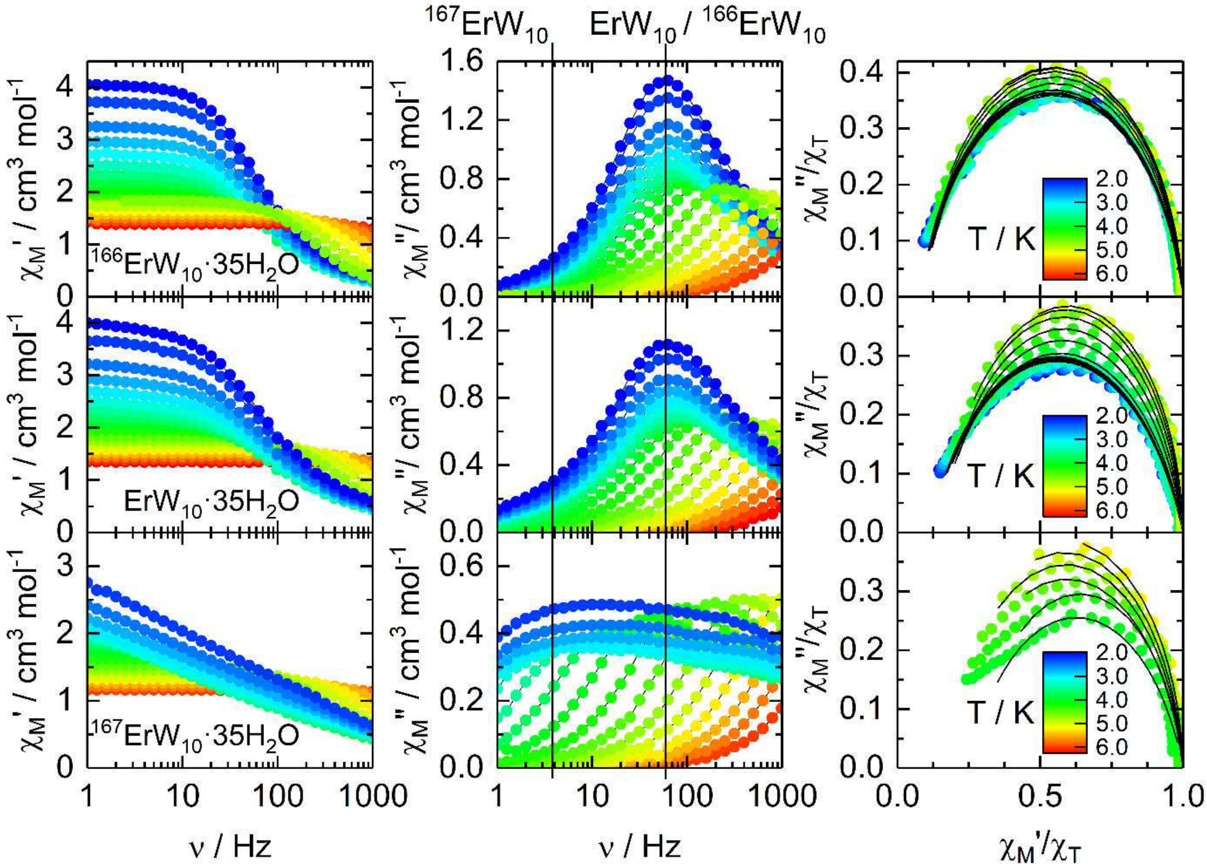

Figure 5. 4. AC measurements of the three compounds under zero- applied magnetic field, for temperatures between 2 and 6.25 K. First column corresponds to the in-phase susceptibility component (χ_M'); second, the out-of-phase susceptibility component (χ_M''). Vertical full lines signal the frequency position of the maxima at 3.5 K; and third, the Argand diagram with the black lines resulted from the best fitted curves using the extended Debye model.

The representation of the temperature dependence of the relaxation time of the magnetization for the three are shown in Figure 5. 5. However, for **^{167}ErW$_{10}$·35H$_2$O** (green curve) and below 4 K, the different τ where found by peaking the position of maxima intensity in the χ_M'' vs. v plots, with $\tau = 1/2\pi\nu$. These lasts points, give us information about a possible temperature independent regime at lower temperature but the isotopic effect is already determined at higher temperatures.

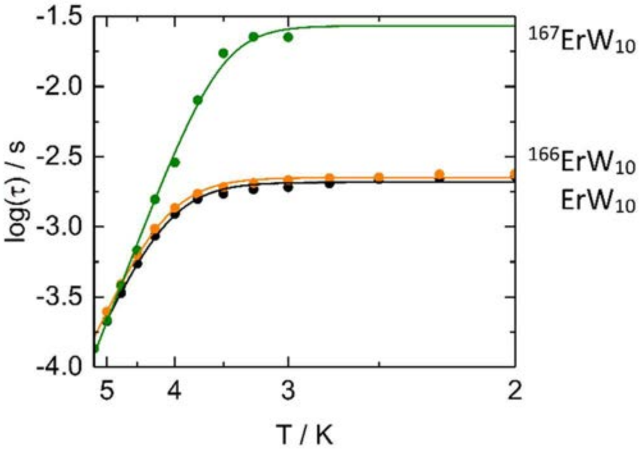

Figure 5. 5. Temperature dependence of the relaxation time between 2 and 15 K at H_{DC}= 0 Oe for ***$^{167}ErW_{10}{\cdot}35H_2O$*** *(green),* ***$^{166}ErW_{10}{\cdot}35H_2O$*** *(orange) and* ***$ErW_{10}{\cdot}35H_2O$*** *(black). Full lines correspond to the best fitted curves.*

The temperature dependences follow a modified Arrhenius law (Equation 3.1)[157] defined by the contribution of an Orbach regime up to 4 K, and a QTM for lower temperatures. The intrinsic relaxation time τ_0 ($1.1{\cdot}10^{-8}$ s) and the energy barrier (50 K) remain invariable for the three isotopologues while the temperature independent relaxation time shows isotopic dependence. As already predicted by the χ_M'' vs. v curves, the major contribution of the nuclear spin free component to the natural mixture hinder the possible isotopic effect for **$^{166}ErW_{10}{\cdot}35H_2O$** and **$ErW_{10}{\cdot}35H_2O$** ($\tau_{TI}$= 2.24 ms). Thus, whereas the previous show a similar relaxation mechanism, the isotope I= 7/2 shows a greater distribution of the relaxation relaxing already 8 times slower (τ_{TI}= 16 ms) at 3.5 K.

Table 5. 2. Best fitted parameters for the three isotopologues.

	$^{166}ErW_{10}{\cdot}35H_2O$ (I= 0)	***$ErW_{10}{\cdot}35H_2O$***	***$^{167}ErW_{10}{\cdot}35H_2O$ (I= 7/2)***
Δ / K	50 ± 2	50 ± 3	58 ± 2
τ_0 / s	$(1.3 \pm 0.4){\cdot}10^{-8}$	$(1.1 \pm 0.6){\cdot}10^{-8}$	$(2 \pm 1){\cdot}10^{-9}$
τ_{TI} / s	$(2.24 \pm 0.03){\cdot}10^{-3}$	$(2.08 \pm 0.05){\cdot}10^{-3}$	$(2.7 \pm 0.3){\cdot}10^{-2}$

As already seen in previous chapters, by applying a H_{DC}, the different contributions to the relaxation coming from the hyperfine or the dipolar interactions can be easily suppressed. The most interesting sample for the field dependence study is the isotopically enriched **$^{167}ErW_{10}{\cdot}35H_2O$**, due to the limited information about its behavior at low temperature. Hence, measurements were performed at 3.5 K, which corresponds to the QTM-region and a large distribution of the relaxation. The χ_M vs. ν curves were studied under different magnetic fields from 0 to 2 kOe and are represented in Figure 5. 6.

At zero magnetic field, the χ_M'' component show a large distribution in the delay of the magnetic susceptibility, as previously seen in Figure 5. 4. By applying a small H_{DC}, this large distribution is minimized, and a typical peak signal reappears at the same time that the maximum is shifted to lower frequencies. The first consequence could point to an isotopic origin of the low temperature distribution, whereas the second corresponds to the progressively suppression of the QTM. However, as it can be seen from 400 Oe up to 2 kOe, this large contribution seems to change into two different contributions, given by a defined peak (≈ 1.6 Hz) and a shoulder at lower frequencies. If we focus on the main peak, an optimal magnetic field can be set from 600 to 1200 Oe. At these H_{DC}, the main peak is effectively shifted to 1.6 Hz.

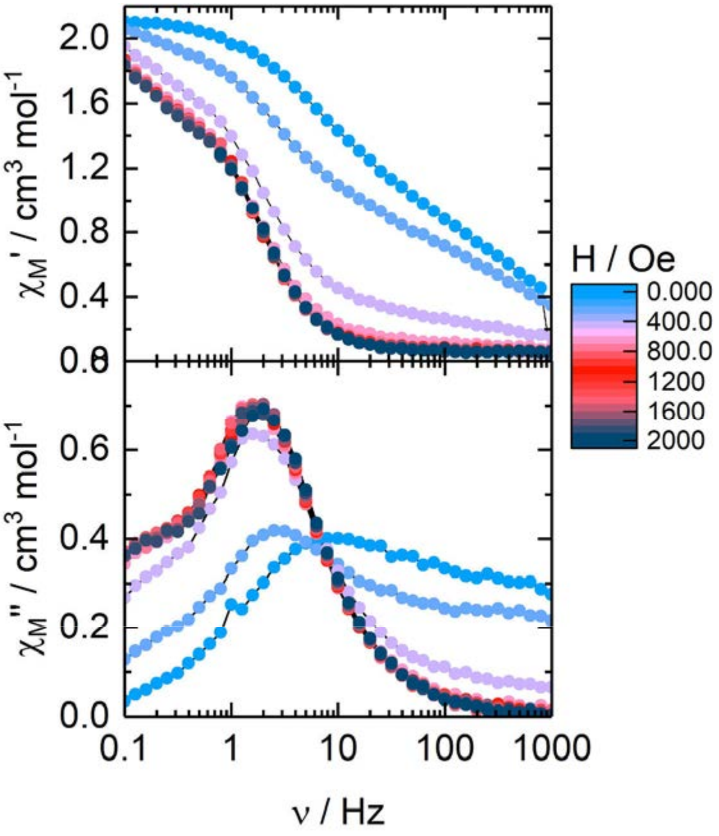

*Figure 5. 6. Field dependence of the χ_M' and χ_M'' as a function of the frequency (ν) at 3.5 K for **^{167}ErW$_{10}$·35H$_2$O**.*

By applying an optimal magnetic field, the temperature independent regime of the relaxation is suppressed, thus meaning that the difference given by the isotopic enrichment disappears. For that reason, the ac properties under magnetic applied field are just studied for the natural complex **$ErW_{10}·35H_2O$** (Figure 5. 7; Annex 3, table A3.15) and can be extrapolated for the other two systems. That can be proved also by comparing the curve of the previous Figure 5. 6 at 1200 Oe (**^{167}ErW$_{10}$·35H$_2$O**) (neglecting the appearance of the second peak) and the curve at 3.5 K of Figure 5.6 (**ErW$_{10}$·35H$_2$O**).

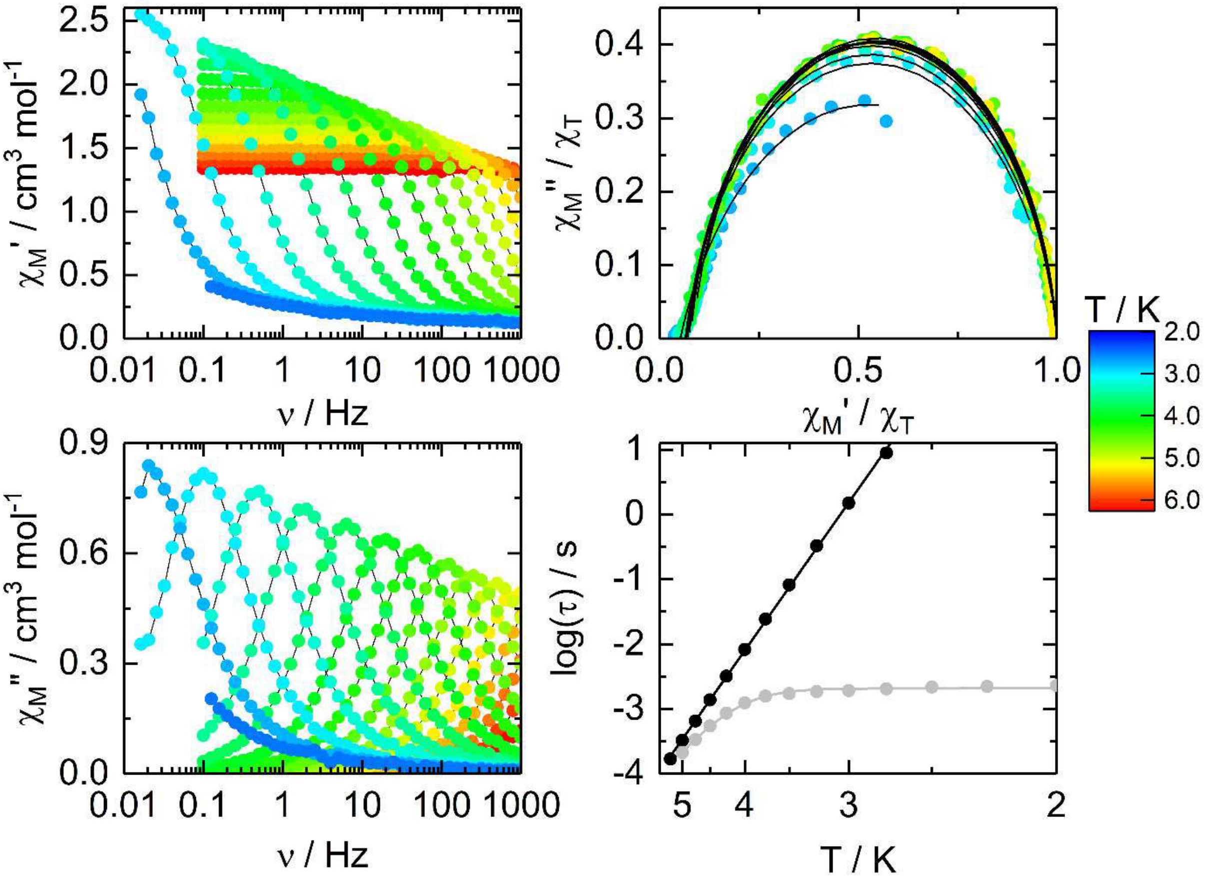

*Figure 5. 7. AC measurements of **ErW$_{10}$·35H$_2$O** under H$_{DC}$= 1200 Oe for temperatures between 2 and 6.25 K. First column corresponds to the in-phase susceptibility component (χ_M') and the out-of-phase susceptibility component (χ_M''). Second column the Argand diagram and Arrhenius plot are represented, with the full lines corresponding to the best fitted curves.*

As seen in Figure 5. 7, the application of the H$_{DC}$ results in a relaxation of the magnetization with exponential dependence on the temperature, meaning a definition of the Arrhenius law with only the contribution of the Orbach process (Δ= 63.0 ± 0.4 K and τ_0= (1.1 ± 0.1)·10^{-9} s).

To conclude this part, as already reported by F. Luis *et al.*[141], it seems that the hyperfine interactions in that system contributes to the slow of the relaxation but the affirmation is difficult as the relaxation path is clearly not followed by one single relaxation but a great distribution. For what concerns the nuclear spin free erbium, the small difference in the response are not sufficient to confirm that both relaxation curves are different. At the same time, much difference could not be expected, as 77 % of the natural cation is already *I*= 0.

D. Solvation effect on the magnetic properties

D.1. Water molecules and the structure:

Water molecules in this system occupy an important place in the crystallographic structure (Figure 5. 8). They are placed creating an octahedral coordination around the counter Na^+ ions and forming a framework around the inorganic cluster. In terms of mass, these water molecules represent 18.4 % of the total molecular mass of the sample. Hence, some may wonder if water molecules can be removed and how it affects the electronic properties of the system.

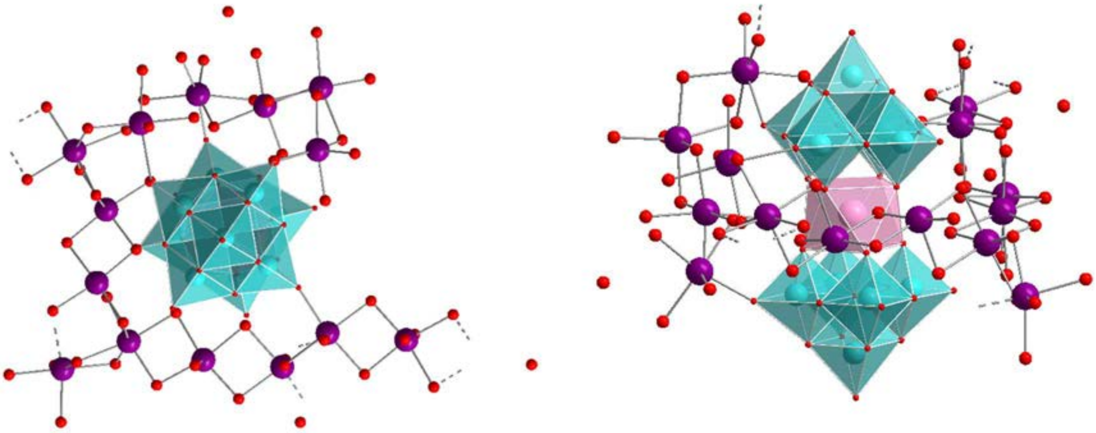

Figure 5. 8. Visualization of the lattice of sodium and water molecules surrounding the ErW_{10}.

A more detailed observation of the XRD structure (Figure 5. 9) make us distinguish three different types of water molecules. They can be found as free solvent molecules in the structure (3 H_2O, in blue) but also linked to the counter-ions, bounded by one (terminal (15 H_2O), in green) or two (bridged (17 H_2O), in red) oxygen atoms. Moreover, weak interactions of hydrogen type can have a minor but existent role. O···H distances between 2.6 and 2.9 Å, give rise to hydrogen bonding that could differ in the way water molecules are released inside the same type of water molecules.

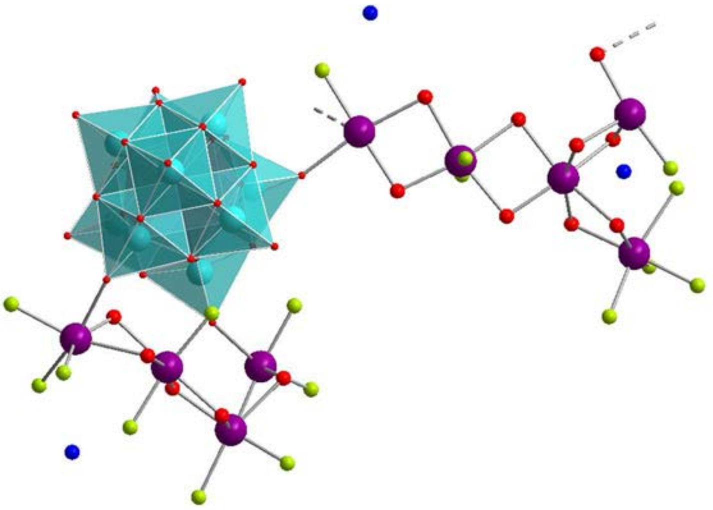

Figure 5. 9. XRD structure of **ErW_{10}· 35 H_2O**, *with different colors of water molecules depending of the coordination mode i.e. free (blue), terminal (green) and bridged (red).*

Taking into account the three different groups of water molecules (free, terminal and bridged) and the fact that inside each group the hydrogen bonds are not equally distributed to all the molecules, the existence of three main departures can be proposed and the possibility of intermediate ones are not discard. While heating the sample, the release of water should occur following the direction of increase in the bonding strength (free to bridged molecules). In order to have a greater insight of this evolution, a thermogravimetric analysis is performed. This, coupled to a mass spectrometer, verifies that the loss of weight comes only from the loss of water (m=18; Annex 4, Figure A4.1). The heat flow and the loss of weight are observed while increasing the temperature from 30°C to 135°C, as shown in Figure 5. 10.

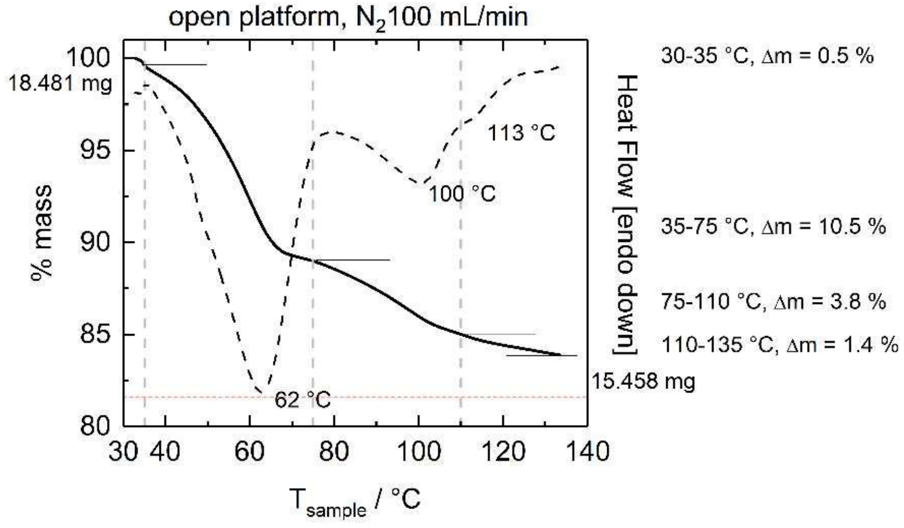

Figure 5. 10. Temperature dependence of the loss of mass (%, continuous black line) and heat flow in **ErW_{10}·$35H_2O$** *(dashed black line). The grey dashed lines separate the different stages of the departure, and the red dashed line the limit when all the water molecules have left the sample.*

In order to remove the water molecules, the system needs to absorb sufficient energy in order to break the interactions that retain them. Once this energy is reached, it is followed by an exothermic process in which the system comes back to the state of minimum energy. This moment is monitored in order to differentiate between the different stages.

Four general stages are determined. At room temperature, the solvent molecules already escape from the structure. For that reason, at 35°C we consider that the three free solvent molecules have been released. The second stage comprises temperatures between 35 and 75 °C, which corresponds to the terminal molecules leaving the structure. Finally, the two last stages can be summarized as the departure of all the bridged molecules: first, from 75 °C to 110 °C, with 5 remaining molecules, and then beyond 110°C, the dehydration is completed.

Single crystal X-Ray diffraction and the results obtained by TGA gave us information about the starting point of the product and the way the molecules are firstly distributed and the different departures of water. However, in order to have information about future states of the sample when heating some X-Ray Diffraction must be performed while heating the sample through the different stages. In Figure 5. 11, the diffractogram of the powdered sample at room temperature is compared to a powder simulated curve from the crystallographic structure at low temperature (150 K) with Mercury (Cambridge CCDC 4.0.0). The different peak positions are related with the interatomic distances, according to Bragg's Law ($n\lambda = 2d sin\theta$, where: n is an integer number; λ, the wavelength of the X-ray; d, the spacing between the planes in the atomic lattice; and θ, the angle between the incident X-ray beam and the scattering planes). Hence, the increase of temperature results in a small increase of the distances, which is translated into a slight displacement to smaller θ values. A small deviation between both curves apart from the small displacement, could be sign of a beginning of dehydration already at room temperature.

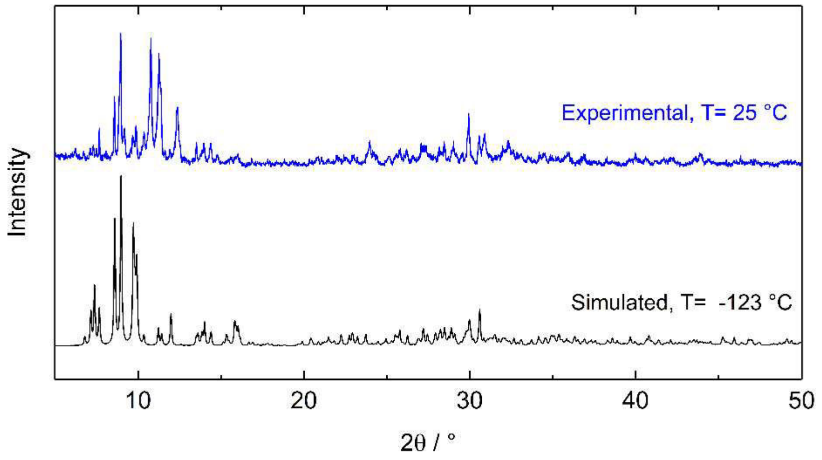

Figure 5. 11. Comparison of the crystallographic pattern between the crystal XRD simulation at -123°C, and the powder diffractogram at 25°C of ***$ErW_{10}·35H_2O$****.*

Several crystallographic patterns have been recorded by increasing the temperature from 25°C up to 200°C. If we observe the evolution of the diffractogram with the heating, we can observe the gradual loss of its crystallinity until being transformed into an amorphous powder. In Figure 5. 12, different temperatures have been carefully selected in order to point these structural changes. First, the peaks located at small angles are the first to disappear, those corresponding to the more distant atomic positions. Then, for temperatures greater than 115°C, the system losses completely any sign of crystallinity.

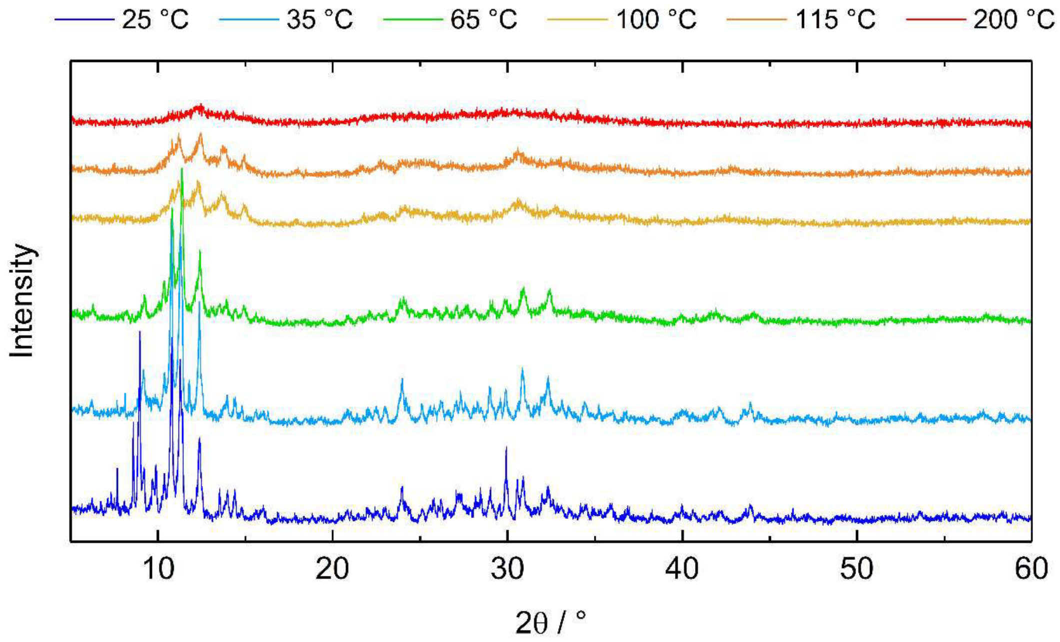

Figure 5. 12. Temperature evolution of the XRD pattern of ***$ErW_{10}·35H_2O$*** *from 25 to 200°C.*

Surprisingly, if the dehydrated sample is let in a humid environment overnight, it recovers most of its initial weight. Different TGA cycles after rehydration prove that the sample recovers its water content, and the different heat profiles are reproducible for temperatures below 100°C (Figure 5. 13). Above this temperature, the two different phases (100°C and 113°C) are changed. In Annex 4 (Figure A4.2), it can be seen as those transitions at higher temperature are not only shifted at each rehydration but also depend on the rehydration procedure (if the time of exposure or the way the sample is hydrated) and can appear and disappear indistinctly.

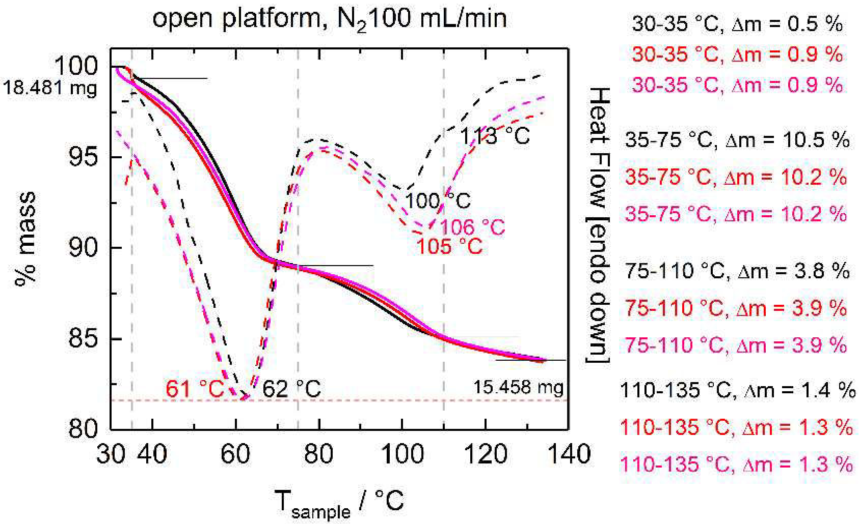

Figure 5. 13. Different cycles of TGA of **$ErW_{10}\cdot 35H_2O$**. *The initial sample is represented in black, the red curve corresponds to the first rehydrated sample and in pink the second. The grey dashed lines separate the different losses and the red dashed line the limit in the absence of water molecules.*

Nevertheless, even if the heat flow curves are slightly varying, the mass evolution for the different cycles is maintained. For what concerns the crystallographic structure, different cycles of the dehydration have been followed as for the TGA. From the comparison of Figure 5. 14, it can be seen that the system recovers the crystallinity state, but also that it is different from the initial state. Consequently, after rehydration the water molecules occupy different places following another distribution of energy minimum. Different rehydration process give rise to a wide range of possible crystallographic structures (other images in Annex 1, Figure A1.1), which at the same time will offer different stages of dehydration through temperature.

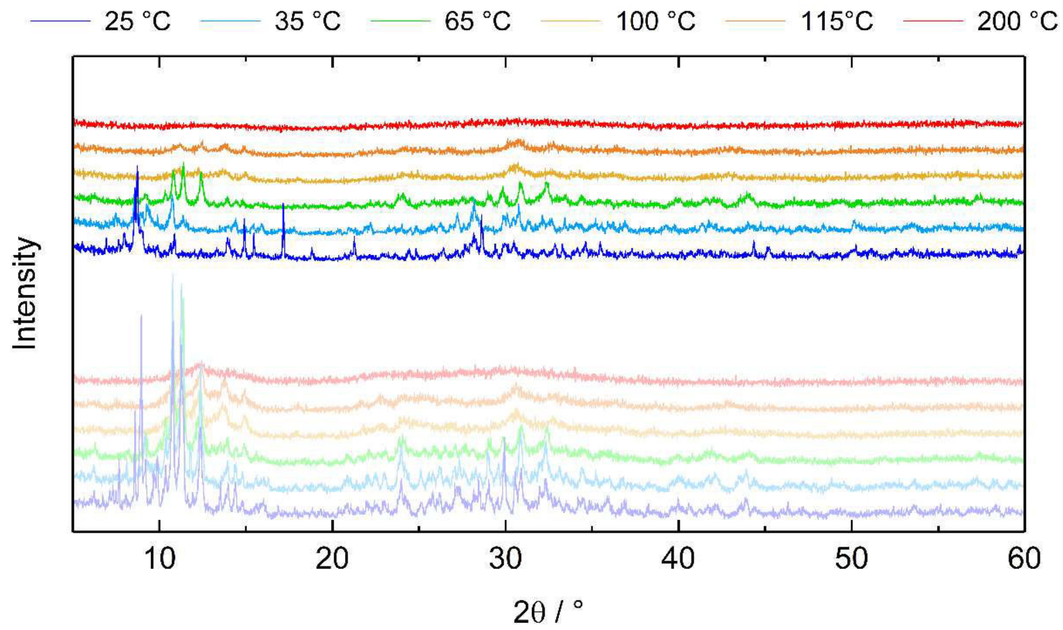

Figure 5. 14. Temperature evolution of the XRD pattern of ***$ErW_{10}·35H_2O$*** *from 25 to 200 °C. Light colors correspond to the first heat of the sample and bright colors to the second heat after rehydration procedure.*

Owing to the fact that these changes in the inorganic framework produce real changes in the crystallographic structure, we suspect that the magnetic properties are also sensitive to those changes.

D.2. Switching the SMM properties by playing with the water molecules

A full study of the magnetic properties has been realized for the **$^{166}ErW_{10}·35H_2O$** compound passing through different cycles of solvation and desolvation. DC magnetic measurements (Figure 5. 15) show the same value at saturation, which is expected as the electronic configuration does not suffer any change. However, some variation can be seen on the magnetic response at low temperature, meaning different splitting of the ground state multiplet in the low energy region.

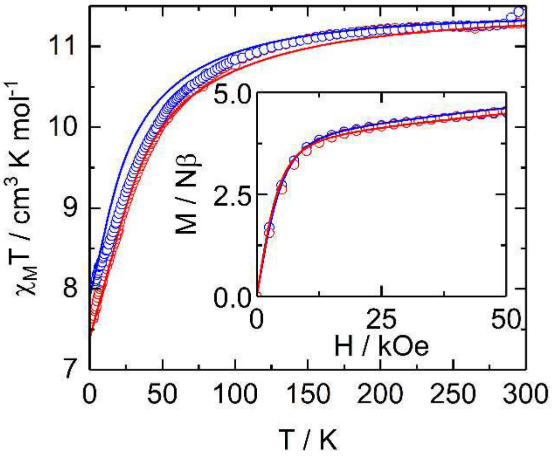

Figure 5. 15. Comparison of the DC susceptibility of ^{166}**ErW$_{10}$·xH$_2$O** *from x= 35 (blue) to x= 6 (red). Continuous lines correspond to ab initio calculated curves.*

Concerning the dynamic study, summarized in Figure 5. 16, the frequency dependence of the magnetic susceptibility significantly changed depending on the history of the sample. That can be seen in the χ_M'' vs. ν plots, where the sample shows a slow relaxation of the magnetization for ^{166}**ErW$_{10}$·35H$_2$O** (hydrated and rehydrated form) but a fast relaxation for ^{166}**ErW$_{10}$·5H$_2$O** (dehydrated form). At the beginning, the sample shows a frequency dependency which leads to a maximum at 2 K at 63 Hz on χ_M'' vs. ν plot. After rehydration, the frequency dependence lost with the dehydration reappears. Although, this slow relaxation shows a greater distribution given by wider peaks and is shifted to higher frequencies by a factor of 2 (126 Hz). This difference in the SMM properties was expected as by reducing the number of water molecules the symmetry of the coordination sphere changes and thus, the electronic distribution around the metal cation too. By changing the electronic distribution coming from the ligand, the stabilization of the M_J sublevels can be different, and thus the SMM behavior. This will be studied in the next section when the correlation between the structure and the magnetic properties is studied by ab initio calculations.

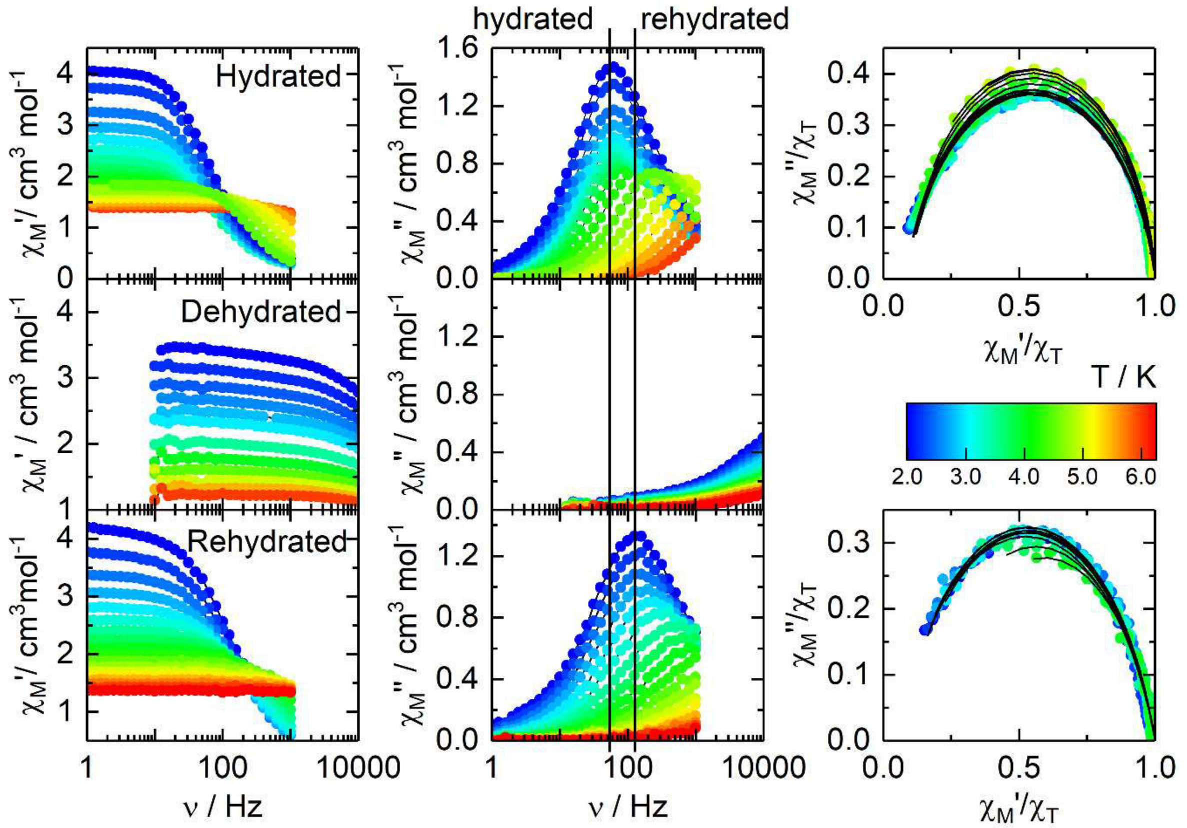

Figure 5. 16. AC measurements of ^{166}**ErW$_{10}$·35H$_2$O** under zero magnetic field, for temperatures between 2 and 6.25 K. First column corresponds to the in-phase susceptibility component (χ_M'); second, the out-of-phase susceptibility component (χ_M''), with the vertical full lines corresponding to the frequency position of the maxima at 2 K; and third, the Argand diagram is represented, with the full lines corresponding to the best fitted curves.

For the hydrated and rehydrated forms, the relaxation times have been extracted as a function of the temperature (Figure 5. 17) following the extended Debye model and the relaxation mechanism governing each case have been analyzed (Annex 3, tables A3.12 and A3.16).

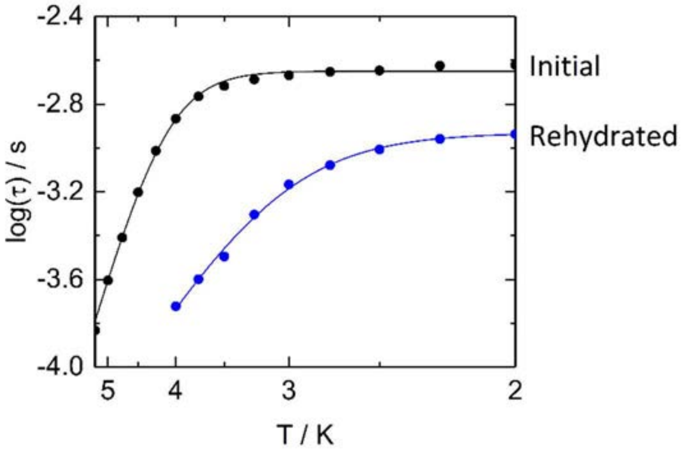

Figure 5. 17. Comparison of the relaxation times of the magnetization as a function of the temperature for initial (black) and rehydrated (blue) form of ^{166}**ErW$_{10}$·35H$_2$O**, with the full lines corresponding to the best fitted curves.

There is a big difference between both relaxation curves giving the certitude that the processes participating to the relaxation mechanism or their global contribution are different. The hydrated sample (black curve) shows a relaxation mechanisms described by the appearance of two well defined regimes: an exponential temperature-dependent one above 4 K, and a temperature- independent one for temperatures below 4 K. After rehydration (blue curve), the second region is not that clearly described as the temperature-dependent contribution is clearly reduced. The best fitted parameters lead to a relaxation mechanism defined by the contribution of Orbach and QTM. Even though, as it can be seen in Table 5. 3, the relaxation rates differ from one to the other.

Table 5. 3. Best fitted parameters for the hydrated and rehydrated samples $^{166}\mathbf{ErW_{10}\cdot 35H_2O}$.

	Hydrated	*Rehydrated*
Δ / K	50 ± 3	23 ± 1
τ_0 / s	$(1.1 \pm 0.6)\cdot 10^{-8}$	$(7 \pm 2)\cdot 10^{-7}$
τ_{TI} / s	$(2.08 \pm 0.05)\cdot 10^{-3}$	$(1.17 \pm 0.04)\cdot 10^{-3}$

As a result, the role of Orbach in the general relaxation expression is greater for the hydrated form than for the rehydrated, and the opposite when talking about the QTM.

To observe the relaxation phenomena as a function of the external magnetic field, different hysteresis loops have been measured at 2 K for hydrated and dehydrated samples. The characteristic hysteresis is present for both hydrated and rehydrated samples. This is strangled at zero-field because of the fast relaxation giving rise to the classical butterfly shape. In Figure 5. 18, the three different situations, already presented in Figure 5. 16, have been considered. We can conclude that $^{166}\mathbf{ErW_{10}\cdot 35H_2O}$ (hydrated and rehydrated) show some bistability depending on the field's history, while $^{166}\mathbf{ErW_{10}\cdot 5H_2O}$ do not show hysteresis at any field. Again, different rearrangements of water molecules give rise to butterfly shaped hysteresis of greater or smaller aperture while suppressing this water the complex does not behave as an SMM.

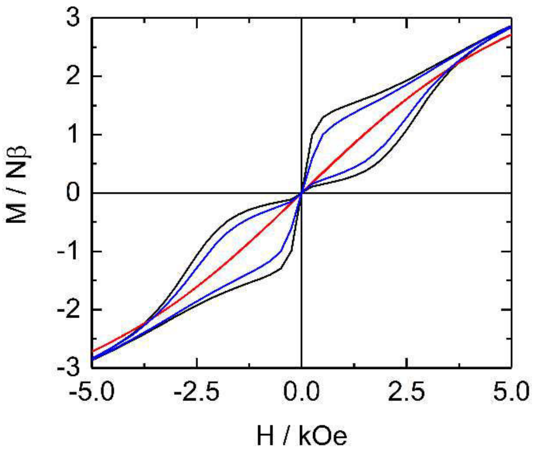

Figure 5. 18. Magnetic hysteresis loops at 2 K and at a sweep rate of 16 Oe s^{-1} of ***^{166}ErW$_{10}$ xH$_2$O****. The black curve correspond to the hydrated system, the red curve to the dehydrated system and the blue, the rehydrated.*

The same sample has been submitted to three rehydration processes before being measured. In Figure 5. 19 the 2 K susceptibility curve has been compared for several hydrated states of **^{166}ErW$_{10}$·xH$_2$O**: the initial crystallized state (in black), the dehydrated sample (in red), the rehydrated sample (blue) and finally, the sample following three dehydration/rehydration cycles (in green).

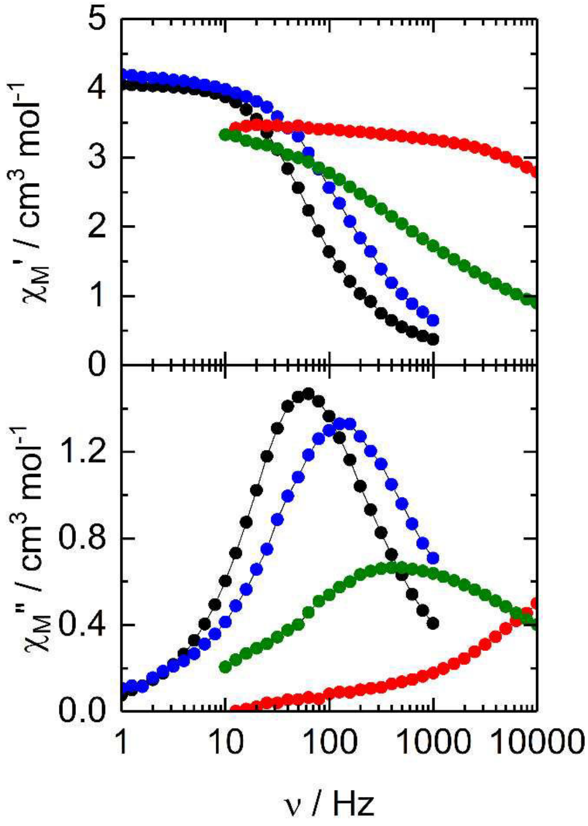

Figure 5. 19. Comparison of the AC susceptibility of ***^{166}ErW$_{10}$·xH$_2$O*** *at different hydrated states under zero magnetic field and at 2 K. Black circles correspond to the initial sample; the blue to the first hydration; the green to the third hydration; and the red to the dehydrated sample.*

By reproducing the rehydration cycles, the susceptibility curve tends to widen, thus meaning that the relaxation phenomenon is comprised in a larger frequency windows. At the same time, the maximum shifts to higher frequencies (398 Hz), denoting a higher contribution of the transverse components of the anisotropy tensor.

Finally, for what it has been presented up to now, the magnetic properties are directly correlated to the structure and thus, to the water molecules. Nevertheless, which is the real role of the water molecules hasn't been still proven. In other words, the water molecules could interfere in different ways to the electronic density of the coordination sphere, whereas it is only structural manner (they maintain to a certain distance the Na^+ counter ions) or they are involved in the electronic distribution of the system. The hydrogen atoms in the water molecules have some nuclear spin which can interfere in the electronic structure, in order to verify (discard) the existent role of the hydrogen nuclei, the water molecules have been replaced by their analogue deuterated, and the dynamic study of the magnetic susceptibility has been performed.

Figure 5. 20 faces the two different susceptibility responses from 2 to 6 K and zero magnetic field. As expected, no clear shift in the out-of-phase maxima is seen between **$ErW_{10}{\cdot}35H_2O$** (63 Hz) and **$ErW_{10}{\cdot}35D_2O$** (75 Hz) at 2 K. Thus, suggesting that the ^1H nuclei in water molecules do not represent an important factor in the physical properties of the complex, but maybe the electrostatic interactions with sodium framework do.

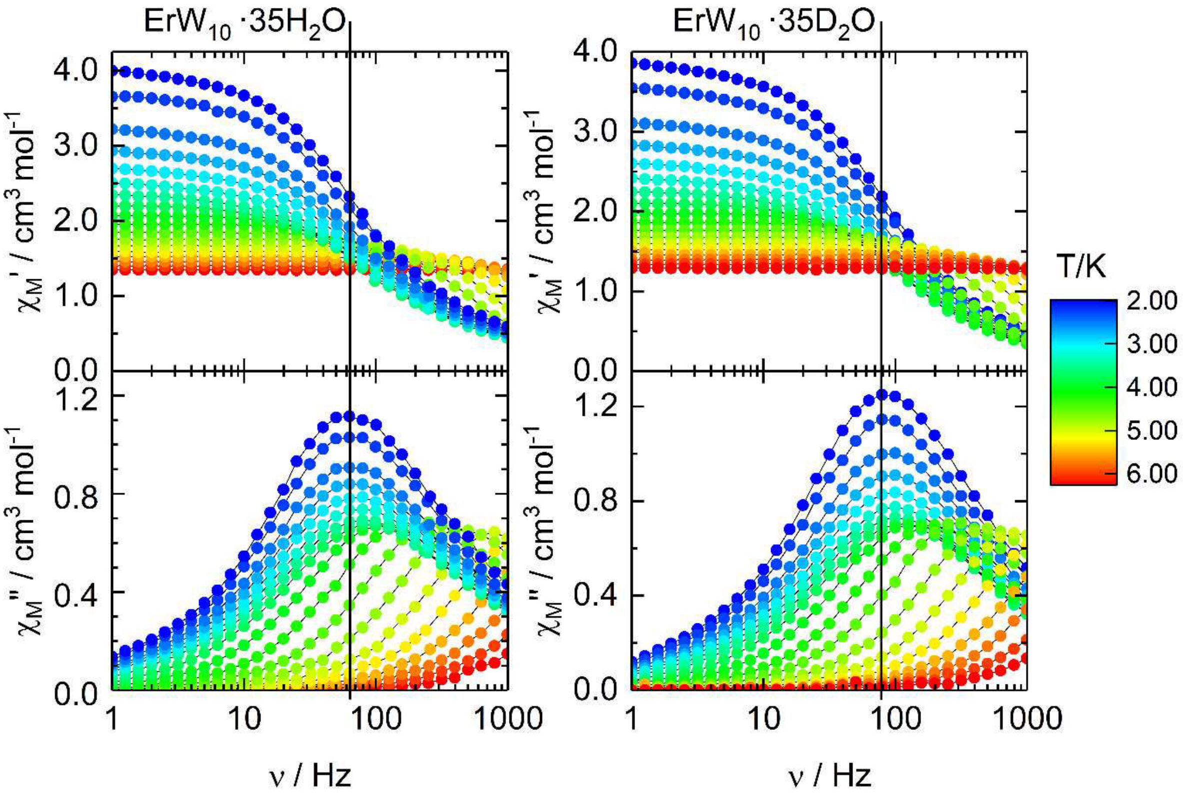

Figure 5. 20. Comparison of the temperature dependence of the AC Susceptibility for ***ErW$_{10}$·35H$_2$O*** *and* ***ErW$_{10}$·35D$_2$O****, from 2 to 6.25 K at 0 Oe.*

Other studies with deuterated water were reported by Vonci *et al.* arriving to the same conclusions about the importance of the water molecules.[158]

D.3. Theoretical approach: structure and magnetism

In order to rationalize the experimental observations, computational calculations have been done in the *ISCR* by Vincent Montigaud and Boris Le Guennic. The evolution of the structure with the loss of water molecules is studied by periodic DFT calculations taking into account the number of water molecules found in the different stages during the thermal analyses.

Figure 5. 21 show the evolution of the structure as a function of the water loss, and the corresponding cell parameters are compared in Table 5. 4. As qualitatively observed with the evolution of the diffractogram with the temperature, the removal of water molecules from the structure causes a change in the cell parameters. Taking out the free water molecules generates a small contraction of the unit cell, but no perceptible changes in the geometry of the complex. Further water molecules loss causes stronger contractions in the unit cell which

provokes a blending in the geometry of the cluster, starting from O22-Er-O36 (Figure 5. 2, with the O, in the opposite of the lacunar space) angle of 178 ° and diminishing down to 152°.

Table 5. 4. Evolution of the different unit cell parameters through dehydration of the complex.

ErW_{10} $\cdot xH_2O$	*Unit cell parameters / Deviation from reference*					
	a / Å	*b / Å*	*c / Å*	*α / °*	*β / °*	*γ / °*
x= 35	12.36	13.06	20.48	81.7	71.7	88.1
x= 30-31	12.35 / 3%	12.78 / 2%	20.09 / 2%	82.3	72.7	88.3
x= 20-21	11.71 / 8 %	12.20 / 7%	18.45 / 10 %	85.1	68.4	89.0
x= 5-6	11.54 / 7 %	13.83 / 6 %	17.19 / 19 %	77.9	66.3	94.6
x= 0	11.15 / 10%	12.18 / 7%	15.83 / 30 %	79.9	66.7	113.2

This contraction of the structure is given by the different ionic interactions. Once the water molecules leave the structure, the free sodium cations tend to feel attracted to the oxygens coordinated to the erbium. More water molecules are lost, more these counter ions approach the coordination sphere of the erbium and smaller will be the defined unit cell. However, by coming closer to the oxygen, the counter ions feel at the same time the repulsion exerted by the positive erbium as well as the neighboring Na^+, thus favoring the blending and the loss of the cluster structure in the extreme circumstances.

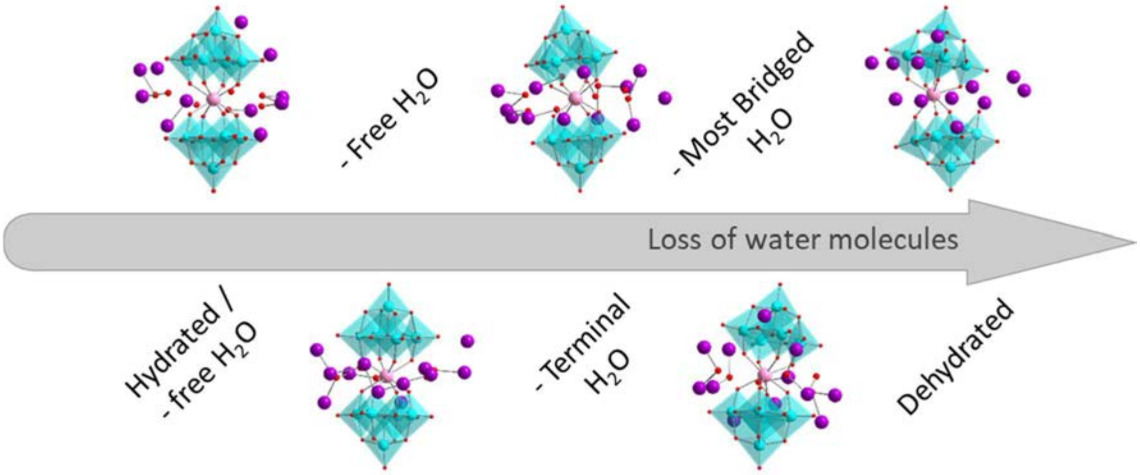

Figure 5. 21. Representation of the changes in the structure after the different water departures. Images are obtained by applying periodic DFT calculations to the crystallographic structure once removed the molecules determined experimentally.

Taking the optimized structures from the ab initio calculations, the symmetry in the coordination sphere has been studied by SHAPE Analysis.[155] Table 5. 5 summarizes the evolution of the symmetry with the loss of water molecules, highlighting the reduction of the symmetry as the water molecules are removed. The three closest symmetries and the deviation to the ideal symmetry are exposed in Table 5.5. It demonstrates the increase of deviation from the ideal square antiprism (D_{4d}) symmetry from 0.046 to 1.412, before breaking the geometry.

Table 5. 5. First three closest symmetries for the ErO_8 coordination polyhedron as water molecules are being removed.

$ErW_{10}·xH_2O$	*$CShM_{SAPR-8}$ (square antiprism D_{4d})*	*$CShM_{TDD-8}$ (triangular dodecahedron D_{2d})*	*$CShM_{BTPR-8}$ (biaugmented trigonal prism C_{2v})*
x= 35	0.046	2.647	2.078
x= 30-31	0.123	2.548	2.218
x= 20-21	0.653	2.169	2.789
x= 5-6	1.412	2.177	3.400
x= 0	2.363	2.084	2.328

The magnetic properties of mononuclear transition metal complexes are correlated to the relative energy spacing of the lowest lying magnetic sublevels, as well as the composition of those. The crystal field splitting, g-tensor components and wavefunction composition for the ground state multiplet ($^4I_{15/2}$) for the Er^{3+} cation have been determined for the different hydration levels (Table 5. 6– Table 5. 7). The calculated crystal field splitting for the hydrated (x= 35) and dehydrated (x= 5- 6) form of the ground multiplet state leads to a calculated $\chi_M T$ product which is in agreement with the experimental data (Figure 5.13). The composition of the ground doublet reproduces finely the experimental magnetization at 2 K for both cases.

As presented in Table 5.6, the ground state doublet of both forms is composed mainly of M_J= |±13/2> with lower contribution of M_J= |±15/2> and |±11/2> for both cases, but with different distribution of sublevels: for the hydrated form, we have a ratio of 0.58/ 0.29/ 0.11, while the dehydrated form is composed of 0.53/ 0.20/ 0.14, respectively. They are defined by the g-tensor values with a clear Ising behavior for the hydrated compound, g_Z= 15.9 (pure Ising: g_Z= 18) and negligible transverse components g_x= 0 and g_y= 0.01; and a lower z- value g_Z= 15.36 and greater transverse components, g_x= 0.33 and g_y= 0.71, for the last. This description of the ground state suggests the possibility of relaxation through QTM for both cases, but more present in the second.

*Table 5. 6. Computed ground state and first excited state energy levels (the ground state is set at zero), composition of the g-tensor and the main components of the Kramers doublets wavefunctions of the ground-state multiplet of the Er^{3+} center from **$ErW_{10}{\cdot}35H_2O^{opt}$** and **$ErW_{10}{\cdot}6H_2O^{opt}$** (opt for optimized). *: Only the M_J contributions > 10% are shown.*

KD	*Energy / cm^{-1}*	g_X	g_Y	g_Z	*Wavefunction composition**
$ErW_{10}{\cdot}35\ H_2O$ (hydrated)					
GS	0.0	0.00	0.01	15.90	58 % |±13/2> + 29 % |±15/2> + 11 % |±11/2>
ES	29.1	0.02	0.00	17.90	70 % |±15/2> + 26 % |±13/2>
$ErW_{10}{\cdot}6\ H_2O$ (dehydrated)					
GS	0.0	0.33	0.71	15.36	53 % |±15/2> + 20 % |±13/2> + 14 % |±11/2>
ES	50.0	0.26	0.27	17.12	40 % |±15/2> + 36 % |±13/2> + 12 % |±11/2>

The calculated ground-state easy axis (Figure 5. 22) is positioned perpendicular to the plane of more negative charge of the coordination polyhedral, corresponding to the vertical direction. In parallel, by measuring the angular dependence of the magnetization on an oriented single crystal of **$^{166}ErW_{10}{\cdot}35H_2O$** at low temperature and in three perpendicular planes, by Angular-Resolved Magnetometry (details in Chapter II), and considering the effective spin ½ formalism, the orientation of the three components of the g-tensor has been determined. This revealed a uniaxial magnetic anisotropy with a g-tensor of 14.57 close to the expected value of 15.9 (18.4° between experimental data and calculations).

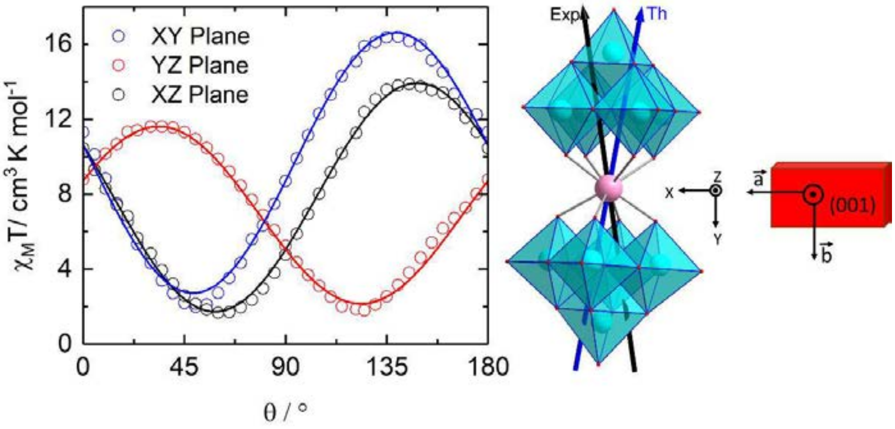

*Figure 5. 22. (Left) Angular dependence of $\chi_M T$ of a single crystal rotating in three perpendicular planes with H = 1 kOe at 2 K. Full lines are best-fitted curves; (right) crystallographic structure of **$^{166}ErW_{10}{\cdot}35H_2O$** orientation of the single crystal within the XYZ crystal reference frame.*

To sum up, while dehydrating the inorganic complex the theoretical calculations show us that the transverse components of the anisotropy gain more and more importance. The evolution of the ground state composition and g-factors is summarized in Table 5. 7, and it can be seen as the axial 15.9 value falls down to 14.23 from going from the hydrated system to the completely dehydrated. At the same time, g_x and g_z increase facilitating the QTM process.

*Table 5. 7. Computed energies, g-tensor components and wavefunction composition for Kramer' doublet ground-state for **$ErW_{10}·xH_2O$** at different stages of hydration.*

$ErW_{10}·xH_2O$	*g_X*	*g_Y*	*g_Z*	*Wavefunction composition (G.S.)*
x= 35	0.00	0.01	15.90	58 % |±13/2> + 29 % |±15/2> + 11 % |±11/2>
x= 30-31	0.02	0.03	17.21	87 % |±15/2>
x= 20-21	0.07	0.11	15.86	49 % |±15/2> + 28 % |±13/2> + 19 % |±11/2>
x= 6	0.33	0.71	15.36	53 % |±15/2> + 20 % |±13/2> + 14 % |±11/2>
x= 0	0.10	1.45	14.23	44 % |±11/2> + 44 % |±15/2>

Actually, if we were able to finely control the quantity of water in the crystallographic structure, the optimized system corresponds to x= 30-31. At that moment, the GS is mainly constituted by |±15/2> (87%), and as a result, if we look at the g_Z-component increased to 17.21.

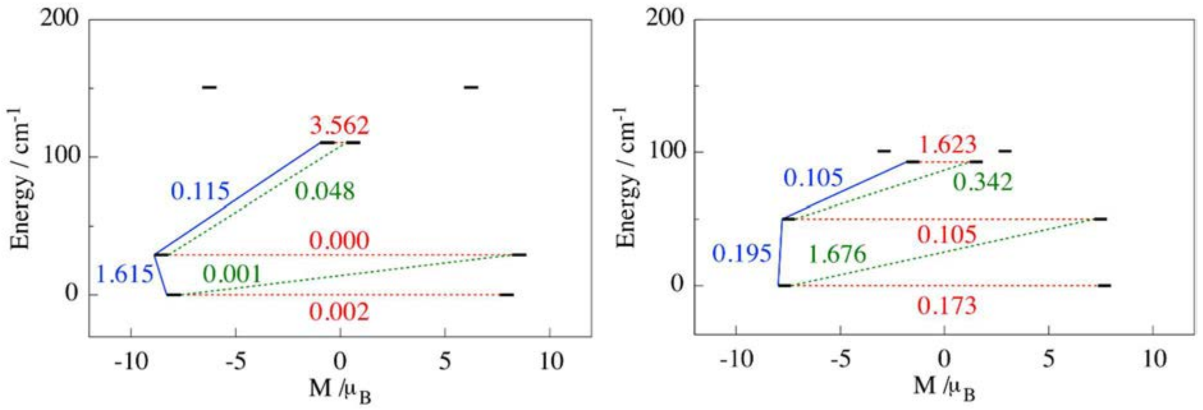

Figure 5. 23. Relaxation pathways of Er^{3+} centers for $ErW_{10}·35H_2O$ (left) and $ErW_{10}·6H_2O$ (right). Black lines are Kramers doublets as a function of computed magnetic moment, red arrows correspond to the QTM, in blue arrows to the Orbach and green, the TA-QTM relaxation pathways. The mean absolute values for the corresponding matrix element of transition magnetic dipole moment are represented with the numbers along the arrows

By observing the different relaxation pathways of Er^{3+} centers, in Figure 5. 23, for x=35 (left) and x= 6 (right), it can be confirmed as there is a greater probability of fast relaxation for the dehydrated compound, increasing the QTM (red dashed lines) from 0.002 to 0.173. At the same time, the values corresponding to the thermal dependent Orbach, diminish from 1.615 to 0.195.

III. CONCLUSIONS

To conclude, the full study of the SMM properties of the ^{A}**ErW$_{10}$** shows that this system has many parameters that need to be taken into account in order to well-characterized the physical properties. The elevated presence of water molecules which modifies the axiality of the anisotropy and the events happening in the quantum region of the ^{167}Er isotopes (the broad and dissymmetric ac magnetic susceptibility below 4 K), complicates an extensive description. Nevertheless, as already shown by F. Luis *et al.*[141], the performances of such SMM appear to be enhanced by increasing the hyperfine interactions (enriching with $^{167}Er^{3+}$ (I=5/2)) but the opposite influence cannot be confirmed as $^{166}Er^{3+}$ do not show any clear difference from the natural mixture.

This isotopic effect is in opposition with the resulted trends in the **Dy** and **Yb@Y** complexes. Being the Dy^{3+}, oblate and the Yb^{3+}, prolate, the possible explanation of different electronic density of the metal cation is discarded, thus pointing to a possible environmental influence (N_2O_6 vs O_8). Some magnetic dilution with **YW$_{10}$** is expected to be done in order to verify if the difference between the natural Er (constituted in 77 % of Er I=0) and the pure isotopic ^{166}Er (I= 0) in more isolated systems is real. Other clues could be extracted from studying at the same time the dilution in the ^{167}Er system, in order to understand if the phenomenon is dependent of the nuclear spin value and if it comes directly from the magnetic center. From the literature, a third Er-system has been chosen in order to certify if the results are reproducible to other Er-based SMM systems,[144] and in next chapter an entirely oxygenated coordinated system is presented, thus with Dy^{3+}.

On the other hand, $ErW_{10}{\cdot}xH_2O$ has shown SMM behavior dependent on hydration. Hence, by decreasing the number of water molecules in the structure, the complex is blended diminishing the anisotropy preferential direction and thus losing the SMM behavior. This switch behavior of the magnetic properties is shown to be reversible, even if the “ON” state appears with a multitude of possible redistributions with the same probability. Last, this SMM behavior is not coming from the water framework itself, but from the crystallographic structure of the cluster, determining a molecular origin of it. Indeed, the changes in this cationic and water molecule framework result in changes in the magnetic properties because, by approaching the positive charges to the cluster, the molecular structure of this one is modified.

REFERENCES:

[141] F. Luis, M. J. Martí-Perez, and O. Montero, *Phys. Rev. B*, **2010**, *82*, 060403(R).

[142] Q. Zhou, F. Yang, B. Xin, G. Zeng, X. Zhou, K. Liu, D. Ma, G. Li, Z. Shi and S. Feng, *Chem. Commun.*, **2013**, *49*, 8244.

[143] M. A. Aldamen, J. M. Clemente-Juan, E. Coronado, C. Martí-Gastaldo and A. Gaita-Ariño, *J. Am. Chem. Soc.,* **2008**, *130*, 8874.

[144] A. J. Brown, D. Pinkowicz, M. R. Saber, and K. R. Dunbar, *Angew. Chem. Int. Ed.*, **2015**, *54*, 5864.

[145] P. Zhang, J. Jung, L. Zhang, J. Tang, and B. Le Guennic, *Inorg. Chem.*, **2016**, *55*, 1905.

[146] H. Zhang, R. Nakanishi, K. Katoh, B. K. Breedlove, Y. Kitagawa, and M. Yamashita, *Dalton Trans.*, **2018**, *47*, 302.

[147] Carlos M. Granadeiro, B. de Castro, S. S. Balula, L. Cunha-Silva, *Polyhedron*, **2013**, *52*, 10.

[148] C. Boglio, G. Lemière, B. Hasenknopf, S. Thorimbert, E. Lacôte, and M. Malacria, *Angew. Chem. Int. Ed.*, **2016**, *45*, 3324.

[149] M. A. AlDamen, S. Cardona-Serra, J. M. Clemente-Juab, E. Coronado, A. Gaita-Ariño, F. Luis and O. Montero, *Inorg. Chem.,* **2009**, *48*, 3467.

[150] C. Boskovic, *Acc. Chem. Res.*, **2017**, *50*, 2205.

[151] R. D. Peacock, T.J. R. Weakley, *J. Chem. Soc. A.*, **1971**, 1836.

[152] S. Ghosh, S. Datta, L. Friend, S. Cardona-Serra, A. Gaita-Ariño, E. Coronado and S. Hill, *Dalton Trans.*, **2012**, *41*, 13697.

[153] J. D. Rinehart and J.R. Long, *Chem. Sci.*, **2011,** *2*, 2078.

[154] M. Vonci and C. Boskovic, *Aust. J. Chem.*, **2014**, *67*, 1542.

[155] M. Llunell, D. Casanova, J. Cirera, J. M. Bofill, P. Alemany, S. Alvarez, SHAPE (version 2.1), Barcelona, **2013**.

[156] O. Kahn, *Molecular Magnetism*, VCH, Weinheim, Germany, **1993**.

[157] A. Abragam and B. Bleany*, Electron Paramagnetic Resonance of Transition Ions*, Dover Publications, Inc., New York, **1986**.

[158] M. Vonci, M. J. Giansiracusa, W. Van den Heuvel, R. W. Gable, B. Moubaraki, K. S. Murray, D. Yu, R. A. Mole, A. Soncini and C. Boskovic, *Inorg. Chem.*, **2017**, *56*, 378.

CHAPTER VI

POLARIZATION EFFECT IN THE SMMS PROPERTIES AND ISOTOPIC BEHAVIOR

Until now the role of the internal field, created mostly by the hyperfine and dipolar interactions, has been studied in different system, thus changing the possible sources for which the influence of the internal field in SMM properties could change. This includes the comparison of different metal cations (oblate (Dy^{3+}) and prolates (Yb^{3+} and Er^{3+})) as well as different coordination spheres (N_2O_6 and O_8) in order to determine a common (or not) trend of the magnetic dilution and isotopic enrichment.

In the present chapter, we return to the Dy^{3+} cation as a metal center, this time exhibiting an entirely oxygenated surrounding (O_8). The particularity of this system, is the addition of diamagnetic cationic species (Zn^{2+}) in the second coordination sphere of the metal, in order to polarize the bridging oxygens and favor an Ising-type anisotropy, resulting in an enhancement of the SMM properties. The aim is to verify the performance of our two strategies (dilution and isotopic enrichment) in this type of polarized systems, as well as the common tendency with ***ErW_{10}*** *(O_8-coordinated) or not.*

I. INTRODUCTION

Most literature focused on creation of compounds containing both 3d and 4f cations for their application as SMMs and in luminescence. The Schiff bases resulted from the condensation of *o*-vanillin have been proposed as a good strategy for the heterometallic complexation, following a stepwise procedure: first, the formation of the mononuclear complex with the divalent metal ion (M= Cu^{2+}, Ni^{2+}, Zn^{2+}, *etc*…); followed by the coordination of the lanthanide cation (mainly Dy^{3+}, Tb^{3+} and Gd^{3+}).[159] In those systems, lanthanide coordination can be completed by the oxygen atoms from the accompanying anions (coming from the atoms precursors or solvent), or by a second ligand-M unit. The first, would lead to a [(ML)Ln] binuclear system whereas the second to a trinuclear [$(ML)_2Ln$] species and thus, depending on the chelating strength of the different species in solution.

Among the different M possibilities, we are interested in diamagnetic species. Different examples have been reported in the literature, in which the addition of Co^{3+}[160] or Zn^{2+}[161,162] diamagnetic species induces large charge polarization on the phenoxido oxygen atoms and some dilution effects. This polarization consisting in a higher electronic density in the phenoxido oxygens bridge, compared to the plane formed by the rest of oxygens in the coordination sphere. Consequently, the axial distribution of the electron density favors an Ising anisotropy, QTM relaxation would be minimized, and the energy barrier increased. Further studies reported that small modifications in the ligand cause drastic changes in the SMM behavior, as for example the addition of halide ligand in the apical position of the M^{2+} leading to still larger Δ.[163,167b]

Hereafter, we focus on systems based on the double coordination Dy^{3+}/ Zn^{2+} for the understanding of the magneto-structural correlation and improvement of the slow relaxation of the magnetization. Different studies are reported in the literature taking a Schiff base-derivative as a ligand and inducing small changes in the system in order to observe the tendency in the physical properties.[163-168] By substituting the heteroatom occupying the apical position of both Zn^{2+} and Dy^{3+} ions (X=-OH, -Cl, -Br, $-NO_3$, *etc*…) different series of compounds are formed and along them the SMM properties can be compared. The results of three different groups have been chosen, in order to resume the achievements in the field regarding this strategy.

The first series of compounds (Figure 6. 1) comprises different publications of J. Long *et al.* (from 2012 to 2018) in which they used a common $H_2\mathbf{L^{15}}$ = N, N'-bis (3-methoxysalicylidene)-1,2-diaminoethane ligand.[164,165,166] Thus, the mentioned strength of the chelating unit can be observed by the use of different Dy-precursors. Whereas the first studies include the $Dy(NO_3)_3{\cdot}5H_2O$[164,165], inducing binuclear $[(\mathbf{L^{15}}Zn(NO_3)Dy(NO_3)_2(H_2O)]$ (**30**) and $[(\mathbf{L^{15}}Zn(NO_3)Dy_{0.05}Y_{0.95}(NO_3)_2(H_2O)]$ (**30@Y**) compounds, the last concern $DyCl_3{\cdot}5H_2O$[166] salts, inducing $[(\mathbf{L^{15}}ZnCl)_2Dy(H_2O)]^{4+}$ trinuclear (**31**) complex.

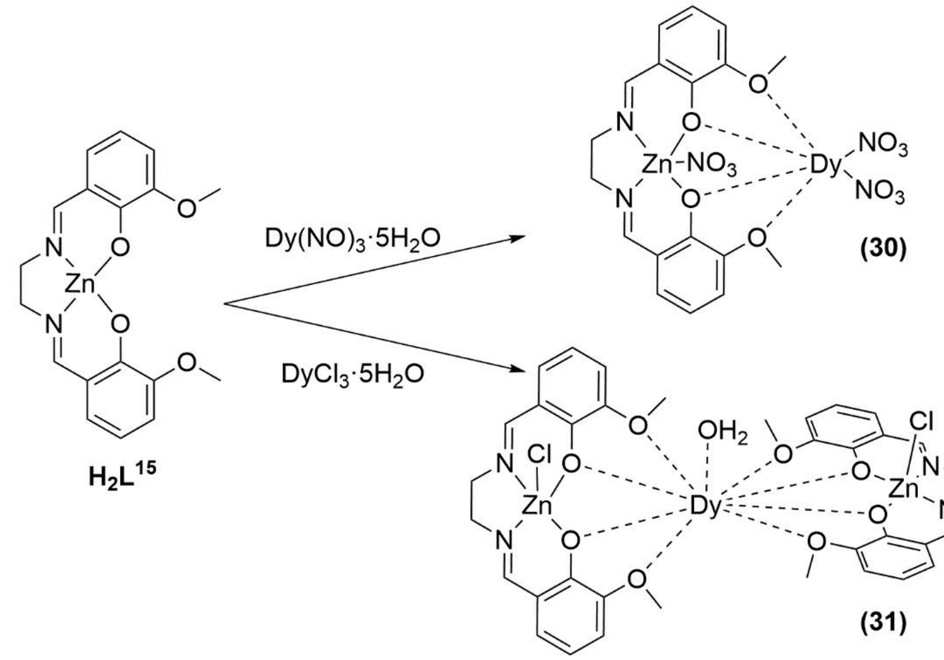

*Figure 6. 1. Schema of the different routes for the formation of compounds **30** and **31** from ligand H_2**L^{15}**.*

Moreover, an evolution in the magnetic properties due to the changes in the structure, and mostly on the direct coordination sphere to the Dy^{3+}, can be seen from **30** which is field-induced SMM to **31**, with a zero-field SMM behavior. A reinforce of the dilution effect, by doping the Dy^{3+} in a diamagnetic Y^{3+}-matrix, **30@Y**, enhances a slow-down of the relaxation showing some frequency-dependence. However, no maxima in the out-of-phase component of the magnetic susceptibility is displayed and thus the magnetic properties need to be characterized under DC field.

A second group involves the work of Colacio *et al.* (2015) with the use of a H_2**L^{16}**= N,N'-2,2-dimethylpropylenedi(3-methoxysalicylideneiminato as a ligand.[163]

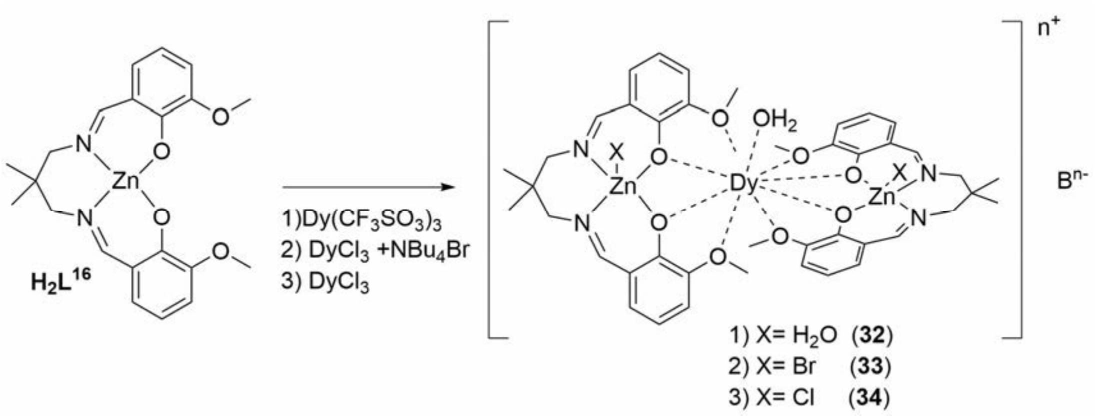

*Figure 6. 2. Schema of the different routes for the formation of compounds **32**, **33** and **34** from ligand H_2**L^{16}** and Dy-precursor in the proper stoichiometry. B^{n-} depends on the synthetic root and correspond to the different counter-ion, with n the oxidation state.*

Three different compounds $[(\mathbf{L^{16}}ZnX)_2Dy(H_2O)]^{n+}[B]^{n-}$ are faced during their studies, all of them with the Dy^{3+}-nonacoordinated site occupied by a H_2O molecule but each with a different unit in the apical position of the Zn^{2+} (X= H_2O and B^-= $3CF_3SO_3^-$ (**32**), X=Br and B^-= ClO_4^- (**33**) or X=Cl and B^-= ClO_4^-(**34**)). The three different substitutions induce some distortions in the coordination spheres, thus favoring or not, the electronic polarization in an easy axis and resulting in different performance in the SMM behavior. All three compounds show SMM behavior with frequency dependence χ_M'' up to 25 K (for **32**) or 35.5 K (for **33** and **34**), and effective energy barriers of 96.9(6) K, 146.8(5) K and 146.1(10) K, respectively. At the same time, ab initio calculations confirm the increase of the energy barrier by substituting the water molecule by peripheral halide ligands and the role of the coordination polyhedral geometry.

In the same direction, the group of Gao (2016) presented a series of compounds including small differences in the ligand architecture and X atoms for both Dy^{3+} and Zn^{2+}, in order to obtain further clues about the impact of subtle electronic variation of the first and second coordination sphere on the dynamic magnetic properties.[167] Thus, playing between $\mathbf{H_2L^{17}}$= N, N'-bis(3-methoxysalicylidene)phenylene-1,2-diamine or $\mathbf{H_2L^{18}}$= N, N'-bis(3-methoxysalicylidene)-1,2-diaminocyclohexane and $DyBr_3$ or $DyCl_3$ precursors in different solvent, they obtained 4 different molecules $[(\mathbf{L^{17}}ZnCl)_2DyCl]$ (**35**), $[(\mathbf{L^{17}}ZnBr)_2Dy(MeOH)]$ (**36**), $[(\mathbf{L^{17}}ZnBr)_2Dy(H_2O)]$ (**37**) and $[(\mathbf{L^{18}}ZnCl)_2DyCl]$ (**38**). These structures resulted into a greater enhancement of the effective energy barrier and hysteresis temperatures with respective values of 430 K, 233 K, 121 K and 398 K, for the first, and 8 K, 6 K, 4 K and 8 K, for the last. This work was also complemented by theoretical calculations in order to confirm the different electron density distribution and the correlation with the magnetic properties.

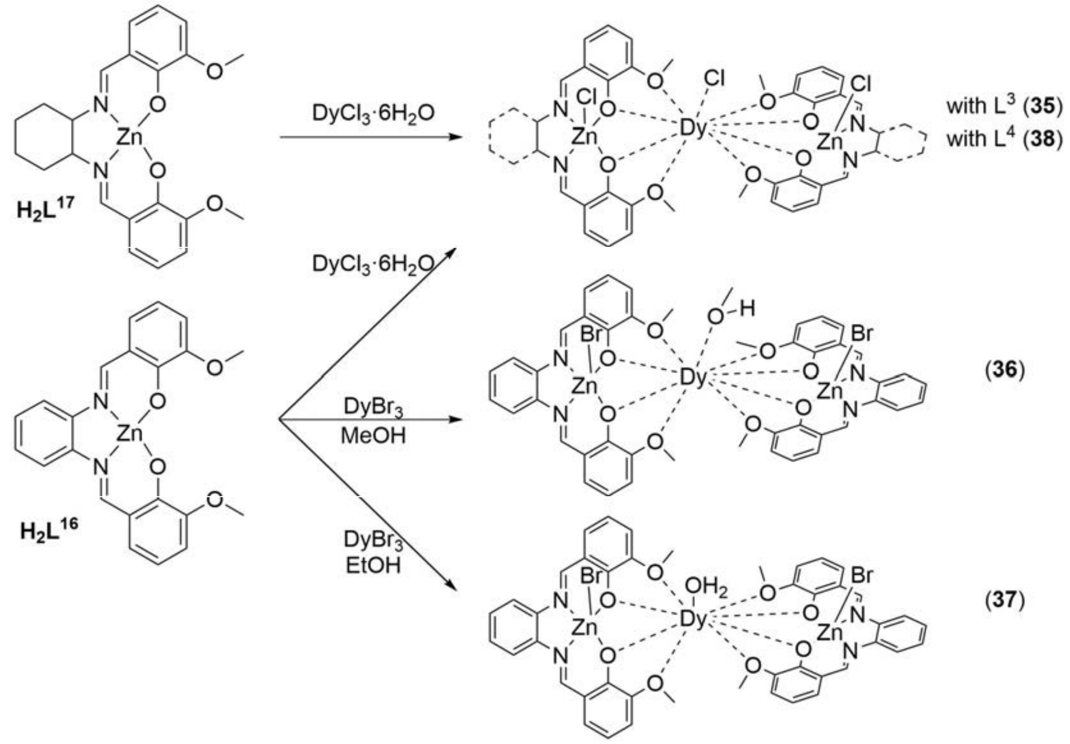

*Figure 6. 3. Schema of the different routes for the formation of compounds **35**-**38** from the reaction between ligand H_2**L^{17}**/ H_2**L^{18}** and Dy-precursor, in the proper stoichiometry.*

II. RESULTS AND DISCUSSIONS

A. *Structural definition:*

Among the different examples of trinuclear complexes which include the mixture of 3d and 4f centers, two different complexes of Zn-Dy-Zn type have been studied, each with a different salen-type Schiff base derivative as a ligand, H_2**L^{15}**= N,N'-bis(3-methoxysalicylidene)phenylene-1,2-diamine and H_2**L^{17}**= N,N'-bis(3-methoxysalicylidene)-1,2-diaminoethane, being termed in the introduction as **31** and **35**.[167,168,166] As it has already been mentioned, this kind of ligand molecules permit the parallel coordination of the dicationic Zn^{2+} species in the inner N_2O_2 cavity, whereas the outer phenoxido oxygens (O_4) will coordinate the $^{A}Dy^{3+}$cations (with A the mass number). In order to guarantee the high coordination of lanthanides, two different ligand moieties encapsulate the trivalent cation, and an external atom, from the solvent or metal precursors, closes the coordination sphere for both, the divalent (5-coordination) and the trivalent (9-coordination) cations.

The first complex, $[Zn_2($**L^{15}**$)_2{}^{A}DyCl_3]\cdot 2H_2O$ (with A= 162 and 163) and referred as **$Dy(ZnL^{15})_2$**, is formed by the mixture of $DyCl_3\cdot 6H_2O$ in methanol with a Zn**L^{15}** suspension solution in acetonitrile followed by a slow diffusion in diethyl-ether. Similar procedure adding $YCl_3\cdot 6H_2O$

is carried for the diluted samples. As a result, the different isotopic and diluted systems crystallize in the monoclinic space group C2/c (N°15), being all isostructural to the published work from Sun *et al.*[167b], hence only the unit cell parameters have been collected by Single Crystal XRD (Annex 1, table A1.5). The ratio Dy^{3+}/Y^{3+} (0.1/0.9) for the three doped compounds $[Zn_2(\mathbf{L^{15}})_2{}^{162}DyCl_3]\cdot 2H_2O]$ (**^{162}Dy(ZnL^{15})$_2$**), $[Zn_2(\mathbf{L^{15}})_2DyCl_3]\cdot 2H_2O]$ (**Dy(ZnL^{15})$_2$**) and $[Zn_2(\mathbf{L^{15}})_2{}^{163}DyCl_3]\cdot 2H_2O]$ (**^{162}Dy(ZnL^{15})$_2$**) has been verified by EDS analysis (Annex 2, Figure A2.4) with resulted values of 0.17/0.83 ($^{162}Dy^{3+}/Y^{3+}$), 0.13/0.87 (Dy^{3+}/Y^{3+}) and 0.15/0.85 ($^{163}Dy^{3+}/Y^{3+}$). A considerable divergence from the theoretical dilution ratio evidences the greater affinity of the Dy^{3+} to occupy the cavity than the Y^{3+}, which could be improve by increasing the proportion of Y^{3+} in the solution.

The molecular structure is depicted in Figure 6. 4, in it the eight oxygens atoms from two different **L^{15}** moieties are coordinated to a Dy^{3+} ion. Moreover, the ninth-coordination side of the Dy^{3+} is occupied by a Cl^- ion, through which a C_2 symmetry axis is driven. When examining the plane defined by the N_2O_4 cavity at each ligand unit, there is an angle of 76.19(7)° between both ligands. The O_8Cl coordination sphere around the Dy^{3+} is characterized by a very small symmetry, being the muffin (Cs) the closest geometry (with $CShMs_{MFF-9}$= 3.321), as reported by Sun *et al.* with the aid of a Shape Analysis.[167b] Because of the polarization effect, driven by the two Zn^{2+} cations, we can distinguish between two types of coordination atoms depending on their electronic density. So that, the bridging oxygen correspond to rich electron density oxygens, whereas the ones situated in the nearly perpendicular plane present a poor density. Thanks to the combination of both theoretical calculations and magnetic experimental data Sun *et al.* determined an easy axis pointing out the middle of the two bridging oxygen atoms (high electronic density axis), whereas the five-membered ring consisting on four methoxyl oxygen atoms from two ligands and one chlorine ion (low electronic density plane) corresponds to the hard plane.

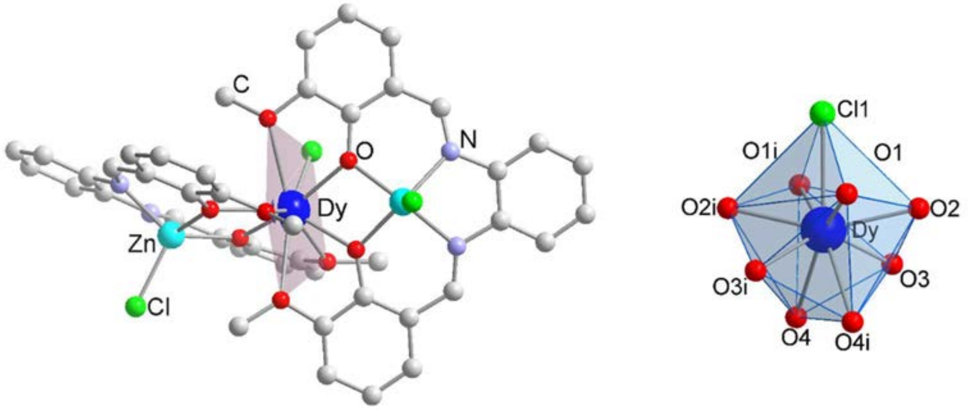

Figure 6. 4. Left: Molecular structure of ***Dy(ZnL^{15})$_2$****, with the hard plane represented Hydrogen atoms and water molecules are omitted for clarity. Right: Coordination environment of Dy cation, polyhedron used for SHAPE analysis. Adapted from ref. [167b].*

In Figure 6. 5 the different orientations of the molecule in the packing are represented, thus highlighting the different orientations of the hard planes and easy axes in the crystal.

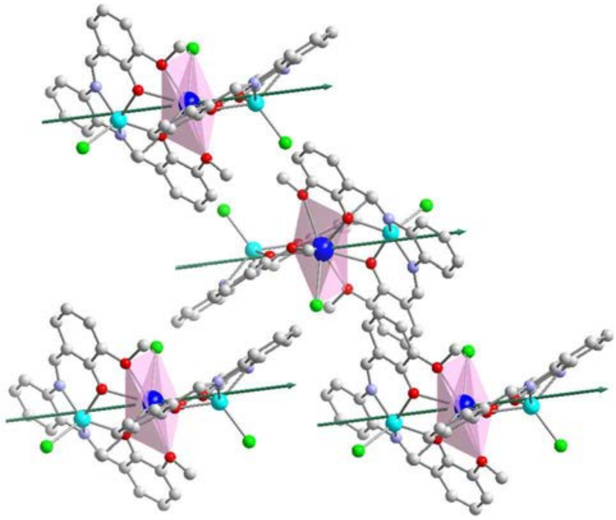

Figure 6. 5. Representation of the packing in ***Dy(ZnL^{15})$_2$*** *highlighting the 5-membered ring forming the hard plane and the approximate direction of the easy-axis (green). Adapted from ref. [167b].*

For simplicity, the easy axis has been determined as the direction of the Dy-Zn, and the Dy-Cl directions have been taken for the comparison of the different hard plane (assumption resulted from ref. [167b]). By comparing the different vectors resulted from the Dy-Zn and Dy-Cl directions, both easy axis (from Dy-Zn vector) and hard plane (from Dy-Cl vector) are considered to be parallel through the crystallographic packing. Hence, the same (0,1,0) vector defines the Dy-Cl directions in the different molecules of the packing, whereas a small tilted angle between the different Dy-Zn directions alternates between 0.00(1)° and 6.13(1)°. The system organization is characterized by π-π stacking of the ligand phenyl groups (3.31(1) Å), and one out of four molecules is orientated antiparallel to the others. The closest distances between Dy molecules are of 10.10(1) Å and 10.40(1) Å.

The second system, [(Zn**L**^{17}Cl)$_2$^{A}Dy(H$_2$O)]$_2$[ZnCl$_4$]·xH$_2$O (with A= 163 and 164, and x not determined in the XRD resolution) and referred as **Dy(ZnL^{17})$_2$**, results from the reaction between ZnCl$_2$·2H$_2$O, H$_2$**L**^{17} and DyCl$_3$·6H$_2$O in 2:2:1 ratio in methanol with the presence of trimethylamine and followed by a slow evaporation. Similar to **Dy(ZnL^{15})$_2$**, the coordination to the Dy^{3+} takes place between two different ligands which are turned of 72.7(3)° if comparing the mean planes formed by the N_2O_2 cavities. Apart from the difference in the external part of the ligand (from phenylene-1,2-diamine to 1,2-diaminoethane), a most relevant difference concerning the first coordination sphere results from the substitution of the chloride atom by a water molecule. The electroneutrality is then ensured by a $[ZnCl_4]^{2-}$ moiety. For that system, cell parameters from XRD differed from those exposed in the literature[166], and the structure was resolved for one of the three compounds. Consequently, the crystallographic structure showed a similar cell composition but constituting the half of the published unit cell forming this. (see Annex 1, Table A.6). The system crystallizes in the P-1 (N°2) space group with two independent trinuclear complexes within the asymmetric unit. The molecular structure is presented in Figure 6. 6, showing a O_9 coordination sphere determined as spherical capped square antiprism (C_{4v}) with small divergences between the two Dy^{3+} centers in the distortion coefficient (Table 6. 1, found by SHAPE analysis [169]).

The hard plane, represented in pink, correspond again to the 5-memebered ring constituted this time by the 4 non-bridged oxygen atoms and one water molecule, whereas the preferential direction follows the bridged oxygen atoms.

Table 6. 1. First three closest symmetries for the Er-coordination environment.

	CShMCSAPR-9 (Spherical capped square antiprism, C4v)	*CShMMFF-9 (Muffin, Cs)*	*CShMTCTPR-9 (Spherical tricapped trigonal prism, D3h)*
Dy1-O_9	2.155	2.481	2.474
Dy2-O_9	2.651	2.686	3.065

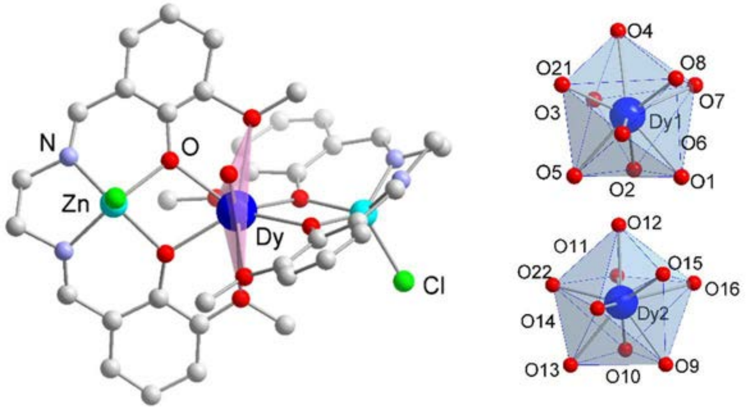

Figure 6. 6. Left: Molecular structure of ***Dy(ZnL^{17})$_2$*** *composed, with the hard plane of density represented. Hydrogen atoms, counter ions and water molecule of crystallization are omitted for clarity. Right: Coordination environment of Dy1 and Dy2 polyhedra used for SHAPE analysis.*

The different organization of the molecule in the crystallographic structure is represented in Figure 6. 7. With a quick view, the completely different organization of the packing can be observed. Thus, looking at the hard plane of the different molecules (represented in pink), two different distributions are alternated whether they are paralleled or perpendicular.

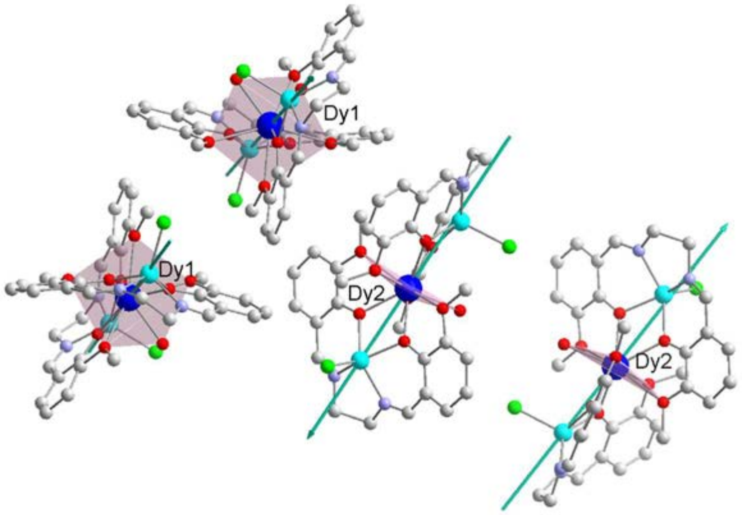

Figure 6. 7. Representation of the packing in ***Dy(ZnL^{17})$_2$*** *highlighting the 5-membered ring forming the hard plane, the approximate direction of the easy-axis (green), and the different orientation of this through the space.*

The same simplification for the easy axis and hard plane has been applied in that system. Within the packing, only the closest molecules have been considered, thus with distances ranging from 8.76 Å to 11.46) Å. The two different orientations, defined before as "parallel" and "perpendicular", are characterized as follows: between neighboring Dy1 atoms, the Dy1-Zn vectors are parallels (deviation of 2.46(5)°); consecutive Dy2 display also parallel Dy2-Zn vectors (deviation of 4.40(7)°); and the orientation between the nearest Dy1-Zn and Dy2-Zn (d= 8.76 Å and 11.46 Å) can be defined as perpendicular, with angles of 71.60(5)° and 69.73(6)°

respectively. In this system, no significant π- π stacking interactions are found to govern the rearrangement of the packing, contrary to **Dy(ZnL^{15})$_2$**.

B. *Magnetic Properties: Isotopic and dilution effect in polarized systems:*

B.1. *Dy(ZnL^{15})$_2$*

DC Susceptibility measurements have been performed as a function of the temperature but due to the quality of the results (Annex 3 Figure A3.1), the interpretation could not be performed. Problems with the purity of the system and the large times needed for the stabilization of the magnetization (we need at least 10 minutes between each point to reach equilibrium) are the main complication of this sample. Further synthetic work is needed in order to complete all the magnetic study.

The field-dependence magnetization at 2 K (Figure 6. 8, left) shows almost a superimposable behavior for all the condensed samples (**^{162}Dy(ZnL^{15})$_2$**, **^{163}Dy(ZnL^{15})$_2$** and the natural **Dy(ZnL^{15})$_2$**) as it would be expected. The field dependence of the magnetization shows a classic behavior with a saturation value M_{sat} close to 5 Nβ, which is in agreement with an Ising Dy-system. However, the problem of this kind of samples to reach the equilibrium can be perceptible, especially at low applied magnetic field. In the right, the different magnetization of the diluted samples **^{A}Dy@Y(ZnL^{15})$_2$** are compared to M_{sat} of 5 Nβ in order to have an insight of the doping percentage.

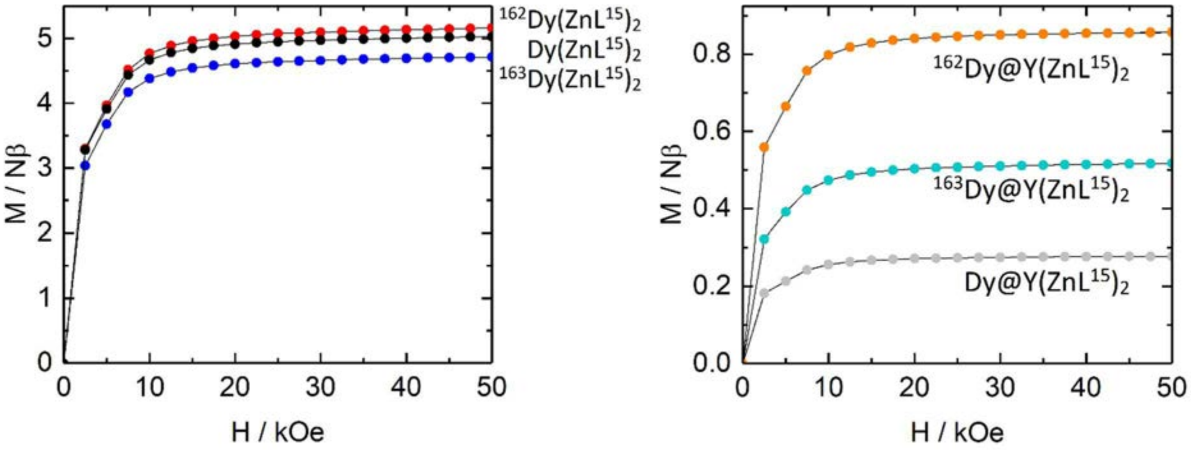

*Figure 6. 8. Magnetization curves out of equilibrium for **Dy(ZnL^{15})$_2$** analogues at 2 K. Left) condensed systems; Right) magnetically diluted systems. In red and orange ^{162}Dy^{3+} (I=0), black and grey Dy^{3+}, and in blue and light blue ^{163}Dy^{3+} (I= 5/2).*

The M_{sat}(**^{A}Dy@Y(ZnL^{15})$_2$**)/M_{sat}(**Dy(ZnL^{15})$_2$**) ratios give doping values of 5.5 % for **Dy@Y(ZnL^{15})$_2$**, 17.14 % for **^{162}Dy@Y(ZnL^{15})$_2$** and 10.34 % for **^{163}Dy@Y(ZnL^{15})$_2$**. Compared with the doping values of the EDS for the three systems (13(1) %, 17(2) % and 15(4) %), magnetism suggests greater effective dilutions. Actually, by measuring the magnetization of the sample we cannot distinguish between the doped crystals itself and pure diamagnetic impurities resulted from the only complexation with Y^{3+}, the lasts were slightly observed in some of the analyzed spots while the EDS analysis. These few impurities would change the real mass of the magnetic compound producing a higher apparent dilution. Nevertheless, the different doping ratios are assumed to be enough so that the dipolar interactions are destroyed, hence being appropriate for their comparison.

The dynamic study of the magnetic susceptibility has already been reported in the literature, showing frequency dependency up to 30 K under zero magnetic field and a great energy barrier of 430 K. The temperature dependence of the relaxation was shown to be exponentially dependent at the highest temperatures with a visible deviation caused by the Raman process. Below 10 K the slow-down of the relaxation is shortcut because of the appearance of a thermally-independent regime (QTM).[167]

A check at 2 K including the condensed samples (**^{162}Dy(ZnL^{15})$_2$**, **^{163}Dy(ZnL^{15})$_2$** and **Dy(ZnL^{15})$_2$**) as well as the diluted **Dy@Y(ZnL^{15})$_2$** was performed in order to have a first insight of the dilution and isotopic enrichment. However, as already seen in the previous chapters, the dipolar interactions partially cancel the effect of the hyperfine interactions. In Figure 6. 9 this situation is presented when in the non-diluted samples, the effect of the hyperfine interaction is hardly visible: the nuclear spin free isotope is centered at the same frequency than the natural mixture (0.70 Hz) and, as it can be seen, **^{163}Dy(ZnL^{15})$_2$** is slightly right-shifted (1.26 Hz) compared to the other two. For that reason, diluted systems have been prepared in parallel. For the ac measurements, a test at 2 K of the **Dy@Y(ZnL^{15})$_2$** analogue evidences the slow behavior of the system, hampering the comparison of the diluted samples by measurements.

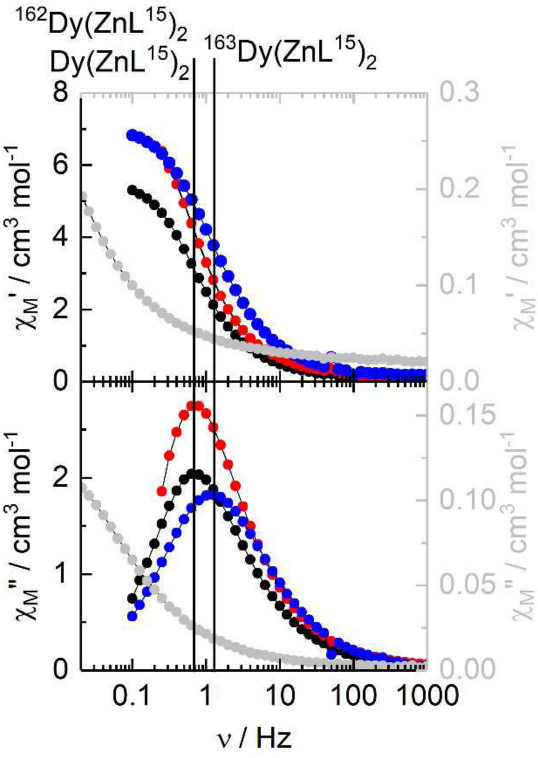

Figure 6. 9. χ_M'/χ_M'' vs. ν curves for ***^{162}Dy(ZnL^{15})$_2$*** *(red),* ***^{163}Dy(ZnL^{15})$_2$*** *(blue),* ***Dy(ZnL^{15})$_2$*** *(black) and* ***Dy@Y(ZnL^{15})$_2$*** *(grey). The left axis corresponds to the condensed samples (**^{162}Dy(ZnL^{15})$_2$**, **^{163}Dy(ZnL^{15})$_2$**, **Dy(ZnL^{15})$_2$**, whereas the right one stands for the diluted* ***Dy@Y(ZnL^{15})$_2$.*** *The black lines are guidance for the maxima position.*

As it can be seen in grey, the magnetic relaxation of the diluted compound is too slow with respect to the achievable frequencies (>0.01 Hz) in the SQUID MPMS magnetometer. Consequently, the ac magnetic measurements were shown not to be a good technique for the study of the low temperature mechanisms in this system, and this was carried on with hysteresis measurements of the magnetization. Indeed, the hysteresis loop of the magnetization is a good figure in order to observe the bistability of the system and the presence or not of a QTM regime by looking at the remnant magnetization at zero field. In Figure 6. 10, the different hysteresis loops as a function of the magnetic field (at 0.5 K and from -10 to 10 kOe) are presented. In order to facilitate the comparison with the diluted compounds, magnetizations have been normalized.

As already proved by Sun *et al.* **Dy(ZnL^{15})$_2$** displays the typical butterfly-type hysteresis loop which evidences the SMM behavior. At the ^{3}He temperature, the mark of the hyperfine interactions in the condensed samples is already present without magnetic dilution to be deemed (Figure 6. 10). The *I*= 5/2 isotope (^{163}Dy^{3+}) shows a hysteresis loop of the magnetization closed at zero, due to the contribution of both dipolar and hyperfine interactions, whereas both the natural mixture and the *I*= 0 isotope (with lower or null HF interactions) present an opening at zero magnetic field. Moreover, the opening of the nuclear spin free isotope is greater than the natural mixture, being the remnant magnetization of 0.32 Nβ for **^{162}Dy(ZnL^{15})$_2$** and 0.21 Nβ for **Dy(ZnL^{15})$_2$**. Through dilution, the dipolar interaction existent between neighboring Dy^{3+} is minimized and thus the QTM mechanism is drastically reduced, enhancing the opening of the hysteresis loop at zero field also for the **^{163}Dy@Y(ZnL^{15})$_2$** isotopologue. At that point, the difference between the three analogous systems at the origin is a direct insight of the strength of the hyperfine coupling. Thus, **^{163}Dy@Y(ZnL^{15})$_2$**, which carries with the greatest influence of the HF, displays the smallest remnant magnetization (0.1 Nβ), followed by **Dy@Y(ZnL^{15})$_2$** (0.27 Nβ) with a 50 % influence of the *I*=5/2, and finally **^{162}Dy@Y(ZnL^{15})$_2$** (0.4 Nβ) with the absence of this interaction. Moreover, a difference in the hysteresis loops is also visible under magnetic field, thus with a greater opening when *I*= 0 than when *I*= 5/2. Recent publication from Ruben's group justifies this change in the opening of the loop under magnetic field, by the idea of a larger possibility of relaxation transitions coming from the 2*I*+1 sublevels as the nuclear spin value *I* increases.[170] Thus, larger is *I* greater would be the interactions with the acoustic phonons, resulting in an increase of the Raman contribution and hence, a closing in the hysteresis. This can be seen at the magnetic field of 2.5 kOe, for both representations of Figure 6. 10, where $^{163}Dy^{3+}$ (*I*= 5/2) analogous shows a narrower loop than the natural mixture, and the $^{162}Dy^{3+}$ (*I*= 0). Same tendency was shown in **Dy@Y** isotopologues in Chapter III, where by increasing the hyperfine strength the wide of the hysteresis loop under field, decreased.

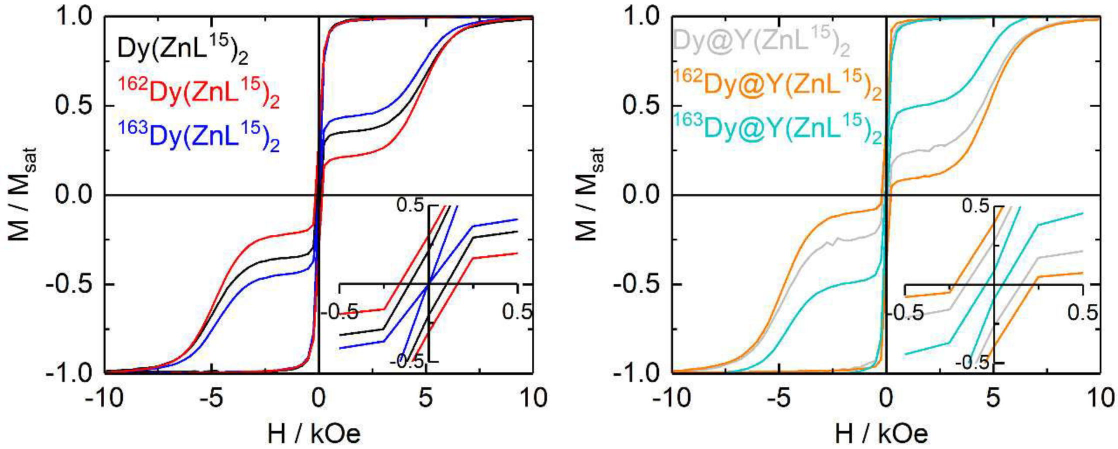

*Figure 6. 10. Normalized magnetic hysteresis loops at 0.5 K and at a sweep rate of 16 Oe s^{-1} for: left) **^{163}Dy(ZnL^{15})$_2$** (blue lines), **^{162}Dy(ZnL^{15})$_2$** (red lines) and **Dy(ZnL^{15})$_2$** (black lines) and right) **^{163}Dy@Y(ZnL^{15})$_2$** (light blue lines), **^{162}Dy@Y(ZnL^{15})$_2$** (orange lines) and **Dy@Y(ZnL^{15})$_2$** (grey lines), the diluted analogues. Insets are a zoomed view of the origin to visualize the remnant magnetization.*

To sum up and as seen for other systems, the HF interaction is hindered by the presence of the dipolar interactions, and thus only if removing the respective dipolar field the real mark of the HF interactions can be observed. In other words, the small differences observed in the condensed matter are considerably increased when examining diluted systems. Until now, the strength of the dipolar interaction was not enough in order to completely hinder the effect of the HF interactions, or in other words the isotopic effect. However, in the present **$Dy(ZnL^{15})_2$** system, this "partial suppression" seems to be complete, thus evidencing the importance of further study of the strength of the dipolar interactions in this system and their role in the visibility of the isotopic differences. Finally, the same tendency in the evolution of the quantum effects in the relaxation process is shown for this kind of complexes without any nitrogen in the coordination sphere and the effect of the polarizing Zn^{2+} cations. In Figure 6. 11 the different steps towards optimization are represented, resulting in the addition of both strategies magnetic dilution and isotopic enrichment with *I*=0 in order to enhance a quantized opening in the butterfly-type loop. As a result, starting with a remnant magnetization of 0.21 Nβ for the **$Dy(ZnL^{15})_2$**, we end up with a two times larger magnetization (0.4 Nβ) with **$^{162}Dy@Y(ZnL^{15})_2$**.

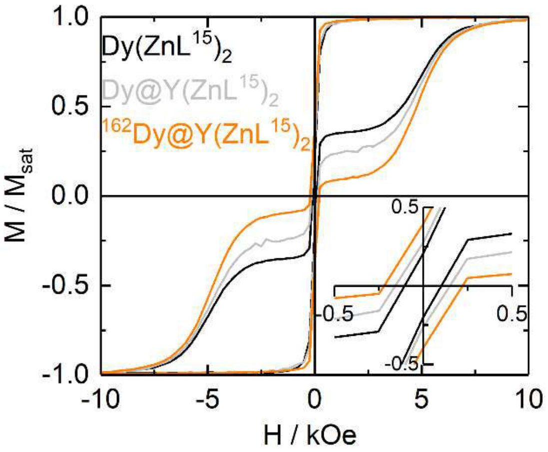

Figure 6. 11. Normalized magnetic hysteresis loops at 0.5 K and at a sweep rate of 16 Oe s^{-1} for the natural ***$Dy(ZnL^{15})_2$*** *(black lines) and the diluted forms of the natural (****$Dy@Y(ZnL^{15})_2$****, grey lines) and I= 0 isotope* ***$^{162}Dy@Y(ZnL^{15})_2$****, orange lines). The Inset is a zoomed view of the origin to visualize the remnant magnetization.*

B.2. *$Dy(ZnL^{17})_2$*

A slightly different system with faster relaxation times has been chosen in order to compare the effect of the hyperfine interactions and dilution in both. Moreover, a slightly faster relaxation mechanism will favor the complete analysis of the magnetic properties. Unfortunately, different approaches performed for the synthesis of the diluted analogues have not been satisfactory and no crystals are obtained yet. Furthermore, some magnetic measurements are still missing, and the study needs to be continued folowing this manuscript.

Faster relaxation systems need shorter times in order to achieve the stabilization state between measurements. Whereas for the previous system, ten minutes did no guarantee the equilibrium state, **Dy(ZnL^{17})$_2$** reaches equilibrium. DC magnetic measurements have been performed from 2 to 300 K for all the different samples (Figure 6.12). At high temperature, the $\chi_M T$ product for an isolated Dy^{3+}: [Xe]4f^9 with an $^6H_{15/2}$ multiplet ground state and g_J= 4/3, is supposed to be 14.17 cm^3 K mol^{-1} which is in agreement with the observed value of 13.5 cm^3 K mol^{-1} at room temperature.[171] Then, by cooling, the curve decreases monotonically to reach 11.7 cm^3 K mol^{-1} at 2 K, because of the depopulation of the ligand-field levels. At 2 K, the magnetization curve reaches 5 Nβ par Dy^{3+} at 50 kOe.

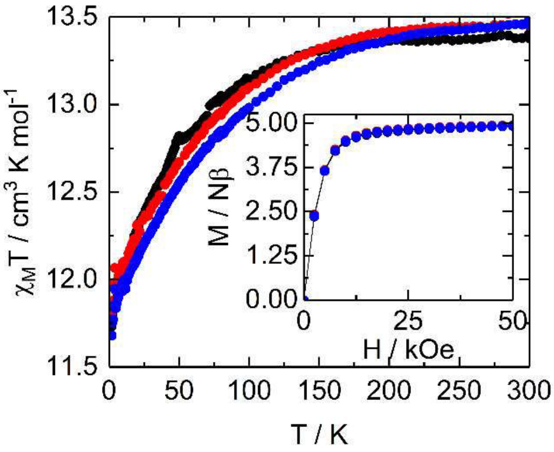

*Figure 6. 12. Thermal variation of $\chi_M T$ is represented by empty circles for **Dy(ZnL^{17})$_2$** (in black), **^{164}Dy(ZnL^{17})$_2$** (in red) and **^{163}Dy(ZnL^{17})$_2$** (in blue)). Inset: field variation of the magnetization at 2 K for the different samples with the same color code.*

Same behavior as in the published dynamic study of the magnetic susceptibility for **35** has been performed, showing frequency dependency up to 30 K under zero magnetic field and a large energy barrier of 430 K. The temperature dependence of the relaxation was shown to be exponentially dependent at the highest temperatures with a visible deviation caused by the Raman process. Below 10 K the slow-down of the relaxation is shortcut because of the appearance of a thermally-independent regime (QTM).[166]

The difference in the dynamic response of the three samples has been verified first at 2 K from 1 to 1000 Hz under zero magnetic field. In Figure 6. 13 the different components of the magnetic susceptibility of the three compounds are presentedand it shows a small effect coming from the isotopic enrichment. Consequently, the χ_M'' curve of the nuclear spin free

^{164}Dy(ZnL^{17})$_2$ is centered at the lowest frequency (37.5 Hz), followed by the natural mixture (50 Hz) and at last, at the higher frequencies, the *I*=5/2 **^{163}Dy(ZnL^{17})$_2$** (120 Hz).

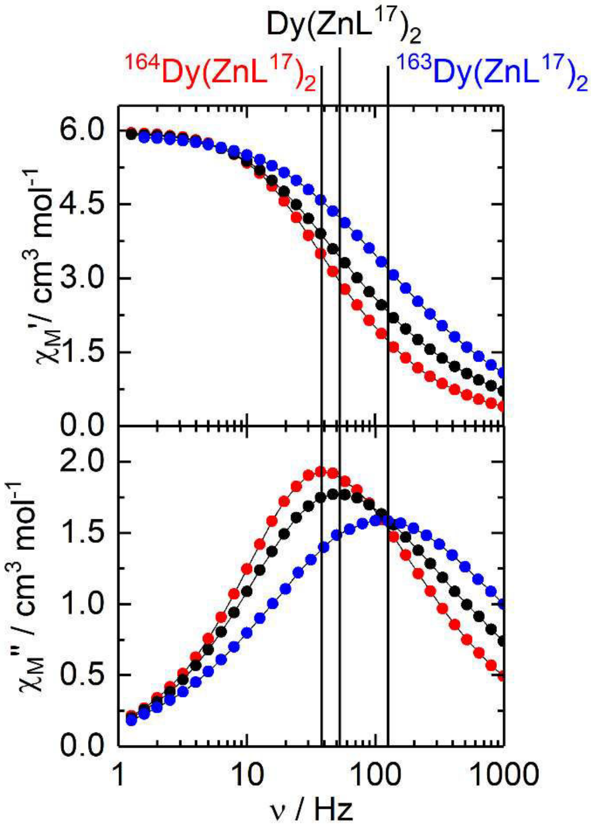

Figure 6. 13. χ_M'/χ_M'' vs. ν curves at 2 K and zero magnetic field for: ***^{164}Dy(ZnL^{17})$_2$*** *(red),* ***^{163}Dy(ZnL^{17})$_2$*** *(blue),* ***Dy(ZnL^{17})$_2$*** *(black). The black lines are guidance for the maxima position.*

Further characterization of the dynamic properties was performed for **^{164}Dy(ZnL^{17})$_2$** and the natural **Dy(ZnL^{17})$_2$**, and the measurements with **^{163}Dy(ZnL^{17})$_2$** are in process. A first comparison can be done with the two first compounds which frequency dependence of the magnetic susceptibility was studied from 2 to 23 K (Figure 6.14). The temperature dependence of the relaxation times can be represented by applying the extended Debye model (Annex 3: Table A3.17-A3.18) and make possible the study of the relaxation mechanism of both samples in this second system. The values obtained for the χ_S and χ_T limits are in accordance with the assumption that the four different crystallographic centers have the same dynamic properties. The α parameter values ranging from 0.21 to 0.29 suggest a small distribution of the relaxation time, which could arise from small differences between the two dysprosium sites.

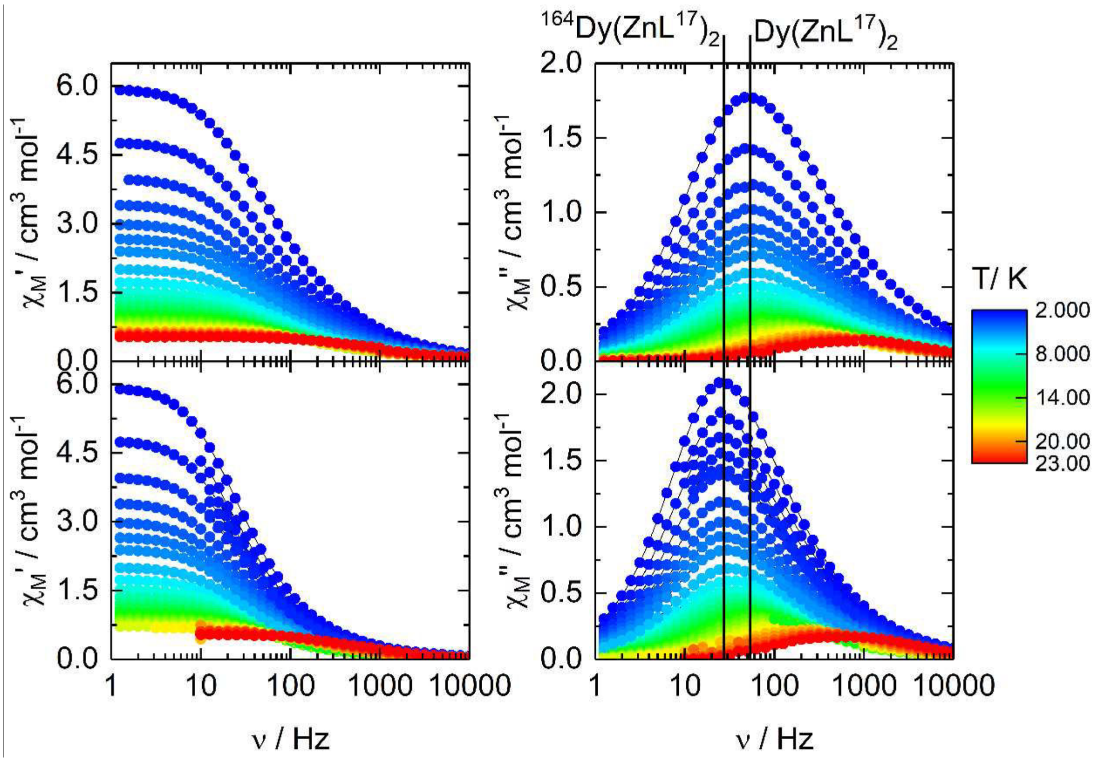

*Figure 6. 14. χ_M'/χ_M'' vs. ν curves of **Dy(ZnL^{17})$_2$** and **^{164}Dy(ZnL^{17})$_2$** under zero magnetic field and from 2 to 23 K. The black lines are an eye guide of the frequency position of each maximum at 2 K.*

The relaxation times of the magnetization have been expressed as a function of the temperature for both systems, and have been simultaneously fitted using a modified Arrhenius law (Equation 6.1). No clear contribution of a thermally activated Orbach was attested by Boulkedid et al., thus leading to a strong contribution from the Raman within their interpretation.[166]

$$\begin{cases} \tau^{-1}_{Dy^{3+}} = C_1 T^{n_1} + \tau^{-1}_{Tl_1} \\ \tau^{-1}_{^{164}Dy^{3+}} = C_2 T^{n_2} + \tau^{-1}_{Tl_2} \end{cases} \tag{6.1}$$

As a result, the description of the relaxation mechanisms for both systems are expressed by the equally Raman contribution, defined by a *C* constant and a *n*-exponent with the temperature, and a different QTM relaxation below 6 K.

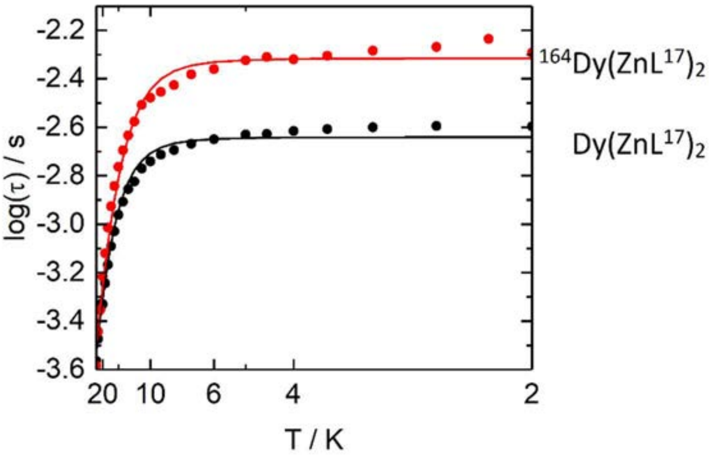

Figure 6. 15. Correlation between the relaxation time (τ) and the temperature (T) for ***Dy(ZnL^{17})$_2$*** *(black) and* ***^{164}Dy(ZnL^{17})$_2$*** *(red) under zero H_{DC}. Full lines correspond to the resulted curves of the best fitted parameters.*

The best fitted parameters are summarized in Table 6. 2, confirming the already visualized isotopic effect, being τ_{TI} (**^{164}Dy(ZnL^{17})$_2$**) two times slower than τ_{TI} (**Dy(ZnL^{17})$_2$**).

Table 6. 2. Best fitted parameters for the relaxation mechanism of ***Dy(ZnL^{17})$_2$****, considering the Raman and QTM.*

	C / $K^{-n}s^{-1}$	n	τ_{TI} / s
Dy(ZnL^{17})$_2$	(1.25 ± 0.71)·10^{-2}	3.9± 0.2	(2.4 ± 0.1)·10^{-3}
^{164}Dy(ZnL^{17})$_2$	(1.12 ± 0.56)·10^{-3}	4.7± 0.2	(4.7 ± 0.1)·10^{-3}

The isotopic effect in these samples has been proven by both AC susceptibility and DC magnetic hysteresis. The hysteresis loops of the magnetization of **^{163}Dy(ZnL^{17})$_2$**, **^{164}Dy(ZnL^{17})$_2$** and **Dy(ZnL^{17})$_2$** were performed at 0.5 K (^{3}He) and for a better overall comparison, the different curves have been normalized (Figure 6. 16). The butterfly-shape in the hysteresis loop is present, sign of magnetic bistability with important contribution of QTM despite the isotopic enrichment (for I= 0). The effective contribution of the dipolar interactions in the sample accelerates a QTM at zero field which hinder the different effect of the HF coupling in the different samples. Unfortunately, effort is being done for the formation of a diluted analogous system but without results for the moment.

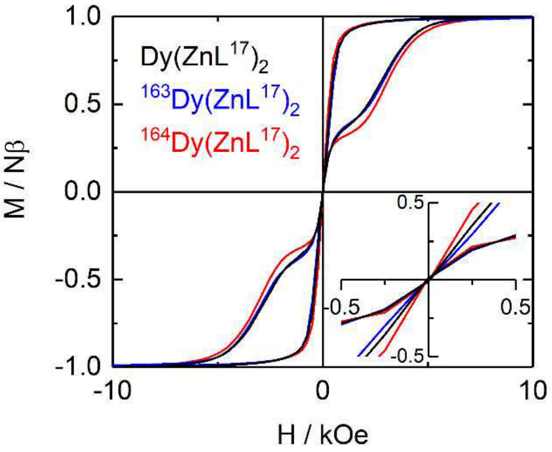

Figure 6. 16. Normalized magnetic hysteresis loops at 0.5 K and at a sweep rate of 16 Oe s^{-1} for ^{163}***Dy(ZnL***^{17}***)***$_2$ *(blue lines),* ^{164}***Dy(ZnL***^{17}***)***$_2$ *(red lines) and* ***Dy(ZnL***^{17}***)***$_2$ *(black lines). Inset is a zoomed view of the origin to visualize the remnant magnetization.*

C. *Small changes drive big changes:*

An explanation is needed to understand the fact that the isotopic enrichment could be hindered in the first system **Dy(ZnL**^{15}**)**$_2$ (no difference in the χ'' is observed between ^{162}**Dy(ZnL**^{15}**)**$_2$ and **Dy(ZnL**^{15}**)**$_2$) but visible in the second **Dy(ZnL**^{17}**)**$_2$. A possible hypothesis is proposed relying in the different intermolecular interactions present in the condensed phase. However, the magnetic dilution of the second system hasn't been achieved.

In the section where the structure and packing are presented, it has been seen as small changes in the ligand and coordination sphere results into a totally different distribution of the molecules in the packing. As a result, π-π stacking interactions are dominating between the different **Dy(ZnL**^{15}**)**$_2$ molecules, contrary to the **Dy(ZnL**^{17}**)**$_2$, thus enhancing higher intermolecular interactions.

So far, intermolecular interactions, such as dipolar interactions, are known to partially suppress the HF coupling. During the previous chapters, some examples confirming the partial suppression of the isotopic enrichment effect have been presented, where in order to have a proper idea on the nuclear spin effects, the dipolar interactions should be suppressed by magnetic dilution. Thus, confirming that as the contribution of the dipolar interactions increases in a system, the effect of the isotopic enrichment decreases. In order to determine the strength of the dipolar interactions, an overall view of the packing is very important, as the interaction depends on the length and orientation of the vector describing their relative position.[172] By comparing both systems it can be seen as the closest Dy^{3+}-Dy^{3+} distances in

Dy(ZnL^{17})$_2$ are slightly shorter than in **Dy(ZnL^{15})$_2$** but, at the same time, the interactions are minimized because of the perpendicular orientation of the easy-axes (Figure 6. 7). On the contrary, in **Dy(ZnL^{15})$_2$** system the dipolar interactions would be optimized by a parallel orientation of the different anisotropy-tensors (Figure 6. 5). This hypothesis would need a theoretical approach to calculate the dipolar contributions in each system. Only after that, one may conclude on the role of intermolecular interactions on the relaxation processes in the quantum regime.

III. CONCLUSIONS

The different results presented within this chapter lead to the confirmation that Dy^{3+}-based SMM, display the same trend in the relaxation mechanisms as the **Dy** or **Yb** compounds presented in Chapter III and IV. Hence, coordination complexes based on these trivalent ions show the same effect towards isotopic enrichment and magnetic dilution, no matters the coordination sphere (entirely oxygenated or not): optimization resides in the suppression of both hyperfine and dipolar interactions.

Moreover, it has been observed that the effect of polarization on the oxygens does not hinder the isotopic effect and that, once again, in order to look at the hyperfine coupling the dipolar interactions are of paramount importance.

When comparing the two systems, it appears that small differences in the coordination spheres of Dy^{3+} and Zn^{2+}, lead to changes in the electronic density distribution and big general changes in the magnetic behavior of the molecule. Thus, by passing from **Dy(ZnL^{15})$_2$** to **Dy(ZnL^{17})$_2$** the slow relaxation of the magnetization is disfavored, thus displaying faster relaxation rates. Furthermore, the AF interactions between neighbors (favored in the first because of the π- π stacking distribution of the molecules) are no longer present, thus diminishing the dipolar field. As a consequence, the isotopic effect in the concentrated samples are hindered in the first, while they are partially visible in the latter.

For reasons of time and availability of the machine, measurements aimed to verify the isotopic and dilution effect were privileged, and some measurements are missing which will have to be performed after this work. Finally, theoretical calculations would need to be performed if a quantitative understanding of the role of the dipolar interactions in the quantum regime is desired, in both systems.

REFERENCES:

[159] a) R. Sessoli, and A. K. Powell, *Coord. Chem. Rev.*, **2009**, *253*, 2328; b) M. Andruh, *Chem. Commun.*, **2011**, *47*, 3025.

[160] a) S. K. Langley, N. F. Chilton, L. Ungur, B. Moubaraki, L. F. Chibotaru, and K. S. Murray, *Inorg. Chem.*, **2012**, *51*, 11873; b) S. K. Langley, N. F. Chilton, B. Moubaraki, and K. S. Murray, *Chem. Commun.*, **2013**, *49*, 6965; c) S. Hazra, J. Titiš, D. Valigura, R. Boča, and S. Mohanta, *Dalton Trans.*, **2016**, *45*, 7510.

[161] a) A. Upadhyay, S. K. Singh, C. Das, R. Mondol, S. K. Langley, K. S. Murray, G. Rajaraman, and M. Shanmugam, *Chem. Commun.*, **2014**, *50*, 8838; b) A. Upadhyay, C. Das, S. Vaidya, S. K. Singh, T. Gupta, R. Mondol, S. K. Langley, K. S. Murray, G. Rajaraman, and M. Shanmugam, *Chem. Eur. J.*, **2017**, *23*, 4903.

[162] a) S. K. Langley, N. F. Chilton, L. Ungur, B. Moubaraki, L. F. Chibotaru, and K. S. Murray, *Inorg. Chem.*, **2012**, *51*, 11873; b) S. K. Langley, N. F. Chilton, B. Moubaraki, and K. S. Murray, *Chem. Commun.*, **2013**, *49*, 6965.

[163] J. P. Costes, S. Titos - Padilla, I. Oyarzabal, T. Gupta, C. Duhayon, G. Rajaraman, and E. Colacio, *Chem. Eur. J.*, **2015**, *21*, 15785.

[164] J. Long, R. Vallat, R. A. S. Ferreira, L. D. Carlos, F. A. Almeida Paz, Y. Guari, and J. Larionova, *Chem. Commun.,* **2012**, *48*, 9974.

[165] J. Long, E. Mamontova, V. Freitas, D. Luneau, V. Vieru, L. F. Chibotaru, R. A. S. Ferreira, G. Félix, Y. Guari, L. D. Carlos, and J. Larionova, *RSC Adv.*, **2016**, 108810.

[166] A.-L. Boulkedid, J. Long, C. Beghidja, Y. Guari, A. Beghidja and J. Larionova, *Dalton Trans*, **2018**, *47*, 1402.

[167] a) W.-K. Lo, W.-K. Wong, W.-Y. Wong, J. Guo, K.-T. Yeung, Y.-K. Cheng, X. Yang and R. A. Jones, *Inorg. Chem*, **2006**, *45(23)*, 9315; b) W.-B. Sun, P.-F. Yan, S.-D. Jiang, B.-W. Wang, Y.-Q. Zhang, H.-F. Li, P. Chen, Z.-M. Wang and S. Gao, *Chem. Sci.*, **2016**, *7(1)*, 684.

[168] X. Lü, W. Bi, W. Chai, J. Song, J. Meng, W.-Y. Wong, W.-K. Wong and R. A. Jones, *New. J. Chem,* **2008**, *32*, 127.

[169] M. Llunell, D. Casanova, J. Cirera, and J. M. Bofill, P. Alemany, S. Alvarez, SHAPE (version 2.1), Barcelona, **2013**.

[170] E. Moreno-Pineda, G. Taran, W. Wernsdorfer, and M. Ruben, *Chem. Sci.*, **2019**, *10*, 5138.

[171] O. Kahn*, Molecular Magnetism*, VCH, Weinheim, Germany, **1993**.

[172] J. Stöhr, H. C. Siegmann, *Magnetism: From fundamentals to Nanoscale Dynamics*, Springer Series in Solid-State Physics, 152, Springer, Berlin Heidelberg, Germany, **2006**.

CHAPTER VII

GENERAL CONCLUSIONS AND OUTLOOK

This thesis presents the different studies of the magnetic behavior of different molecules based on trivalent lanthanide cations, as well as the different routes for the optimization of their physical properties. In general, different compounds have been chosen from the literature and have been synthesized as single crystals. The synthetic routes reported in the literature have been slightly modified in order to include the isotopic lanthanide precursor ($Ln_2O_3{\cdot}xH_2O$) or the diamagnetic analogue for the dilution. The molecular structure has been characterized by single crystal X-ray diffractions (XRD) and their magnetic behavior studied by SQUID (Superconducting Quantum Interference Device) and PPMS (Physical Property Measurement System) magnetometry.

The starting point of this work, as previously explained, are the different works presented by some of the people of the group between 2013 and 2015.[174,175] Within, a mononuclear Dy-based system is characterized, thus including two different strategies for the optimization of the SMM behavior: magnetic dilution and isotopic enrichment with a nuclear spin free isotope. These two strategies have been tested in six different systems in order to acquire a global understanding of the dependence between the quantum effects present in the relaxation mechanisms at low temperature, and the different interactions in the system which may perturb somehow the magnetic properties of the metal center.

First, a Dy-based (**Dy**, in Chapter III) system has been chosen and the missing ^{162}Dy and ^{163}Dy isotopes have been studied, in both condensed and diluted phase. This first work evidences the different HF coupling constants, and thus different relaxation behavior, between the nuclear spin active isotopologues (^{161}Dy vs. ^{163}Dy, both with I= 5/2); and the fact that Orbach and QTM, are not enough for the description of the general relaxation, with a first proposal by adding a non-isotopic dependent Raman.

The second and third systems (named **Yb** and **Er**, in Chapter IV), isostructural to **Dy**, have been presented together to find a possible confirmation about the direction of the earlier findings in systems with a different electronic density distribution in the metal center.

Unfortunately, as it could be predicted from Long's model[176], these systems did not show any slow relaxation of the magnetization at zero field, thus making necessary a magnetic dilution in order to enhance it. Consequently, **Yb@Y** compounds displayed frequency dependence, resulting to the first Yb-based compound showing this property as, until now and for the best of our knowledge, all the examples of slow relaxation were induced by an external magnetic field. This extraordinary discovery, made possible the study of the isotopic effect in this kind of system, which resulted to be in the same direction as **Dy** analogue. The physical properties of the Er-based molecule was studied, resulting a field induced SMM and the hyperfine footprint was determined by EPR. Unfortunately, the appearance of a radical signal in the spectra complicated the different measurements, and the relaxation times were too fast in the temperatures available for the measurements, in order to being able to see any echo, for the possible applicability in qubits.

A second system based on erbium was chosen from the literature (**ErW$_{10}$** in Chapter V), displaying SMM. This molecule of Coronado's group, has been previously studied for the isotopic enrichment and dilution by F. Luis *et al.*, taking into account only I= 5/2 and different dilution ratios. Within this work, they arrived to different conclusions as those shows in ours previous investigations. Reproduction of the natural and ^{167}Er (I= 5/2) complexes were followed by the study of an I= 0 isotopologue (^{166}Er), in order to observe the full study. However, this system appeared to be more complicated than we first thought and isotopic enrichment could not be entirely understood: even if the published trend was confirmed, the appearance of different relaxation contributions in the susceptibility hindered the full analyses, and **^{166}ErW$_{10}$** did not display any significant difference from the natural compound. On the other hand, **ErW$_{10}$** has shown to reversibly switch the SMM behavior depending on hydration. Hence, by decreasing the number of water molecules in the structure, the magnetic anisotropy switches and thus the SMM behavior is lost and, by rehydrating this one is recovered.

In order to verify if the switch in the tendency comes from the coordination sphere of the metal ion (for the firsts it was N_2O_6 whereas for the last O_8). A Dy-based system with a coordination sphere entirely oxygenated was required. To that condition, we include the study of the isotopic and dilution effect to systems where a polarization of the electron density favors already the slow relaxation of the magnetization.

From these two requirements arise the two last systems of this work, **Dy(ZnL^{15})$_2$** and **Dy(ZnL^{17})$_2$**. This work has not been finished because of time and some difficulties found during the different experiments. Even though, the results obtained permitted to give answer to the opened questions, thus proving the isotopic and the dilution effect in this kind of polarized systems, and showing a clear tendency of those effects to the slow of the relaxation, as for the N_2O_6-coordinated systems. By comparing both systems, changes in the second coordination sphere leaded to different magnetic behavior, as the electronic density distribution is changed.

At a broader level, the isotopic effect is, in general, partially hindered by the internal field created by dipolar interactions, being really important for some systems where the intermolecular interactions are favored. Furthermore, the effect of the isotopic enrichment and the magnetic dilution, seems to be addressed to a common direction: the suppression of the quantum events at low temperature by diminishing the different interactions, with the exception of **ErW$_{10}$** which need to be verified by further analyses. Nevertheless, even if the quantum regime is not entirely suppressed in the different systems (the waist-restricted shape of the hysteresis loop of the magnetization still remains at zero field), an important enhancement of the relaxation in the low temperature regime is usually achieved. And moreover, we have been able to demonstrate that by coupling both strategies together, the slow relaxation of the magnetization can be enhanced, for systems where no signal of frequency dependence was observed: **Yb@Y** constitutes the first molecule displaying SMM behavior and which relaxation can be characterized.

Recent publications point out to the not solely contribution of the dipolar and hyperfine interactions for the efficiency of the quantum events, but that the major contribution would come from the different vibrational states bearing from the flexibility of the ligand used.[177,178,179] Other approaches, with special focus in the role of nuclear spin interaction, make use of ac and μ-squid studies at the sub-kelvin level, to evidence that even if *I* enhances a faster relaxation, it does not change the QTM rate but favors the coupling between the different hyperfine states and the acoustic phonons, thus, increasing the contribution of the Raman relaxation. [180]

In order to go a step further in the understanding of the quantum events, more work needs to be done in this field taking into account the newest results found by the different groups. First, the relaxation mechanism needs to be better understood by further investigation about the Raman contribution, which for example can be enhanced by the different interactions of the matrix with the diamagnetic cation (Y^{3+}, Lu^{3+}, La^{3+}, etc.). Moreover, concerning the erbium cation, many questions are still opened: whereas the events occurring at low temperature for the ^{167}Er isotope are of nuclear origin or not; and the reason why the difference in the trend of the isotopic effect on lanthanides for that system, are some of the questions that we want to respond thereafter. This include the study of the dilution in the isotopic systems, so that the HF interactions can be greater observe (we note that the difference in the HF interactions was not visible between **^{166}ErW$_{10}$** and **ErW$_{10}$**), while more information would be obtained about the relaxation mechanism in **^{167}ErW$_{10}$**; as well as the addition of another Er-based system, for the confirmation of the tendency seen heretofore.

---

[174] T. T. da Cunha, J. Jung, M.-E. Boulon, G. Campo, F. Pointillart, C. L. M. Pereira, B. Le Guennic, O. Cador, K. Bernot, F. Pineider, S. Golhen, and L. Ouahab*, J. Am. Chem. Soc.* **2013**, *135*, 16332.

[175] F. Pointillart, K. Bernot, S. Golhen, B. Le Guennic, T. Guizouarn, L. Ouahab, and O. Cador, *Angew. Chem.*, **2015**, *127*, 1524.

[176] J. D. Rinehart, and J. R. Log, *Chem. Sci.*, **2011**, *2*, 2078.

[177] K. R. McClain, C. A. Gould, K. Chakarawet, S. J. Teat, T. J. Groshens, J. R. Long, and B. G. Harvey, *Chem. Sci.*, **2018**, *9*, 8492.

[178] Y.-S. Ding, K.-X. Yu, D. Reta, F. Ortu, R. E. P. Winpenny, Y.-Z. Zheng and N. F. Chilton, *Nat. Commun.*, **2018**, *9*, 3134.

[179] F. Ortu, D. Reta, Y.-S. Ding, C. A. P. Goodwin, M. P. Gregson, E. J. L. McInnes, R. E. P. Winpenny, Y.-Z. Zheng, S. T. Liddle, D. P. Mills, and N. F. Chilton, *Dalton Trans.*, **2019**, *48*, 8541.

[180] E. Moreno-Pineda, G. Taran, W. Wernsdorfer, and M. Ruben, *Chem. Sci.*, **2019**, *10*, 5138.

ANNEXES

A1. CRISTALLOGRAPHIC DATA

Single Crystal:

*Table A1. 1. X-Ray cristallographic data for the complex **Dy** (Chapter III).*

Compounds	$[^{162}Dy(tta)_3(\mathbf{L^2})]\cdot(C_6H_{14})$ ($\mathbf{^{162}Dy}$)	$[^{162}Dy_{0.05}Y_{0.95}(tta)_3(\mathbf{L^2})]\cdot(C_6H_{14})$ ($\mathbf{^{162}Dy@Y}$)
Formula	$C_{58}H_{52}DyF_9N_4O_6S_9$	$C_{58}H_{52}Dy_{0.05}Y_{0.95}F_9N_4O_6S_9$
M / g mol^{-1}	1522.57	1452.19
Crystal system	triclinic	monoclinic
Space group	P-1 (N°2)	P-1 (N°2)
Cell parameters	a = 15.3700(12) Å b = 15.7135(13) Å c = 16.7271(14) Å α = 97.981(3)° β = 110.300(3)° γ = 117.242(3)°	a = 15.3310(11) Å b = 15.6911(12) Å c = 16.7368(13) Å α = 98.060(3)° β = 110.194(2)° γ = 117.203(3)°
Volume / Å^3	3146.7(5)	3139.3(4)
Cell formula units	2	2
T / K	150 (2)	150(2)
Diffraction reflection / °	$5.86 \leq 2\theta \leq 54.96$	$5.86 \leq 2\theta \leq 54.97$
ρ_{calc} / g cm^{-3}	1.607	1.533
μ /mm^{-1}	1.565	1.308
Number of reflections	67713	68306
Independent reflections	14397	14375
$Fo^2 > 2\sigma(Fo)^2$	12668	11375
Number of variables	783	771
R_{int}, R_1, wR_2	0.0438, 0.0547, 0.1356	0.0527, 0.0731, 0.1962
…/…		

Compounds	$[^{163}\text{Dy(tta)}_3(\mathbf{L^2})]\cdot(\text{C}_6\text{H}_{14})$ (**^{163}Dy**)	$[^{163}\text{Dy}_{0.05}\text{Y}_{0.95}\text{(tta)}_3(\mathbf{L^2})]\cdot(\text{C}_6\text{H}_{14})$ (**^{163}Dy@Y**)
Formula	$\text{C}_{58}\text{H}_{52}\text{DyF}_9\text{N}_4\text{O}_6\text{S}_9$	$\text{C}_{58}\text{H}_{52}\text{Dy}_{0.05}\text{Y}_{0.95}\text{F}_9\text{N}_4\text{O}_6\text{S}_9$
M / g mol^{-1}	1523.57	1453.19
Crystal system	triclinic	triclinic
Space group	P-1 (N°2)	P-1 (N°2)
Cell parameters	a = 15.3548(22) Å b = 15.7144(23) Å c = 16.7281(23) Å α = 98.032(5)° β = 110.191(5)° γ = 117.221(5)°	a = 15.3157(10) Å b = 15.6570(10) Å c = 16.7142(10) Å α = 98.058(2)° β = 110.199(2)° γ = 117.307(2)°
Volume / Å^3	3147.3(8)	3120.8(3)
Cell formula units	2	2
T / K	150(2)	150(2)
Diffraction reflection / °	$4.46 \leq 2\theta \leq 55.03$	$5.88 \leq 2\theta \leq 54.97$
ρ_{calc} /g cm^{-3}	1.607	1.543
μ /mm^{-1}	1.565	1.328
Number of reflections	66322	77501
Independent reflections	14444	14299
$Fo^2 > 2\sigma(Fo)^2$	12519	9999
Number of variables	699	783
R_{int}, R_1, wR_2	s0.0670, 0.0606, 0.1515	0.0617, 0.0724, 0.1870

*Table A1. 2. X-Ray cristallographic data for the complex **Yb** (Chapter IV).*

Compounds	$[\text{Yb(tta)}_3(\mathbf{L^2})]\cdot(\text{C}_6\text{H}_{14})$ (**Yb@Y**)	$[^{173}\text{Yb(tta)}_3(\mathbf{L^2})]\cdot(\text{C}_6\text{H}_{14})$ (**^{173}Yb@Y**)	$[^{174}\text{Yb}_{0.05}\text{Y}_{0.95}\text{(tta)}_3(\mathbf{L^2})]\cdot(\text{C}_6\text{H}_{14})$ (**^{174}Yb@Y**)
Crystal system	triclinic	triclinic	triclinic
Cell parameters	a = 15.34(1) Å b = 15.65(2) Å c = 16.73(2) Å α = 98.04(3)° β = 110.35(3)° γ = 117.14(3)°	a = 15.36(2) Å b = 15.73(3) Å c = 16.76(3) Å α = 98.02(4)° β = 109.89(3)° γ = 117.56(4)°	a = 15.17(4) Å b = 15.58(4) Å c = 16.62(4) Å α = 98.23(4)° β = 110.18(7)° γ = 117.40(4)°
Volume / Å^3	3129(9)	3153(16)	3054(25)
T / K	150(2)	150 (2)	150(2)

Table A1. 3. X-Ray cristallographic data for the complex Er (Chapter IV).

Compounds	$[^{166}Er_{0.05}Y_{0.95}(tta)_3(\mathbf{L^2})]\cdot(C_6H_{14})$ (**^{166}Er@Y**)	$[^{167}Er_{0.05}Y_{0.95}(tta)_3(\mathbf{L^2})]\cdot(C_6H_{14})$ (**^{167}Er@Y**)
Crystal system	triclinic	triclinic
Cell parameters	a = 15.27(3) Å b = 15.71(3) Å c = 16.67(3) Å α = 98.15(6)° β = 110.09(4)° γ = 117.21(4)°	a = 15.32(3) Å b = 15.71(3) Å c = 16.67(3) Å α = 98.15(6)° β = 110.09(4)° γ = 117.22(4)°
Volume / Å^3	3153(16)	3121(19)
T / K	150(2)	150(2)

Table A1. 4. X-Ray crystallographic data for the complex $ErW_{10}\cdot 35H_2O$ (Chapter V).

Compounds	$Na_9[Er(W_5O_{18})_2]\cdot 35H_2O$, **$ErW_{10}\cdot 35H_2O$**	$Na_9[^{166}Er(W_5O_{18})_2]\cdot 35D_2O$, **$^{166}ErW_{10}\cdot 35D_2O$**
Formula	$Na_9ErW_{10}O_{71}H_{70}$	-
M / g.mol^{-1}	3418.67	-
Crystal system	Triclinic	triclinic
Space group	P-1	-
Cell parameters	a = 12.7812(6)Å b = 13.0943(7) Å c = 20.5479(11) Å α = 82.822(2)° β = 74.707(2)° γ = 88.805(2)°	a = 12.752(8) Å b = 13.082(9) Å c = 20.54(2) Å α = 82.87(3)° β = 74.48(3)° γ = 88.97(2)°
Volume / Å^3	3290.9(3)	3275(7)
Cell formula units	2	-
T / K	150(2)	150(2)
Diffraction reflection / °	$2.24 \leq 2\theta \leq 27.55$	-
ρ_{calc} / g cm^{-3}	1.607	-
μ /mm^{-1}	18.843	-
Number of reflections	52171	-
Independent reflections	15021	-
$Fo^2 > 2\sigma(Fo)^2$	12484	-
Number of variables	766	-
R_{int}, R_1, wR_2	0.0727, 0.0625,0.1769	-
…/…		

Compounds	$Na_9[^{166}Er(W_5O_{18})_2]\cdot 35H_2O$, **$^{166}ErW_{10}\cdot 35H_2O$**	$Na_9[^{167}r(W_5O_{18})_2]\cdot 35H_2O$, **$^{167}ErW_{10}\cdot 35H_2O$**
Crystal system	triclinic	triclinic
Cell parameters	a = 12.75 Å b = 13.06 Å c = 20.50 Å α = 82.83 ° β = 74.52 ° γ = 88.55 °	a = 12.763(4) Å b = 13.117(5) Å c = 20.52(1) Å α = 82.82(3) ° β = 74.41(2) ° γ = 88.81(2) °
Volume / Å^3	3264	3283(4)
T / K	293	150(2)

Table A1. 5. X-Ray crystallographic data for the complex ***$Dy(ZnL^{15})_2$*** *(chapter VI).*

Compounds	$[Zn_2(\mathbf{L^{15}})_2DyCl_3]\cdot 2H_2O]$ **$Dy(ZnL^{15})_2$**	$[Zn_2(\mathbf{L^{15}})_2{}^{162}DyCl_3]\cdot 2H_2O]$ ^{162}**$Dy(ZnL^{15})_2$**	$[Zn_2(\mathbf{L^{15}})_2{}^{163}DyCl_3]\cdot 2H_2O]$ **$^{163}Dy(ZnL^{15})_2$**
Crystal system	monoclinic	monoclinic	monoclinic
Cell parameters	a = 16.6(1) Å b = 23.3(2) Å c = 14.6(1) Å α = 90° β = 104.8(1)° γ = 90°	a = 16.00(3) Å b = 22.24(5) Å c = 14.17(3) Å α = 90° β = 104.59(5)° γ = 90°	a = 16.21(2) Å b = 22.66(2) Å c = 14.25(1) Å α = 90° β = 105.06(3)° γ = 90°
Volume / Å^3	5490(137)	4883(30)	5053(16)
T / K	293(2)	150(2)	150(2)
Compounds	$Dy_{0.1}Y_{0.9}(Zn\mathbf{L^{15}})_2$ (**$Dy@Y(ZnL^{15})_2$**)	$^{162}Dy_{0.1}Y_{0.9}(Zn\mathbf{L^{15}})_2$ (^{162}**$Dy@Y(ZnL^{15})_2$**)	$^{163}Dy_{0.1}Y_{0.9}(Zn\mathbf{L^{15}})_2$ (**$^{163}Dy@Y(ZnL^{15})_2$**)
Crystal system	monoclinic	monoclinic	monoclinic
Cell parameters	a = 16.114(2) Å b = 22.449(3) Å c = 14.233(2) Å α = 90° β = 104.371(5)° γ = 90°	a = 15.94(3) Å b = 22.39 (5) Å c = 14.11(3) Å α = 90° β = 104.58(7)° γ = 90°	a = 16.17(3) Å b = 22.62(5) Å c = 14.28(2) Å α = 90° β = 104.71(6)° γ = 90°
Volume / Å^3	4987(2)	4874(28)	5053(27)
T / K	150(2)	150(2)	293(2)

Table A1. 6. X-Ray crystallographic data for the complex ***Dy(ZnL^{17})$_2$*** *(chapter VI).*

Compound	[(Zn**L^{17}**Cl)$_2$^{A}Dy(H$_2$O)]$_2$ [ZnCl$_4$]·xH$_2$O (**Dy(ZnL^{17})$_2$**)	[(Zn**L^{17}**Cl)$_2$^{163}Dy(H$_2$O)]$_2$ [ZnCl$_4$]·xH$_2$O (**^{163}Dy(ZnL^{17})$_2$**)	[(Zn**L^{17}**Cl)$_2$^{164}Dy(H$_2$O)]$_2$ [ZnCl$_4$]·xH$_2$O (**^{164}Dy(ZnL^{17})$_2$**)
Formula	$C_{72}H_{72}Cl_8Dy_2N_8O_{18}Zn_5$	-	-
M / g mol^{-1}	2272.82	-	-
Crystal system	P-1 (N° 2)	-	-
Space group	triclinic	triclinic	triclinic
Cell parameters	a = 15.564(2) Å b = 18.308(3) Å c = 20.091(4) Å α = 108.827(6)° β = 101.066(6)° γ =111.798(6)°	a = 15.42(2) Å b = 18.45(3) Å c = 19.63(3) Å α = 107.88(4)° β = 100.29(4)° γ = 114.41(4)°	a = 15.5(2) Å b = 18.5(3) Å c = 19.9(3) Å α = 108.2(2)° β = 100.4(2)° γ = 114.4(2)°
Volume / Å^3	4704(1)	4530(16)	4600(200)
Cell formula units	2	-	-
T / K	150(2)	150 (2)	150(2)
Diffraction reflection / °	$6.03 \leq 2\theta \leq 54.97$	-	-
ρ_{calc} / g cm^{-3}	1.605	-	-
μ / mm^{-1}	3.110	-	-
Number of reflections	90180	-	-
Independent reflections	20015	-	-
$Fo^2 > 2\sigma(Fo)^2$	10374	-	-
Number of variables	676	-	-
R_{int}, R_1, ωR_2	0.2507, 0.1161, 0.2766	-	-

<u>Crystalline powder:</u>

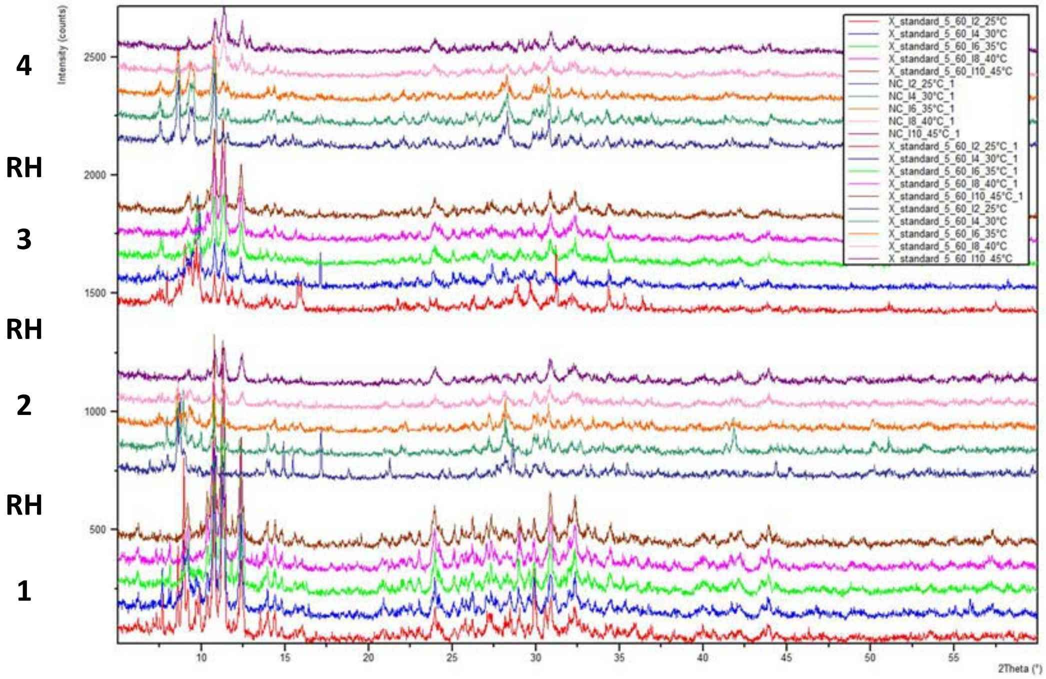

Figure A1. 1. Four different consecutive heating procedures displayed in stack, showing the different evolution after the different cycles of rehydration and dehydration of **ErW_{10}**$\cdot 35H_2O$.

A2. EDS ANALYSES

The different values exposed during this manuscript related with the EDS analyses, correspond to an average value resulted from different analyses of different spots (visualized in the following images and tables).

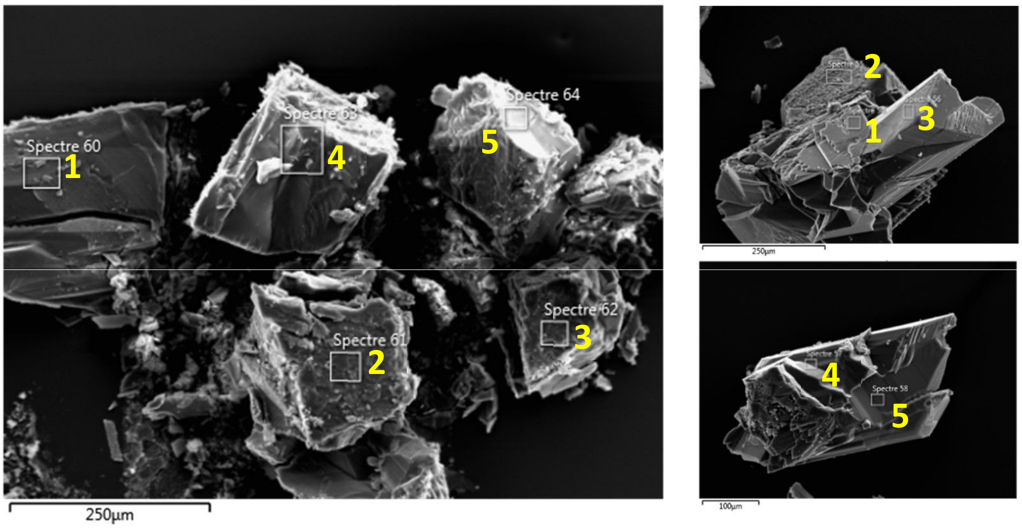

*Figure A2. 1. Images from the Scanning Electron Microscopy for the EDS Analysis of (left) ^{162}Dy@Y and (right) ^{163}**Dy@Y**.*

*Table A2. 1. Atomic percentage of Dy:Y for the different spots for ^{162}**Dy@Y** and ^{163}**Dy@Y**.*

^{162}**Dy@Y**	*% atomic of Y*	*% atomic of Dy*
1	96.23	3.77
2	95.85	4.15
3	95.52	4.48
4	93.52	6.48
5	95.75	4.25
average	95.4(7)	4.6(7)
^{163}**Dy@Y**	*% atomic of Y*	*% atomic of Dy*
1	95.84	4.16
2	95.82	4.18
3	95.75	4.24
4	96.00	4.00
5	95.37	4.63
average	95.8(2)	4.2(2)

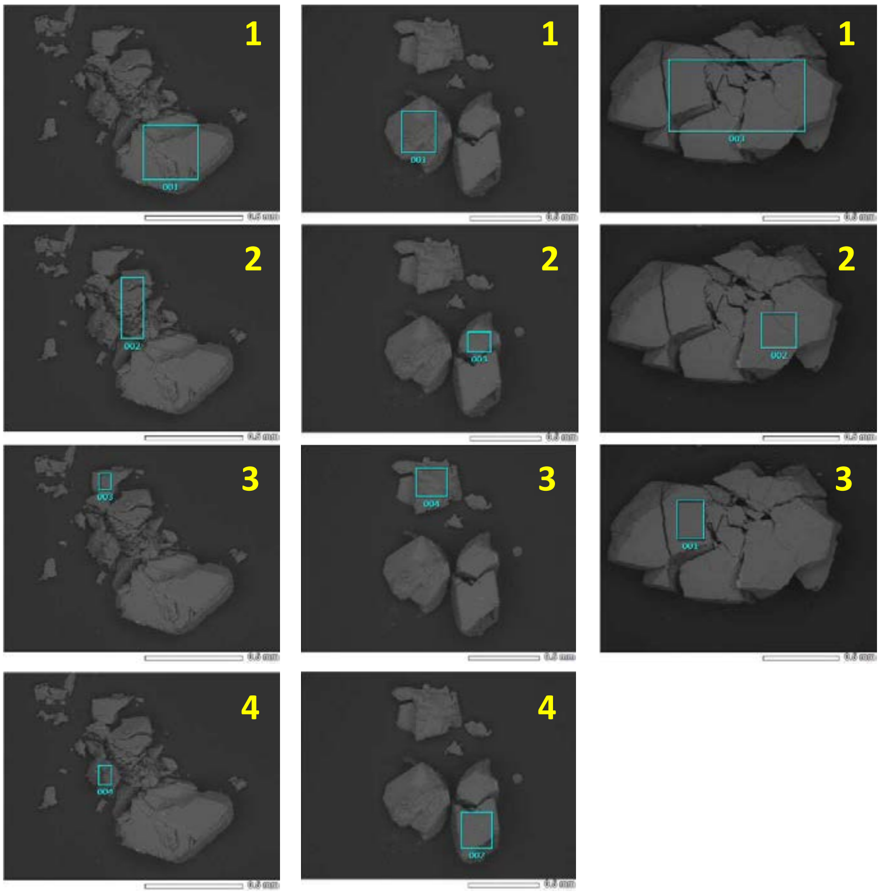

Figure A2. 2. Images from the Scanning Electron Microscopy for the EDS Analysis of (left) ***Yb@Y****, (middle**)*** ^{173}***Yb@Y*** *and (right)* ^{174}***Yb@Y****.*

Table A2. 2. Atomic percentage of Dy:Y for the different spots for) ***Yb@Y****,* ^{173}***Yb@Y*** *and* ^{174}***Yb@Y****.*

Yb@Y	*% atomic of Y*	*% atomic of Yb*
1	91.223	8.77
2	90.61	9.39
3	91.75	8.25
4	90.17	9.83
average	*90.9(5)*	*9.1(6)*
^{173}**Yb@Y**	*% atomic of Y*	*% atomic of Yb*
1	93.18	6.82
2	93.52	6.48
3	92.25	7.75
4	94.60	5.40
average	*93.4(7)*	*6.6(7)*
^{174}**Yb@Y**	*% atomic of Y*	*% atomic of Yb*
1	89.40	10.60
2	89.87	10.13
3	91.92	8.08
average	90(1)	10(1)

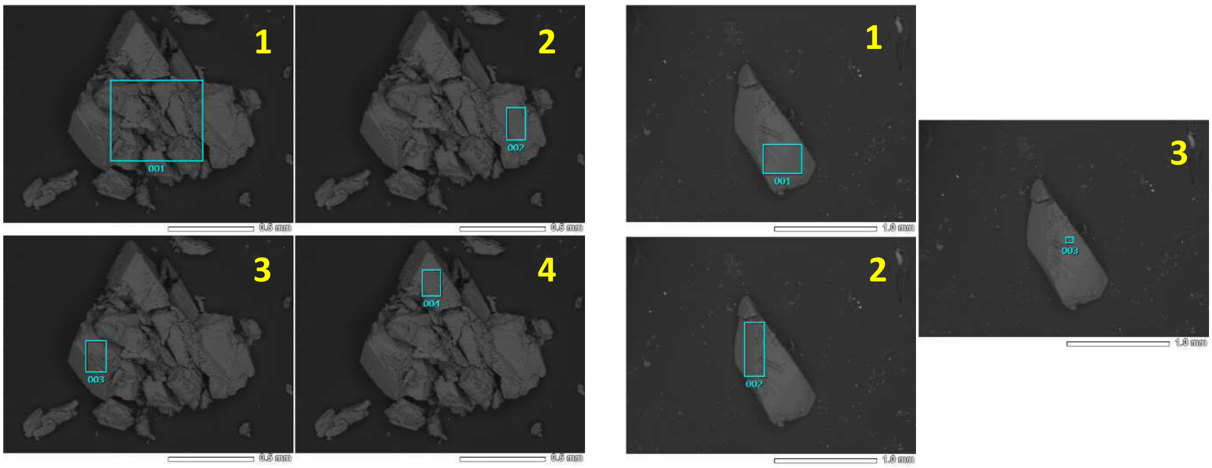

Figure A2. 3. Images from the Scanning Electron Microscopy for the EDS Analysis of (left) ^{166}***Er@Y*** *and (right)* ^{167}***Er@Y****.*

Table A2. 3. Atomic percentage of Dy:Y for the different spots for ^{166}***Er@Y*** *and* ^{167}***Er@Y****.*

^{166}**Er@Y**	*% atomic of Y*	*% atomic of Er*
1	95.12	4.88
2	96.34	3.66
3	96.79	3.21
4	96.43	3.57
average	96.2(5)	3.8(5)
^{167}**Er@Y**	*% atomic of Y*	*% atomic of Er*
1	97.78	2.22
2	98.11	1.89
3	97.12	2.88
average	97.7(4)	2.3(4)

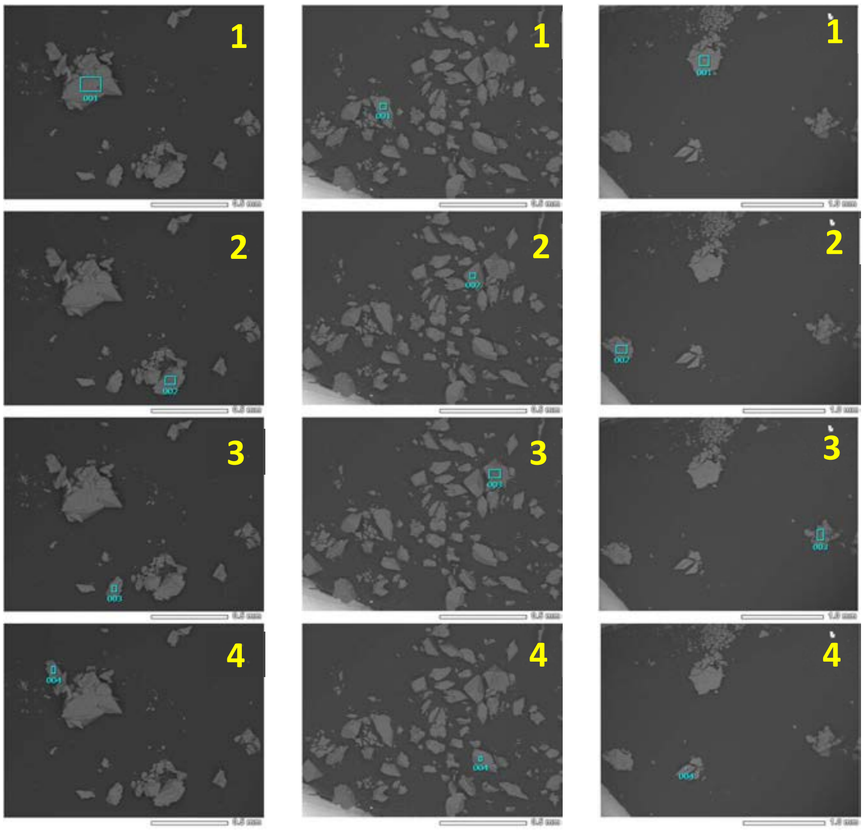

Figure A2. 4. Images from the Scanning Electron Microscopy for the EDS Analysis of (left) **Dy@Y(ZnL^{15})$_2$**, *(middle)* ^{162}**Dy@Y(ZnL3)$_2$** *and (right)* ^{163}**Dy@Y(ZnL3)$_2$**.

Table A2. 4. Atomic percentage of Dy:Y for the different spots for **Dy@Y(ZnL^{15})$_2$**, ^{162}**Dy@Y(ZnL^{15})$_2$** *and* ^{163}**Dy@Y(ZnL^{15})$_2$**. *(*)These date correspond to isolated crystals which are not taken into account in the average doping value and do not interfere in the AC magnetic properties of the studied molecule.*

Dy@Y(ZnL^{15})$_2$	*% atomic of Y*	*% atomic of Dy*
1	88.07	11.93
2	88.52	11.48
3	100(*)	0(*)
4	83.96	16.04
average	*87(2)*	*13(2)*
^{162}Dy@Y(ZnL^{15})$_2$	*% atomic of Y*	*% atomic of Dy*
1	81.54	18.46
2	100(*)	0(*)
3	82.65	17.35
4	85.37	14.63
average	*83(2)*	*17(2)*
^{163}Dy@Y(ZnL^{15})$_2$	*% atomic of Y*	*% atomic of Dy*
1	79.62	20.38
2	87.07	12.93
3	83.46	16.64
4	92.30	8.70
average	86(4)	15(4)

A3. MAGNETIC PROPERTIES

DC information:

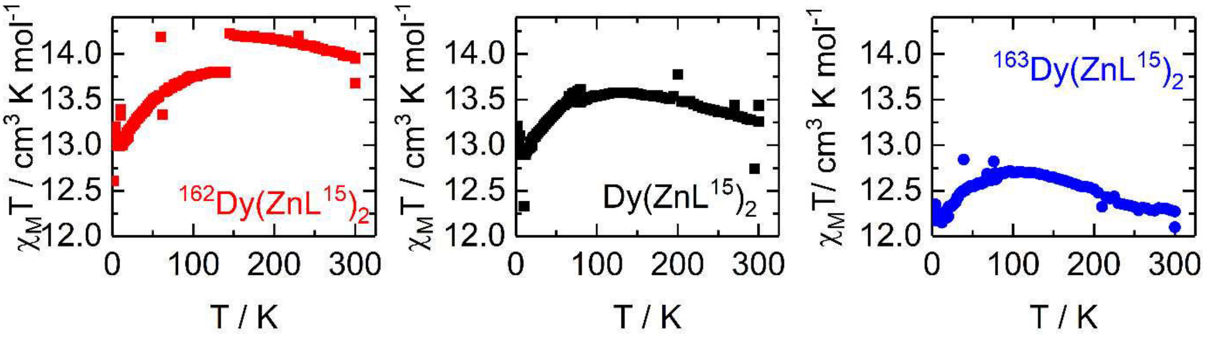

Figure A3. 1. DC magnetic susceptibility measurements of ^{A}***Dy(ZnL***^{15}***)***$_2$ *compounds.*

AC information:

Table A3. 1. Best fitted parameters (χ_T, χ_S, τ and α) with the extended Debye model for compound ^{162}***Dy*** *at 0 Oe in the temperature range 2-15 K.*

T / K	χ_T / cm^3 mol^{-1}	χ_S / cm^3 mol^{-1}	α	τ / s	R^2
15	0.76651	0.34054	0.07877	0.00013	0.99997
14	0.82041	0.29118	0.10072	0.00017	0.99996
13	0.88221	0.25056	0.11371	0.00022	0.99991
12	0.95395	0.20491	0.12714	0.00030	0.99982
11	1.04771	0.15944	0.13615	0.00043	0.99969
10	1.15525	0.12596	0.14186	0.00066	0.99952
9	1.28144	0.11612	0.13763	0.00105	0.99946
8	1.44212	0.12053	0.13587	0.00169	0.99937
7	1.65172	0.13272	0.14278	0.00266	0.99911
6	1.93405	0.15273	0.15961	0.00396	0.99872
5.5	2.11595	0.16535	0.17112	0.00471	0.99850
5	2.33470	0.17688	0.18439	0.00545	0.99827
4.5	2.59873	0.19113	0.19574	0.00615	0.99814
4	2.92940	0.20890	0.20472	0.00675	0.99805
3.5	3.35070	0.23031	0.21098	0.00720	0.99798
3	3.90719	0.26058	0.21324	0.00756	0.99796
2.8	4.18384	0.27999	0.21247	0.00770	0.99800
2.4	4.88459	0.31994	0.21220	0.00792	0.99801
2	5.83351	0.37376	0.21157	0.00811	0.99798

Table A3. 2. Best fitted parameters (χ_T, χ_S, τ and α) with the extended Debye model for compound ^{163}**Dy** *at 0 Oe in the temperature range 2-15 K.*

T / K	χ_T / cm^3 mol^{-1}	χ_S / cm^3 mol^{-1}	α	τ / s	R²
15	0.80669	0.35287	0.10102	0.00010	0.99997
14	0.86240	0.32644	0.10376	0.00014	0.99995
13	0.92650	0.27661	0.13364	0.00016	0.99995
12	1.00140	0.22560	0.14916	0.00020	0.99989
11	1.09990	0.20614	0.15542	0.00027	0.99986
10	1.20898	0.18310	0.16554	0.00036	0.99982
9	1.34358	0.18310	0.17573	0.00048	0.99975
8	1.51242	0.19077	0.19139	0.00060	0.99965
7	1.72893	0.21156	0.20908	0.00072	0.99959
6	2.01690	0.22844	0.23185	0.00080	0.99955
5.5	2.20004	0.24306	0.24020	0.00084	0.99954
5	2.41820	0.25295	0.24938	0.00086	0.99958
4.5	2.67923	0.30046	0.24777	0.00090	0.99955
4	3.01828	0.29785	0.26169	0.00090	0.99963
3.5	3.44736	0.32953	0.26560	0.00092	0.99964
3	4.01898	0.36854	0.27018	0.00093	0.99965
2.8	4.30593	0.38356	0.27225	0.00094	0.99965
2.4	5.02994	0.44492	0.27339	0.00096	0.99966
2	6.01177	0.51840	0.27485	0.00097	0.99967

Table A3. 3. Best fitted parameters (χ_T, χ_S, τ and α) with the extended Debye model for compound ^{162}**Dy** *at 1000 Oe in the temperature range 4.5-15 K.*

T / K	χ_T / cm^3 mol^{-1}	χ_S / cm^3 mol^{-1}	α	τ / s	R²
15	0.76719	0.32071	0.12145	0.00019	0.99995
14	0.82236	0.27867	0.14585	0.00031	0.99983
13	0.88586	0.23913	0.16845	0.00050	0.99957
12	0.96188	0.18809	0.20113	0.00079	0.99904
11	1.06264	0.12504	0.23161	0.00131	0.99835
10	1.17644	0.07533	0.24780	0.00221	0.99823
9	1.31353	0.04491	0.25163	0.00406	0.99853
8	1.48767	0.03073	0.25326	0.00813	0.99893
7	1.71732	0.02299	0.25832	0.01788	0.99935
6	2.01831	0.02277	0.26492	0.04450	0.99954
5.5	2.17559	0.02730	0.26109	0.07280	0.99942
5	2.31044	0.03361	0.25035	0.11947	0.99938
4.5	2.40781	0.04207	0.23336	0.19762	0.99953

*Table A3. 4. Best fitted parameters (χ_T, χ_S, τ and α) with the extended Debye model for compound ^{163}**Dy** at 1000 Oe in the temperature range 2-15 K.*

T / K	χ_T / cm^3 mol^{-1}	χ_S / cm^3 mol^{-1}	*α*	*τ* / s	R²
15	0.80654	0.34223	0.12206	0.00019	0.99993
14	0.86428	0.31084	0.14007	0.00032	0.99986
13	0.93138	0.26156	0.16920	0.00050	0.99955
12	1.01084	0.20786	0.20423	0.00077	0.99906
11	1.11718	0.14261	0.23420	0.00127	0.98380
10	1.23610	0.09500	0.24952	0.00215	0.99830
9	1.37988	0.06937	0.25254	0.00399	0.99851
8	1.56291	0.05649	0.25437	0.00792	0.99903
7	1.80577	0.05423	0.26088	0.01743	0.99939
6	2.12412	0.05833	0.26931	0.04324	0.99964
5.5	2.30272	0.06653	0.26968	0.07127	0.99962
5	2.46570	0.07743	0.26335	0.11832	0.99954
4.5	2.63172	0.09178	0.25527	0.20356	0.99956

*Table A3. 5. Best fitted parameters (χ_T, χ_S, τ and α) with the extended Debye model for compound ^{162}**Dy@Y** at 0 Oe in the temperature range 2-15 K.*

T / K	χ_T / cm^3 mol^{-1}	χ_S / cm^3 mol^{-1}	*α*	*τ* / s	R²
15	0.04344	0.01002	0.21240	0.00012	0.99930
14	0.04652	0.01166	0.20149	0.00022	0.99915
13	0.05006	0.01167	0.19627	0.00039	0.99906
12	0.05437	0.00788	0.24203	0.00053	0.99841
11	0.05993	0.00547	0.25397	0.00086	0.99858
10	0.06618	0.00420	0.25272	0.00144	0.99864
9	0.07385	0.00313	0.25730	0.00254	0.99850
8	0.08345	0.00306	0.25115	0.00488	0.99912
7	0.09634	0.00305	0.26149	0.00988	0.99935
6	0.10950	0.00447	0.24614	0.02090	0.99930
5.5	0.12013	0.00469	0.25991	0.03292	0.99920
5	0.13318	0.00550	0.27632	0.05523	0.99928
4.5	0.14995	0.00613	0.30435	0.09874	0.99929

*Table A3. 6. Best fitted parameters (χ_T, χ_S, τ and α) with the extended Debye model for compound ^{163}**Dy@Y** at 0 Oe in the temperature range 2-15 K.*

T / K	χ_T / cm^3 mol^{-1}	χ_S / cm^3 mol^{-1}	*α*	τ / s	R²
15	0.05009	0.01744	0.17803	0.00012	0.99966
14	0.05391	0.01388	0.21544	0.00018	0.99933
13	0.05803	0.01340	0.21551	0.00030	0.99928
12	0.06305	0.01095	0.24195	0.00045	0.99877
11	0.06958	0.00758	0.26459	0.00071	0.99825
10	0.07666	0.00632	0.26212	0.00120	0.99830
9	0.08541	0.00572	0.25452	0.00208	0.99885
8	0.09644	0.00609	0.24782	0.00380	0.99912
7	0.11065	0.00754	0.24229	0.00721	0.99892
6	0.12638	0.00841	0.23603	0.01308	0.99910
5.5	0.13818	0.00923	0.24212	0.01843	0.99917
5	0.15267	0.00988	0.25747	0.02608	0.99905
4.5	0.17087	0.01020	0.28085	0.03699	0.99828
4	0.19361	0.01174	0.30258	0.05268	0.99894
3.5	0.22354	0.01249	0.33594	0.07390	0.99898
3	0.26433	0.01266	0.37648	0.10238	0.99905
2.8	0.28480	0.01268	0.39339	0.11641	0.99908
2.6	0.30811	0.01291	0.40900	0.13214	0.99928
2.4	0.33561	0.01314	0.42576	0.15063	0.99936
2.2	0.37028	0.01290	0.44485	0.17270	0.99935
2	0.40254	0.01341	0.45805	0.19260	0.99947

*Table A3. 7. Best fitted parameters (χ_T, χ_S, τ and α) with the extended Debye model for compound **Dy** at 0 Oe in the temperature range 2-20 K.*

T / K	χ_T / cm^3 mol^{-1}	χ_S / cm^3 mol^{-1}	α	τ / s	R²
20	0.55651	0.27783	0.09931	9.00667E-6	0.99956
18	0.63142	0.17118	0.26065	1.44788E-5	0.99958
16	0.7168	0.15584	0.29034	3.71904E-5	0.99903
15	0.77038	0.18045	0.24438	6.24009E-5	0.99944
14	0.81874	0.24491	0.17202	1.20337E-4	0.99977
13	0.88023	0.24042	0.17436	1.67203E-4	0.99974
12	0.95302	0.2201	0.18732	2.21636E-4	0.99968
11	1.05105	0.19412	0.20605	3.01937E-4	0.99894
10	1.15991	0.18445	0.21447	4.19607E-4	0.99867
9	1.294	0.194	0.22666	5.96607E-4	0.99811
8	1.46762	0.20618	0.2458	8.18649E-4	0.99717
7	1.69637	0.21079	0.27676	0.00106	0.99614
6	1.92235	0.26134	0.25784	0.00124	0.99741
5.5	2.09575	0.27122	0.26771	0.00133	0.99714
5	2.30175	0.29091	0.2765	0.00143	0.99732
4.5	2.5537	0.31289	0.2786	0.00151	0.99713
4	2.87759	0.33895	0.28276	0.00159	0.99718
3.5	3.28923	0.36209	0.28692	0.00165	0.99692
3	3.83387	0.40598	0.28725	0.00171	0.99696
2.8	4.10512	0.42336	0.28815	0.00173	0.99695
2.6	4.42137	0.45319	0.28782	0.00176	0.997
2.4	4.79335	0.48707	0.28734	0.00179	0.99688
2.2	5.26556	0.51963	0.28894	0.0018	0.99618
2	5.67318	0.65428	0.28314	0.00186	0.99717

*Table A3. 8. Best fitted parameters (χ_T, χ_S, τ and α) with the extended Debye model for compound **Yb** at 2 K in the H range 200-3000 Oe.*

H / Oe	χ_T / cm^3 mol^{-1}	χ_S / cm^3 mol^{-1}	α	τ / s	R²	$\frac{\chi_T - \chi_S}{\chi_T}$
200	0.64642	0.36919	0.07758	0.00189	0.99992	42.80
400	0.64668	0.17693	0.11148	0.00237	0.99967	72.56
600	0.64726	0.09643	0.13102	0.00256	0.99949	85.02
800	0.64566	0.06177	0.13629	0.0026	0.99941	90.35
1000	0.63944	0.05783	0.13448	0.00262	0.9994	92.38
1200	0.63287	0.05307	0.12778	0.0026	0.99977	92.20
1400	0.62989	0.04014	0.14072	0.00254	0.99975	93.50
1600	0.62439	0.03561	0.14485	0.00248	0.99981	94.13
1800	0.62013	0.02017	0.1545	0.00239	0.99974	95.22
2000	0.61107	0.02687	0.16327	0.00232	0.99962	95.45
2200	0.60376	0.01888	0.1725	0.00222	0.99974	96.79
2400	0.59384	0.01525	0.1769	0.00213	0.99956	97.29
2600	0.58162	0.01361	0.17822	0.00203	0.99953	97.58
2800	0.57151	0.01403	0.18319	0.00191	0.99971	97.47
3000	0.56009	0.00991	0.1869	0.00181	0.99948	98.15

*Table A3. 9. Best fitted parameters (χ_T, χ_S, τ and α) with the extended Debye model for compound **Yb** at 1000 Oe in the temperature range 2-4 K.*

T / K	χ_T / cm^3 mol^{-1}	χ_S / cm^3 mol^{-1}	α	τ / s	R²
4	0.94487	0.18529	-	1.56884E-4	0.99975
3.5	1.07457	0.13105	0.01913	2.83238E-4	0.99957
3	1.25479	0.11053	0.06198	5.72236E-4	0.99963
2.8	1.34415	0.10144	0.08108	7.56741E-4	0.99916
2.6	1.43869	0.13427	0.07592	0.00106	0.99877
2.4	1.56305	0.13549	0.09505	0.00143	0.99887
2.2	1.7262	0.12139	0.13209	0.00193	0.99928
2	1.88534	0.10914	0.16104	0.00247	0.99921

Table A3. 10. Best fitted parameters (χ_T, χ_S, τ and α) with the extended Debye model for compound ***Er*** *at 2 K in the H range 200-2000 Oe.*

H / Oe	χ_T / cm^3 mol^{-1}	χ_S / cm^3 mol^{-1}	α	τ / s	R^2	$\frac{\chi_T - \chi_S}{\chi_T}$
200	0.01231	1.59287	0.12277	4.52176E-5	0.99992	45.77
400	0.01677	0.77581	0.12049	5.30686E-5	0.99973	73.11
600	0.01347	0.45981	0.11492	5.31454E-5	0.99979	83.54
800	0.0158	0.28726	0.1215	4.89844E-5	0.99973	89.25
1000	0.01882	0.17791	0.13085	4.31413E-5	0.99966	92.96
1200	0.03399	0.06793	0.15559	3.64498E-5	0.99916	97.15
1400	0.02688	0.03221	0.15498	3.09087E-5	0.99949	98.54
1600	0.02259	0.01078	0.15434	2.58032E-5	0.99965	99.47
1800	0.0208	-	0.16365	2.11139E-5	0.99977	100.00
2000	0.02733	-	0.19275	1.59608E-5	0.99982	100.00

Table A3. 11. Best fitted parameters (χ_T, χ_S, τ and α) with the extended Debye model for compound ***Er*** *at 800 Oe in the temperature range 2-3 K.*

T / K	χ_T / cm^3 mol^{-1}	χ_S / cm^3 mol^{-1}	α	τ / s	R^2
3	1.95637	0.43609	0.05338	1.22507E-5	0.9999
2.8	2.07161	0.41255	0.06429	1.57526E-5	0.99989
2.6	2.2069	0.37676	0.07896	2.05013E-5	0.9999
2.4	2.35198	0.34522	0.09149	2.69139E-5	0.99987
2.2	2.51266	0.30947	0.10718	3.58358E-5	0.99986
2	2.67301	0.26346	0.13508	4.58185E-5	0.9996

Table A3. 12. Best fitted parameters (χ_T, χ_S, τ and α) with the extended Debye model for compound ***^{166}ErW$_{10}$·35H$_2$O*** *at 0 Oe in the temperature range 2-5 K.*

T / K	*χ_T / cm^3 mol^{-1}*	*χ_S / cm^3 mol^{-1}*	*α*	*τ / s*	*R²*
5	1.65865	0.17142	0.05963	2.48379E-4	0.99996
4.75	1.74471	0.1583	0.06635	3.89598E-4	0.99996
4.5	1.83714	0.17831	0.07376	6.27211E-4	0.99204
4.25	1.95223	0.19048	0.08844	9.70294E-4	0.99966
4	2.06672	0.21174	0.10393	0.00136	0.99903
3.75	2.21432	0.21266	0.12757	0.00172	0.99919
3.5	2.36851	0.21404	0.14289	0.00192	0.99936
3.25	2.54497	0.23138	0.14756	0.00205	0.99934
3	2.7475	0.25474	0.13944	0.00215	0.99752
2.75	2.99323	0.26295	0.14202	0.00223	0.99923
2.5	3.2915	0.27966	0.14416	0.00226	0.99931
2.25	3.76075	0.32312	0.13525	0.00237	0.99926
2	4.08724	0.33604	0.13737	0.00239	0.9987

Table A3. 13. Best fitted parameters (χ_T, χ_S, τ and α) with the extended Debye model for compound ***ErW$_{10}$·35H$_2$O*** *at 0 Oe in the temperature range 2-5 K.*

T / K	*χ_T / cm^3 mol^{-1}*	*χ_S / cm^3 mol^{-1}*	*α*	*τ / s*	*R²*
5	1.66894	0.32615	0.0291	2.11899E-4	0.99997
4.75	1.75526	0.30703	0.05543	3.37699E-4	0.9999
4.5	1.85165	0.30394	0.08515	5.4717E-4	0.9998
4.25	1.96391	0.31927	0.12159	8.59423E-4	0.99964
4	2.08371	0.32421	0.16284	0.00124	0.99959
3.75	2.22142	0.30929	0.21685	0.00158	0.99954
3.5	2.371	0.28803	0.25332	0.00172	0.99977
3.25	2.53693	0.29152	0.26051	0.00185	0.9998
3	2.73646	0.31035	0.26091	0.00191	0.99979
2.75	2.98122	0.32907	0.26078	0.00204	0.99959
2.5	3.26278	0.38057	0.25189	0.00218	0.99954
2.25	3.72717	0.42093	0.25014	0.00221	0.99939
2	4.04432	0.46215	0.24466	0.00229	0.99923

Table A3. 14. Best fitted parameters (χ_T, χ_S, τ and α) with the extended Debye model for compound ^{167}***ErW$_{10}$·35H$_2$O*** *at 0 Oe in the temperature range 4-5.25 K.*

T / K	χ_T / cm^3 mol^{-1}	χ_S / cm^3 mol^{-1}	α	τ / s	R²
5.25	1.32433	0.23947	0.03888	1.35164E-4	0.99996
5	1.38885	0.23553	0.0795	2.1611E-4	0.99987
4.75	1.46555	0.26453	0.10738	3.79187E-4	0.99975
4.5	1.55376	0.28977	0.14941	6.81374E-4	0.99917
4.25	1.63682	0.45617	0.12557	0.00157	0.99959
4	1.77323	0.4488	0.23538	0.00287	0.99827

Table A3. 15. Best fitted parameters (χ_T, χ_S, τ and α) with the extended Debye model for compound ***ErW$_{10}$·35H$_2$O*** *at 1200 Oe in the temperature range 4-5.25 K.*

T / K	χ_T / cm^3 mol^{-1}	χ_S / cm^3 mol^{-1}	α	τ / s	R²
5.25	1.2156	0.11211	0.07072	1.6944E-4	0.99994
5	1.2709	0.13435	0.06262	3.28225E-4	0.99997
4.75	1.33407	0.12661	0.07278	6.49183E-4	0.99994
4.5	1.40294	0.12621	0.06793	0.00138	0.99988
4.25	1.48125	0.12522	0.0783	0.00321	0.99994
4	1.56884	0.12281	0.08283	0.00827	0.99988
3.75	1.67032	0.12375	0.0886	0.0243	0.99978
3.5	1.79113	0.12733	0.09711	0.08158	0.99937
3.25	1.96083	0.13084	0.11919	0.32874	0.99863
3	2.13236	0.13754	0.13996	1.49712	0.99826
2.75	2.5895	0.13428	0.24705	8.86396	0.99455
2.25	3.76075	0.32312	0.13525	0.00237	0.99926
2	4.08724	0.33604	0.13737	0.00239	0.9987

Table A3. 16. Best fitted parameters (χ_T, χ_S, τ and α) with the extended Debye model for compound ^{166}**ErW$_{10}$·35H$_2$O** *(Rehydrated) at 0 Oe in the temperature range 2-5 K.*

T / K	χ_T / cm^3 mol^{-1}	χ_S / cm^3 mol^{-1}	α	τ / s	R²
4	2.12636	0.39657	0.23781	1.89629E-4	0.99979
3.75	2.26946	0.28004	0.24702	2.51636E-4	0.99979
3.5	2.43226	0.12296	0.26397	3.19775E-4	0.99978
3.25	2.62057	0.19122	0.23762	4.97027E-4	0.9997
3	2.83848	0.21017	0.23222	6.81564E-4	0.99981
2.75	3.08935	0.18363	0.23285	8.33973E-4	0.99977
2.5	3.401	0.21847	0.22871	9.83963E-4	0.99986
2.25	3.83946	0.22256	0.2483	0.0011	0.99964
2	4.23164	0.26678	0.23874	0.00116	0.99982
2.75	2.12636	0.26295	0.23781	1.89629E-4	0.99979
2.5	2.26946	0.27966	0.24702	2.51636E-4	0.99979
2.25	2.43226	0.32312	0.26397	3.19775E-4	0.99978
2	2.62057	0.33604	0.23762	4.97027E-4	0.9997

Table A3. 17. Best fitted parameters (χ_T, χ_S, τ and α) with the extended Debye model for compound ***Dy(ZnL^{17})$_2$*** *at 0 Oe in the temperature range 2-23 K.*

T / K	χ_T / cm^3 mol^{-1}	χ_S / cm^3 mol^{-1}	α	τ / s	R²
23	1.07694	0.30895	0.2169	2.72865E-4	0.99954
22	1.13219	0.30136	0.22165	3.35448E-4	0.99922
21	1.24487	0.25764	0.23773	4.66893E-4	0.99939
20	1.24487	0.25764	0.23773	4.66893E-4	0.99939
19	1.3022	0.26124	0.23052	5.69545E-4	0.99906
18	1.37568	0.25175	0.23272	6.78625E-4	0.99931
17	1.45706	0.2565	0.22842	8.08907E-4	0.99932
16	1.54866	0.2432	0.24383	9.34772E-4	0.99935
15	1.66397	0.23571	0.25352	0.00109	0.99915
14	1.78096	0.22864	0.25955	0.00124	0.99894
13	1.91438	0.23446	0.2629	0.0014	0.99887
12	2.06535	0.22748	0.27088	0.0015	0.99902
11	2.27893	0.22606	0.28017	0.0017	0.99888
10	2.50746	0.22785	0.28859	0.00182	0.99901
9	2.78209	0.22961	0.2926	0.00194	0.99892
8	3.12666	0.23376	0.29518	0.00202	0.99913
7	3.57335	0.25155	0.29679	0.00215	0.99904
6	4.16017	0.27707	0.29591	0.00224	0.99904
5	4.98071	0.31986	0.29487	0.00234	0.99905
4.5	5.55601	0.31321	0.29825	0.00235	0.99887
4	6.21072	0.39671	0.29369	0.00242	0.99909
3.5	7.08619	0.43328	0.29404	0.00247	0.99911
3	8.25537	0.50821	0.2935	0.00251	0.99913
2.5	9.90487	0.6105	0.29151	0.00254	0.9991
2	12.31522	0.72668	0.29056	0.00254	0.99905

*Table A3. 18. Best fitted parameters (χ_T, χ_S, τ and α) with the extended Debye model for compound ^{164}**Dy(ZnL^{17})$_2$** at 0 Oe in the temperature range 2-23 K.*

T / K	χ_T / cm^3 mol^{-1}	χ_S / cm^3 mol^{-1}	α	τ / s	R²
23	1.13199	0.00421	0.29249	2.60597E-4	0.99857
22	1.20542	0.02999	0.25607	3.60185E-4	0.99427
21	1.21089	0.02524	0.25184	4.41973E-4	0.9991
20	1.29934	0.02999	0.25039	6.07301E-4	0.99848
19	1.33098	0.03611	0.23594	7.58015E-4	0.99779
18	1.39871	0.05677	0.20218	9.66786E-4	0.99956
17	1.47152	0.0664	0.19034	0.00119	0.99945
16	1.5655	0.074	0.19329	0.00144	0.99922
15	1.6701	0.08185	0.19365	0.00172	0.99906
14	1.78974	0.08066	0.19747	0.00202	0.99915
13	1.93167	0.08675	0.20615	0.00233	0.99893
12	2.09179	0.09401	0.21445	0.00265	0.99869
11	2.28205	0.16003	0.19305	0.00311	0.99912
10	2.56105	0.09851	0.23923	0.00332	0.99858
9	2.8165	0.10806	0.23746	0.00351	0.99854
8	3.1681	0.11261	0.24271	0.00375	0.99864
7	3.65927	0.14377	0.24721	0.00416	0.9989
6	4.25513	0.10641	0.26106	0.00437	0.99886
5	5.12153	0.11318	0.26103	0.00475	0.9989
4.5	5.723	0.11533	0.26181	0.0049	0.99894
4	6.23791	0.151	0.23976	0.0048	0.99881
3.5	7.10575	0.18015	0.23399	0.00496	0.99882
3	8.37574	0.20248	0.23933	0.00521	0.99891
2.5	9.81482	0.56702	0.19362	0.0054	0.99916
2.2	11.47165	0.13942	0.27121	0.00582	0.99904
2	12.33442	0.25659	0.22555	0.00511	0.99879

A4. TGA ANALYSES

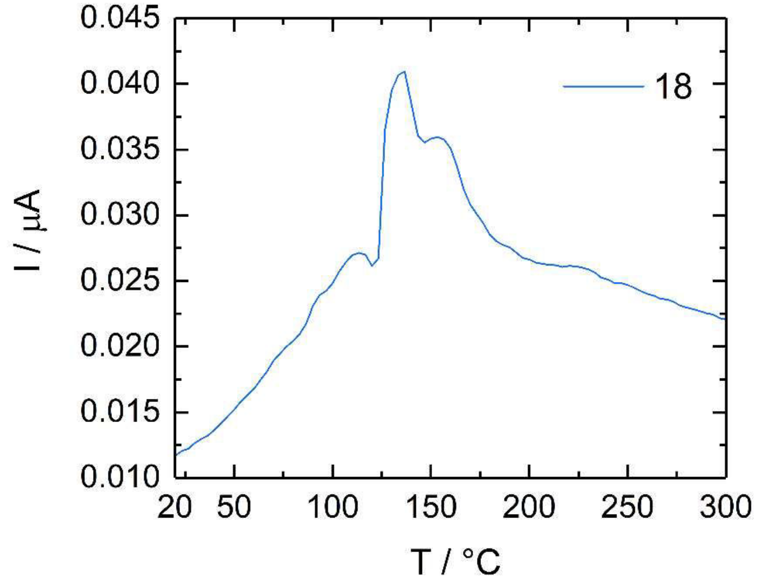

Figure A4. 1. Mass spectrum coupled to the TGA spectra, confirming M_w= 18 g mol^{-1}

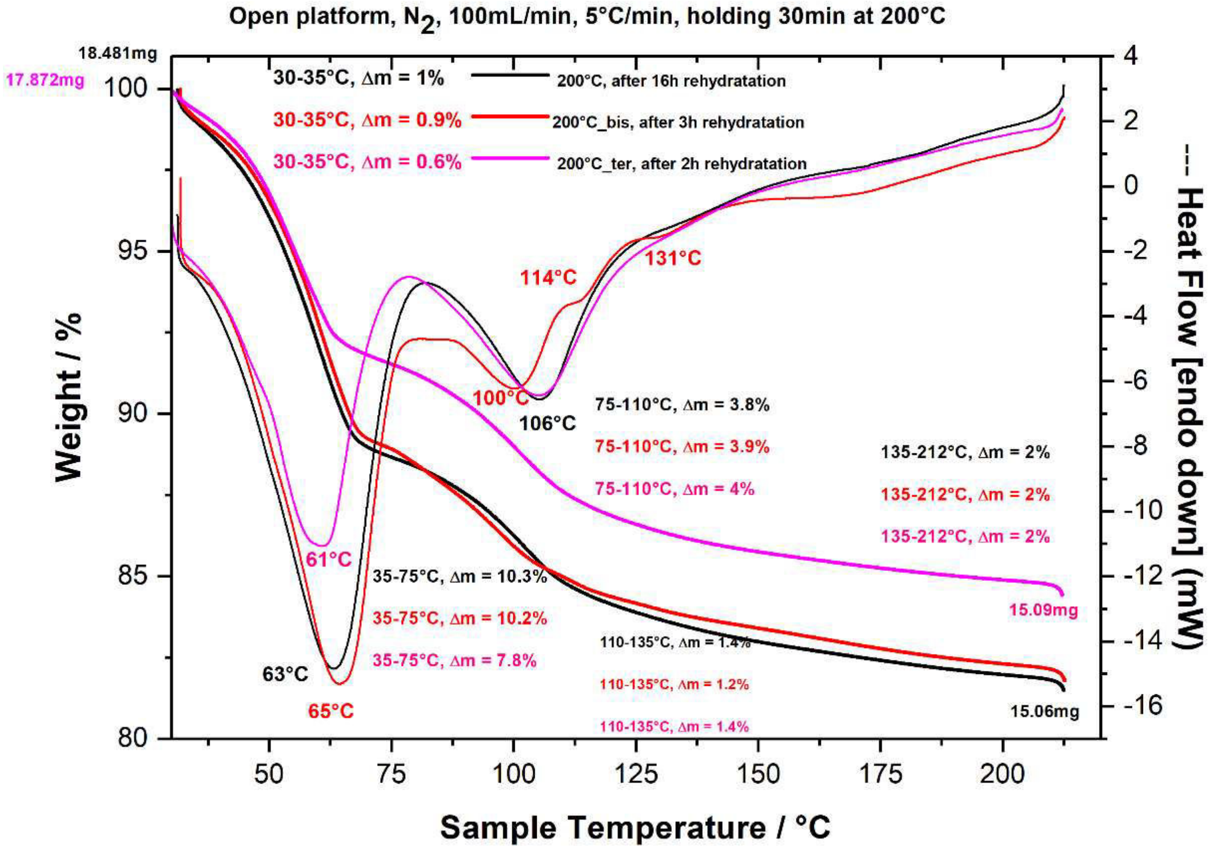

Figure A4. 2. Different consecutive cycles of TGA taking into account different rehydration conditions.

RESUME EN FRANÇAIS

Le magnétisme moléculaire réuni dans un même domaine de recherche le travail de chimistes, physiciens et scientistes des matériaux, afin de créer des objets moléculaires possédant des propriétés potentiellement intéressantes pour le traitement de l'information. Dans ce domaine, l'évolution des technologies sont basées sur l'augmentation de la capacité de stockage tout en miniaturisant le dispositif.

A la vue de cette évolution, les systèmes basés sur des molécules apparaissent comme des candidats idéals car ils donnent la possibilité d'une scalabilité dans leur fabrication avec des entités identiques à chaque fois et leur structure peut être adaptée afin de favoriser des propriétés désirées, comme la capacité de stocker une information magnétique à basse température. Cette capacité de stockage apparait lors de l'obtention d'un système possédant une bistabilité magnétique.

Les molécules aimants (SMMs) sont des objets qui possèdent une bistabilité magnétique d'origine purement moléculaire à basse température, montrant une hystérèse de son aimantation. Elle peut-être schématisée par un diagramme de double puits énergétiques chacun caractéristique d'une orientation du moment magnétique (« up » et « down », Figure R.1). Les deux puits énergétiques sont séparés par une barrière énergétique qu'il faut vaincre pour permettre le retournement de l'aimantation. Ce premier chemin est caractérisé par un régime thermiquement activé et une relaxation lente de l'aimantation, aussi nommée Orbach.[181]

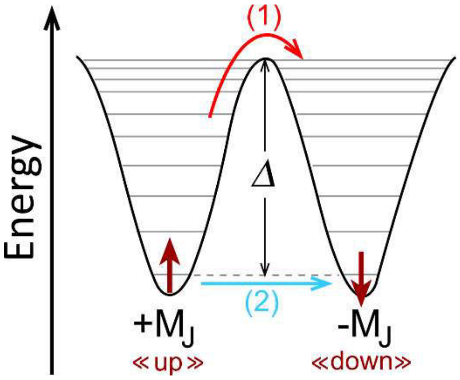

Figure R. 1. Schéma des chemins de relaxation d'un SMM (1) sur la barrière (Orbach) et (2) au-dessous (QTM and Raman).

Cependant, leur efficacité est fortement affaiblie par l'existence d'interactions inter- et intra- moléculaires, qui permettent d'autres chemins de relaxation d'énergie inférieure au processus Orbach, effet tunnel (QTM pour *Quantum Tunneling of the Magnetization* en anglais) et Raman, qui favorisent une accélération du temps de relaxation. Le premier, thermiquement indépendant, inclue le mélange des différents états M_J dans l'état fondamental, le deuxième, comporte des échanges avec la matrice à travers un état virtuel provenant des vibrations du système.[182] Dans le contexte de cette thèse, nous nous focalisons dans la compréhension des processus permettant une relaxation rapide de l'aimantation, et comment les différentes interactions dans le système modulent de tels mécanismes de relaxation.

Nous avons étduié le comportement magnétique de différentes molécules à base de lanthanides ainsi que les possibles stratégies pour son optimisation. De façon générale, différents complexes sont synthétisés sous forme de monocristaux. Leur structure est ensuite caractérisée par diffraction de rayons X sur monocristal (DRX) et le comportement magnétique est étudié par magnétométrie SQUID (Superconducting Quantum Interference Device) et PPMS (Physical Property Measurement System). Les détails sur les différentes étapes sont résumés dans le Chapitre II.

Des résultats publiés en 2013[183] puis 2015[184] par le laboratoire sont le point de départ de ces travaux. A ce niveau, le comportement aimant d'une molécule à base de Dy^{3+} [Dy(tta)$_3$(**L**^{2})] (avec tta= 2-thenoyltrifluoroacetonate et **L**^{2}= 4,5-bis(propylthio)-tetrathiafulvalene-2-(2-pyridyl)-benzimidazole methyl-2-pyridine) est prouvé et deux stratégies sont proposées pour l'optimisation des propriétés magnétiques: 1) la dilution magnétique et 2) l'enrichissement isotopique du centre métallique. Le dysprosium est constitué principalement de 4 isotopes stables: ^{161,163}Dy (qui possèdent un spin nucléaire *I*=5/2) et ^{162,164}Dy (qui possèdent un spin nucléaire *I*=0). Ces premières études ont montré que lors de l'enrichissement isotopique (à partir des complexes ^{161,164}**Dy**) et lors de la dilution magnétique, le comportement électronique du complexe (χT vs. T et M vs. H) ne varie pas, mais qu'on peut moduler les différents processus de relaxation. La diminution des interactions dipolaires entre les ions Dy^{3+} voisins par dilution magnétique et la suppression des interactions hyperfines entre le noyau et les électrons (*I*=0) engendre une relaxation de l'aimantation beaucoup plus lente pour ^{164}**Dy@Y**.

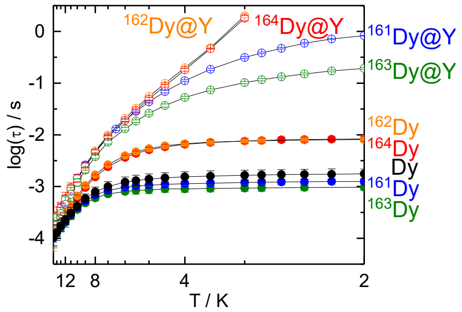

Figure R. 2. Évolution thermique de la relaxation τ en fonction de la température pour les 4 complexes isotopiques $^{161\text{-}164}$***Dy*** *(cercles pleins) et les dilués* $^{161\text{-}164}$***Dy@Y*** *sans champ appliqué.*

Toutefois, les interactions hyperfines ne dépendent pas seulement du spin nucléaire (*I*) mais aussi de certaines constantes de couplage qui sont différentes en fonction de l'isotope.

Dans le Chapitre III nous trouvons l'étude complète pour les 4 isotopes stables (Figure R.2) et l'importance de ces constantes de couplage est mise en évidence. Si nous comparons ^{161,163}**Dy**, il apparait une légère différence dans les temps de relaxation, qui devient beaucoup plus importante lors du processus de dilution ^{161,163}**Dy@Y**. La suppression des interactions dipolaires permet d'appréhender la contribution des interactions avec le noyau : Plus l'interaction hyperfine est forte et plus la relaxation va être rapide.[185]

Par la suite (Chapitre IV), le cation métallique est modifié pour étudier la tendance des mécanismes de relaxation face aux deux stratégies lors d'une distribution électronique différente (de «prolate» avec le dysprosium à «oblate» avec l'erbium et l'ytterbium). Comme conséquence du changement de cation lanthanide le système ne montre plus une dépendance avec la fréquence et par conséquent le système perd son caractère SMM. Néanmoins, comme nous avons vu précédement avec le système à base de dysprosium, la relaxation de l'aimantation peut être ralentie d'un facteur 4000 avec l'application simultanée des deux stratégies. La dilution magnétique du système à base d'ytterbium a donné lieu à une relaxation lente de l'aimantation et l'effet dû à l'enrichissement isotopique suit le même comportement que pour le dysprosium (Figure R.3).

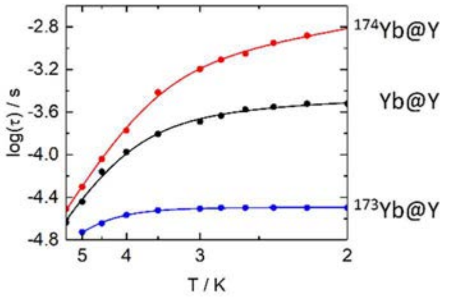

Figure R. 3. Évolution thermique de la relaxation τ en fonction de la température pour les 4 complexes isotopiques ^{173,174}***Yb@Y*** *and* ***Yb@Y****.*

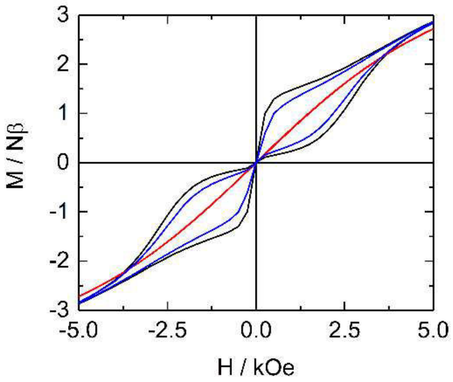

Figure R. 4. Comparaison des différents cycles d'hystérèse selon la nature hydraté/deshydraté de l'échantillon

Le non-comportement de molécule aimant pour l'analogue **Er** fait que nous devons considérer un autre system pour l'étude de l'effet des interactions hyperfines. Dans le Chapitre V, nous avons choisi une molécule aimant déjà existante dans la littérature à base d'ion Er^{3+} (**ErW$_{10}$**: $Na_9[Er(W_5O_{18})_2]\cdot 35H_2O$).[186] Ce composé est formé par deux polyoxometallates lacunaires qui sont liés par l'ion Er^{3+}. Il est à la fois constitué par un réseau d'ion Na^+ et de molécule d'eau, qui ont une influence très importante sur les propriétés magnétiques. L'évolution du composé en fonction de la température a été suivie par une étude thermogravimétrique (ATG) couplée à une spectroscopie de masse. Elle montre la perte progressive des molécules d'eau en trois étapes principales en fonction du nombre de liaisons covalentes que les molécules d'eau entretiennent avec le réseau (libres, terminales et pontantes), et en même temps la recaptation d'eau apparait réversible. Cette réversibilité a été étudiée aussi en fonction de la structure cristalline (par DRX sur poudre et en T) et des propriétés magnétiques. Comme nous pouvons l'observer sur la Figure R.4, ce système peut être défini comme un commutateur hydromagnétique. Dans la littérature il a été montré l'effet isotopique lors de l'enrichissement avec $^{167}Er^{3+}$ ($I \neq 0$). Nous avons par conséquent synthétisé son isotopologue $^{166}Er^{3+}$ ($I=0$). Si nous comparons ce nouvel isotope avec le complexe naturel (**ErW_{10}**), nous remarquons qu'il n'existe pas de différence significative entre les deux. Ceci peut être expliqué par le fait que l'erbium est constitué en grande majorité par des isotopes avec $I=0$ (77%), et que nous n'avons pas éliminé les interactions dipolaires entre voisins. Le comportement à basse température de l'analogue **$^{167}ErW_{10}$** montre une grande dispersion des processus de relaxation, rendant difficile la compréhension.

Pour conclure, le choix des deux derniers systèmes à base de Dy et avec coordinance 9 prétend (chapitre VI) étudier le comportement des propriétés magnétiques et le rôle de différentes interactions en changeant la sphère de coordination du métal, ou dans d'autres mots, la distribution électronique autour de celui-ci. Comme résultat, les effets de la relaxation de l'aimantation face à la dilution et l'enrichissement isotopique suivent la même tendance trouvée pour les systèmes précédents à base de Dy et Yb.

Pour la suite il est envisagé d'étudier un nouveau système à base d'erbium se comportant comme une molécule aimant, pour une meilleure compréhension de l'effet isotopique et des évènements qui ont lieu[187] dans les propriétés dynamiques de ce système.

[181] a) R. Sessoli, D. Gatteschi, A. Caneschi, M. A. Novak, *Nature*, **1993**, *365*, 141. b) R. Sessoli, H. L. Tsai, A. R. Schake, S. Wang, J. B. Vincent, K. Folting, D. Gatteschi, G. Christou and D. N. Hendrickson, *J. Am. Chem. Soc.*, **1993**, *115*, 1804.

[182] J. Tang, and P. Zhang, *Lanthanide Single Molecule Magnets*, Springer, Berlin, **2015**.

[183] T. T. da Cunha, J. Jung, M.-E. Boulon, G. Campo, F. Pointillart, C. L. M. Pereira, B. Le Guennic, O. Cador, K. Bernot, F. Pineider, S. Golhen, and L. Ouahab*, J. Am. Chem. Soc.* **2013**, *135*, 16332.

[184] F. Pointillart, K. Bernot, S. Golhen, B. Le Guennic, T. Guizouarn, L. Ouahab, and O. Cador, *Angew. Chem.*, **2015**, *127*, 1524.

[185] J. Flores Gonzalez, F. Pointillart, and O. Cador, *Inorg. Chem. Front.*, **2019**, *6*, 1081.

[186] a) M. A. Aldamen, J. M. Clemente-Juan, E. Coronado, C. Martí-Gastaldo and A. Gaita-Ariño, *J. Am. Chem. Soc.,* **2008**, *130*, 8874; b) M. A. AlDamen, S. Cardona-Serra, J. M. Clemente-Juab, E. Coronado, A. Gaita-Ariño, F. Luis and O. Montero, Inorg. Chem., **2009**, *48*, 3467; c) F. Luis, M. J. Martí-Perez, and O. Montero, *Phys. Rev. B*, **2010**, *82*, 060403(R).

[187] a) A.-L. Boulkedid, J. Long, C. Beghidja, Y. Guari, A. Beghidja and J. Larionova, *Dalton Trans*, **2018**, *47*, 1402; b) W.-K. Lo, W.-K. Wong, W.-Y. Wong, J. Guo, K.-T. Yeung, Y.-K. Cheng, X. Yang and R. A. Jones, *Inorg. Chem.*, **2006**, *45(23)*, 9315; c) W.-B. Sun, P.-F. Yan, S.-D. Jiang, B.-W. Wang, Y.-Q. Zhang, H.-F. Li, P. Chen, Z.-M. Wang and S. Gao, *Chem. Sci.*, **2016**, *7(1)*, 684; d) X. Lü, W. Bi, W. Chai, J. Song, J. Meng, W.-Y. Wong, W.-K. Wong and R. A. Jones, *New. J. Chem,* **2008**, *32*, 127.

UNIVERSITE BRETAGNE LOIRE / MATIERE MOLECULES ET MATERIAUX

UNIVERSITÉ DE RENNES 1

Titre : Enrichissement isotopique de molécules aimants à base d'ions lanthanides

Mots clés : Magnétisme moléculaire – lanthanides – enrichissement isotopique – dilution magnétique – relaxation lente – cycle d'hystérèse — effet tunnel de l'aimantation

Résumé : Les matériaux moléculaires, et plus précisément ceux à base d'ions lanthanides, ont été largement étudiés pour leur utilisation dans différentes applications, dont le stockage de l'information ou l'ordinateur quantique. Cet intérêt s'explique du fait que des systèmes contenant des ions lanthanides donnent lieu à une large anisotropie et une bistabilité magnétiques d'origine purement moléculaire. Durant les vingt-cinq dernières années, beaucoup d'articles ont été publiés dans lesquels les composés à base de ces ions montraient une relaxation lente de leur aimantation et une hystérèse magnétique à basse température. Récemment, des recherches ont menées à l'obtention de systèmes moléculaires présentant des températures de blocage (température maximale à laquelle le système se comporte comme à superparamagnétique) proche de l'azote liquide ce qui facilite le transfert dans des dispositifs basés sur ces systèmes.

Cependant, cette relaxation lente de l'aimantation est souvent accompagnée des phénomènes quantiques, donnant lieu à d'autres relaxations beaucoup plus rapides. Les phénomènes quantiques peuvent donner lieu à de nouvelles applications mais à condition de bien comprendre leurs mécanismes d'action.

Les interactions dipolaires et les hyperfines, les premiers provenant des molécules voisines et la deuxième de l'interaction spin-noyau dans le métal, sont connus pour participer à l'origine de ces phénomènes. Quelques systèmes ont été choisis durant ce travail de thèse dans le but de mieux comprendre les évènements quantiques et la contribution des différentes interactions. Ceci a mené à la synthèse et aux caractérisations magnétiques de différents systèmes magnétiquement dilués (étude des interactions dipolaires) et isotopiquement enrichis (étude des interactions hyperfines), afin de mettre en évidence une tendance générale pour l'optimisation des processus de relaxation lente.

Title : Isotopic enrichment of lanthanide based single molecule magnets

Keywords : Molecular magnetism – lanthanides – isotopic enrichment – magnetic dilution – slow relaxation – hysteresis loop — quantum tunneling of the magnetization

Abstract : Molecular materials, and in particular those based on Lanthanides, have been extensively studied for their use in data storage, spintronics and quantum computing, as they promise high anisotropic systems and magnetic bistability of the discrete entity. Actually, in the last twenty-five years a plethora of compounds have been reported, thus showing slow of their magnetic relaxation and the characteristic magnetic hysteresis at low temperature. Moreover, some of the last investigations have reach blocking temperatures (temperature for which the system shows superparamagnetic behavior) at the liquid nitrogen level, hence facilitating the applicability of devices based on these molecules.

However, the slow relaxation is commonly accompanied by quantum phenomena, favoring a fasten relaxation. The quantum effects open the possibility to different magnetic objects, but only if the operating mechanisms are well known.

Dipolar interactions, with the neighboring molecules, and hyperfine interactions, with the metal ion, are known to be some of the reasons why this fast relaxations occurs. With the aim of acquiring a better understanding of the quantum events, and the contribution of the different interactions, different systems have been chosen to be studied in this work. Thus, the synthesis and magnetic characterization of magnetically diluted (suppression of dipolar interactions) and isotopic enrichment (tuning of the hyperfine interactions) of the different systems have been performed in order to find a general direction for the optimization of the slow relaxation process.